

Alma Mater Studiorum - Università di Bologna

DOTTORATO DI RICERCA IN
CHIMICA

Ciclo 33

Settore Concorsuale: 03/A2 - MODELLI E METODOLOGIE PER LE SCIENZE CHIMICHE

Settore Scientifico Disciplinare: CHIM/02 - CHIMICA FISICA

ADVANCED LUMINESCENT MATERIALS FOR TECHNOLOGICAL
APPLICATIONS

Presentata da: Sheng Gao

Coordinatore Dottorato

Domenica Tonelli

Supervisore

Letizia Sambri

Co-supervisori

Nicola Armaroli

Andrea Barbieri

Esame finale anno 2021

Abstract

This thesis focusses on the study of several luminescent materials and investigates some related technological applications. It is made of six chapters. Chapter 1 introduces a brief history, basic principles and applications of photoluminescence, as well as a short introduction to DFT calculations.

In chapter 2, I present the basic photophysical properties of five bright benzoheterodiazole dyes with large Stokes' shifts. These conjugated molecules were then incorporated in PMMA- and PDMS-based LSC-PV devices to determine the emission quantum yields as well as transmission, re-absorption and IPCE properties. DFT calculations were also performed to investigate the structures and energy levels of these dyes.

Chapter 3 concerns the preparation of a luminescent film to calibrate an ESA satellite that will monitor the fluorescence of terrestrial vegetation. ZnPc was selected as a suitable dye to make the film, as it exhibits NIR fluorescence. Ferrocene was then selected as a quencher of ZnPc to control the emission intensity of the luminescent film. An industrial printing technology was used to produce large-area calibration wood sheets coated with a green water-based pigment that simulates the NIR reflectance of green plants in which the ZnPc fluorophore is embedded.

Photophysical properties of a novel series of alkynyl gold *N*-heterocyclic carbene complexes containing a naphthalimide chromophore were studied in Chapter 4. All of the compounds were studied in solution (air-equilibrated and deoxygenated) and solid state both at 298 K and 77 K. Further investigations were carried out by incorporating these compounds in PMMA matrix to make transparent films. XRD and DFT calculations were also made to determine the structures and energy levels of the complexes.

In chapter 5, we studied the stability and photophysical properties of two star-shaped molecular systems which can operate as molecular rotary motors when attached onto a surface, along with those of their related ligands/moieties in tetrahydrofuran solution both at 298 and 77 K. The photophysical properties of these two star-shaped molecular systems can show if they are suitable to operate as light-triggered molecular machines.

Finally, chapter 6 concerns the photoluminescence behavior of three *N*-heterocyclic carbene half-sandwich Ir/Rh metal complexes. The photophysical properties of these compounds were examined in CH₂Cl₂ solutions (298 K and 77 K) and PMMA films. These complexes may prove potential candidates for organic phosphorescent materials.

Author Declaration

This thesis is submitted for the Chemistry degree of Doctor of Philosophy (PhD) at the University of Bologna (33rd cycle). Work made at CNR-ISOF (photochemistry/photophysics, DFT calculations, LSC device fabrication and characterization) was carried out by Sheng Gao, under the supervision of Filippo Monti, Barbara Ventura, Alessandro Venturini, Elisa Bandini, Andrea Barbieri and Nicola Armaroli. The research illustrated herein has been made in cooperation with CSIR-NIIST (molecular design and synthesis in chapter 2, Bamisha Balan and Dr. Karuvath Yoosaf), Renner Italia (preparation of the large-area calibration film in chapter 3, Dr. Luigi Benni); CNR-IBIMET (study on field of large-area calibration surfaces in chapter 3, Dr. Lorenzo Genesisio and Dr. Francesco Miglietta), IPCM-CNRS (molecular design and synthesis in chapter 4 and 6, group of Prof. Hani Amouri), CEMES-CNRS (molecular design and synthesis in chapter 5, group of Prof. Gwenael Rapenne).

*CSIR-NIIST: Council of Scientific & Industrial Research of National Institute for Interdisciplinary Science and Technology, Thiruvananthapuram, Kerala (India).

*CNR-IBIMET: Institute of Biometeorology of the National Research Council of Italy, Florence.

*Renner Italia S.p.A., via Ronchi Inferiore, 34 - 40061 Minerbio (BO) Italy.

*IPCM-CNRS: Parisian Institute for Molecular Chemistry of the French National Centre for Scientific Research, Paris (France).

*CEMES-CNRS: Centre d'Elaboration de Matériaux et d'Etudes Structurales of the French National Centre for Scientific Research, Toulouse (France).

Copyright Declaration

The copyright of this thesis rests with the author and is made available under a Creative Commons Attribution Non-Commercial No Derivatives licence. Researchers are free to copy, distribute or transmit the thesis on the condition that they attribute it, that they do not use it for commercial purposes and that they do not alter, transform or build upon it. For any reuse or redistribution, researchers must make clear to others the licence terms of this work.

List of Abbreviations

ADF	Amsterdam Density Functional
AM1	Austin Model 1
ATP	Adenosine Triphosphate
B3LYP	Becke 3-parameter Lee-Yang-Parr method
BIPV	Building-Integrated Photovoltaics
BQ	p-Benzoquinone
CT	Charge Transfer
DCM	Dichloromethane
DFT	Density Functional Theory
DMF	Dimethylformamide
DNA	Deoxyribonucleic Acid
ECP	Effective Core Potential
EET	Electronic Energy Transfer
EQE	External Quantum Efficiency
ESA	Excited State Absorption or European Space Agency
ESI	Electrospray Ionization
ETU	Energy Transfer Upconversion
Fc	Ferrocene
FLEX	Fluorescence Explorer mission
FRET	Fluorescence Resonance Energy Transfer
FTIR	Fourier Transform Infrared spectroscopy
GGA	Generalized Gradient Approximation
GOME-2	Global Ozone Monitoring Experiment 2
GOSAT	Greenhouse Gases Observing Satellite
GSB	Ground State Bleaching
GTOs	Gaussian-Type Orbitals
HF	Hartree-Fock method
HOMO	Highest Occupied Molecular Orbital
IC	Internal Conversion
IPCE	Incident Photon-to-electron Conversion Efficiency
IR	Infrared
ISC	Intersystem Crossing

LDA	Local Density Approximation
LED	Light Emitting Diode
LSC	Luminescent Solar Concentrator
LUMO	Lowest Unoccupied Molecular Orbital
M06	Minnesota functional 06
M06-2X	Minnesota functional 06-2X
MeOH	Methanol
meta-GGAs	Meta-Generalized-Gradient Approximations
MP	Melting Point
MP2	Moller-Plesset perturbation theory 2
MP4	Moller-Plesset perturbation theory 4
MS	Mass Spectroscopy
MV	Methyl Viologen
NBS	<i>N</i> -bromosuccinimide
NHC	<i>N</i> -heterocyclic Carbene
NI	Naphthalimide
NIR	Near Infrared
NMR	Nuclear Magnetic Resonance
NTOs	Natural Transition Orbitals
NUV	Near Ultra Violet
OCO-2	Orbiting Carbon Observatory 2
OLEDs	Organic Light-Emitting Diodes
OQE	Optical Quantum Efficiency
ORTEP	Oak Ridge Thermal-Ellipsoid Plot
PA	Photon Avalanche
PBAC	Poly(bisphenol A carbonate)
PC	Poly-Carbonate
PCM	Polarizable Continuum Model
RDFT	Relativistic Density Functional Theory
PDMS	Polydimethylsiloxane
PEBC	Cholesterol-modified Perylene Bisimide derivative
PLQY	Photoluminescence Quantum Yield
PM6	Parametric Model 3
PMMA	Poly(methyl methacrylate)

PS	Polystyrene
PSI	Photosystem I
PSII	Photosystem II
PV	Photovoltaic
rISC	Reverse Intersystem Crossing
SCIAMACHY	Scanning Imaging Absorption Spectrometer for Atmospheric CHartographY
SDD	Stuttgart/Dresden pseudopotential basis set
STOs	Slater-Type Orbitals
STO-NG	Slater-Type Orbital combined by N Gaussian-Type Orbitals
sTTA	Sensitized Triplet-Triplet Annihilation
TCSPC	Time-Correlated Single-Photon Counting
TDDFT	Time-Dependent Density Functional Theory
THF	Tetrahydrofuran
TMS	Tetramethylsilane
TPP	Meso-tetraphenylporphyrin
TROPOMI	TROPOspheric Monitoring Instrument
TTA	Triplet-Triplet Annihilation
UV	Ultra Violet
VASP	Vienna Ab Initio Simulation Package
Vis	Visible
VR	Vibrational Relaxation
XRD	X-ray Diffraction
ZnPc	Zinc Phthalocyanine

List of Symbols

λ	Wavelength of light
λ_{abs}	Absorption wavelength
λ_{exc}	Excitation wavelength
λ_{ems}	Emission wavelength
ν	Frequency of light
h	Planck's constant
ϵ	Molar absorption coefficient
S_0	Ground state
S_n	Singlet excited state
T_n	Triplet excited state
Φ	Quantum yield
Φ_{PL}	Photoluminescence quantum yield
k_r	Rate constant of radiative deactivation
k_{nr}	Rate constant of non-radiative deactivation
τ	Excited-state lifetime
τ_r	Radiative lifetime
τ_n	Intrinsic or natural lifetime
A%	Absorption factor
T%	Transmittance
R%	Reflectance
G	Geometric gain of the PMMA LSC device
F	Flux gain of the PMMA LSC device
S_{surf}	Surface area of the PMMA LSC device
S_{edge}	Edges area of the PMMA LSC device
η_{trap}	Trapping efficiency of the PMMA LSC device
P_E	Edge-emitted power of the PDMS LSC device
P_0	Incident power of the PDMS LSC device
η_0	Responsivity of the SM1PD2A silicon photodiode
A_E	Edge areas of the PDMS LSC device
A_{PV}	Effective surface areas of KXOB22-12X1F PV cells
ΔA	Differential absorbance

Φ_{Δ}	Singlet oxygen sensitization efficiency
λ_{fluo}	Wavelength of fluorescence
λ_{phos}	Wavelength of phosphorescence
Φ_{fluo}	Fluorescence quantum yield
Φ_{phos}	Phosphorescence quantum yield
τ_{fluo}	Fluorescence lifetime
τ_{phos}	Phosphorescence lifetime

Contents

Abstract	2
Author Declaration	4
Copyright Declaration	4
List of Abbreviations	5
List of Symbols	8
Chapter 1	14
Introduction	14
1.1 Brief history of photoluminescence	14
1.2 Basic principles of photophysics	16
1.2.1 Light and absorption spectra	16
1.2.2 Electronic excited states.....	17
1.2.3 Excited states deactivation.....	18
1.2.4 Triplet state and phosphorescence	21
1.2.5 Emission and excitation spectra	22
1.2.6 Stokes' shift, mirror image law and Kasha's rule.....	23
1.2.7 Quantum yield and excited-state lifetime	25
1.2.8 Fluorescence quenching.....	26
1.3 A short introduction to DFT calculation	28
1.4 Applications of photoluminescence	31
Chapter 2	34
Benzoheterodiazole dyes and their application on LSC	34
2.1 Introduction	34
2.2 Experimental section	35
2.2.1 Synthesis of benzoheterodiazole dyes	35
2.2.2 Photophysics	40

2.2.3 Preparation and characterization of the PMMA based LSCs.....	41
2.2.4 Preparation and characterization of the PDMS based LSCs.....	42
2.2.5 DFT calculation methods.....	43
2.3 Results and Discussion.....	43
2.3.1 Photothermal stability in DCM.....	43
2.3.2 Photophysics in solutions and DFT calculation results.....	44
2.3.3 Photophysics and optical properties of PMMA based LSCs.....	52
2.3.4 Photophysics and IPCE of PDMS based LSCs.....	60
2.4 Conclusion.....	67
Chapter 3.....	69
Preparation and characterization of a luminescent film to calibrate a satellite for vegetation monitoring.....	69
3.1 Introduction.....	69
3.2 Experimental section.....	71
3.2.1 Preparation of luminescent films.....	71
3.2.2 Photophysical measurements.....	72
3.3 Results and Discussion.....	72
3.3.1 Photophysics in PMMA films.....	72
3.3.2 Photophysics in PS films.....	75
3.3.3 Photophysics in PBAC films.....	78
3.3.4 Fluorescence quenching of ZnPc in PBAC films.....	81
3.3.5 Large area luminescent calibrator.....	84
3.4 Conclusion.....	86
Chapter 4.....	87
Photophysical investigations of luminescent gold(I) alkynyls complexes adorned with <i>N</i>-heterocyclic carbenes and naphthalimide chromophores.....	87
4.1 Introduction.....	87

4.2 Experimental section	88
4.2.1 Synthesis of NHC alkynyl gold(I) complexes	88
4.2.2 X-Ray crystal structure characterization	93
4.2.3 Photophysical measurements	93
4.2.4 Preparation and characterization of the PMMA films	94
4.2.5 Computational details	95
4.3 Results and Discussion	95
4.3.1 XRD structure analysis	95
4.3.2 Photothermal stability in solutions	97
4.3.3 Photophysics in solutions	100
4.3.4 Photophysics of the solid samples	109
4.3.5 Photophysics in PMMA matrix	109
4.3.6 Theoretical calculation results	112
4.4 Conclusion	114
Chapter 5	115
Photophysical properties of molecular motors based on star-shaped ruthenium complexes containing a tripodal ligand	115
5.1 Introduction	115
5.2 Experimental section	116
5.3 Results and Discussion	117
5.3.1 Photothermal stability in THF	117
5.3.2 Absorption in THF	118
5.3.3 Emission in THF	119
5.4 Conclusion	122
Chapter 6	123
Photophysical properties of <i>N</i>-heterocyclic carbenes based half-sandwich iridium/rhodium complexes containing naphthalimide chromophore	123

6.1 Introduction	123
6.2 Experimental section	124
6.2.1 Photophysical measurements	124
6.2.2 Preparation and characterization of the PMMA films	125
6.2.3 Computational details	125
6.3 Results and discussion	126
6.3.1 Photothermal stability in solutions	126
6.3.2 Photophysics in solutions.....	126
6.3.3 Photophysics in PMMA matrix	130
6.3.4 Theoretical calculation results.....	134
6.4 Conclusion.....	136
Chapter 7.....	137
Conclusions and Outlook.....	137
7.1 Conclusions	137
7.2 Outlook.....	138
References	139
Acknowledgements	148

Chapter 1

Introduction

1.1 Brief history of photoluminescence

In our natural and artificial world, a lot of materials can be excited by electromagnetic radiation and release luminescence, i.e., photoluminescence. The phenomenon of luminescence has been observed from lightning, aurora borealis, fireflies and certain sea bacteria since the early human history, as testified by records in ancient Greek, Indian and Chinese literature.^[1] But all of these early observations do not concern photoluminescence, until in 1565 the Spanish physician and botanist Nicolas Monardes observed a special blue light emission from a solution of lignum nephriticum (a traditional diuretic extracted from the wood of narra tree).^[2]

The historical moment for photoluminescence occurred in 1603, when the Italian shoemaker and alchemist Vincenzo Casciarolo synthesized the first artificial luminescent material through heating the natural mineral barium sulphate (BaSO_4) with coal during alchemy experiments. He found that the resulting material glowed for hours in the dark after being exposed to sunlight; accordingly, the stone was named “lapis solaria” or “sun stone”. It was also called the “Bologna stone”, because the original mineral was extracted from volcanic rocks near Bologna. The luminous mechanism of the Bologna stone has been a mystery for a long time, but now we know that this material was doped with transition metals^[3] and the luminescence of the Bologna stone is indeed phosphorescence. In 1640, Fortunius Licetus wrote the first book about the Bologna stone with the title “Litheosphorus” (Figure 1.1). Since then, many experiments on the phenomenon of luminescence were made.

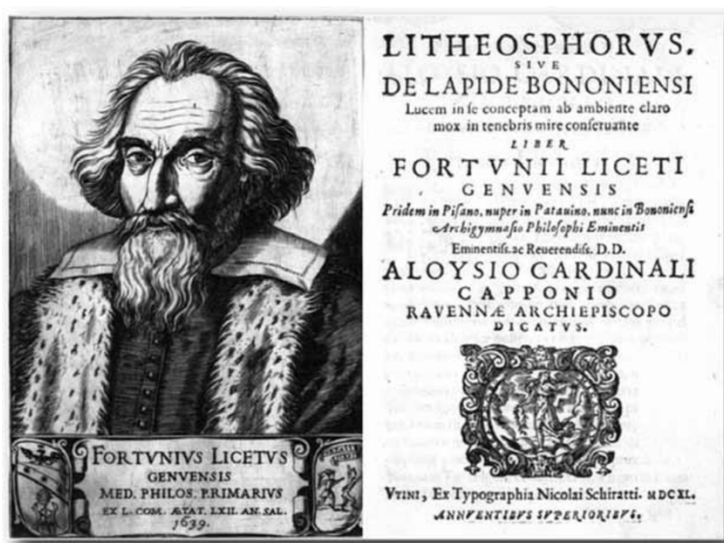


Figure 1.1: Portrait of Fortunius Licetus and the book Litheosphorus Sive de Lapide Bononiensi (Bologna, Italy, 1640).^[4]

In the following history of photoluminescence, lots of minerals, plants and artificial luminescent materials were investigated. The most important research was carried out by Sir George Gabriel Stokes, an Anglo-Irish physicist and mathematician from the University of Cambridge. In 1852, he described the fluorescence behavior of both organic (quinine) and inorganic (fluorspar) materials in his famous paper entitled “On the Refrangibility of Light”.^[5] In his experiment – where sunlight passed through a blue glass (excitation filter) to get invisible UV light as excitation light source, and a yellow glass of white wine served as emission filter – Stokes observed a light-blue glow from the quinine solution (Figure 1.2). He also used a prism to obtain the monochromatic light, and observed that the quinine solution remained transparent under visible light, but glowed with blue light under invisible UV radiation. These experiments led Sir George Gabriel Stokes to make an important discovery for the photoluminescence: the wavelengths of photoluminescence is always longer than the excitation light.

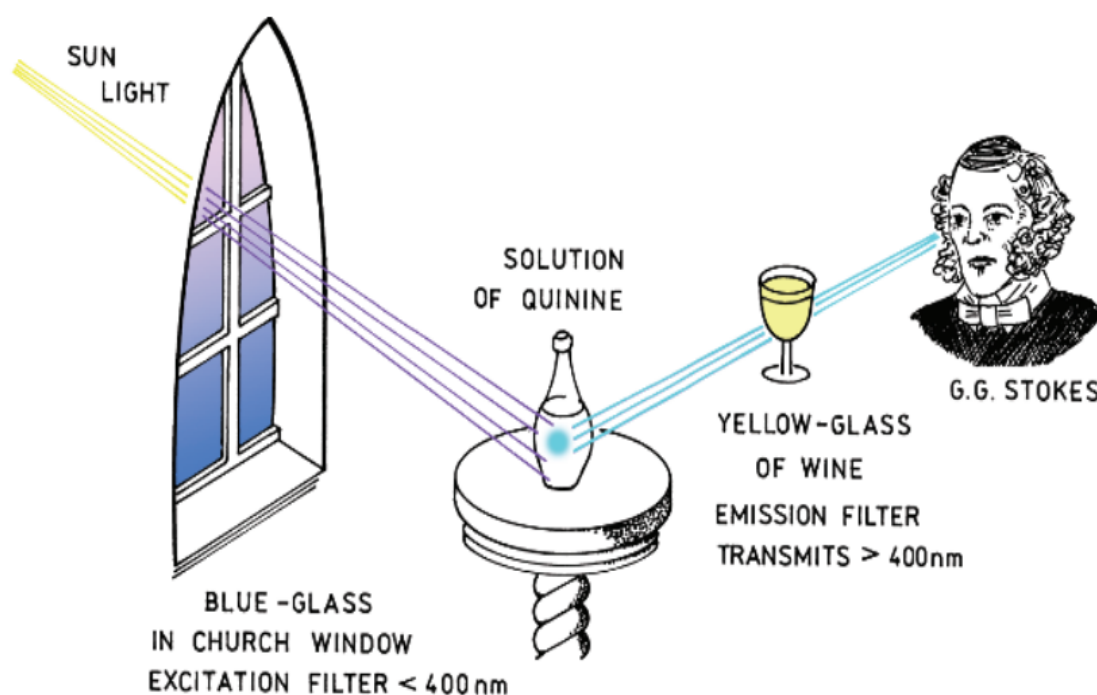


Figure 1.2: Experimental observation of fluorescence by George Gabriel Stokes.^[6]

In 1888, the word luminescence was first used by the German physicist Eilhard Wiedemann, who also made a classification.^[7] Between the end of 19th century and the beginning of 20th century, with the continuous development of quantum theory and theory of relativity, various theoretical models and experimental methods were established to explain and study the phenomenon of photoluminescence. Nowadays, we are still continuing this story, with more and more photoluminescent materials being synthesized or discovered, and applied in many applications all over the world.

1.2 Basic principles of photophysics

1.2.1 Light and absorption spectra

Compared with other portions of the electromagnetic spectrum (radio waves, microwaves, infrared, ultraviolet, X-rays and gamma rays), visible light was first discovered and studied by humans, because it can be observed by our eyes and felt by our skin. Visible light only covers a minuscule part of the electromagnetic spectrum (Figure 1.3); besides visible light, a portion of ultraviolet (UV) and infrared (IR) light is also very important to photochemistry and photophysics. The wavelength of light (λ) is defined as follows:

$$\lambda = c/\nu \quad (1.1)$$

in which c is the speed of propagation (2.998×10^8 m/s in vacuum), and ν is the frequency of the wave (SI unit : Hz). The energy (E) of the electromagnetic wave follows the equation:

$$E = h\nu \quad (1.2)$$

where h is the Planck's constant (6.626×10^{-34} J·s = 4.136×10^{-15} eV·s). The portion of the electromagnetic spectrum which is most relevant for photochemistry/photophysics ranges from 200 nm to 1000 nm and includes the near ultraviolet (NUV), visible and near infrared (NIR) regions (Figure 1.3).

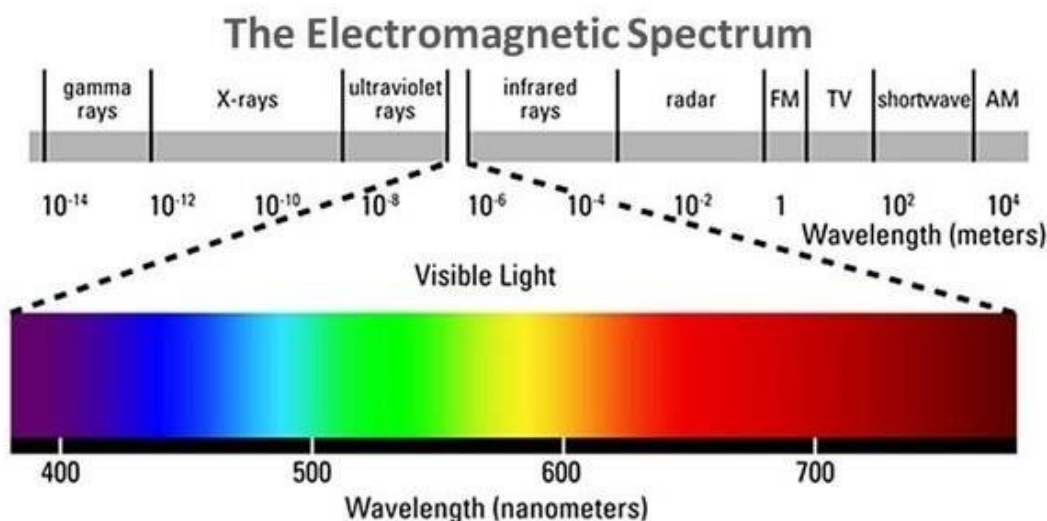


Figure 1.3: The electromagnetic spectrum and the close-up of visible light.^[8]

Due to the physiological limitations of the human eye, we cannot perceive UV and IR light. In the visible region, light can be distinguished by our eyes with a series of colors (red, orange, yellow, green, cyan, blue and violet), which corresponds to radiation of increasing energy. Light interacts with matter, which can absorb specific

frequencies, with the other ones (termed complementary) being reflected back into our eyes. Ultimately, the different interaction of light with different types of matter makes our colorful world. The interaction of light and matters can originate photophysical and photochemical phenomena. In the latter, the chemical nature of the matter changes (photochemical reaction), in the former it does not change.

The absorption capacities of substances to different monochromatic wavelengths are not the same. In transparent solution, the absorption capacity of a substance to absorb monochromatic light is described by Lambert-Beer law:

$$I = I_0 \times 10^{-\epsilon bc} \quad (1.3)$$

in equation (1.3), I is the intensity of transmitted light, I_0 is the intensity of the incident light, ϵ is the molar absorption coefficient with unit $M^{-1}cm^{-1}$, b is the pathlength (in cm units), and c is the molar concentration of the sample.

The absorption spectrum of a substance can be obtained by measuring the absorbance (A) at different wavelengths, where A is described by the following equation:

$$A = \log(I_0 / I) = \epsilon bc \quad (1.4)$$

Usually, we use the molar absorption coefficients (ϵ) to evaluate the absorption capacity of a substance to absorb light, and ϵ refers to a specific wavelength of light absorbed.

1.2.2 Electronic excited states

According to the Stark-Einstein law, when ambient light interacts with matter, one molecule absorbs only one photon and reaches the electronically excited state.^[9] This process is schematically written as follows:



where A represents the ground state molecule, $h\nu$ is the energy of the absorbed photon, A^* denotes the molecule in its electronically excited state. Compared with the ground state molecule A , an extra energy $h\nu$ is loaded onto excited molecule A^* . Because of this extra energy, the excited state molecule acquires new physical and chemical properties.

The photophysical processes typically occurring in an organic molecule are easily described by the so-called Jablonski diagram^[10] (Figure 1.4) which includes absorption, emission, internal conversion and intersystem crossing processes. In Figure 1.4, S and T indicate the singlet and triplet energy levels (the details of the multiplicity of electronic excited states will be discussed in 1.2.4), S_0 is the ground state, S_1 and S_2

represent the first and second singlet electronic excited states. At each electronic energy level, the numbers 0, 1, 2, etc. denote different vibrational energy levels.

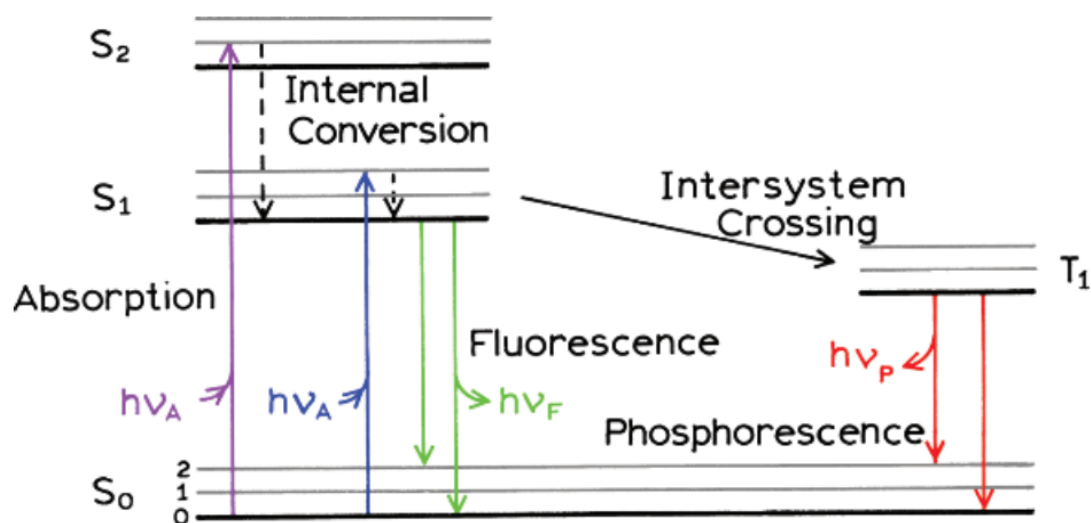


Figure 1.4: A typical Jablonski diagram of the photophysical process.^[6]

In order to reach the electronic excited state, the absorbed energy from the excitation photon ($h\nu_A$) must be greater than the energy gap between the ground state and the first singlet electronic excited state, equation (1.6).

$$h\nu_A \geq \Delta E_{S_0 \rightarrow S_1} \quad (1.6)$$

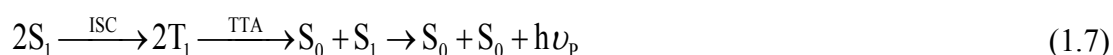
The ground state molecule can be excited to various vibrational levels (0, 1, 2, etc.) of the different excited states (S_1 , S_2 , etc.), but the excess energy above the lowest vibrational level of S_1 will be quickly dissipated through internal conversion and vibrational relaxation processes. Therefore, the ground state molecule can absorb the excitation light at a certain wavelength range, which results in the absorption spectrum.

We can also use the theory of frontier molecular orbitals^[11] to explain the energy transition of a molecular excitation process. When a molecule is in the ground state, the outer electrons occupy the highest occupied molecular orbital (HOMO). Upon light absorption, such electrons may jump to the lowest unoccupied molecular orbital (LUMO) and generate A^* .

1.2.3 Excited states deactivation

As we reported in 1.2.2, upon light absorption, a ground state molecule will be excited to an electronically excited state. Molecules in the excited state have the tendency to release their energy. Usually, there are five processes that enable the delivery of this excess energy: radiative transition, non-radiative transition, energy transfer, electron transfer and chemical reaction.

Radiative transition implies the emission of a photon, i.e., through the processes of fluorescence, delayed fluorescence and phosphorescence. Fluorescence is a radiative deactivation between electronic excited states having the same spin multiplicity, whereas phosphorescence involves states with different spin multiplicities (the details will be discussed in 1.2.4). Typically, in organic molecules fluorescence and phosphorescence come from the deactivation of the lowest excited states to the ground state ($S_1 \rightarrow S_0$ and $T_1 \rightarrow S_0$), but sometimes $S_2 \rightarrow S_0$ transition or higher excited state deactivations can also be observed.^[12-13] Delayed fluorescence occurs through two mechanisms (Figure 1.5). The so-called P-type delayed fluorescence is produced by triplet-triplet annihilation (TTA) process, which can be schematized as follows:



E-type delayed fluorescence (or thermally activated delayed fluorescence) is generated through reverse intersystem crossing (rISC). It occurs when S_1 and T_1 are very close in energy and T_1 may repopulate the upper-lying S_1 via thermal activation, as schematized below:

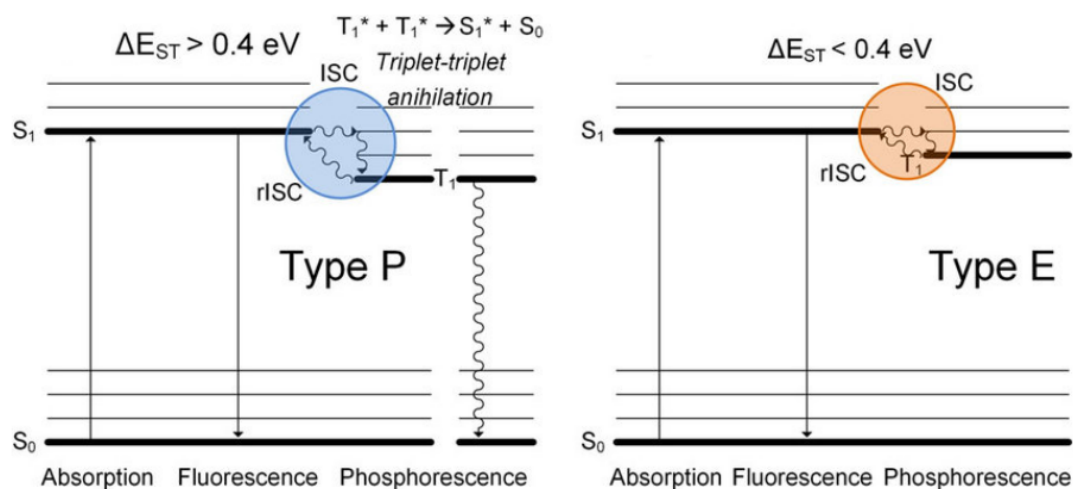


Figure 1.5: The two types of delayed fluorescence.^[14]

Non-radiative transitions are deactivation processes without the emission of light, which include vibrational relaxation (VR), internal conversion (IC) and intersystem crossing (ISC) (Figure 1.6). Vibrational relaxation occurs among different vibrational levels ($V_m \rightarrow V_n$) within the same electronic state. Internal conversion occurs between two electronic states of the same spin multiplicity (i.e., $S_m \rightarrow S_n$ or $T_m \rightarrow T_n$). Intersystem crossing is a kind of non-radiative transition between two electronic states with different spin multiplicity (e.g., $S_1 \rightarrow T_1$).

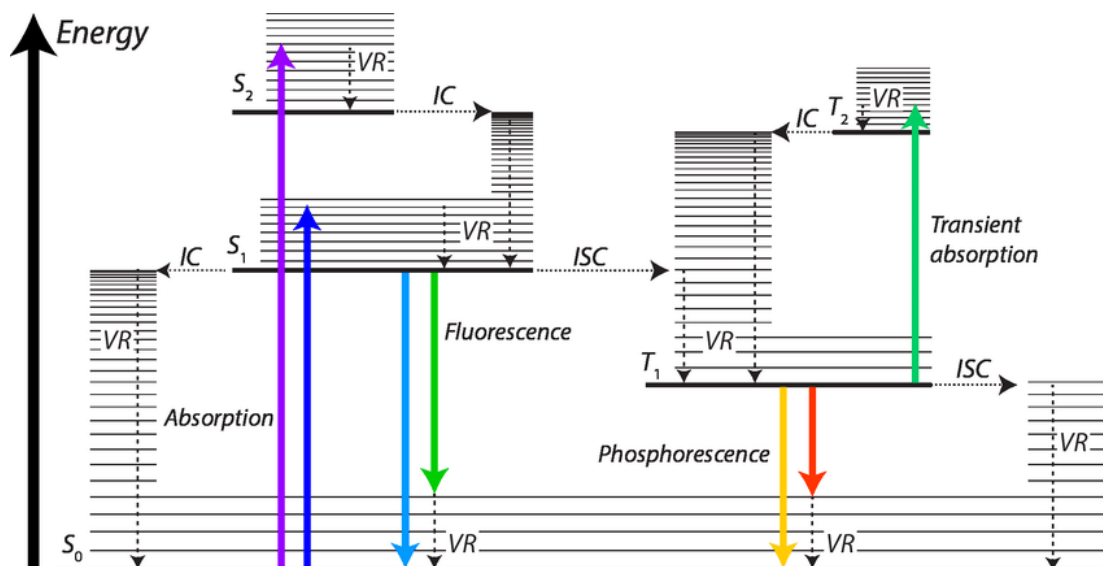


Figure 1.6: A Jablonski diagram includes the radiative and non-radiative transitions of the deactivation process that may occur upon light excitation.^[15]

Another excited state deactivation process is energy transfer, which implies the transfer of the excess energy of an excited state donor (D*) to a ground state acceptor (A) according to equation 1.9.



The most common energy transfer processes are singlet-singlet energy transfer (1.10) and triplet-triplet energy transfer (1.11).



Compared to the ground state molecule, an excited state molecule is typically not only a better electron donor, but also a better electron acceptor. Therefore, electron transfer to an acceptor (A) molecule or from a donor (D) molecule is also a relevant process to deactivate the excited state, according to the following two reactions:



The result of electron transfer is to produce a pair of ionic free radicals.

The other way to deactivate the excited state molecule is chemical reaction. Through the chemical reaction, the excited state molecule generates a new ground state molecule:



1.2.4 Triplet state and phosphorescence

According to quantum mechanics, Pauli's exclusion principle requires the electron pairs occupying one molecular orbit having different quantum states.^[16] Therefore, in the ground state, the electron pairs occupying HOMOs must keep anti-parallel spins (Figure 1.7), and the spin multiplicity (defined as $2S+1$) is equal to 1 (singlet state). When the molecule is excited to the singlet excited state, one electron jumps to the LUMO, the other one remaining in the HOMO (Figure 1.7). During the transition $S_0 \rightarrow S_n$, these two electrons always keep an opposite spin state, hence the spin multiplicity of the S_n state also equal to 1. A similar process occurs between the $T_n \rightarrow T_m$ transition, but the difference is that these two electrons always keep the same spin orientation (Figure 1.7), and the spin multiplicity is 3 (triplet state). According to the spin selection rule, the transition processes of $S_n \rightarrow S_m$ or $T_n \rightarrow T_m$ are spin-allowed.

If the energy levels of the singlet and triplet excited states are very close – such as S_1 and T_1 shown in Figure 1.7 – there will be the probability for ISC from S_1 to T_1 to occur. During the ISC process, the electron must change the spin state.

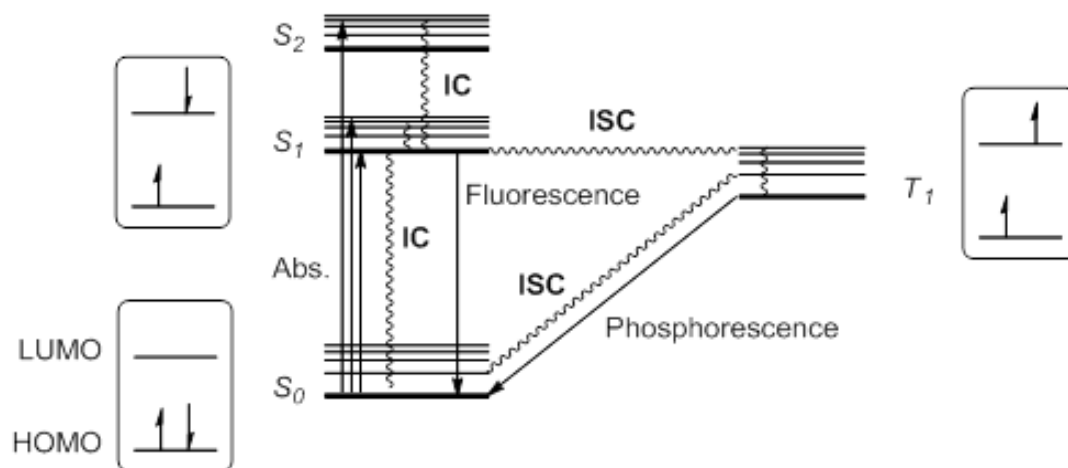


Figure 1.7: A Jablonski diagram describes the singlet and triplet states and their corresponding electronic spin states.

Phosphorescence is generated from the relaxation of the triplet excited state, which usually originates from the deactivation process from T_1 to S_0 . Generally, the phosphorescence lifetime is much longer than the fluorescence, the time range of the phosphorescence lifetime is from microseconds to hours. And due to the energy losses of the ISC process, the emission wavelength of the phosphorescence is always longer than the fluorescence.

Phosphorescence is very sensitive to oxygen,^[17] even trace amount of O_2 in solvents can quench phosphorescence. This is because molecular oxygen is a triplet in

the ground state, it can therefore interact through triplet-triplet energy transfer, leading to reduction or elimination of the phosphorescence intensity. So, phosphorescence is typically only observed in deoxygenated solutions or at the solid/crystal states.

1.2.5 Emission and excitation spectra

Emission and excitation spectra can be collected through a photoluminescence spectrometer (Figure 1.8), which consists of two optical channels, i.e., excitation and emission channel. The key components of a photoluminescence spectrometer include light source, excitation monochromator, sample cell, emission monochromator, detector, data collection and analysis system. Commonly used excitation light sources are lasers, LED and lamps (e.g. xenon arcs and mercury-vapor lamps). The monochromator can selectively transmit the incident or emitted light at a specific wavelength range. The sample cell is located between the two light channels, which are set at an angle of 90° . The detector measures the intensity of the emitted light at different wavelengths. Finally, the signals are collected and analyzed by a computer that displays the spectra.

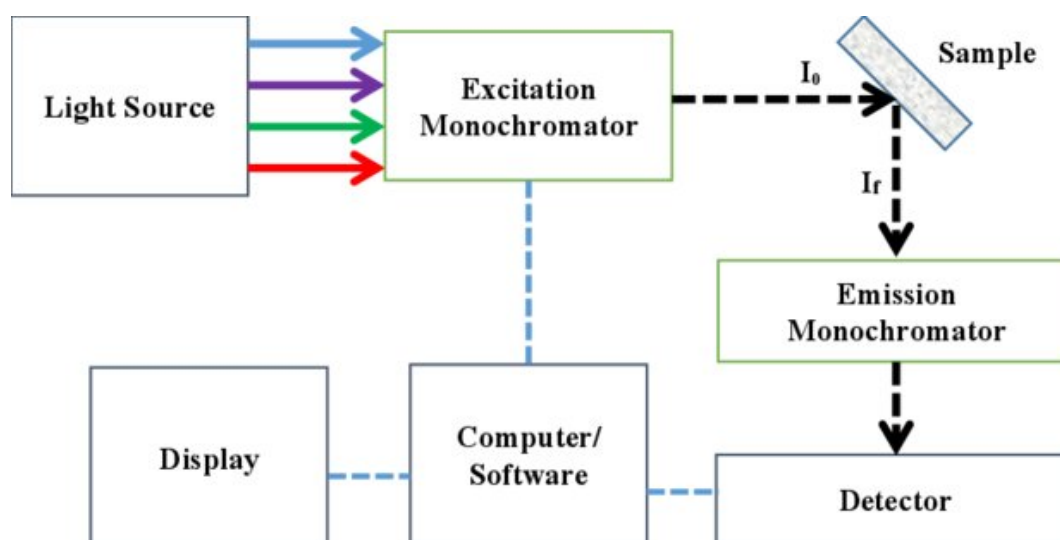


Figure 1.8: Schematic diagram of the main components of a typical photoluminescence spectrometer.

An emission spectrum is obtained by scanning the emission monochromator at a fixed excitation wavelength. The difference between fluorescence and phosphorescence is that, in the former, irradiation is made with continuous light, whereas phosphorescence is recorded with pulsed excitation light sources, in order to get rid of the shorter-lived fluorescence signal.

On the other hand, the excitation spectrum is collected by scanning the excitation monochromator at a fixed emission wavelength. Usually, the excitation spectrum overlaps with the absorption spectrum.

1.2.6 Stokes' shift, mirror image law and Kasha's rule

In 1852, Sir George Gabriel Stokes found that the wavelengths of photoluminescence are always longer than the wavelength of the excitation light. In other words, compared to the absorption spectrum, the emission spectrum is always red-shifted to longer wavelengths, which is the so-called Stokes' shift. In Figure 1.9, the absorption/excitation spectra, emission spectra and Stokes' shifts of two kinds of organic compounds are shown. When a ground state molecule absorbs photons to generate the excited state, not only the lowest vibrational level of S_1 (S_1, V_1) can be populated, but also different vibrational levels of S_1 , S_2 or even higher levels. Eventually, these electronic excited states with higher energy levels will quickly deactivate to the V_1 vibrational level of S_1 through VR and IC processes. The energy is usually dissipated as heat, then the excited molecule may emit fluorescence from the V_1 vibrational level of S_1 to the ground state.

The Stokes' shift is very important in the field of photophysics and is observed in countless photoluminescent materials. There are however some exceptions, with materials releasing emission light on wavelengths shorter than the excitation light (anti-Stokes); this phenomenon is called luminescence upconversion. For inorganic materials, upconversion can occur in three ways, which include energy transfer upconversion (ETU), excited-state absorption (ESA) and photon avalanche (PA).^[18] Organic molecules can undergo up-conversion through sensitized triplet-triplet annihilation (sTTA) and energy pooling.^[19] The processes of two-photon absorption and second-harmonic generation can also produce anti-Stokes luminescence, but their generation mechanism are quite different with respect to up-conversion.^[20]

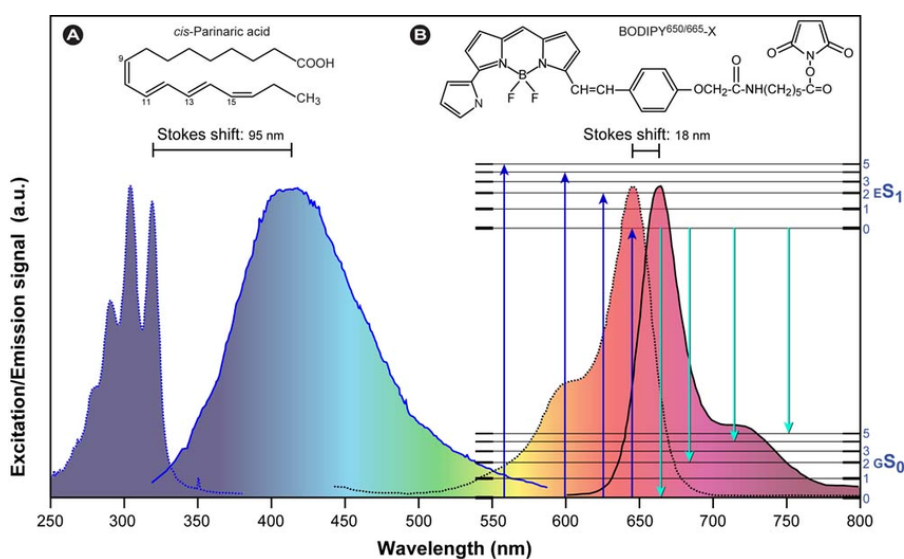


Figure 1.9: Absorption/excitation spectra, emission spectra and Stokes shifts of two organic compounds.^[21]

Since the mass of the nucleus is much larger than the electron and the electronic transition is a very fast process (10^{-15} s), during the electronic transition, the nuclear position of the atoms can be considered unchanged to an excellent approximation. This is called the Franck-Condon principle.^[22] Figure 1.10 shows the schematic diagram of the Franck-Condon principle and the so-called mirror image law. According to the Franck-Condon principle, an electronic transition is a vertical process. The transition probability from the ground state to the excited state is similar to the transition probability from the excited state to the ground state, which results in the similarity of the shapes of absorption/excitation and emission spectra.

For most photoluminescent molecules, their excited state energy levels (S_1 , S_2 , etc.) are very close or even cross each other. The Franck-Condon principle suggests that a greater overlap of the vibrational wavefunctions, results in faster decays from higher to the lower levels. Hence the excess energy will be quickly dissipated through “horizontal” IC and “vertical” VR processes (Figure 1.6), until the lowest vibrational level of S_1 is reached. Therefore, most molecules emit luminescence from the lowest vibrational levels of S_1 or T_1 to the S_0 state. In other words, the emission wavelength is independent from the excitation wavelength, which is called the Kasha’s rule.^[23] But for some particular molecules, the energy gap between S_1 and S_2 is large enough and the IC process from S_2 to S_1 is difficult to occur, which causes luminescence directly from the S_2 state,^[12-13] disobeying the Kasha’s rule.

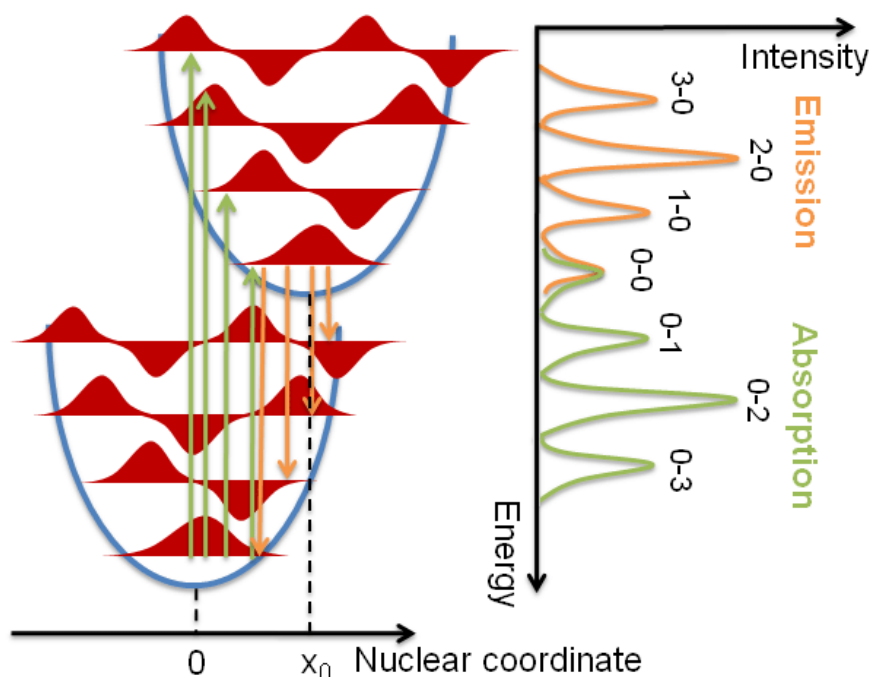


Figure 1.10: The schematic diagram of the Franck-Condon principle and the mirror image law.^[24]

1.2.7 Quantum yield and excited-state lifetime

Emission quantum yield (Φ) is a very important parameter for photoluminescent materials, which directly indicates the conversion efficiency of the absorbed photons into emitted photons. Φ is defined by the following equation:

$$\Phi = \frac{\text{number of emitted photons}}{\text{number of absorbed photons}} \quad (1.15)$$

If we just consider the radiative and non-radiative deactivation processes of the electronic excited state, Φ can also be described as:

$$\Phi = \frac{k_r}{k_r + k_{nr}} \quad (1.16)$$

where k_r is the rate constant of radiative deactivation, k_{nr} is the rate constant of non-radiative deactivation. Because of the Stokes losses, the emission quantum yield is virtually always smaller than 1.

Experimentally, there are relative and absolute methods for measuring the quantum yield.^[25] Relative quantum yield (Φ_R) are typically used for solution samples and can be assessed by means of a standard reference solution and calculated through the following equation:

$$\Phi_R = \Phi_{st} \frac{F_x f_{st} n_x^2(\lambda_{em})}{F_{st} f_x n_{st}^2(\lambda_{em})} \quad (1.17)$$

in which x represents the sample, st represent the standard, F is the integral photon flux, n is the refractive index of the given solvent, Φ_{st} is the quantum yield of the standard reference solution; the absorption factor f can be calculated by equation (1.18).

$$f = 1 - 10^{-A(\lambda_{ex})} \quad (1.18)$$

where A is the absorbance of the sample of the standard solution at the selected excitation wavelength.

On the other hand, an integrating sphere is normally used to measure the absolute quantum yield (Φ_A). Compared to the relative method, the absolute method does not need the standard reference, but a blank spectrum. Usually, a pure solvent or blank matrix (glass or polymer without luminophore) is used to acquire the blank spectrum, and calculate Φ_A with the following equation:

$$\Phi_A = \frac{F}{F_{abs}} \quad (1.19)$$

where F is the integrated emission photon flux and F_{abs} represents the integrated

absorbed photon flux.

The excited-state lifetime (τ) is another important parameter for photoluminescent materials. It is dictated by the interplay between radiative and non-radiative processes (when energy transfer, electron transfer and chemical reaction are not involved). The excited-state lifetime (also called measured lifetime) indicates how long the molecule stays in the excited state, and τ can be defined by the equation (1.20).

$$\tau = \frac{1}{k_r + k_{nr}} \quad (1.20)$$

Radiative lifetime (τ_r), also called intrinsic or natural lifetime (τ_n), indicates the lifetime of the radiative transition process (i.e. assuming the absence of non-radiative decays) and is given by:

$$\tau_r = \tau_n = \frac{1}{k_r} \quad (1.21)$$

The natural lifetime (τ_n) can also be calculated through the measured lifetime (τ) and quantum yield (Φ).

$$\tau_n = \frac{\tau}{\Phi} \quad (1.22)$$

Usually, the fluorescence lifetime of organic compounds is shorter than 10 ns, but the phosphorescence lifetime can reach to the microsecond scale or even longer. Four methods can be used to measure the excited-state lifetime, including pulsed illumination, time-correlated single-photon counting (TCSPC), gating methods and phase modulation.

1.2.8 Fluorescence quenching

The emission intensity of fluorescence and phosphorescence can be reduced or eliminated by some materials (termed quenchers), such as halogen ions,^[26] heavy metal ions,^[27] oxygen molecules,^[28] nitro compounds,^[29] carbonyl compounds,^[30] or even ordinary organic compounds. The fluorescence quenching mechanisms include dynamic quenching and static quenching. Dynamic quenching can occur by fluorescence resonance energy transfer (FRET), electronic energy transfer (EET) and formation of excimer or exciplex.

FRET (Figure 1.11) is based on the dipole-dipole interactions and transfer the energy from an excited state donor to a ground state acceptor. FRET depends on the distance of the donor and acceptor molecules (typically within 10-20 nm) and the relative orientation of the donor-acceptor transition dipole moments; it also requires the absorption spectrum of the acceptor to overlap with the emission spectrum of the donor

(Figure 1.11).

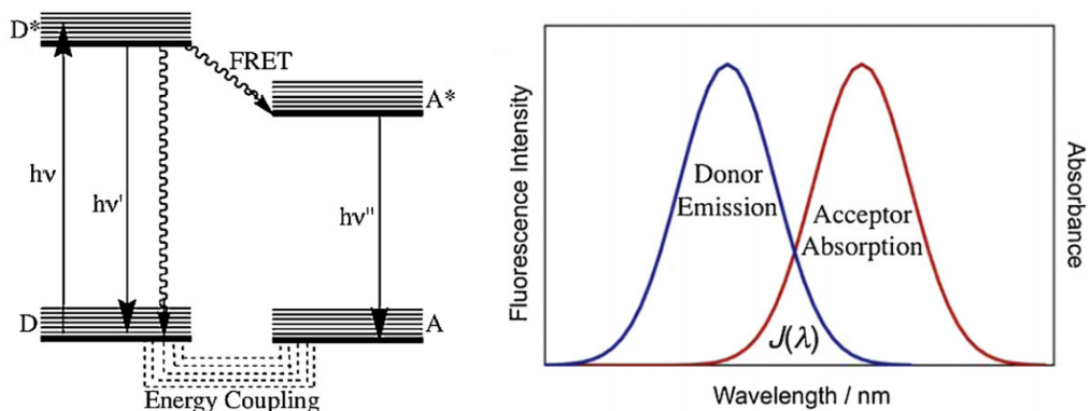


Figure 1.11: A Jablonski diagram of the FRET process (left) and the spectral overlap of the donor and acceptor (right).^[31]

EET is also called Dexter electron exchange, which can be described by assuming that an excited electron is transferred from the excited donor to the acceptor through a non-radiative process^[32] (Figure 1.12). EET is a short-range process (within 1 nm), which requires the molecular orbitals of the donor and acceptor to overlap. FRET and EET processes only reduce the fluorescence intensity, the original shape of the spectrum being unchanged.

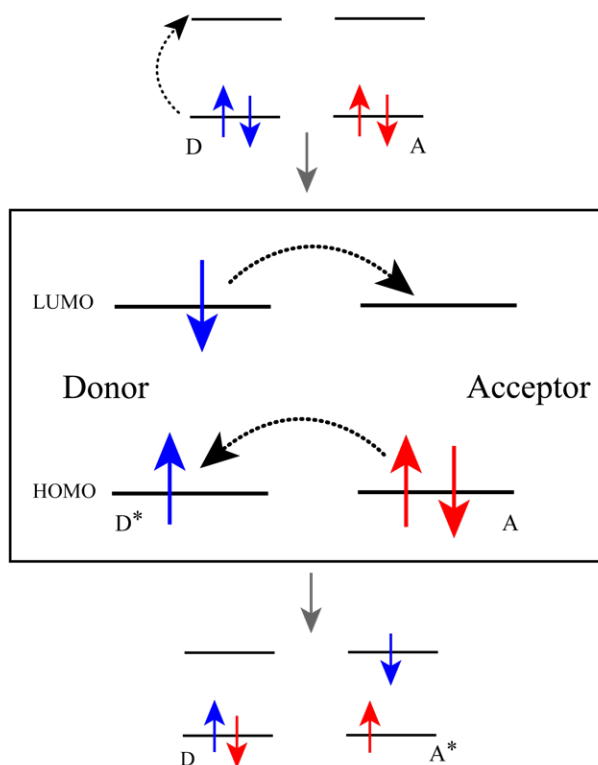


Figure 1.12: A schematic diagram of the Dexter electron exchange energy transfer process.

Formation of excimer or exciplex is another mechanism of fluorescence quenching. Both excimer and exciplex are generated through an excited molecule and a ground state molecule. Excimer (excited dimer) is a short-lived homonuclear system, whose formation process is described below.



Exciplex (i.e., excited complex) is a heteronuclear system made of two different molecules:



The lifetime of the excimer and exciplex are very short, usually in the nanosecond scale. Compared with the fluorescence of the excited monomer, excimer and exciplex usually emit at longer wavelengths.

Dynamic quenching also called collisional quenching is described by the famous Stern-Volmer equation:

$$\frac{I_0}{I} = \frac{\tau_0}{\tau} = \frac{\Phi_0}{\Phi} = 1 + K[Q] = 1 + k_q \tau_0 [Q] \quad (1.25)$$

where I_0 and I represent the unquenched and quenched fluorescence intensity, τ_0 and τ indicate the unquenched and quenched lifetime, Φ_0 and Φ are the unquenched and quenched quantum yield, K is the Stern-Volmer constant, k_q is the bimolecular quenching constant, and $[Q]$ is the concentration of the quencher.

Static quenching requires that the luminescent molecule interact with the quencher and form a non-luminescent complex. For static quenching, the Stern-Volmer equation is written as (1.26).

$$\frac{I_0}{I} = 1 + K_s [Q] \quad (1.26)$$

where K_s is the static quenching constant.

1.3 A short introduction to DFT calculation

Density functional theory (DFT)^[33] is a quantum mechanical method to investigate the structural and electronic properties of the multi-electronic system. DFT has a wide range of applications in physics and chemistry, its calculation objects range from atoms and molecules to crystals and classical fluids. Especially used to study the properties of molecules, it is one of the most common methods in the field of computational chemistry because of its compromise between accuracy and computational cost. DFT uses the electron density as the related physical parameter, and provides various properties of a system, including optimized molecular structures,

vibrational frequencies, ionization energies, molecular orbitals, electric and magnetic properties, transition-state structures, reaction pathways, etc.

In wavefunction-based methods, the Schrodinger wave equation^[34] is used as the basic assumption of quantum mechanics to investigate the system of interest. The time-independent Schrodinger equation can be described as follow:

$$H\Psi = E\Psi \quad (1.27)$$

where H is the Hamiltonian operator, E is the energy operator, Ψ represents the wave function. The Hamiltonian in many-body system includes the kinetic energy operator T, the potential energy operator V and the particle-particle interaction operator W:

$$H = T + V + W \quad (1.28)$$

A lot of information can be obtained through solving the wave function, but for multi-electronic system, the equation will become too complicated to be resolved.

Therefore, in 1927, Llewellyn Thomas and Enrico Fermi indicate that the problem can be solved through using the electronic density as the relevant physical quantity (Thomas-Fermi model).^[35-36] However, the Thomas-Fermi theory is inaccurate in most applications. Until to 1964, the emergence of the famous Hohenberg-Kohn theorem^[37-38] marks the beginning of the modern density functional theory. The Hohenberg-Kohn theorem describes the following two statements:

1. The external potential and the ground state energy (E) are uniquely determined by the ground-state electron density.
2. If and only the input density is the right ground state density, the function of the system to delivers the ground state energy gives the lowest energy.

And only one year later, Kohn and his postdoctor Sham restated the problem in the mathematical form (Kohn-Sham equations)^[38] and opened the gate to DFT on practical applications (Figure 1.13).

Since then, a lot of approximations of the exchange-correlation functionals were established for the DFT calculations, such as local density approximation (LDA)^[38], generalized gradient approximation (GGA),^[39] meta-generalized-gradient approximations (meta-GGAs),^[40] hybrid approximations,^[41] double-hybrid approximations,^[42] range-separated hybrid approximations,^[43] semiempirical dispersion corrections,^[44] and etc. Combined with the developments of the time-dependent density functional theory (TDDFT)^[45] and the relativistic density functional theory (RDFT),^[46] the family of the DFT methods has become more and more large and complete.

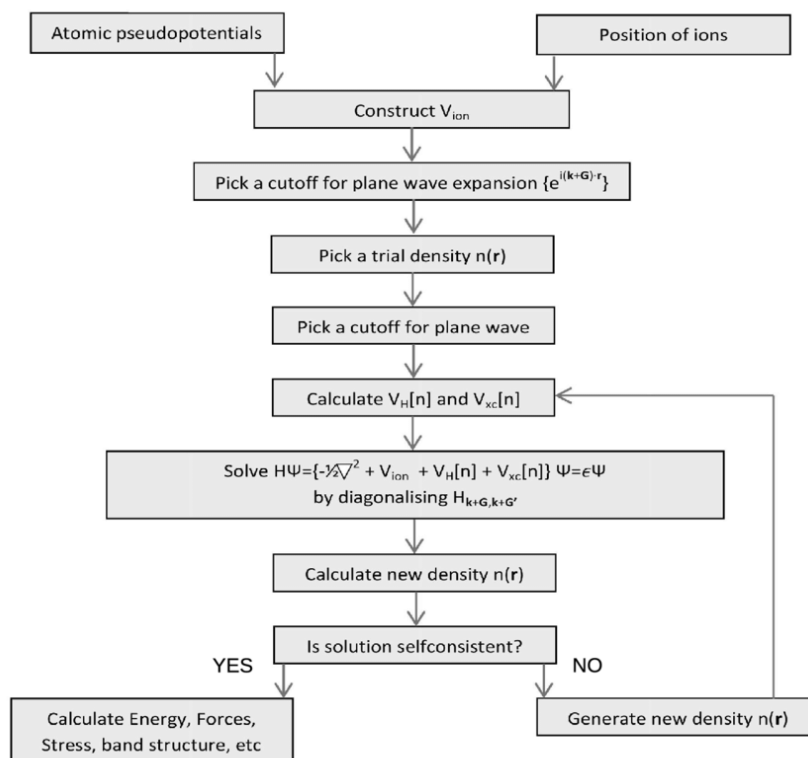


Figure 1.13: The self-consistency cycle to solve the Kohn-Sham equations within the plane-wave pseudopotential method.^[47]

DFT calculation must be carried out by a computer software, like Gaussian, Orca, VASP and ADF, etc. Before the calculation, it is very important to select a suitable model chemistry for a DFT calculation job. The simplest model chemistry consists of a theoretical method in combination with a chosen functional, together with selected basis sets, but sometimes, it includes also the electronic spin state, solvent environment, integration grid and fitting basis sets.

There have a variety of theoretical methods,^[48] which can treat the jobs at different levels of accuracy and chemical environments, apart from the semi-empirical methods (e.g., PM6 and AM1) and wavefunction-based ones (e.g., Hartree-Fock method (HF), Moller-Plesset perturbation theory (MP2 and MP4), etc.) there are different class of functionals, as the Becke 3-parameter Lee-Yang-Parr method (B3LYP), Minnesota functionals (M06 and M06-2X), and ect. Usually, the theoretical method with higher levels of theory provides the more accurate calculation results, but it also needs the higher computational costs. In order to save the equipment resources, computation time and/or to better explore multiple scenarios, the suitable theoretical method is not always the higher-level one.

Basis set is a group of mathematical functions used to model the atomic orbitals for a molecular system during the DFT calculations. The most primitive basis set is

Slater-type orbitals (STOs),^[49] which used to treat the hydrogen-like atoms. But the STOs is difficult to calculate the multi-center systems and it was later instead by a linear combinations (STO-NG) of Gaussian-type orbitals (GTOs).^[50] Furthermore, split-valence basis sets were used to divide the valence orbitals into two or more basis functions with different size, such as, 6-31G and 6-311G. For higher calculation accuracy, polarization function (e.g 6-31G(d, p)), diffusion function (e.g 6-31++G(d, p)) and high angular momentum basis set (e.g 6-311++G(3df, 2df, p)) are also used frequently. When dealing with large and complicated molecular systems with heavy atoms, the application of the effective core potential (ECP) basis sets in combination with mixed basis sets for other elements is used to replace the inner-core electrons to effectively save computing resources and time.

Open-shell calculation are mandatory when computing the properties of triplet states (particularly important to model the photophysics of metal complexes) and are more computationally demanding with respect to singlet closed-shell calculations. When the target molecule is sensitive to the solvent environment, the continuum solvation models (e.g polarizable continuum model, PCM)^[51] must be added for the model chemistry. If you plan to compare the energies, it is very important to apply the same integration grid for all calculations. And the larger integration grids are available to set up for the model chemistry when needed, such as the tight geometry optimization for some certain systems. Apart from the classic orbital basis sets, the auxiliary or fitting basis sets are occasionally used for the model chemistry.

DFT methods can be used for several types of different calculations, but we maybe just need a portion of them. Therefore, after determining the appropriate model chemistry, the calculation type (e.g., single-point energy calculation, geometry optimization, frequency calculation) should also be specified. And last, we can compare the DFT calculation results with the experimental data to explain and support the experimental results.

1.4 Applications of photoluminescence

Photoluminescence techniques are widely used in many fields of scientific research and even in our daily life; they include luminescent solar concentrators (LSC), fluorescence sensors, fluorescence remote sensing, fluorescence microscopy, fluorescent probes, live cell imaging, fluorescent dyes, anti-counterfeiting, etc. Herein, some examples will be presented, taken from recent literature.

P. Moraitis and coworkers described in detail (Figure 1.14) the operational principle of Luminescent Solar Concentrators (LSC), along with their characterization and loss mechanisms in a review article.^[52] They indicated that the candidates for LSC luminophores can be organic dyes, rare earth ions, colloidal semiconductors, and the

hosts (waveguides) are usually made of poly (methyl methacrylate) (PMMA), polycarbonate (PC) and glass. They also introduced the application of LSC in building-integrated photovoltaics; a detailed discussion of this topic has been made by Francesco Meinardi and coworkers.^[53]

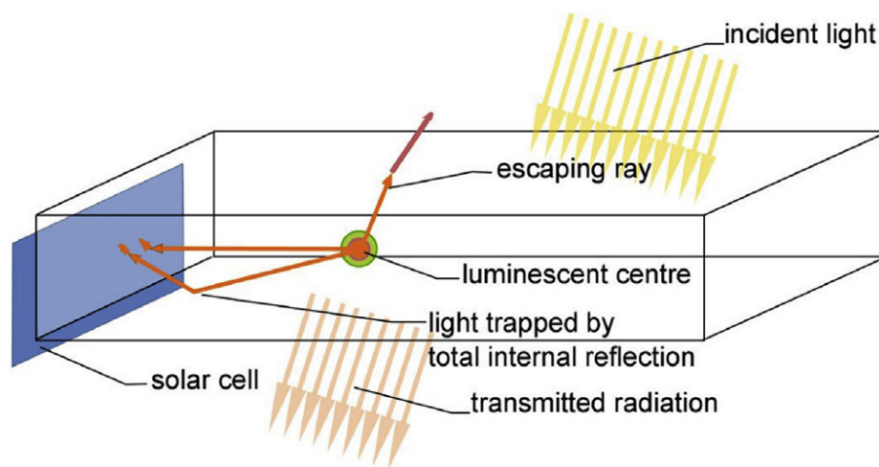


Figure 1.14: A schematic picture of the classic LSC device.^[52]

Yu Fang group has performed a lot of excellent work in the field of fluorescence sensors (Figure 1.15). For example, a cholesterol-modified perylene bisimide derivative (PEBC) was used selectively to detect lung cancer sniffing (aniline and o-toluidine).^[54] A fluorescent sensor array based on organoboron-containing polymers was used to discriminate saturated alkanes and relevant volatile organic compounds.^[55] The phenomenon of photoluminescence can also be utilized for remote sensing. M. Meroni and coworkers wrote a review article on the development of fluorescence remote sensing methods, introducing the techniques used for the detection of solar-induced chlorophyll fluorescence.^[56]

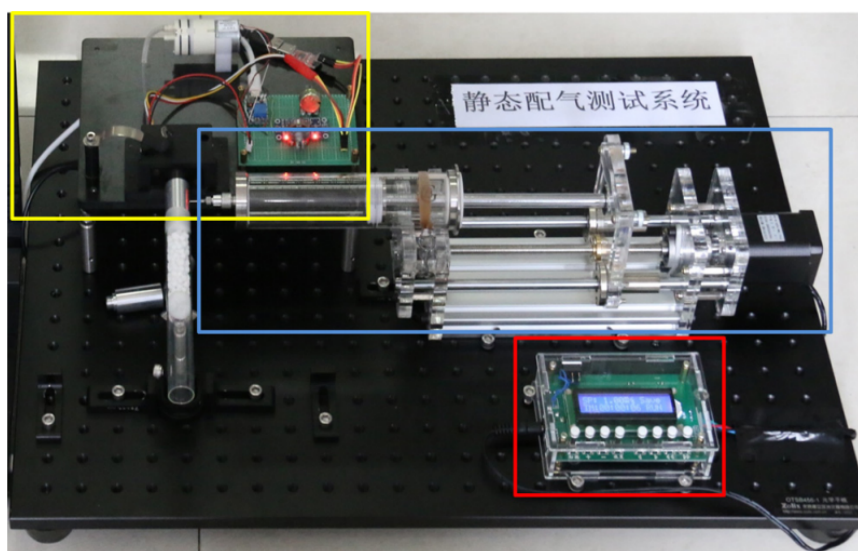


Figure 1.15: Gas-phase fluorescence sensing system designed by the Yu Fang group.^[54]

Nowadays, the fluorescence microscope has become a very important instrument in many scientific fields. It is particularly relevant for the emergence of super-resolution fluorescence microscopy, which brings the traditional optical microscopy into the nanoscale world. The contribution of Eric Betzig, W. E. Moerner and Stefan Hell to the development of super-resolved fluorescence microscopy, was awarded the Nobel Prize in chemistry in 2014. Thanks to fluorescence microscopy, many photoluminescence studies are developing rapidly. For instance Shijiang He and coworkers studied graphene as a nanoprobe to rapidly and sensitively analyse DNA molecules^[57] (Figure 1.16). On the other hand, reversible fluorescent probes were designed by Keitaro Umezawa and coworkers for live cell imaging.^[57]

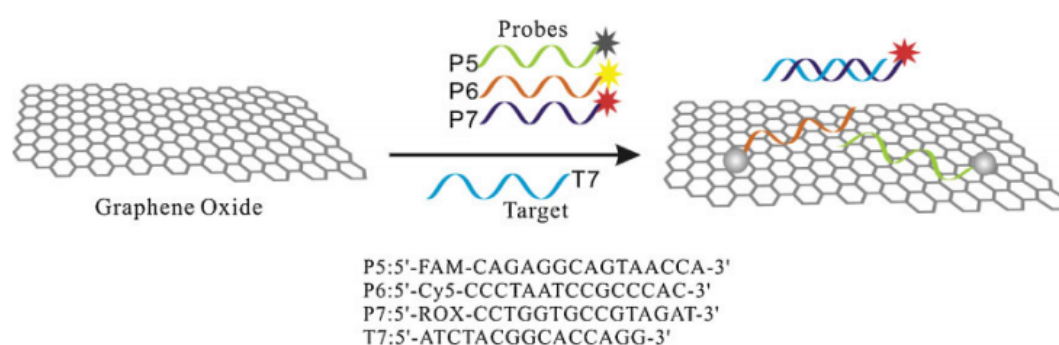


Figure 1.16: Scheme of the analysis process for DNA molecules through graphene based fluorescence probes.^[57]

Finally, some fluorescent dyes can be used as anti-counterfeiting materials. For example, lanthanide-doped nanocrystals were designed and prepared for anti-counterfeiting through up- and down-conversion luminescence.^[58] Zhao Gao and coworkers designed and synthesized some anthracene-endoperoxide based supramolecular polymers, and explored their applications in this domain (Figure 1.17).^[59]

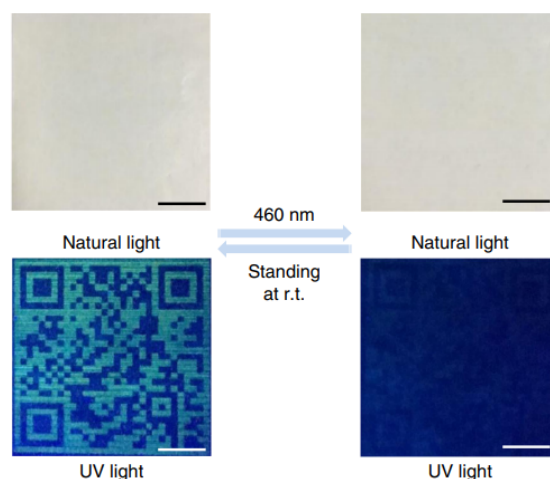


Figure 1.17: Application of photoluminescent materials in anti-counterfeiting.^[59]

Chapter 2

Benzoheterodiazole dyes and their application on LSC

2.1 Introduction

In the field of renewable electricity production for urban settings, building-integrated photovoltaics (BIPV) are an attractive solution to achieve high power density requirements,^[60] with sunlight harvested not only on the roof surfaces, but also on external walls and windows. Luminescent solar concentrators (LSC) are a promising and intensively investigated solution for the development of BIPV. In LSC devices, sunlight penetrates the surface of an inexpensive and transparent waveguide (glass or plastic plate), in which luminescent materials (e.g., organic dyes, inorganic phosphors, quantum dots) are dispersed. Incident solar photons are absorbed by the dyes and then isotropically re-emitted at longer wavelengths. A portion of these photons is guided by total internal reflection towards a photovoltaic (PV) cells that is placed on the edge of the LSC. Since the edge area is smaller than the receiving surfaces, it turns out to be possible to concentrate sunlight without solar tracking. LSC-PV devices have several advantages, such as easy manufacturing, substantial reduction on the PV surface, multifunctional building integration and cheap production costs.^[61] Essentially, the performance of LSC devices is determined and limited by four mechanisms, the transmission loss (due to the incomplete light absorption by the fluorophores), the photoluminescence quantum yield of the dye, the escape cone loss of the waveguide, and the re-absorption of emitted photons. Transmission and escape cone losses can be controlled by adjusting the concentration of the dye and/or the thickness of the waveguide, or by using high refractive index matrices.^[62] Recently, bright fluorophores with large Stokes shifts have attracted remarkable attention as active materials in LSC.^[63-64]

In the research described herein, we deal with the basic photophysical properties of five bright benzoheterodiazole dye molecules (Figure 2.1) with large Stokes' shifts and determine emission quantum yields as well as transmission and re-absorption properties by making LSC-PV devices. The investigated dyes consist of extended π -conjugated architectures with donor (D) and acceptor (A) moieties of different strengths. **S2T** is a D-A-D system which constitutes the central structure of the series, whilst the other molecules are larger or heavier homologues. **Se2T** also exhibits a D-A-D structure, the only difference is that sulfur (S) is replaced by selenium (Se). In the structure of **Se4T**, π -conjugation is extended with two more additional thiophene units. Furthermore, **CS2T** includes an additional stronger donor moiety (N-carbazole) at one end of the **S2T** to form a D'-D-A-D system. Similarly, **CS2TCHO** is equipped with another functional acceptor unit (carbonyl group) at the other extremity to yield a D'-

D-A-D-A' type system.

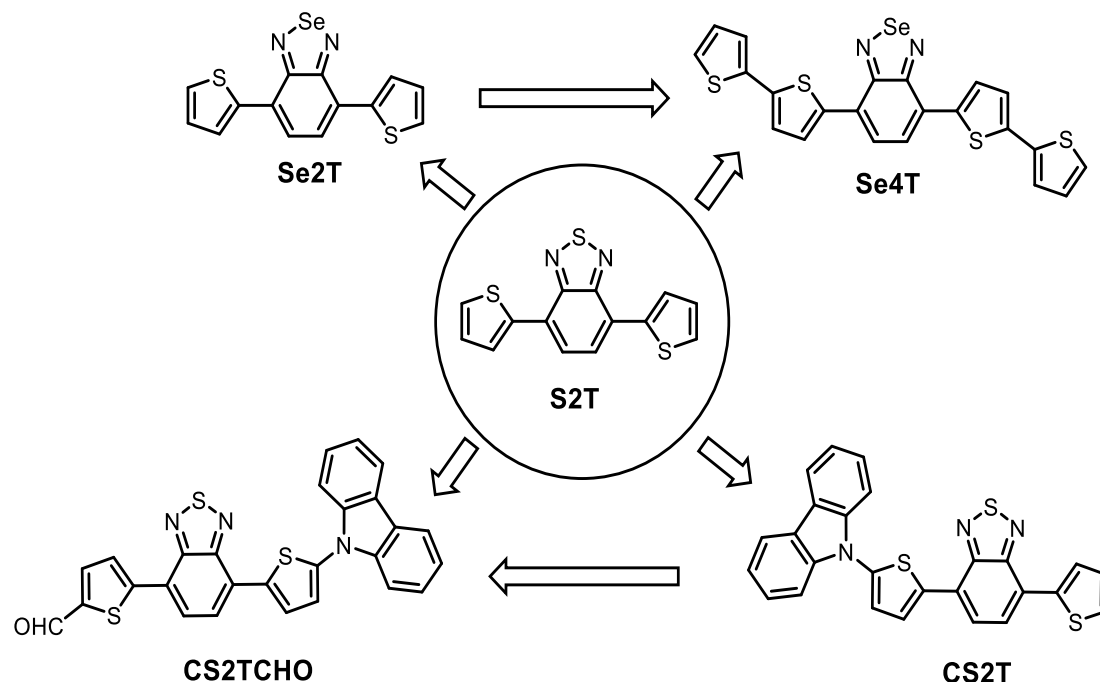


Figure 2.1: Molecular structures of the five investigated luminescent molecules.

2.2 Experimental section

2.2.1 Synthesis of benzoheterodiazole dyes

Materials and methods

All the reagents and materials involved in the synthesis process were provided by Sigma–Aldrich, Merck, and Spectrochem Chemical suppliers, and used as received without further purification. The air and moisture sensitive synthetic steps were carried out under the protection of argon atmosphere. Before the reaction of Stille coupling, the mixed reactant solution was treated through the freeze–pump–thaw process to remove the dissolved oxygen, and the freezing process was performed by using the liquid nitrogen (77 K). ^1H and ^{13}C nuclear magnetic resonance (NMR) spectra were recorded for the resulted and intermediated compounds through a Bruker Advance II spectrometer (500 MHz) and tetramethylsilane (TMS) was used as the internal standard. Fourier transform infrared (FTIR) spectra were collected through the diffused reflection mode of an IR Prestige-21 FTIR-8400 s spectrometer (Shimadzu Corporation, Japan), and the samples were prepared by dispersing the compounds into potassium bromide (KBr) tablets. Mass spectroscopy (MS) were characterized for all compounds through a Thermo Scientific Exactive Orbitrap Spectrometer with electrospray ionization (ESI) mass spectrometric mode. Mel-Temp II melting point instrument was used to determine the melting points (MP) for all compounds.

Synthetic route

The synthetic routes for preparation of the D-A-D molecular systems are shown in Figure 2.2 and 2.3. Molecule **S2T** as the basic unit was prepared through the Stille coupling reaction (a) by using the 4,7-dibromobenzo[*c*][1,2,5]thiadiazole with 2-(tributylstannyl)thiophene. Then **S2T** was brominated by N-bromosuccinimide (b) to form the **CS2T** through the Ullman-type cross coupling reaction (c) of the monobromo derivative (**1**) with 9H-carbazole. At last, the D'-D-A-D-A' system **CS2TCHO** was obtained from the formylation reaction (d) of **CS2T**.

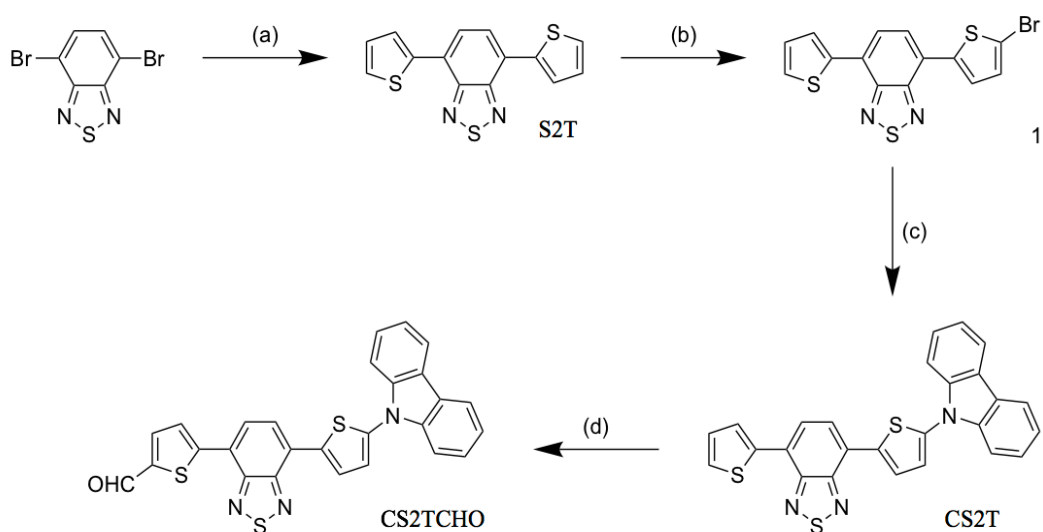


Figure 2.2: Synthetic process for the preparation of D-A systems of **S2T**, **CS2T** and **CS2TCHO**. (a) 2-(Tributylstannyl)thiophene, Pd(PPh₃)₄, 90 °C, 24 h; (b) NBS, 0 °C, 24 h; (c) 9H-carbazole, (+)-trans-1,2-diaminocyclohexane, tBuONa; (d) POCl₃, DMF, sodium acetate.

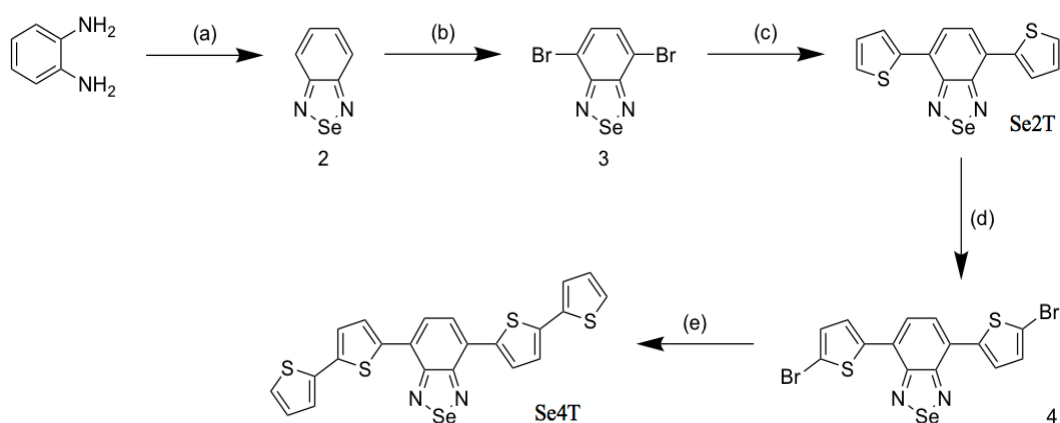


Figure 2.3: Synthetic process for the preparation of D-A systems of **Se2T** and **Se4T**. (a) SeO₂, 75 °C; (b) Br₂, Ag₂SO₄, H₂SO₄, 2 h; (c) 2-(tributylstannyl) thiophene, Pd(PPh₃)₄; (d) acetic acid, NBS, (s) 2-(tributylstannyl)thiophene, Pd(PPh₃)₄.

The compound **2** was generated through mechanical grinding the mixture of o-phenylenediamine and SeO₂ (a), then compound **3** was synthesized by bromination reaction (b). **Se2T** was obtained through the Stille coupling reaction (c) of compound **3** with 2-(tributylstannyl)thiophene. Followed **Se2T** was converted to compound **4** by the further bromination reaction (d) and Stille coupling (e) to form the **Se4T**.

Synthetic details

Synthesis of 4,7-di(thiophen-2-yl)benzo[c][1,2,5]thiadiazole (S2T):

First, 0.76 g 4,7-Dibromobenzo[c][1,2,5]thiadiazole (2.6 mmol) and 2.24 g 2-(Tributylstannyl)thiophene (6.0 mmol) were dissolved by 44 mL dry toluene, and degassed with bubbling nitrogen for 30 minutes. 72 mg Pd(PPh₃)₄ (0.06 mmol) were then added into the mixed reactant solution and kept under stirring at 90 °C for 24 h. Eventually, the solution was cooled down to room temperature and poured into distilled water. In the next step, the product was extracted with chloroform, then the extracted solution was concentrated and dried in vacuum. Further purification was carried out through column chromatography using 100-200 mesh silica gel and a 1:1 hexane/chloroform solution as eluent. Finally, the orange solid product (**S2T**) was obtained with yield of 74%. MP: 128-129 °C; ESI-MS: calculated 299.98, found 300.99 [M+H]⁺; ¹H-NMR (500 MHz, CDCl₃): 8.12 (d, J = 4.5 Hz, 2 H), 7.88 (s, 2H) 7.46 (d, J = 5 Hz, 2H), 7.22 ppm (dd, J = 4.5 Hz, 2H); ¹³C-NMR (CDCl₃, 125 MHz): 152.67, 139.37, 128.04, 127.53, 126.83, 126.03, 125.82 ppm; FTIR (KBr): 3428, 3092, 3011, 1805, 1788, 1578, 1540, 1525, 1483, 1425, 1377, 1356, 1311, 1279, 1234, 1215, 1200, 1178, 1074, 1043, 924, 881, 849, 824, 706, 694, 640, 511 cm⁻¹.

Synthesis of 4-(5-bromothiophen-2-yl)-7-(thiophen-2-yl)benzo[c][1,2,5]thiadiazole (1):

0.29 g NBS (1.6 mmol) were dissolved in 10 mL of DMF, then the solution was dropped into 15 mL DMF solution of **S2T** (500 mg, 1.7 mmol) and kept under stirring at 0 °C for 24 h. Eventually, the mixed solution was extracted with diethyl ether, the organic phase was washed with water and then the solvent removed in vacuum. The crude product was further purified through column chromatography using 100-200 mesh silica gel and a 4:1 hexane/chloroform solution as eluent. Finally, 379 mg pure product was obtained through recrystallization from ethanol with yield of 59%. MP: 119-120 °C; FTIR (KBr): 3094, 3047, 3010, 2920, 2849, 1541, 1483, 1423, 1379, 1275, 1215, 1074, 1043, 970, 920, 881, 825, 797, 702, 690, 670, 640, 600, 565, 509 cm⁻¹.

Synthesis of CS2T:

45 mg 9H-carbazole (0.27 mmol), 100 mg compound **1** (0.26 mmol), 74 mg (+)-trans-1,2-diaminocyclohexane (0.65 mmol), 37 mg tBuONa (0.39 mmol), and 12.3 mg were dissolved by 100 mL 1,4-dioxane. After the mixture was refluxed overnight,

the solvent was removed under reduced pressure to get the crude product. Further purification was carried out through column chromatography using 100-200 mesh silica gel and pure hexane as eluent. At last, 100 mg pure **CS2T** was obtained with the yield of 80%. MP: 175-176 °C; ESI-MS: calculated 465.04, found 465.04 [M]⁺; ¹H-NMR (500 MHz, CDCl₃): 8.2 (d, J = 4 Hz, 1H), 8.16 (d, J = 3.5 Hz, 1H), 8.14 (d, J = 7.5 Hz, 2H), 7.9 (s, 2H), 7.64 (d, J = 8 Hz, 2H), 7.49-7.46 (m, 4H), 7.35-7.34 ppm (m, 4H); FTIR (KBr): 3410, 3300, 3245, 1534, 1490, 1336, 1260, 1220, 1040, 826, 806, 748, 702 cm⁻¹.

Synthesis of CS2TCHO:

Vilsmeier reagent was prepared by adding 18.39 mg POCl₃ (1.2 mmol) and 10.3 mg dry DMF (1.41 mmol) into 5 mL of dichloroethane. The prepared reagent was added into an ice-cold solution of 200 mg **CS2T** (0.43 mmol) in 30 mL dichloroethane. The reaction mixture was heated to reflux for 12 h, hydrolysed with 50 mL saturated aqueous sodium acetate solution for 3 h. Then it was extracted with CH₂Cl₂, and the organic phase was collected and dried by anhydrous Na₂SO₄. The crude product was further purified by column chromatography using 100-200 mesh silica gel and a 1:1 dichloromethane/hexane solution as eluent. Eventually, 26 mg red solid product (**CS2TCHO**) were obtained with yield of 12%. MP: 214-215 °C; ESI-MS: calculated 493.04, found 494.04 [M+H]⁺. ¹H-NMR (500 MHz, CDCl₃): 10.00 (s, 1H), 8.29 (d, J = 4 Hz, 1H), 8.26 (d, J = 4 Hz, 1H), 8.14 (d, J = 7.5 Hz, 2H), 8.07 (d, J = 8 Hz, 1H), 7.97 (d, J = 7.5 Hz, 1H), 7.88 (d, J = 4 Hz, 1H), 7.65 (d, J = 8 Hz, 2H), 7.50-7.47 (m, 3H), 7.36-7.33 ppm (m, 3H). ¹³C-NMR (CDCl₃, 125 MHz): 183.05, 152.50, 143.60, 141.59, 136.84, 128.14, 126.43, 125.41, 125.12, 123.78, 120.94, 110.37 ppm. FTIR (KBr): 3410, 3230, 2922, 2813, 1665, 1520, 1442, 1337, 1234, 1220, 1067, 873, 848, 810, 755, 728 cm⁻¹.

Synthesis of 1,3-benzoselenadiazole (2):

1 g of o-Phenylenediamine (9.2 mmol, 1 equiv.) and 1.02 g SeO₂ (9.2 mmol, 1 equiv.) were grinded in the mortar, then the mixture was heated at 75 °C for 30 minutes. After cooling down to room temperature, the crude product was washed with distilled water and recrystallized from ethanol. Finally, the brown solid compound **2** was obtained with yield of 75%. MP: 74.5 °C; ¹H-NMR (CDCl₃, 500 MHz): 7.8 (d, J = 10 Hz, 2H) 7.47 ppm (d, J = 10 Hz, 2H); ESI-MS: calculated 183.95, found 184.95 [M+H]⁺; FTIR (KBr): 3082, 3059, 3038, 3009, 2972, 1952, 1933, 1911, 1828, 1805, 1745, 1709, 1610, 1508, 1475, 1437, 1354, 1290, 1219, 1142, 1132, 1076, 974, 949, 852, 798, 750, 743, 712, 596, 555, 489 cm⁻¹.

Synthesis of 4,7-dibromobenzo[c][1,2,5]selenadiazole (3):

0.53 mL of bromine (10 mmol) were added into a solution of 1 g of 2,1,3-benzoselenadiazole (5 mmol) and 1.6 g of silver sulphate (5 mmol) in 11 mL concentrated H₂SO₄. After the mixed solution was shaken for 2 h at room temperature, the formed silver bromide precipitate was filtered out and the filtrate was poured into ice-water. The crude product from the water was recrystallized with 500 mL ethyl acetate, then washed with Na₂S₂O₃ to remove the excess bromine. Finally, the solid golden yellow compound **3** was obtained with yield of 14%. MP: 263.3 °C; ¹H-NMR (CDCl₃, 500 MHz): 7.64 ppm (s, 2H); ESI-MS: calculated 339.77, found 340.78 [M+H]⁺, 342.78 [M+2H]⁺; FTIR (KBr): 3167, 3070, 3050, 3030, 2952, 2912, 1870, 1672, 1585, 1485, 1475, 1355, 1329, 1310, 1076, 945, 925, 914, 837, 797, 764, 750, 578 cm⁻¹.

Synthesis of Se2T:

A degassed solution of 1 g of compound **3** (2.9 mmol, 1 equiv.) and 2.1 g of 2-(tributylstannyl)thiophene (5.6 mmol, ≈2 equiv.) in 20 mL were put dry toluene, then Pd(PPh₃)₄ (5 mol%) was added and refluxed for 20 h. When the reaction was finished, the mixed solution was poured into distilled water, extracted with chloroform, dried and concentrated in vacuum. Further purification was performed through a column chromatography using 100-200 mesh silica gel and a 1:3 hexane/chloroform mixture as eluent. The compound **Se2T** was obtained as dark brown solid with yield of 21%. MP: 126.7 °C; ¹H-NMR (CDCl₃, 500 MHz): 8.01 (d, J = 3.5 Hz, 2H) 7.8 (s, 2H); 7.47 (d, J = 5 Hz, 2H); 7.2 ppm (dd, J = 4, 4.5 Hz, 2H); ¹³C-NMR (CDCl₃, 125 MHz): 158.23, 139.68, 127.73, 127.51, 127.40, 127.14, 126.10 ppm; ESI-MS: calculated 347.93, found 348.93 [M+H]⁺; FTIR (KBr): 3444, 3105, 3086, 3068, 1583, 1524, 1510, 1470, 1433, 1383, 1350, 1296, 1277, 1213, 1072, 1045, 910, 847, 816, 770, 708, 690 cm⁻¹.

Synthesis of 4,7-bis(5-bromothiophen-2-yl)benzo[c][1,2,5]selenadiazole (4):

1.2 g of N-bromosuccinimide (6.7 mmol) was added into a solution containing 1.07 g of **Se2T** (3 mmol) in 24 mL of chloroform and 24 mL of acetic acid and kept under stirring overnight at room temperature under the protection of N₂ atmosphere. The collected red precipitate was recrystallized from DFM. Finally, compound **4** was obtained as brown needle crystals with yield of 54%. MP: 220.3 °C; ESI-MS: calculated 503.75, found 503.75 [M]⁺, 505.75 [M+2]⁺; FTIR (KBr): 3416, 3092, 1745, 1640, 1618, 1475, 1423, 1373, 1308, 1215, 1202, 1097, 1068, 972, 846, 831, 783, 762, 731, 696, 683 cm⁻¹.

Synthesis of **Se4T**:

Pd(PPh₃)₄ (5 mol%) was added into a degassed solution of 0.61 g of compound **4** (1.2 mmol) and 0.88 g of 2-(tributylstannyl)thiophene (2.4 mmol) in 20 mL toluene, and kept under refluxing for 20 h. After cooling down to room temperature, reaction mixture was poured into distilled water, then extracted with chloroform, dried and concentrated under vacuum. Further purification was carried out by column chromatography using 100-200 mesh silica gel and a 1:4 hexane/chloroform mixture as eluent. The final pure compound **Se4T** was obtained with yield of 19%. MP: 181.2 °C; ¹H-NMR (CDCl₃, 500 MHz): 7.95 (d, J = 4 Hz, 2H), 7.8 (s, 2H), 7.3 (d, J = 3.5 Hz, 2H), 7.27 (2H), 7.26 (2H), 7.06 ppm (dd, J = 4 Hz, 2H); ¹³C-NMR (CDCl₃, 125 MHz): 158.23, 139.68, 127.73, 127.51, 127.40, 127.14, 126.10 ppm; ESI-MS: calculated 511.9, found 511.9 [M]⁺; FTIR (KBr): 3070, 1575, 1505, 1497, 1475, 1423, 1373, 1308, 1285, 1215, 1204, 1097, 1068, 972, 847, 831, 814, 804, 795, 783, 762, 731, 696, 682 cm⁻¹.

2.2.2 Photophysics

The spectroscopic investigations of the dyes were carried out in spectrofluorimetric grade dichloromethane (DCM) and methanol (MeOH) (Merck Uvasol®). A PerkinElmer Lambda 950 spectrophotometer was used to record the absorption spectra. In order to carry out photoluminescence experiments, dye solutions were put into fluorimetric Suprasil quartz gas-tight cuvettes (1 cm) in which oxygen was removed by bubbling argon for 20 minutes. Uncorrected emission spectra were recorded with an Edinburgh Instruments FLS920 spectrometer equipped with a Peltier-cooled Hamamatsu R928P photomultiplier tube (185-900 nm). Corrected spectra were obtained through a calibration curve supplied with the instrument. The excitation light source was a 450 W xenon arc lamp. Photoluminescence quantum yields (Φ_{PL}) in solution were determined from the corrected emission spectra, using Coumarin 153 ($\Phi_{\text{PL}} = 0.53$) and Rhodamine 6G ($\Phi_{\text{PL}} = 0.91$) in ethanol solutions as reference for **S2T**, **CS2T**, **CS2TCHO**, and **Se2T**, **Se4T**, respectively.^[25] Photoluminescence quantum yields were also determined with the absolute method, using a barium sulfate-coated integrating sphere (diameter of 3 inches), elaborating corrected emission spectra.^[25] The excited state lifetimes (τ) were obtained by the time-correlated single photon counting (TCSPC) technique with an HORIBA Jobin Yvon IBH FluoroHub equipped with a pulsed NanoLED ($\lambda_{\text{exc}} = 465$ nm) excitation source and a TBX-05C Picosecond Photon Detection Module (300-850 nm). The luminescence decay profiles were analyzed with the DAS6 Decay Analysis Software Software, and the quality of the fit was assessed with the χ^2 value (close to unity) and with the residuals randomly distributed along the time axis. Low-temperature luminescence spectra (77 K) were recorded by means of 2 mm inner diameter quartz tubes (sample inside) fitted into a special quartz cold finger Dewar filled with liquid nitrogen. Experimental uncertainties

are estimated to be $\pm 8\%$ for τ determinations, $\pm 20\%$ for Φ_{PL} , and ± 2 nm and ± 5 nm for absorption and emission peaks, respectively.

2.2.3 Preparation and characterization of the PMMA based LSCs

Poly(methylmethacrylate) (PMMA) with average MW ≈ 350000 (by GPC) was obtained from Sigma-Aldrich. Dye-PMMA films (1.0% w/w, 0.5% w/w and 0.2% w/w) were prepared by dissolving 200 mg of PMMA powder in 4 mL dye-DCM solutions (0.5 mg/mL, 0.25 mg/mL and 0.1 mg/mL, respectively); solvent was then evaporated overnight in a 5 cm glass Petri dish. The resulted Dye-PMMA films were separated through sonication from the glass dish and the thickness of the films was measured as 71 ± 4 nm.

Transmission and reflection spectra of dye-PMMA films were measured with a PerkinElmer Lambda 950 spectrophotometer equipped with 100 mm diffuse reflectance and transmission integrating sphere accessory, including PMT/PbS detectors. And the absorption factors of the dye-PMMA films were possible to calculate as:

$$A\% = 100 - T\% - R\% \quad (2.1)$$

where A%, T% and R% are the absorption factor, transmittance and reflectance, respectively. Absolute fluorescence quantum yields of the dye-PMMA films were calculated from the corrected emission spectra using a barium sulfate-coated integrating sphere (diameter of 3 in.).^[25]

The geometric gain (G) of the dye-PMMA devices (dimensions: $25 \times 25 \times 0.071$ mm) is defined as:

$$G = \frac{S_{\text{surf}}}{S_{\text{edge}}} \quad (2.2)$$

where S_{surf} and S_{edge} are the area of the surface and edges of the film, respectively. For our devices, it turns out to be 88. Optical quantum efficiency (OQE) is defined as the ratio of the edge output and the absorbed photons:

$$\text{OQE} = \frac{n_{\text{edge}}}{n_{\text{abs}}} = \Phi_{PL} - 2\Phi_F \quad (2.3)$$

in which n_{edge} and n_{abs} are the number of photons collected from all the edges of the devices and absorbed by the sample, respectively. It has been determined by comparing the absolute quantum yield of the films inside (Φ_{PL}) and in front (Φ_F) of an integrating sphere. The flux gain (F) is the geometric gain (G) corrected for the efficiency losses in the concentrator:

$$F = \frac{I_{\text{edge}}}{I_{\text{abs}}} = \frac{1}{4} \text{OQE} \times G \quad (2.4)$$

where I_{edge} and I_{abs} are the intensity of light output at the edge and absorbed at the surface, respectively. The experimental trapping efficiency (η_{trap}) can be obtained from the ratio of OQE and Φ_{PL} :

$$\eta_{\text{trap}} = \frac{\text{OQE}}{\Phi_{\text{PL}}} \quad (2.5)$$

At last, the external quantum efficiency (EQE) is calculated as the ratio of the photons emitted at the edges (n_{edge}) and the total incident photons (n_{inc}):

$$\text{EQE} = \frac{n_{\text{edge}}}{n_{\text{inc}}} = \text{OQE} \times A\% \quad (2.6)$$

where $A\%$ is the absorption rate in percentage (absorptance or absorption factor).

2.2.4 Preparation and characterization of the PDMS based LSCs

For preparation of the dye-PDMS devices, a polydimethylsiloxane (PDMS) matrix from Dow (SYLGARD 184) was used. Devices based on PDMS (0.02% w/w, 0.01% w/w and 0.004% w/w) were fabricated by mixing 6.8 g of PDMS component A (elastomer) and 0.68 g of PDMS component B (curing agent) with 1.5 mL of dye solution in DCM (1.0 mg/mL, 0.5 mg/mL and 0.2 mg/mL, respectively) under stirring for 20 minutes in a 10 mL glass vial. After homogenizing the PDMS and dye solutions, samples were put for 3 days into a 3×3 cm (bottom area) mold to evaporate the solvents and form the dye-polymer device at room temperature.

A 100 mm diffuse reflectance and transmission integrating sphere accessory (include PMT/PbS detectors) was equipped on the PerkinElmer Lambda 950 spectrophotometer to collect the transmission and reflection spectra of dye-PDMS devices. The absorption factors of the dye-PDMS devices were calculated by using the equation 2.1. Absolute fluorescence quantum yields of the dye-PDMS devices were obtained by using a barium sulfate-coated integrating sphere (diameter of 3 in.).^[25]

Edge emission light of the PDMS based LSCs was collected through four IXYS KXOB22-12X1F silicon PV cells (6.5×20 mm) connected in a series/parallel network placed at the four edges of the 30×30×8.5 mm PDMS matrix. The devices were illuminated orthogonally at the center of the receiving surface with a monochromatic beam of 10x5 mm², avoiding direct irradiation of the side PVs. To investigate the monochromatic incident photon-to-electron conversion efficiency (IPCE) of the PDMS-LSCs, a 150 W Xenon arc lamp (LOT Oriel) equipped with a MSH3101 150 mm monochromator (LOT Oriel) was used as the light source. The power of the

excitation light source at different wavelengths was measured by a calibrated SM1PD2A silicon photodiode (Thorlabs), and the current signals were recorded using a PDA200C photodiode amplifier (Thorlabs). The values of the IPCE (including all optical losses, PV interface losses and the quantum efficiency of the PV cell) were calculated from the equation:^[65-66]

$$\text{IPCE} = \frac{P_E}{P_0} = \frac{\eta_0 I_{PD}}{I_0} \frac{1240}{\lambda} \frac{A_E}{A_{PV}} \quad (2.7)$$

in which P_E and P_0 are the edge-emitted power and incident power, respectively, η_0 is the responsivity of the SM1PD2A silicon photodiode, I_{PD} and I_0 are the currents of edge-emitted light on the KXOB22-12X1F silicon PV cells and the currents of incident radiation on the SM1PD2A silicon photodiode, respectively, λ is the wavelength of the incident light, A_E and A_{PV} are the edge areas of the LSCs and the effective surface areas of four KXOB22-12X1F silicon PV cells.

2.2.5 DFT calculation methods

Density functional theory (DFT) calculations^[33] were performed by using the B.01 revision of the Gaussian 16 program package,^[67] in combination with the M06-2X hybrid meta exchange-correlation functional,^[68-69] which has been specifically designed to work well with charge-transfer excitations having intermediate spatial overlap.^[70] The fully relativistic Stuttgart/Cologne energy-consistent pseudopotential with multielectron fit was used to replace the first 10 inner-core electrons of the selenium atoms (i.e., ECP10MDF) and it was combined with the associated augmented double- ζ basis set (i.e., aug-cc-pVDZ-PP);^[71] for all other atoms, the Pople 6-31+G(d) basis set was adopted.^[72-73] The polarizable continuum model (PCM) was employed to take into account dichloromethane solvation effects.^[51,74] TD-DFT calculations, at the same level of theory used for ground-state optimizations, were used to compute Franck-Condon excitations and to fully optimize the lowest energy excited state (S_1) of all the molecules.^[75-76] The **S2T**, **Se2T**, **Se4T** dyads were investigated within the C_2 -symmetry point group, while no symmetry constraints were imposed to the **CS2T** and **CS2TCHO** derivatives (i.e., C_1 point group). Analytical frequency calculations were always carried out to confirm the nature of the stationary points found on the potential energy surfaces of both S_0 and S_1 . All the pictures of molecular orbitals and density surfaces were created using GaussView 6.^[77]

2.3 Results and Discussion

2.3.1 Photothermal stability in DCM

Before further photophysical characterizations, the photothermal stability properties of all the dyes were checked through UV/Vis absorption spectroscopy in

DCM as a function of time. The results show that all the dye-DCM solutions are stable at room temperature under daylight for several days (Figure 2.4).

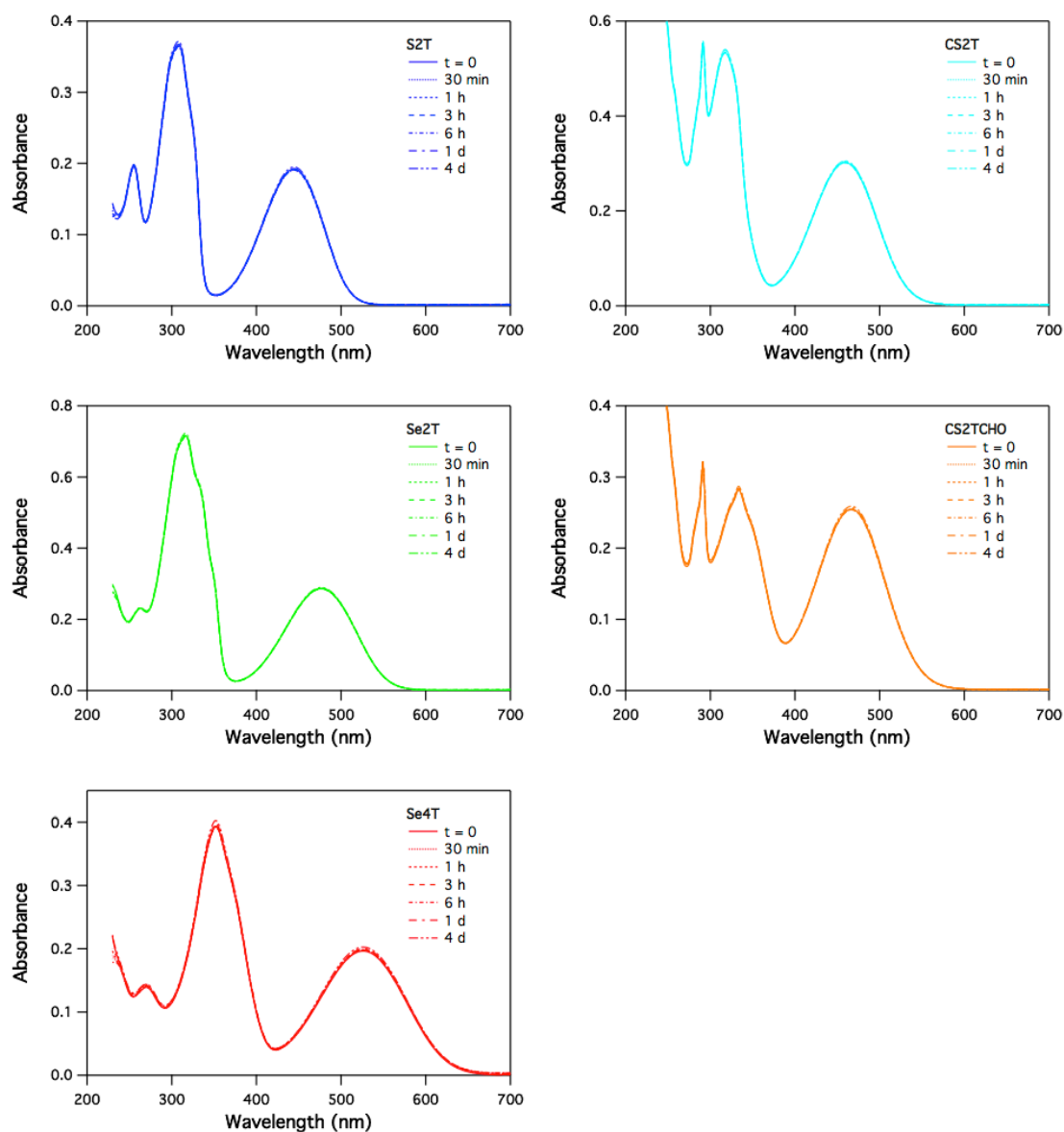


Figure 2.4: Absorption spectra of the dyes in DCM at 298 K at different time after preparation under daylight.

2.3.2 Photophysics in solutions and DFT calculation results

Absorption in solution:

In Figure 2.5 are reported the absorption spectra of **S2T**, **Se2T**, **Se4T**, **CS2T** and **CS2TCHO**; the related photophysical data are collected in Table 2.1. All samples exhibit strong absorption in the UV (peaking in the range 308-330 nm) and in the visible (400-600 nm) region, with molar absorption coefficients in the range 16-24,000 and 8-20,000 $\text{M}^{-1} \text{cm}^{-1}$, respectively (Table 2.1).

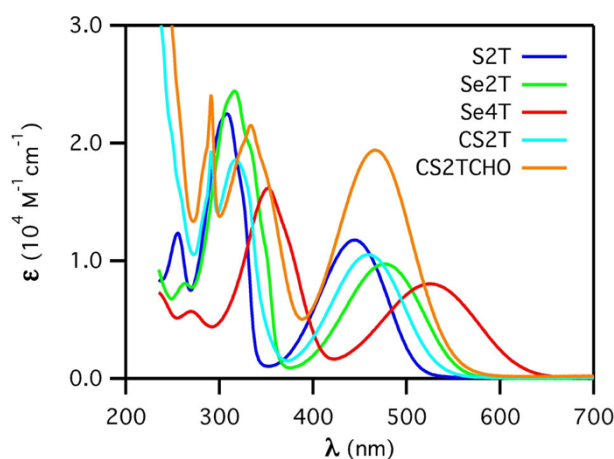


Figure 2.5: Absorption spectra of the five dyes in DCM solution at 298 K.

Table 2.1: Main absorption parameters in DCM solution at 298 K.

	λ_{max} , nm (ϵ_{max} , $\text{M}^{-1}\text{cm}^{-1}$)
S2T	255 (12,350), 308 (22,500), 444 (11,700)
Se2T	263 (8,100), 316 (24,400), 476 (9,750)
Se4T	270 (5,700), 352 (16,200), 524 (8,050)
CS2T	291 (19,350), 318 (18,600), 459 (10,500)
CS2TCHO	291 (24,100), 333 (21,500), 467 (19,400)

For all of the dyes, the wide band in the visible region is entirely attributable to the $S_0 \rightarrow S_1$ transition, corresponding to an almost pure HOMO \rightarrow LUMO excitation having a strong charge-transfer character (Figure 2.6-2.10). In this transition, one electron is promoted from the oligo-thiophene-phenylene moiety to the central benzoheterodiazole core (Table 2.2). On the other hand, the higher-energy band envelope around 308-330 nm is attributable to an admixture of electronic excitations involving both charge-transfer and locally-excited states (Figure 2.6-2.10).

Compared to the sulfur derivative **S2T**, the absorption spectrum of the selenium analogue **Se2T** is red-shifted. The lowest energy band in the VIS region is displaced by about 30 nm (1510 cm^{-1} , that is, 0.18 eV) to longer wavelengths (Figure 2.5). This is a common feature of benzodiazole derivatives including Se vs. S atoms, and it is mainly due to the stabilization of the LUMO (centered on benzoheterodiazole core) caused by the heavier selenium atom with respect to lighter sulphur (Figure 2.11), as also described in the literature.^[78]

In the case of **Se4T**, which incorporates four thiophene units, the absorption spectrum moves further to the red, basically due to the strong destabilization of HOMO and HOMO-1 caused by the increased delocalization of the oligo-thiophene-phenylene moiety (Figure 2.11). This causes a considerable red-shift of the $S_0 \rightarrow S_1$ absorption band

(1,925 cm^{-1} , that is, 0.24 eV) with respect to **Se2T**. Such experimental evidence is in line with TD-DFT calculations, which indicates a shift of 2,296 cm^{-1} (i.e., 0.285 eV as in Figure 2.7-2.8 and Figure 2.12).

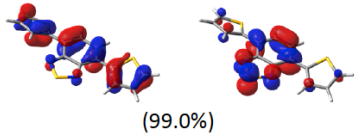
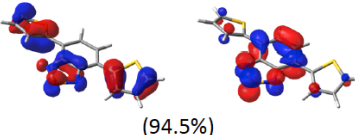
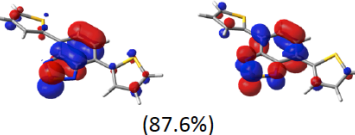
	Transition energy [eV (nm)]	NTO couple hole \rightarrow electron (λ)	Nature
$S_0 \rightarrow S_1$ (B)	3.01 (412) $f = 0.541$	 (99.0%)	CT transition mainly from thiophene moieties to the core
$S_0 \rightarrow S_2$ (A)	4.28 (289) $f = 0.045$	 (94.5%)	CT transition mainly from thiophene moieties to the core
$S_0 \rightarrow S_3$ (A)	4.47 (278) $f = 0.119$	 (87.6%)	centered on the benzothiadiazole central unit

Figure 2.6: Calculated NTOs couples describing the first three singlet excitations for dye **S2T** in DCM. The f value is the oscillator strength of each transition, while λ value is the natural transition orbital eigenvalue associated with each NTOs couple; orbital isovalue: $0.04 \text{ e}^{1/2} \text{ bohr}^{-3/2}$.

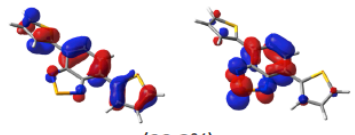
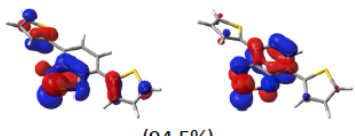
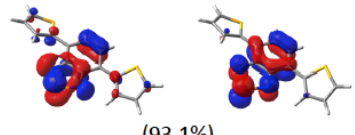
	Transition energy [eV (nm)]	NTO couple hole \rightarrow electron (λ)	Nature
$S_0 \rightarrow S_1$ (B)	2.86 (434) $f = 0.425$	 (99.2%)	CT transition mainly from thiophene moieties to the core
$S_0 \rightarrow S_2$ (A)	4.03 (308) $f = 0.144$	 (94.5%)	CT transition mainly from selenium p orbital to the core
$S_0 \rightarrow S_3$ (A)	4.18 (297) $f = 0.128$	 (93.1%)	centered on the benzoselenadiazole central unit

Figure 2.7: Calculated NTOs couples describing the first three singlet excitations for dye **Se2T** in DCM. The f value is the oscillator strength of each transition, while λ value is the natural transition orbital eigenvalue associated with each NTOs couple; orbital isovalue: $0.04 \text{ e}^{1/2} \text{ bohr}^{-3/2}$.

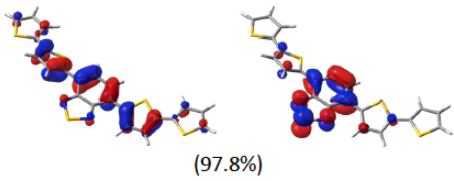
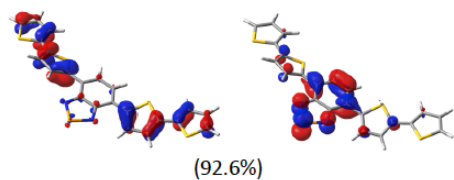
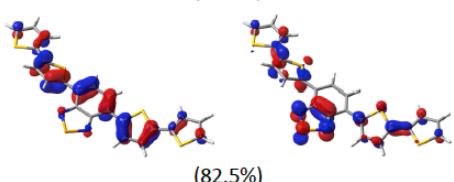
	Transition energy [eV (nm)]	NTO couple hole → electron (λ)	Nature
$S_0 \rightarrow S_1$ (B)	2.57 (482) $f = 0.872$	 (97.8%)	CT transition mainly from thiophene moieties to the core
$S_0 \rightarrow S_2$ (A)	3.49 (355) $f = 0.144$	 (92.6%)	CT transition purely from thiophene moieties to the core
$S_0 \rightarrow S_3$ (B)	3.78 (328) $f = 0.846$	 (82.5%)	very delocalized transition

Figure 2.8: Calculated NTOs couples describing the first three singlet excitations for dye **Se4T** in DCM. The f value is the oscillator strength of each transition, while λ value is the natural transition orbital eigenvalue associated with each NTOs couple; orbital isovalue: $0.04 e^{1/2} \text{ bohr}^{-3/2}$.

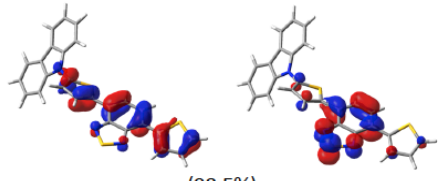
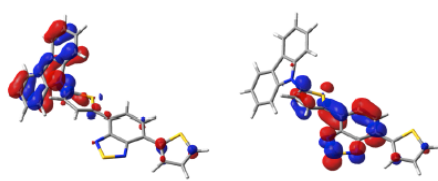
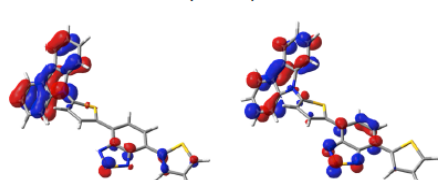
	Transition energy [eV (nm)]	NTO couple hole → electron (λ)	Nature
$S_0 \rightarrow S_1$	2.98 (416) $f = 0.683$	 (98.5%)	CT transition mainly from thiophene moieties to the core
$S_0 \rightarrow S_2$	3.85 (322) $f = 0.015$	 (95.4%)	CT transition mainly from the carbazole moiety to the core
$S_0 \rightarrow S_3$	4.36 (284) $f = 0.168$	 (55.9%)	mixed transition centered on carbazole and the central core TRANSITION MIXED WITH $S_0 \rightarrow S_4$ (35.0%)

Figure 2.9: Calculated NTOs couples describing the first three singlet excitations for dye **CS2T** in DCM. The f value is the oscillator strength of each transition, while λ value is the natural transition orbital eigenvalue associated with each NTOs couple; orbital isovalue: $0.04 e^{1/2} \text{ bohr}^{-3/2}$.

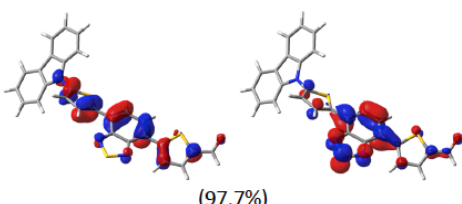
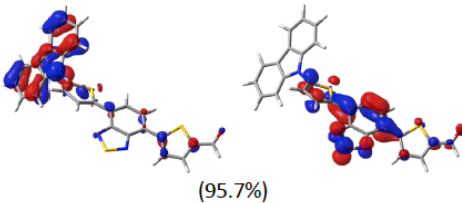
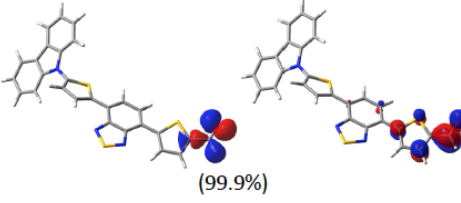
	Transition energy [eV (nm)]	NTO couple hole → electron (λ)	Nature
$S_0 \rightarrow S_1$	2.94 (421) $f = 0.893$	 (97.7%)	CT transition mainly from thiophene moieties to the core
$S_0 \rightarrow S_2$	3.73 (333) $f = 0.042$	 (95.7%)	CT transition mainly from the carbazole moiety to the core
$S_0 \rightarrow S_3$	3.79 (327) $f = 0.000$	 (99.9%)	$n-\pi^*$ transition on the aldehyde moiety

Figure 2.10: Calculated NTOs couples describing the first three singlet excitations for dye **CS2TCHO** in DCM. The f value is the oscillator strength of each transition, while λ value is the natural transition orbital eigenvalue associated with each NTOs couple; orbital isovalue: $0.04 e^{1/2} \text{ bohr}^{-3/2}$.

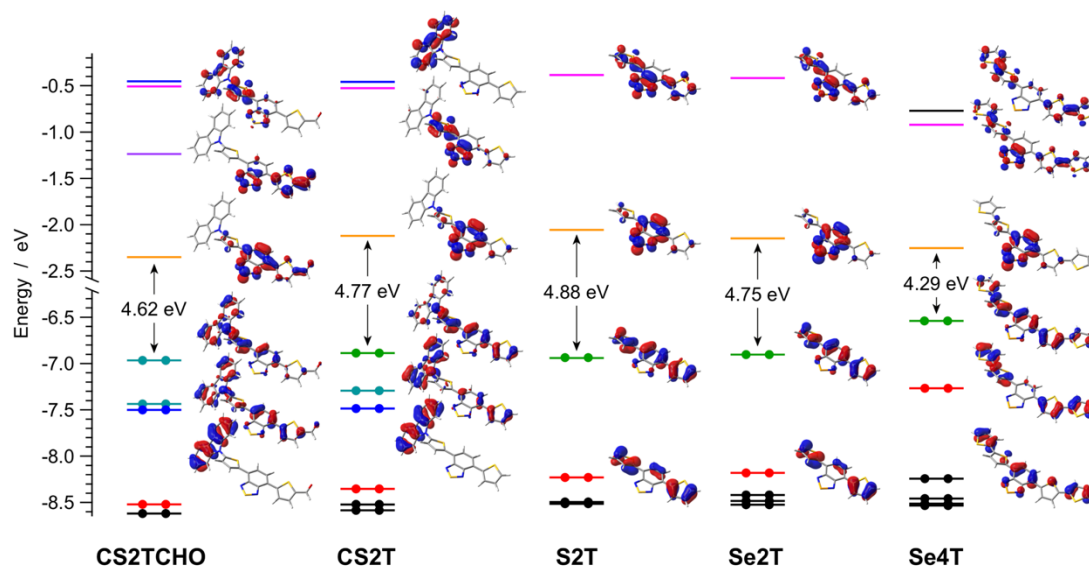


Figure 2.11: Frontier molecular orbitals computed at the PCM-M06-2X/6-31+G(d) level of theory in DCM at 298 K.

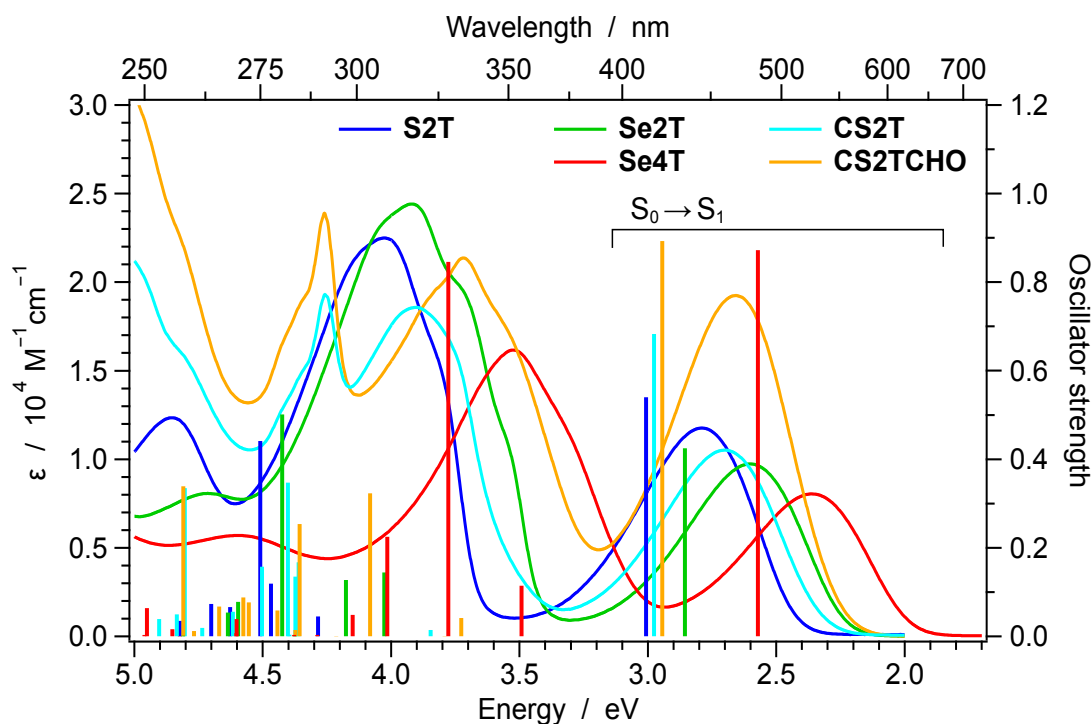


Figure 2.12: Comparison between the experimental absorption spectra in DCM at 298 K (full lines) of all the investigated dyes and their lowest singlet vertical excitations (bars) computed at the PCM-TD-M06-2X/6-31+G(d) level of theory in the same solvent, using the linear-response formalism. If present, the ECP10MDF pseudopotential was used for the Se element in combination with the associated aug-cc-pVDZ-PP basis set.

On the other hand, if a carbazole moiety is attached to the **S2T** scaffold, as in **CS2T**, a slight reduction in the HOMO-LUMO gap is observed, despite no direct contribution of the carbazole to these frontier orbitals (i.e., carbazole π orbitals mainly contribute to HOMO-1, HOMO-2 and to LUMO+2, see Figure 2.11).

The addition of an aldehyde terminal units to **CS2T**, as in **CS2TCHO**, further reduces the HOMO-LUMO gap by 0.15 eV, mainly due to LUMO stabilization (Figure 2.11). Accordingly, the absorption spectra of **CS2TCHO** displays a slightly red-shifted $S_0 \rightarrow S_1$ absorption band, compared to **CS2T** (Figure 2.5).^[79] Moreover, the presence of the aldehyde group in **CS2TCHO** has a strong influence on the intensity of the lower energy absorption band, the absorption coefficient of which is almost doubled with respect to the aldehyde-free **CS2T** analogue ($\epsilon_{\text{max}} = 19,400$ vs. $10,500 \text{ M}^{-1} \text{ cm}^{-1}$, Table 2.1). These findings are in line with TD-DFT results, which properly model the gradual decrease of the $S_0 \rightarrow S_1$ transition energy along the series **S2T** > **CS2T** > **CS2TCHO** and predict the corresponding oscillator strength to be the highest for **CS2TCHO** (Figure 2.12).

Emission in solution:

The five dyes exhibit intense fluorescence in DCM at 298 K (Figure 2.13, top and Table 2.2) and all emission profiles are broad and unstructured, as expected for charge-transfer (CT) transitions. The photoluminescence quantum yields (Φ_{PL}) are very high for all the luminophores (close to unity for **S2T**) and decrease as the emission shifts to lower energies, due the energy-gap law, but still displaying Φ_{PL} as high as 0.22 for **Se4T** (Table 2.2), the weakest and most red-shifted emitter of the series. In line with the absorption behavior, by replacing the sulfur atom with selenium, the fluorescence spectra are red shifted (Figure 2.13, top),^[78] with emission maxima spanning from the visible (e.g., 582 nm for **S2T**) to the NIR (i.e., 704 nm for **Se4T**, see Table 2.2). Similarly, the addition of the carbazole moiety on the **S2T** scaffold-with or without the presence of an extra aldehyde group as in **CS2T** and **CS2TCHO**, respectively-is also able to red shift the emission of the related luminophores by approx. $1,900\text{ cm}^{-1}$ (i.e., 0.24 eV), but without affecting the nature of the emitting state.

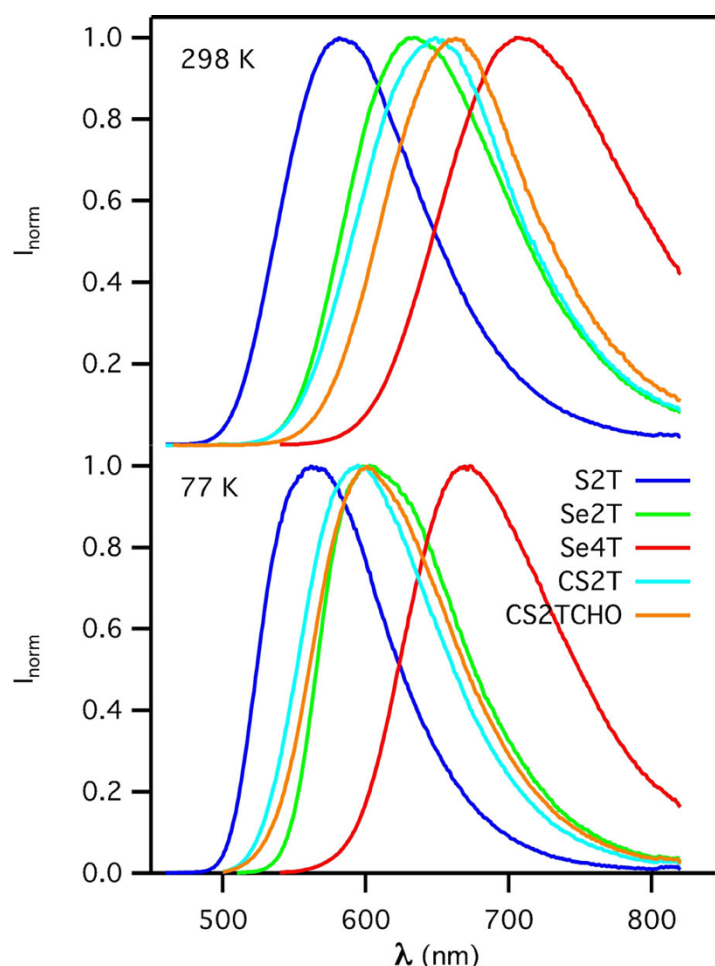


Figure 2.13: Intensity normalized emission spectra of the five dyes in DCM solution at 298 K (top), and in MeOH:DCM 1:1 (v/v) glass at 77 K (bottom). Excitation wavelengths are 450, 480, 530, 450 and 460 nm for **S2T**, **Se2T**, **Se4T**, **CS2T** and **CS2TCHO**, respectively.

Table 2.2: Main emission parameters.

	298 K ^[a]			77 K ^[b]	
	λ_{ems} (nm)	Φ_{PL}	τ (ns)	λ_{ems} (nm)	τ (ns)
S2T	582	0.92	13.8	562	11.6
Se2T	634	0.54	14.3	603	14.2
Se4T	704	0.22	5.7	669	7.1
CS2T	648	0.58	8.7	594	8.9
CS2TCHO	663	0.56	6.1	601	5.8

[a] In DCM solution at 298 K; [b] In MeOH/DCM (1:1) glass solution at 77 K.

As suggested by TD-DFT calculations, all the molecules of the series emit from the same excited state, which is also the one responsible for the lowest energy absorption band (i.e., S_1). Upon excitation, such charge-transfer state undergoes important structural relaxations, inducing a full planarization of the oligothiophene lateral moiety with respect to the central benzoheterodiazole core (Figure 2.14). Therefore, in their fully relaxed S_1 minimum, all the symmetric molecules (i.e., **S2T**, **Se2T** and **Se4T**) increase their symmetry from the initial C_2 point group to the highly symmetrical C_{2v} . The same relaxation mode also occurs in the carbazole- equipped molecules (i.e., **CS2T** and **CS2TCHO**), in which also the carbazole moiety experiences a partial flattening (e.g., the dihedral angle between the carbazole plane and the nearby thiophene passes from $\approx 70^\circ$ in S_0 to $\approx 40^\circ$ in S_1 minimum, Figure 2.15).

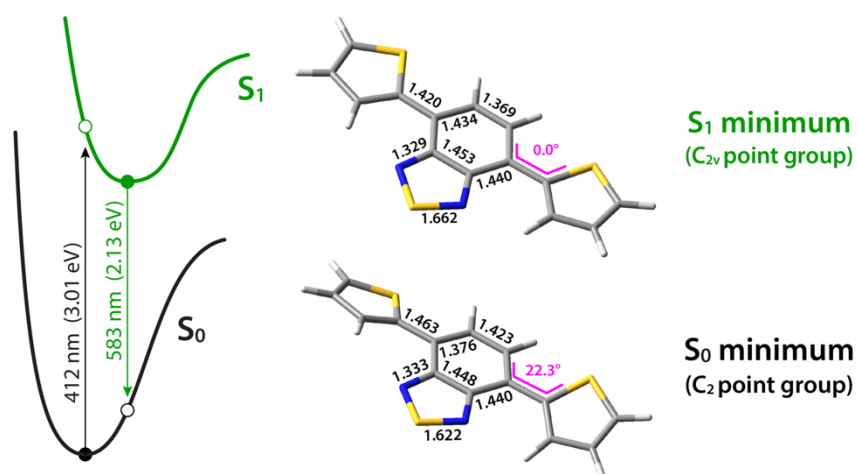


Figure 2.14: Comparison between the optimized ground-state (S_0) and excited-state (S_1) geometries of **S2T**, together with a simplified energy diagram showing the effect of the excited-state structural relaxation. Due to planarization, the S_1 geometry displays higher symmetry compared to S_0 (i.e., C_{2v} vs. C_2 , respectively). All data are computed at the PCM-TD-M06-2X/6-31+G(d) level of theory in DCM.

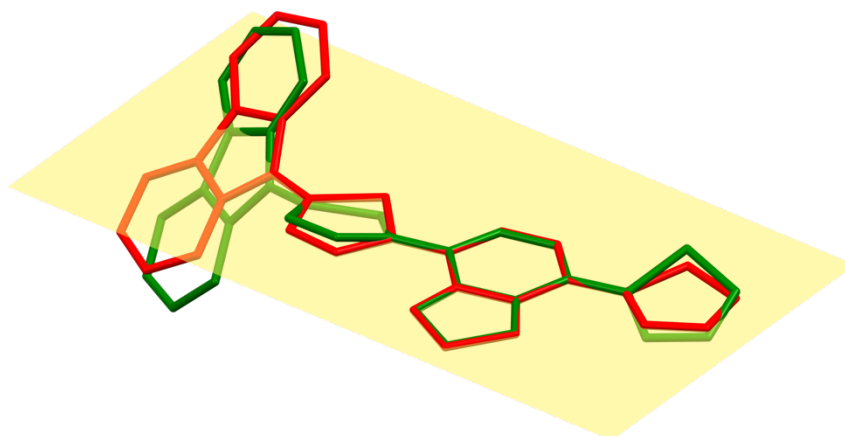


Figure 2.15: Structural overlay (H atoms omitted) between the optimized ground-state (S_0 , green) and excited-state (S_1 , red) geometries of **CS2T**. Molecules are overlapped by minimizing the root-mean-square deviation of all the atoms of the benzothiadiazole. Due to excited-state relaxation, in the S_1 minimum-energy geometry, the thiophene moieties and the central benzothiadiazole core are virtually coplanar, as shown by the best-fit plane in yellow. It is worth noting that also the angle between the carbazole plane and the nearby thiophene unit undergoes flattening, passing from 69.6° to 43.0° in S_0 and S_1 , respectively. All data are computed at the PCM-TD-M06-2X/6-31+G(d) level of theory in DCM.

Because of these excited-state relaxations, all compounds display remarkable Stokes shifts, ranging from $5,340$ to $4,880\text{ cm}^{-1}$ for **S2T**, **Se2T** and **Se4T** (i.e., 0.66 – 0.60 eV) and up to $6,350\text{ cm}^{-1}$ (i.e., $\approx 0.79\text{ eV}$) in the carbazole derivatives **CS2T** and **CS2TCHO**. Such results are in line with TD-DFT calculations, which estimate a larger Stokes shift for **CS2T** and **CS2TCHO** (i.e., $0.98\pm 0.02\text{ eV}$), compared to the carbazole-free compounds **S2T**, **Se2T** and **Se4T** (i.e., $0.86\pm 0.02\text{ eV}$).

Low-temperature fluorescence spectra were recorded in a transparent glass mixture (MeOH:DCM 1:1 v/v) at 77 K (Figure 2.13, bottom). All the emission profiles remain broad and unstructured, displaying a blue shift of the emission maxima with respect to those recorded at room temperature. These findings are a further indication of the predicted charge-transfer character of the emitting states. Excited state lifetimes (τ) of the five dyes are not much affected by the temperature and the nature of the solution, liquid or frozen. This behavior, together with the lifetime values in the ns range, is indicative of the singlet nature of the luminescence (Table 2.2).

2.3.3 Photophysics and optical properties of PMMA based LSCs

Photophysics in PMMA matrix:

The photophysical properties of the five dyes were investigated in PMMA matrix. The films were prepared at three different dye concentrations (0.2% , 0.5% and 1.0% w/w) from evaporation of DCM solutions. Figure 2.16 shows the films under

daylight and UV light; the films exhibit strong fluorescence and excellent transparency. The thermal stability of the dye-PMMA films was checked by transmission spectroscopy (Figure 2.17); all prepared samples are stable for months.

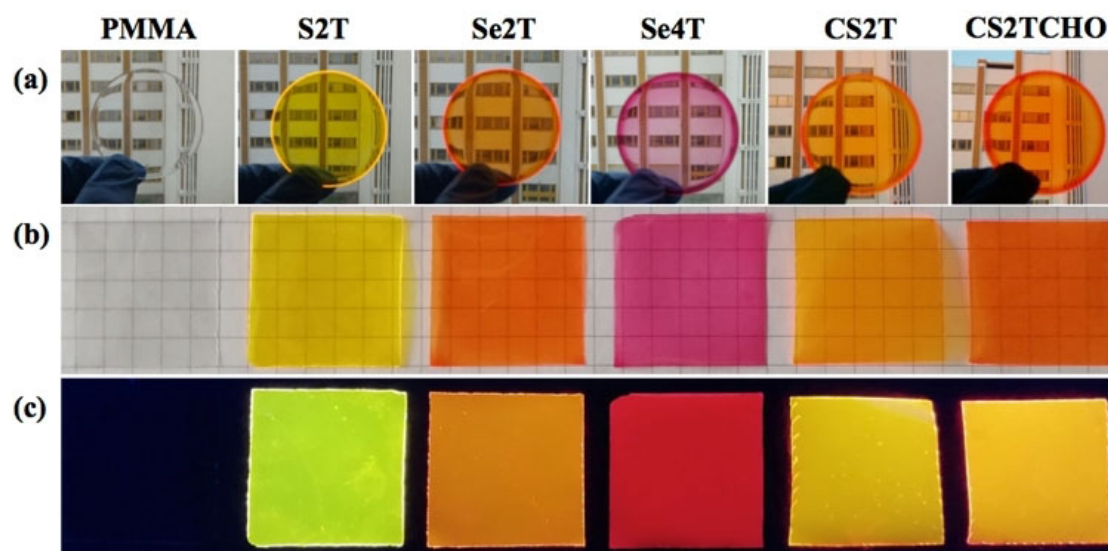


Figure 2.16: Pictures of the dye-PMMA films (0.5% w/w) under day (a and b) and UV light (c).

Table 2.3: Main photophysical parameters of dyes in PMMA matrix at 298 K.

	conc. (% w/w)	λ_{abs} (nm)	λ_{ems} (nm)	Φ_{PL} (%) ^[a]	τ (ns)
S2T	0.2	445	576	83.2	13.4
	0.5	447	585	77.9	13.6
	1.0	443	588	68.5	13.7
Se2T	0.2	477	621	65.4	14.5
	0.5	476	630	54.3	15.8
	1.0	474	636	47.7	15.8
Se4T	0.2	523	694	28.6	6.0
	0.5	523	705	21.9	7.1
	1.0	522	718	16.1	6.9
CS2T	0.2	458	612	76.9	10.2
	0.5	458	623	73.2	10.5
	1.0	450	626	67.9	10.4
CS2TCHO	0.2	466	633	72.7	7.3
	0.5	466	642	64.2	7.4
	1.0	472	733	21.1	6.3

[a] Absolute quantum yield.

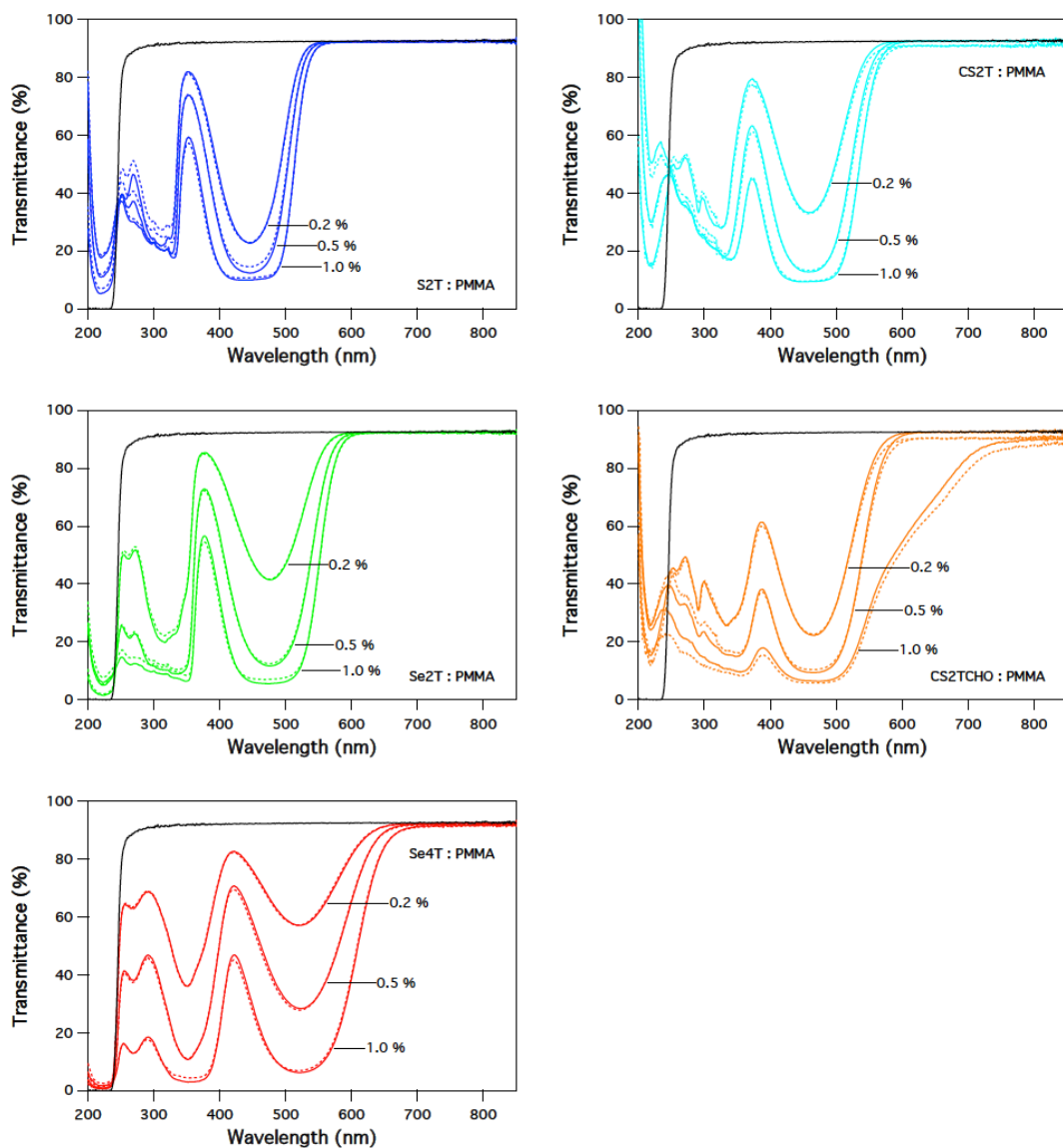


Figure 2.17: Transmittance spectra of the dyes in PMMA matrix as prepared (full lines) and after 2 months (dotted lines) in the dark. The concentration of the dye (w/w) is indicated in the graph; PMMA (black line).

The transmission spectra of the dye-PMMA films in Figure 2.17 shows that the transmittance outside the absorption range of the dyes is over 90%. In the case of **CS2TCHO**, the sample prepared at the highest concentration (1.0% w/w) displays a transmittance (hence, transparency) much lower than the others. This is due to its limited solubility in the PMMA matrix, that causes precipitation of the dye with formation of microcrystals that scatter the incoming light. From the measured transmittance and diffuse reflectance spectra (Figure 2.18), the absorption factor of the films were calculated as Figure 2.19, and the relevant main parameters (λ_{\max} and A_{\max}) are collected in Table 2.3, Table 2.4 and Table 2.5. All spectra show two absorption bands, one in the UV (280-400 nm) and a second at a lower energy in the visible (400-

760 nm) range with similar absorption factor. The absorption band maxima are very close to those already observed in DCM solution, indicating that the electronic properties of the systems are not significantly affected by the change in the nature of the matrix.

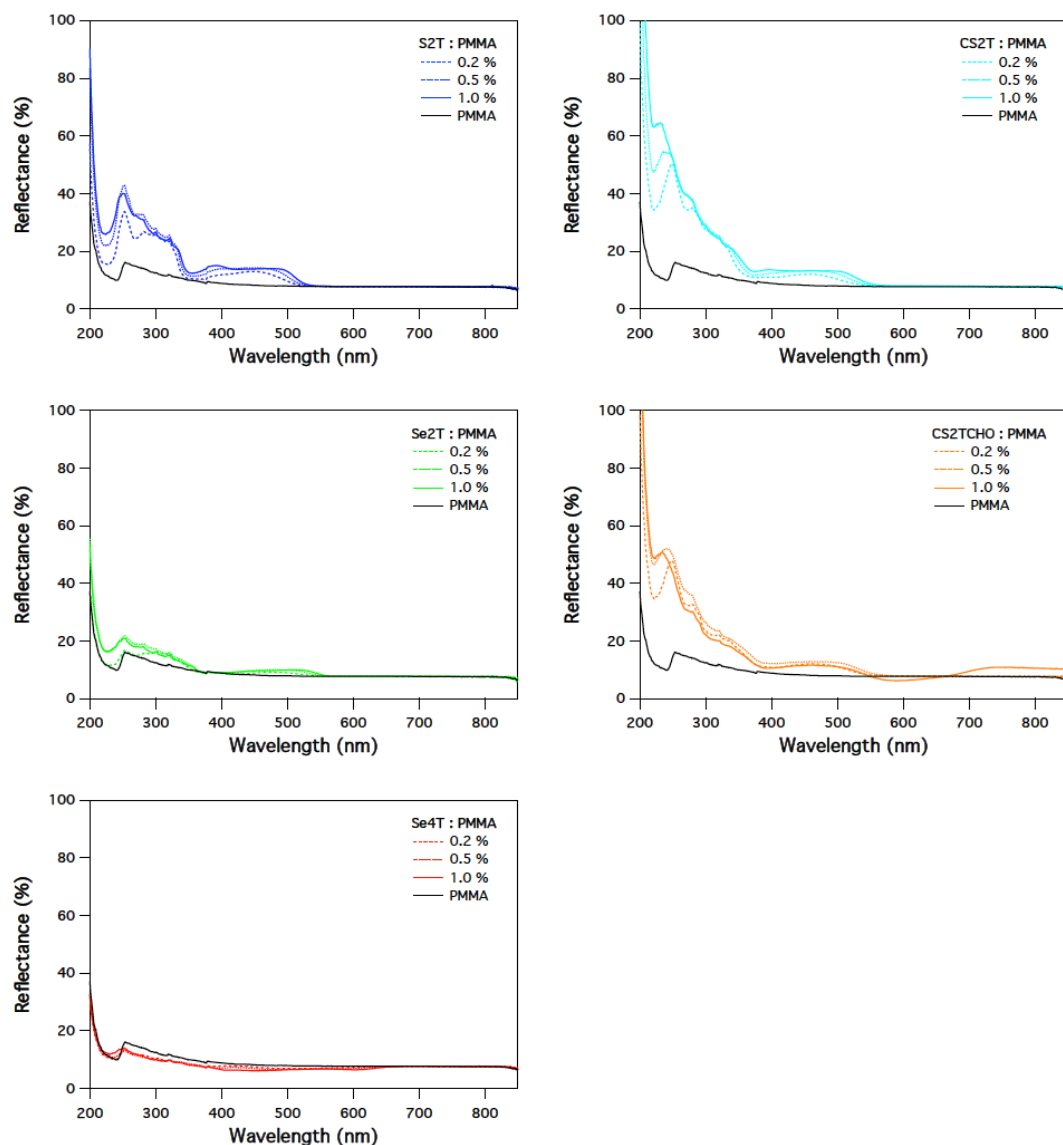


Figure 2.18: Reflectance spectra of the dyes at different concentration (0.2, 0.5, 1.0 % w/w) in PMMA matrix.

The fluorescence emission spectra (the intensity is proportional to the quantum yield) of dye-PMMA films at different concentrations are reported in Figure 2.20. An apparent shift of the emission maxima to longer wavelengths in the concentrated samples is observed, due to the reabsorption effects.^[80-81] The great reduction in emission intensity (also in quantum yield) of 1.0% w/w **CS2TCHO** film is because the solid dyes inside the PMMA matrix.

Absolute photoluminescence quantum yield (Φ_{PL}) and excited state lifetimes (τ) of all the dye-PMMA films are gathered in Table 2.3. The most concentrated samples exhibit apparently low Φ_{PL} , which is clearly due to the reabsorption effects, because the excited state lifetimes are not affected. Noteworthy, the relative decrease in the apparent quantum yield with a 5-times increase of the concentration of the dye is limited to 18% and 12% for **S2T** and **CS2T**, respectively. Indeed, the two thiadiazole derivatives display some of the largest Stokes shift in the series (5,110 and 5,490 cm^{-1} , for **S2T** and **CS2T**).

Table 2.4: Main optical parameters in PMMA matrix at 298 K.

	c (%) ^[a]	A _{max} (%)	OQE (%) ^[b]	η_{trap} ^[c]	EQE (%) ^[d]
S2T	0.2	64.3	47.6	0.572	30.6
	0.5	73.4	42.7	0.548	31.3
	1.0	76.2	35.1	0.512	26.7
Se2T	0.2	49.3	36.2	0.554	17.9
	0.5	78.2	28.1	0.517	22.0
	1.0	84.6	25.5	0.535	21.6
Se4T	0.2	35.9	7.4	0.259	2.7
	0.5	64.8	5.1	0.233	3.3
	1.0	87.0	1.3	0.081	1.1
CS2T	0.2	54.6	39.5	0.514	21.6
	0.5	73.9	37.6	0.514	27.8
	1.0	77.4	35.1	0.517	27.2
CS2TCHO	0.2	65.6	37.7	0.519	24.7
	0.5	77.7	31.2	0.486	24.2
	1.0	82.0	0.7	0.033	0.6

[a] w/w; [b] Optical quantum efficiency $\text{OQE} = n_{\text{edge}} / n_{\text{abs}}$; [c] Trapping efficiency $\eta_{\text{trap}} = \text{OQE} / \Phi_{\text{PL}}$; [d] External quantum efficiency $\text{EQE} = \text{OQE} \times \text{A}\%$.

Optical properties of PMMA based LSCs

The η_{trap} of the samples containing the dyes **S2T**, **Se2T** and **CS2T** in the PMMA matrix remains slightly above 0.5 at all concentrations investigated (Table 2.4). This is lower than the theoretical limit of 0.745 for polymeric luminescent solar concentrators, with refractive index $n=1.5$, embedding randomly oriented chromophores that emit isotropically in the absence of light-scattering defects.^[53] The main reason for this deviation lies in the non-optical quality of the surface of the film, the roughness of which introduces escape losses in the waveguide. The drop of η_{trap} in the **Se4T** and **CS2TCHO** containing samples at the highest concentration (1% w/w) can be ascribed to the low solubility of the dye in the polymer matrix. This induces precipitation of microcrystals, as already commented above, that behaves as scattering centers, reducing the trapping efficiency.

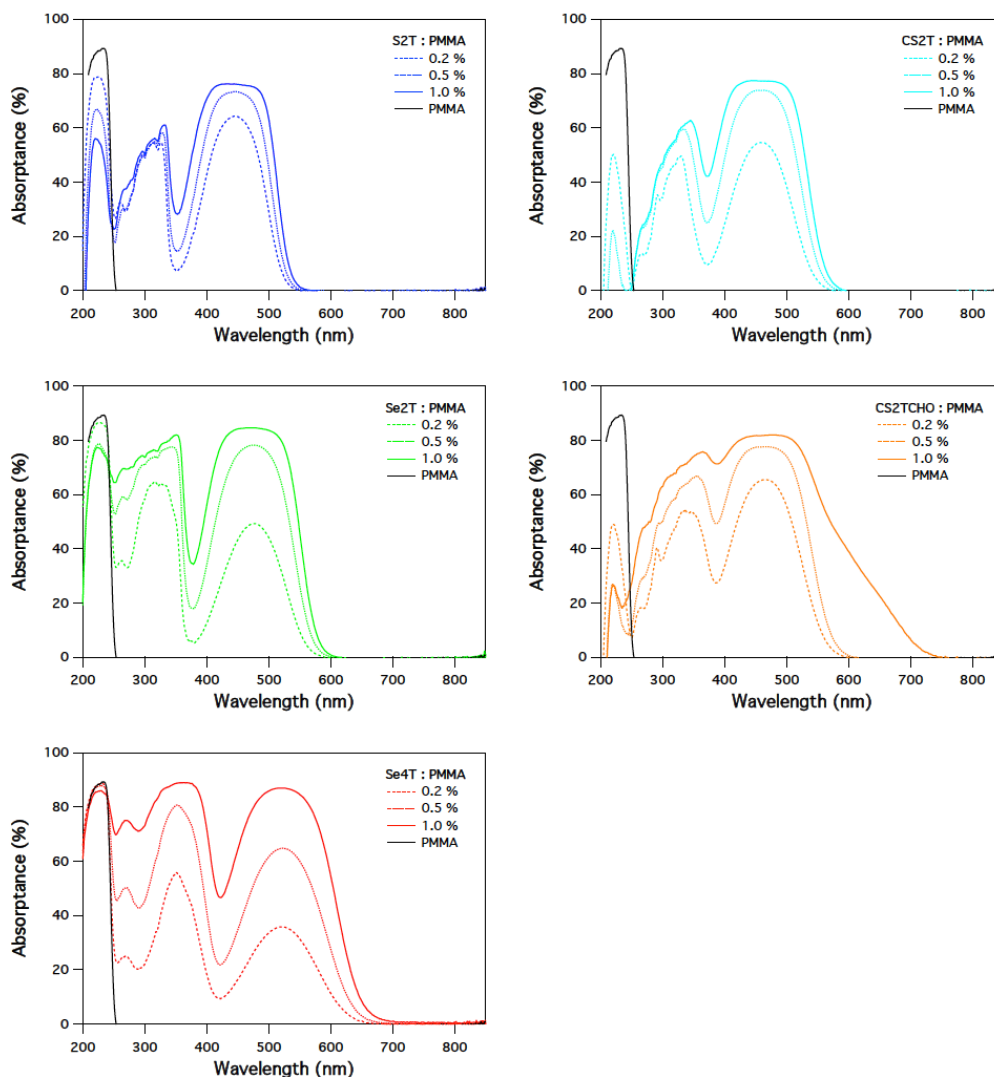


Figure 2.19: Absorbance (absorption factor) spectra of the dyes at different concentration (0.2, 0.5, 1.0 % w/w) in PMMA matrix.

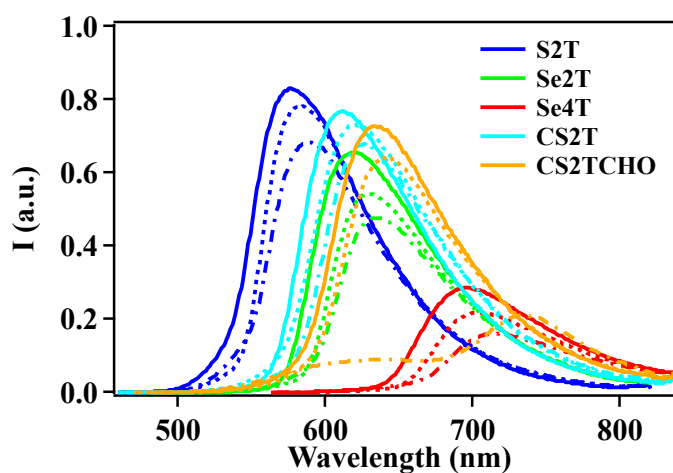


Figure 2.20: Emission spectra of dyes in PMMA matrix at 298 K at different dye concentration: 0.2% (full line), 0.5% (dotted line) and 1.0% w/w (line and point). Excitation wavelengths are 450, 480, 530, 450 and 460 nm for S2T, Se2T, Se4T, CS2T and CS2TCHO, respectively.

Table 2.5: Optical parameters of dyes in PMMA matrix at 298 K.

	conc. (%) ^[a]	A (%) ^[b]			OQE (%) ^[c]	EQE (%) ^[d]			G ^[e]	F ^[f]
		UV	Vis	UV-Vis		UV	Vis	UV-Vis		
S2T	0.2	33.2	16.4	20.6	47.6	15.8	7.8	9.8	86.8	10.3
	0.5	39.8	20.7	25.5	42.7	17.0	8.8	10.9	90.6	9.7
	1.0	49.5	24.1	30.5	35.1	17.4	8.5	10.7	89.3	7.8
Se2T	0.2	40.0	14.6	21.0	36.2	14.5	5.3	7.6	79.1	7.2
	0.5	56.7	27.6	34.9	28.1	15.9	7.8	9.8	96.2	6.8
	1.0	66.0	34.5	42.4	25.5	16.8	8.8	10.8	83.3	5.3
Se4T	0.2	37.1	13.9	19.7	7.4	2.7	1.0	1.5	97.7	1.8
	0.5	63.4	27.9	36.8	5.1	3.2	1.4	1.9	85.6	1.1
	1.0	82.7	45.3	54.6	1.3	1.1	0.6	0.7	86.8	0.3
CS2T	0.2	28.8	15.1	18.5	39.5	11.4	6.0	7.3	82.2	8.1
	0.5	43.4	24.2	29.0	37.6	16.3	9.1	10.9	88.0	8.3
	1.0	51.8	28.8	34.5	35.1	27.2	10.1	12.1	84.5	7.4
CS2TCHO	0.2	41.7	21.0	26.1	37.7	15.7	7.9	9.9	90.6	8.5
	0.5	56.6	29.1	36.1	31.2	17.7	9.1	11.3	89.3	7.0
	1.0	68.9	45.9	51.7	0.7	0.5	0.3	0.4	86.8	0.2

[a] w/w; [b] Integrated absorption factor values in the UV (280-400 nm), Vis (400-760 nm), and UV-Vis (280-760 nm) range; [c] Optical quantum efficiency $OQE = n_{edge} / n_{abs}$; [d] External quantum efficiency $EQE = OQE \times A\%$; [e] Geometric gain $G = S_{surf} / S_{edge}$ calculated for 25×25 mm samples with average film thickness $\approx 71 \mu\text{m}$; [f] Flux gain $F = (OQE / 4) \times G$.

The optical quantum efficiency, OQE (Figure 2.21, bottom), displays an almost linear decrease with increasing concentration of the dye. As the trapping efficiency is not much affected by the concentration, with the exception discussed above, the variation in OQE can be attributed to the variation in the measured apparent quantum yield. This is affected by a reabsorption effect, as evidenced by the emission spectra in Figure 2.20. It should be noted that, despite the non-optimal flatness of the film surface that severely limits the trapping efficiency of the devices, an OQE as high as 48% is observed for **S2T** at 0.2% in PMMA.

The decrease in OQE, due to the re-absorption effect, is somehow offset by the increase in the absorption factor A% by increasing the concentration of the dye. This results in an external quantum efficiency (EQE) that maximizes at intermediate values of dye concentration (Figure 2.21, top). Notably, EQE above 30% at $G \approx 88$ is reached for the **S2T**-PMMA samples. Besides, a flux gain over 10 has been observed for the same sample (Table 2.5). This performance is comparable or exceeds that reported for state-of-the-art single layer LSCs. For instance, Wong and co-workers reported a few systems comprising highly fluorescent perylene diimides with simulated OQEs between 45 and 55% and flux gains around 10 at $G \approx 90$.^[82] On the other hand, the

system with the record power conversion efficiency ($\eta = 6.8\%$) reported by Baldo and co-workers displays higher flux gain and EQE at low G values.^[83] But the performances rapidly drop at higher geometric gains well below the values observed in the present work.

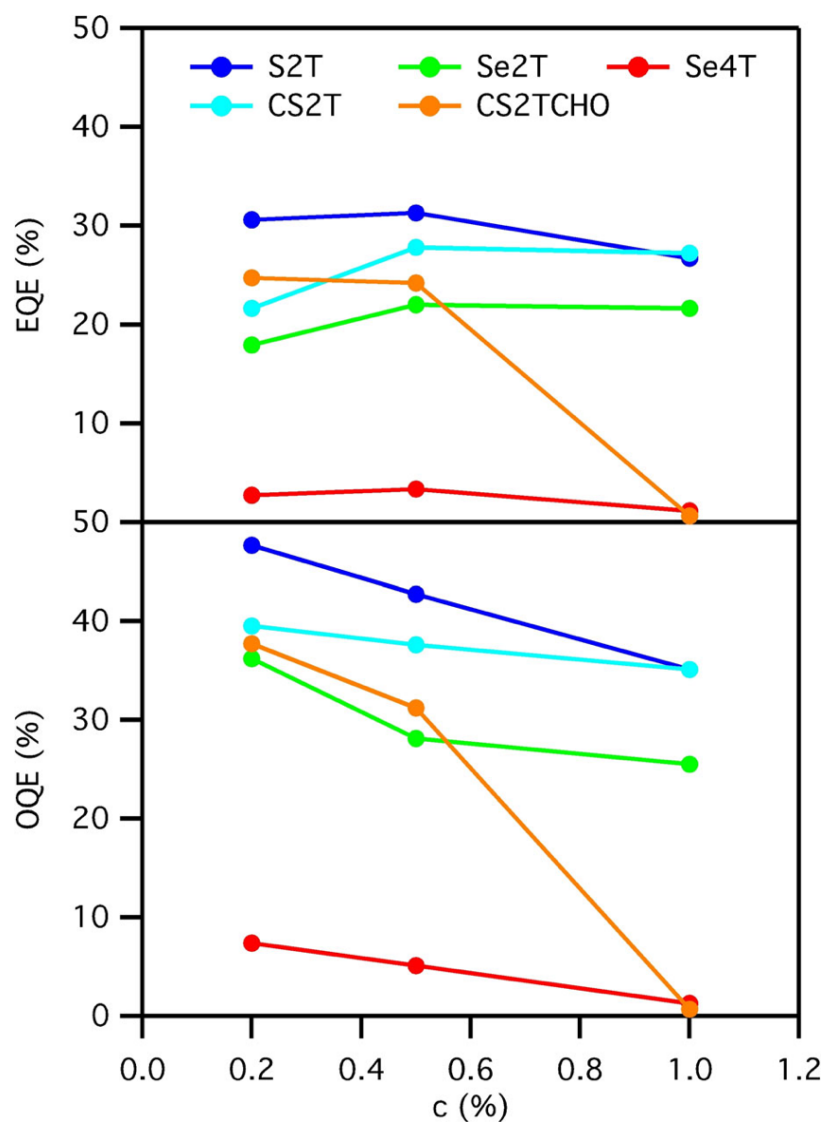


Figure 2.21: Optical (OQE, bottom) and external (EQE, top) quantum efficiency as a function of dye concentration.

From the integration of the absorption spectra (Figure 2.19) it is possible to obtain the overall fraction of photons absorbed in the UV, Vis and UV/Vis range (Table 2.5). Since OQE is wavelength-independent, then we can derive the $EQE(\lambda)$ spectra (Figure 2.22, left) from the equation 2.6, as reported in the experimental section. As expected on the basis of the absorption spectra (Figure 2.19), the main contribution to EQE is from the UV region. Even for the highest concentration of the dye analyzed, the situation does not improve significantly, mainly due to the absence of absorption above 600 nm (Figure 2.22, right).

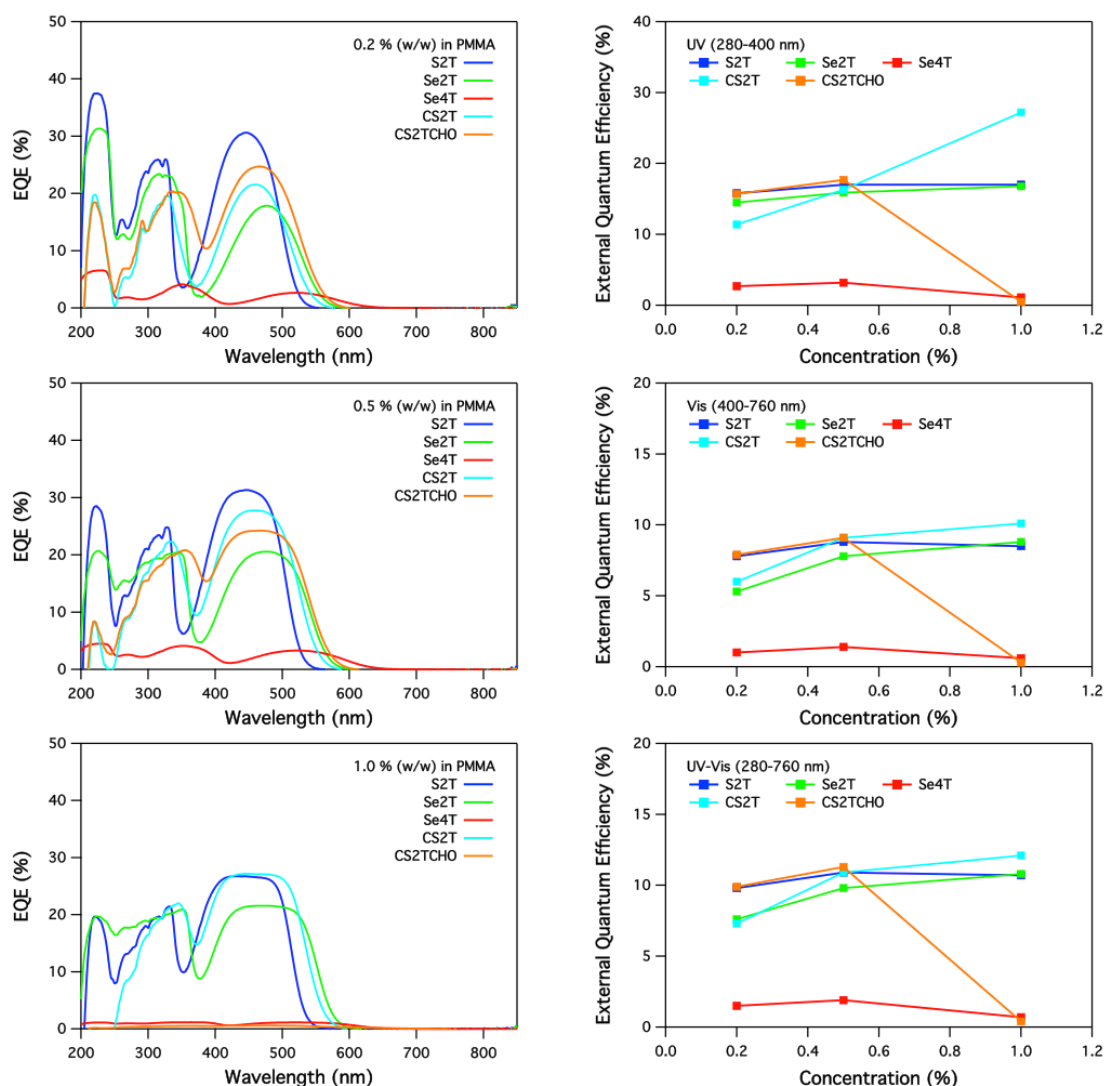


Figure 2.22: External quantum efficiency (EQE) spectra (left) of the devices and EQE over different spectral regions (UV 280-400 nm, Vis 400-760 nm, UV-Vis 280-760 nm) as a function of dye concentration (0.2, 0.5, 1.0 % w/w) in PMMA matrix (right).

2.3.4 Photophysics and IPCE of PDMS based LSCs

Photophysics in PDMS matrix:

The dyes can be easily doped into PDMS matrix to form soft devices.^[84-85] In Figure 2.23, the pictures of the five dye-PDMS devices under daylight and UV light are gathered, Figure 2.24 shows a close-up picture of edge emission. These devices have been prepared in three different dye concentrations (0.004 %, 0.010% and 0.020% w/w). **S2T**, **Se2T** and **Se4T** are perfectly soluble into PDMS matrix to form the colored transparent devices, whereas **CS2T** displays a lower solubility and forms transparent devices only at the lowest concentration tested (0.004% w/w). **CS2TCHO** showed only limited solubility in PDMS, affording samples of lower quality, where the dispersion of dye microcrystals is evident.^[86]

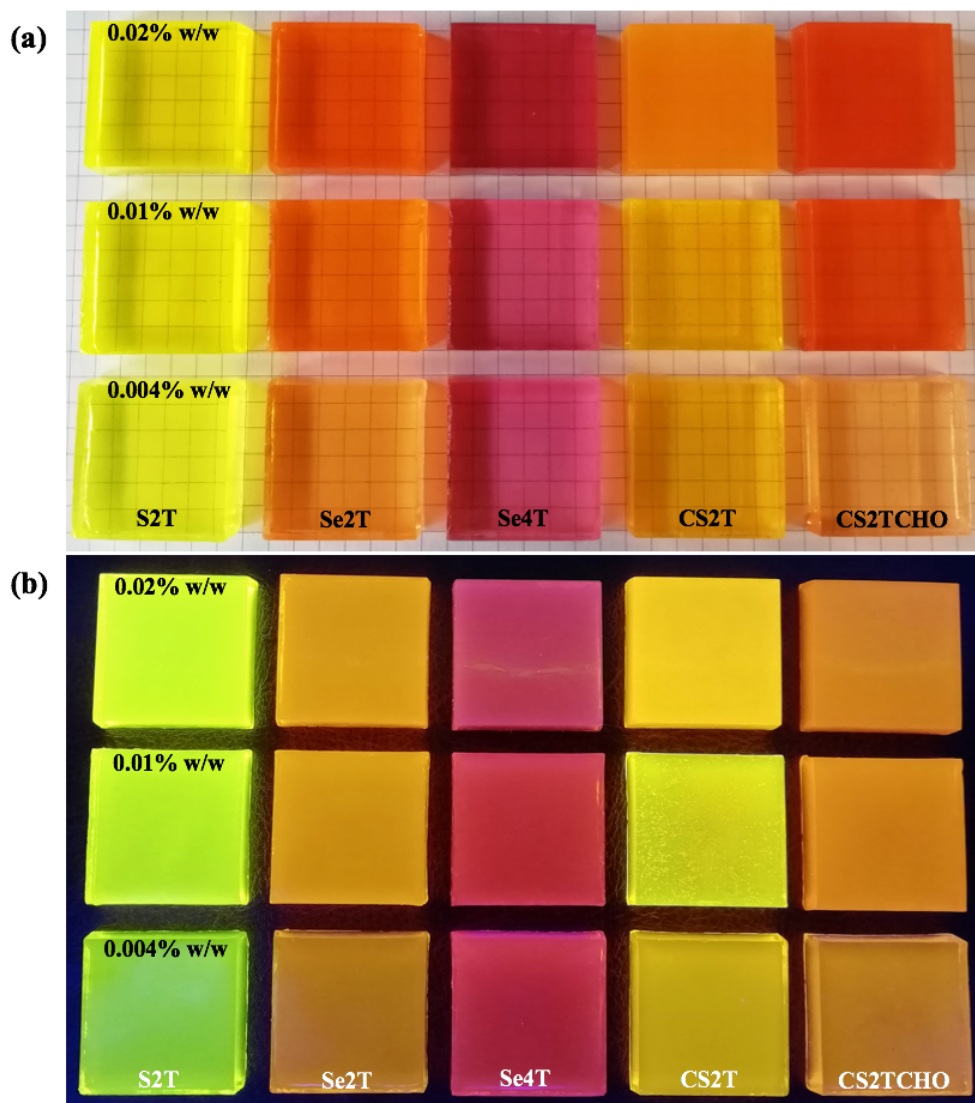


Figure 2.23: Dyes in PDMS matrix with different concentrations (0.004, 0.01, 0.02 % w/w) under daylight (a) and UV light (b) illumination.

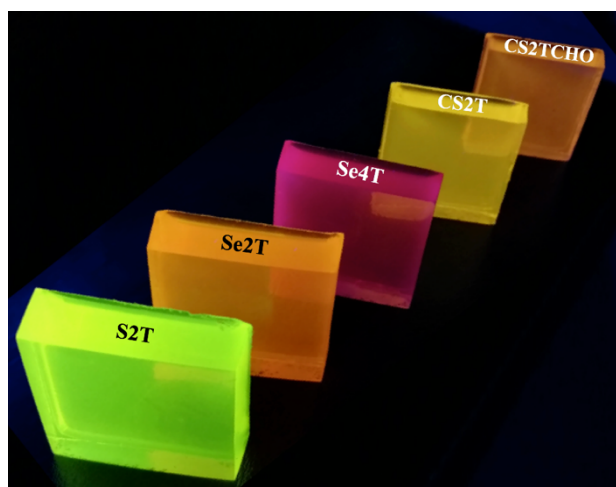


Figure 2.24: A close-up picture of edge emission of the dye-PDMS devices (0.004% w/w) under UV light.

The thermal stability properties of the dyes in PDMS matrix were checked both by transmission and emission spectroscopy. In Figure 2.25 are reported the transmittance spectra of the dyes (0.020 % w/w) in PDMS matrix at different time after preparation. All systems exhibit good stability within two weeks with the exception of Se4T. Its transmittance changes with time, probably due to the growth of nanocrystals or aggregates inside the PDMS matrix, but the emission spectrum and excited state lifetime do not change significantly (Figure 2.26).

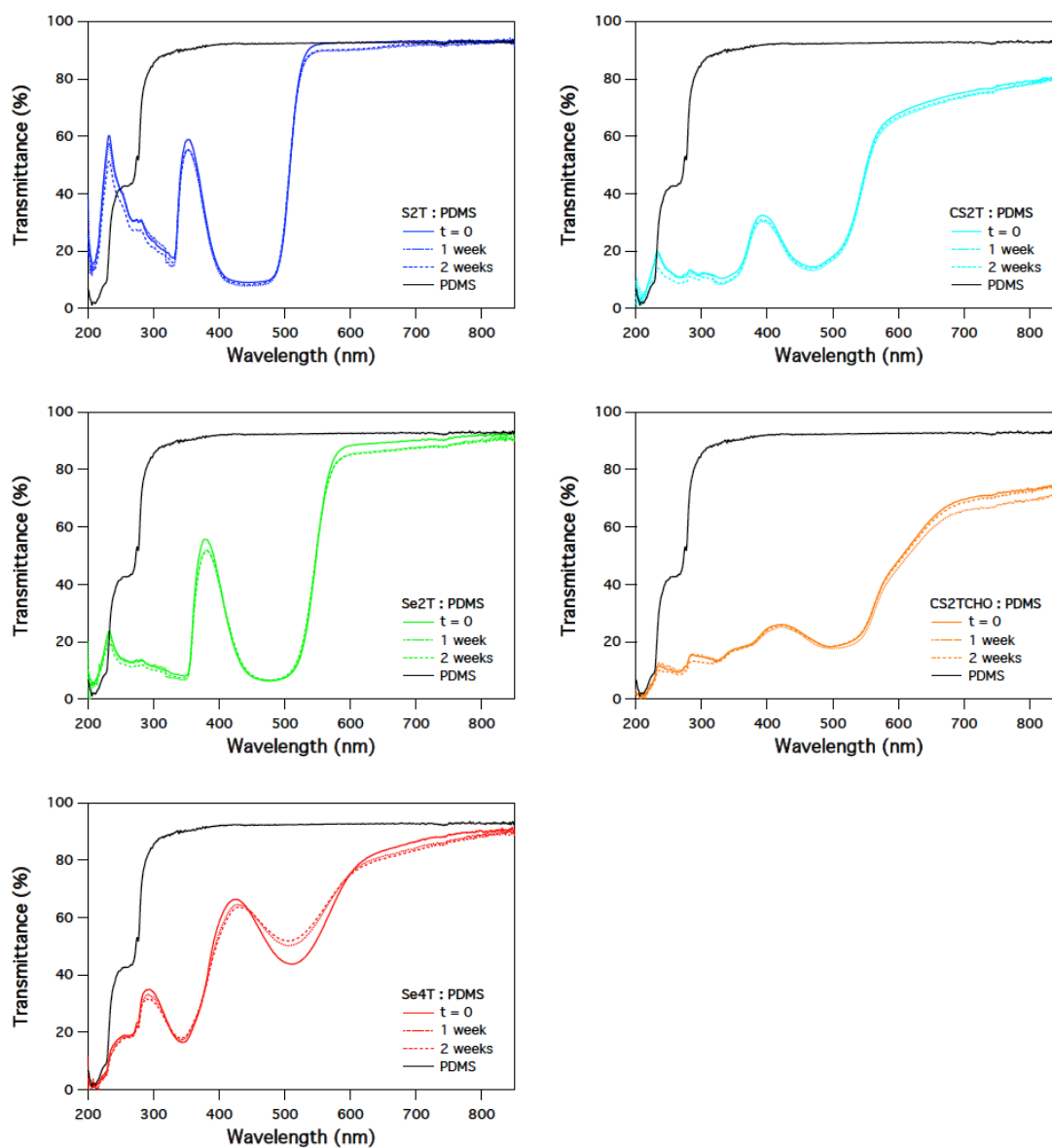


Figure 2.25: Transmittance spectra of the dyes (0.020 % w/w) in PDMS matrix at different time after preparation.

The calculated absorbance (absorption factor) spectra of the dyes at different concentration (0.004, 0.010, 0.020 % w/w) in PDMS matrix are shown in Figure 2.27, and the relevant transmittance and reflectance spectra are collected in Figure 2.28. In

Table 2.6 are reported the key photophysical parameters of the dyes in PDMS matrix at 298 K. The transparency of the PDMS device in the non-absorbing range is again above 90% with the exception of some concentrated samples exhibiting lower transparency, due to the presence of dye crystals or nanocrystals inside the PDMS matrix.

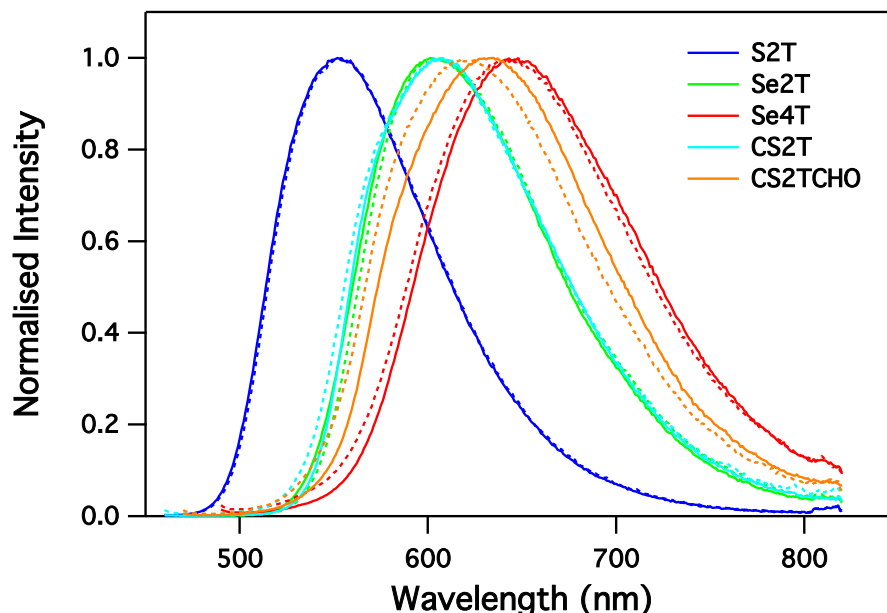


Figure 2.26: Emission spectra of the dyes (0.004 % w/w) in PDMS matrix as prepared (full lines) and after 2 weeks (dotted lines). Excitation wavelengths are 450, 480, 480, 450 and 460 nm for **S2T**, **Se2T**, **Se4T**, **CS2T** and **CS2TCHO**, respectively.

Table 2.6: Main photophysical parameters of the dyes in PDMS matrix at 298 K.

	conc. (%) ^[a]	λ_{abs} (nm)	λ_{ems} (nm)	Φ_{PL} (%) ^[b]	τ (ns) ^[c]	Stokes shift (cm ⁻¹)
S2T	0.004	446	549	90.8	11.7	4210
	0.010	446	553	89.5	12.0	4340
	0.020	444	550	81.4	11.9	4340
Se2T	0.004	478	600	62.0	15.5	4250
	0.010	478	601	61.1	16.0	4280
	0.020	474	604	54.6	15.4	4540
Se4T	0.004	516	647	34.7	8.7	3920
	0.010	513	642	24.8	8.5	3920
	0.020	510	642	19.8	8.6	4030
CS2T	0.004	458	588	79.8	8.9	4830
	0.010	449	571	80.0	10.3	4760
	0.020	450	567	55.1	$\tau_1=4.8$ $\tau_2=11.0$	4590
CS2TCHO	0.004	469	603	61.4	6.9	4740
	0.010	473	607	44.3	$\tau_1=5.8$ $\tau_2=14.6$	4670
	0.020	470	601	35.0	$\tau_1=5.3$ $\tau_2=12.7$	4640

[a] w/w; [b] Absolute quantum yield; [c] Excited state lifetime.

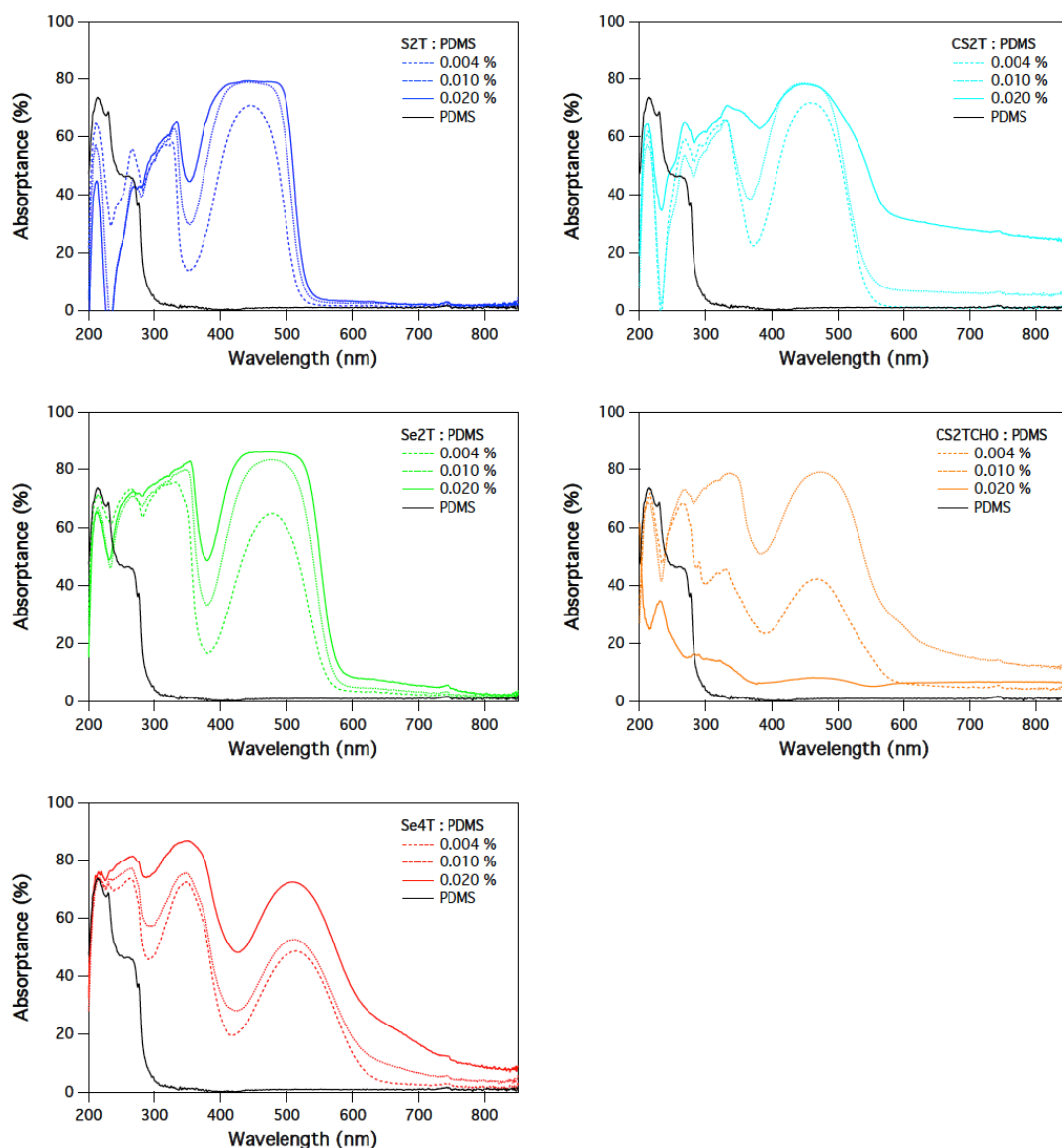


Figure 2.27: Absorbance (absorption factor) spectra of the dyes at different concentration (0.004, 0.010, 0.020 % w/w) in PDMS matrix.

The fluorescence spectra of **S2T**, **Se2T**, **Se4T** and **CS2TCHO** at the three different concentrations (0.004, 0.010, 0.020 % w/w) tested are virtually overlapping (Figure 2.29). Compared with the emission spectra of 0.01% and 0.02% w/w, the diluted sample of **CS2T**-PDMS (0.004% w/w) undergoes an apparently large red shift (Figure 2.29). This is because **CS2T** is completely dissolved into the PDMS matrix at the low concentration (no crystals inside). Absolute fluorescence quantum yields and excited state lifetimes of these dye-PDMS devices were collected in Table 2.6. The most diluted samples exhibit the highest quantum yields, and the lifetimes are also influenced by the PDMS matrix.

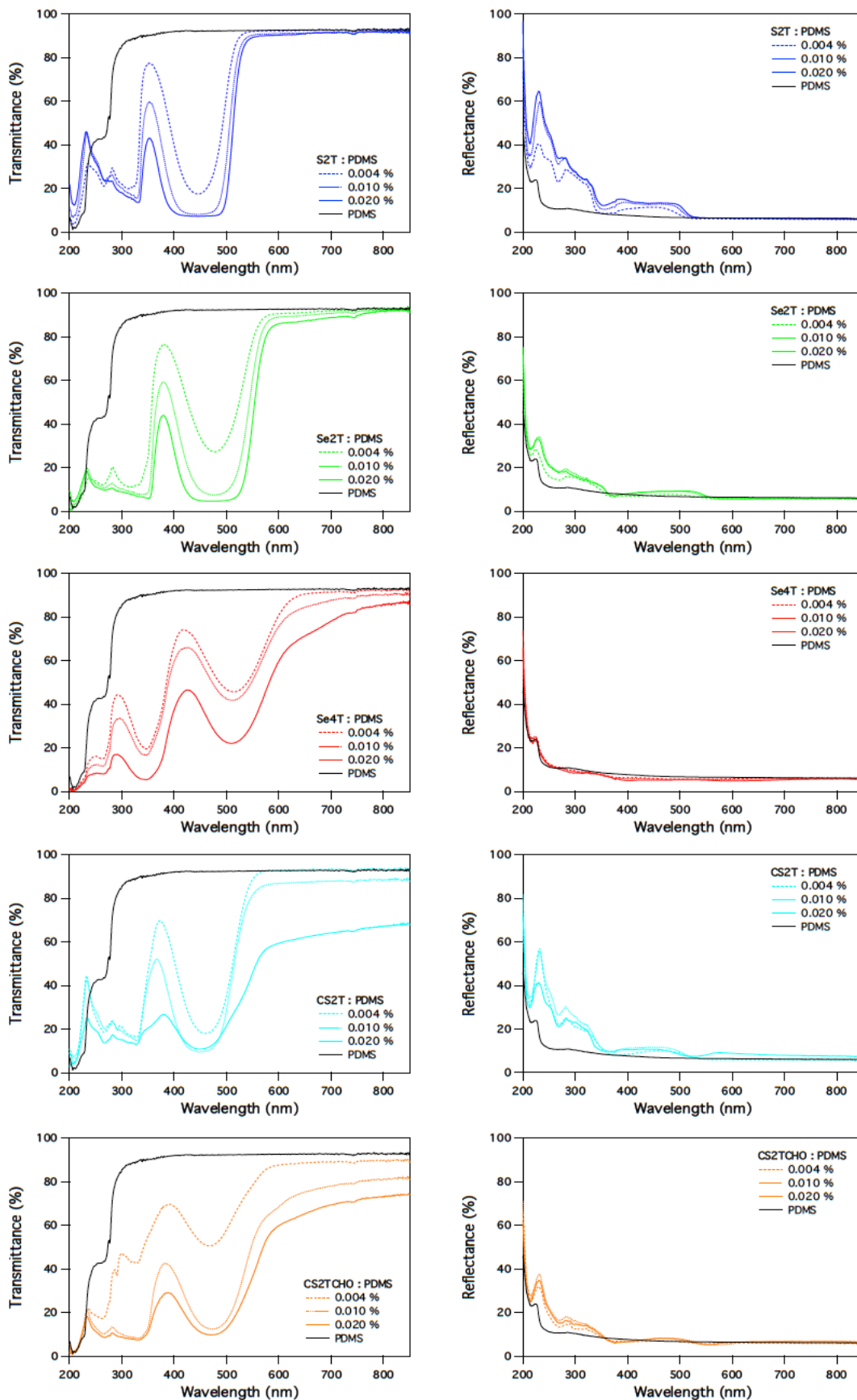


Figure 2.28: Transmittance (left) and reflectance (right) spectra of the dyes at different concentration (0.004, 0.010, 0.020 % w/w) in PDMS matrix.

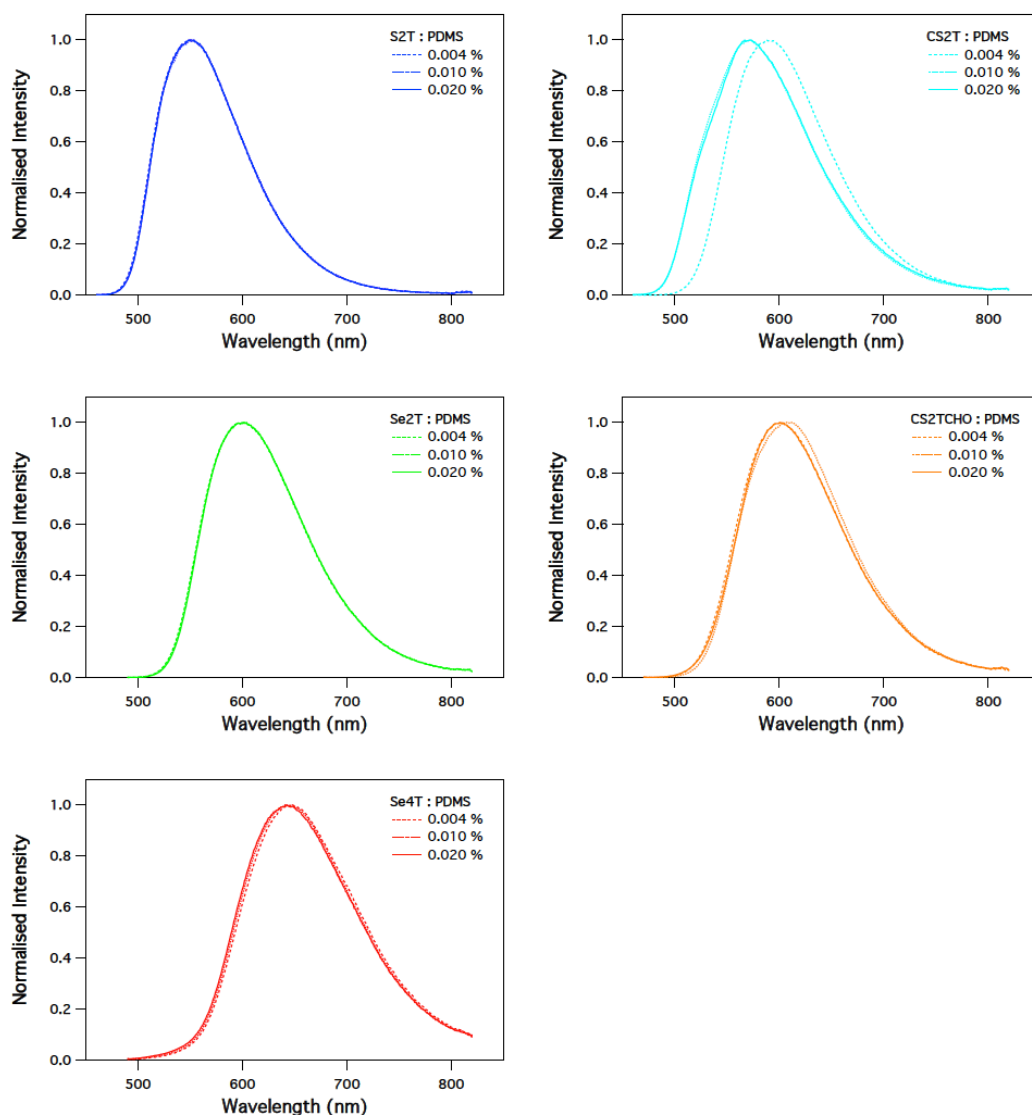


Figure 2.29: Normalized emission spectra of the dyes at different concentration (0.004, 0.010, 0.020 % w/w) in PDMS matrix. Excitation wavelengths are 450, 480, 480, 450 and 460 nm for **S2T**, **Se2T**, **Se4T**, **CS2T** and **CS2TCHO**, respectively.

IPCE of the PDMS based LSCs:

Luminescent solar concentrator devices were assembled starting from the PDMS matrices, by placing four mini Si-c PV cells at the four edges of the dye-PDMS devices. Incident photon-to-electron conversion efficiency (IPCE) spectra (Figure 2.30) of the LSCs were further investigated at three different concentrations (0.004 %, 0.010% and 0.020% w/w). Transparent devices of the **S2T** and **Se2T** show a similar trend. The samples with the highest and lowest concentration display weak IPCE values, whereas samples with intermediate concentration display the strongest IPCE values. IPCE in far-red/nearinfrared (NIR) region above 600 nm have almost the same values as the reference (PDMS with no dye). Because of the scattering effects of the dye crystals in the PDMS devices.^[87-88] the IPCE values of the **CS2T** and **CS2TCHO** in the NIR

region are higher than the PDMS reference; only the sample with 0.004% w/w **CS2T** (transparent) has the same level as the blank (Figure 2.30). For **Se4T**, although the device looks transparent by naked-eye, the IPCE values of the concentrated sample (0.020% w/w) in the NIR region are influenced by scattering effects (Figure 2.30). This is due to the formation of **Se4T** nanocrystals in the PDMS matrix, which also explains the transmittance increase of the **Se4T**-PDMS devices. PMMA films have thin edge surfaces, therefore it is not possible to measure and calculate the IPCE directly and precisely for PMMA-based LSC.

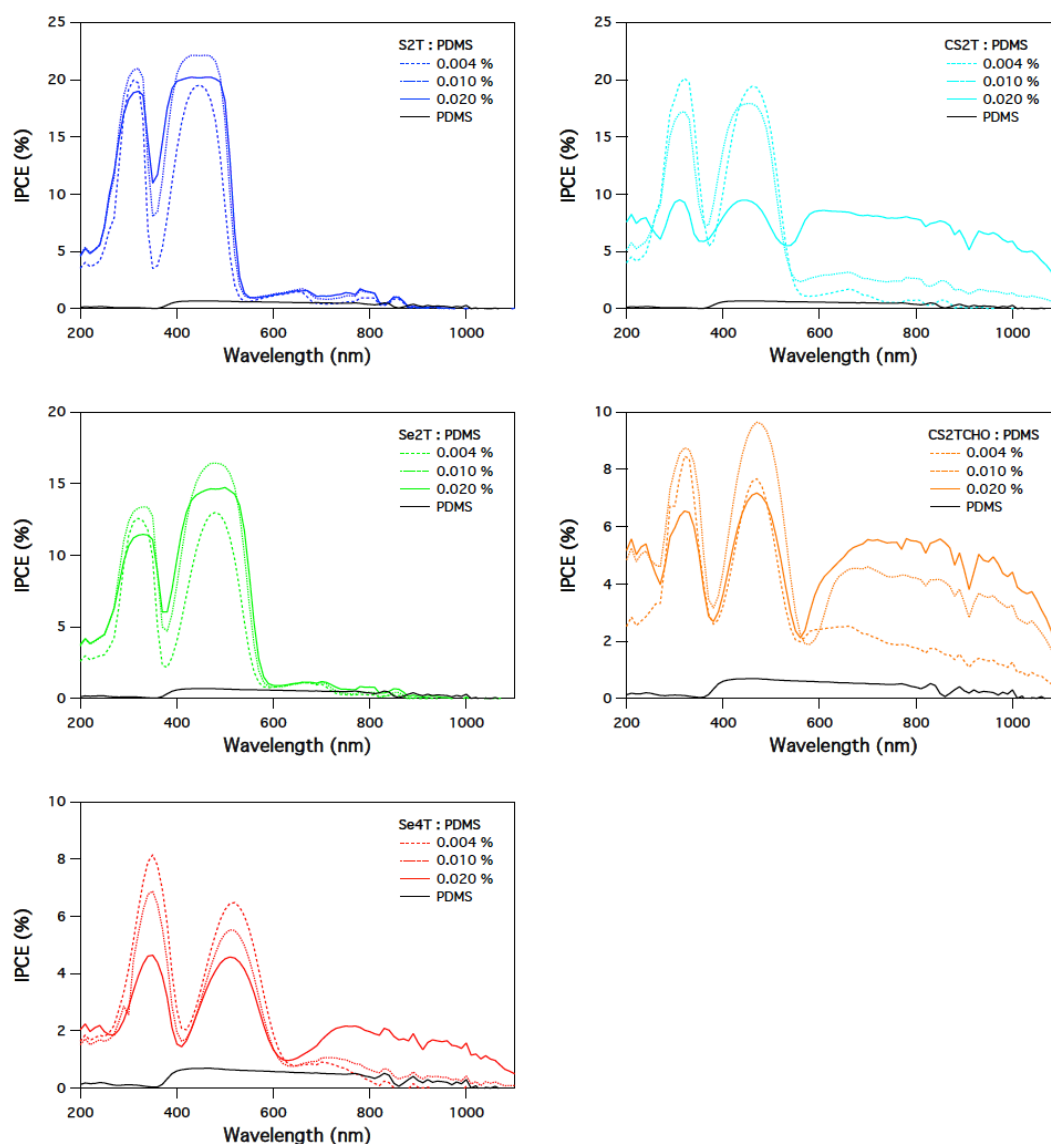


Figure 2.30: IPCE spectra of the LSCs at different concentration of the dyes (0.004, 0.010, 0.020 % w/w) in PDMS matrix.

2.4 Conclusion

A series of donor-acceptor benzoheterodiazo derivatives has been prepared to serve as dyes in luminescent solar concentrator devices. The selection of emitters with

large Stokes shift, up to $5,660\text{ cm}^{-1}$, and high photoluminescence quantum yield, up to 83.2% in PMMA matrix, has allowed to achieve an optical quantum efficiency OQE as high as 47.6% at geometric gain $G = 88$, with EQE maximizing at the intermediate dye concentration of 0.5% (w/w). The OQE value can be predictably enhanced to approximately 70% by improving the quality of the PMMA film surface and, hence, the observed trapping efficiency. For the PDMS-based LSCs, the best results were obtained with **S2T** and **CS2T**; their IPCE can reach 20% at some specific wavelengths. Overall, the output reached by the best performing systems in the series is comparable to those reported for benchmark devices.^[82-83]

Chapter 3

Preparation and characterization of a luminescent film to calibrate a satellite for vegetation monitoring

3.1 Introduction

Photosynthesis^[89] plays a key role for the growth and reproduction of plants and some microorganisms. Through it, sunlight, water, nutrients and carbon dioxide produce energy-rich carbohydrates and release oxygen in the atmosphere. Under solar irradiation, green plants not only absorb, reflect and transmit sunlight, but also release light via fluorescence. Over 80% of the photons absorbed by vegetation are exploited for carbon assimilation through photochemical processes, whereas the remaining energy is dissipated as heat or emitted as chlorophyll fluorescence.^[90] The photosystems I and II (PSI and PSII) display a combination of fluorescence bands exhibiting two features in the range 650-800 nm. One occurs in the red spectral region with a peak at 685 nm, the other one appears in the far-red/near-infrared (NIR) region, with a peak at 740 nm (Figure 3.1).^[91] PSI mainly emits in the NIR region, while PSII emits both in the red and NIR region.

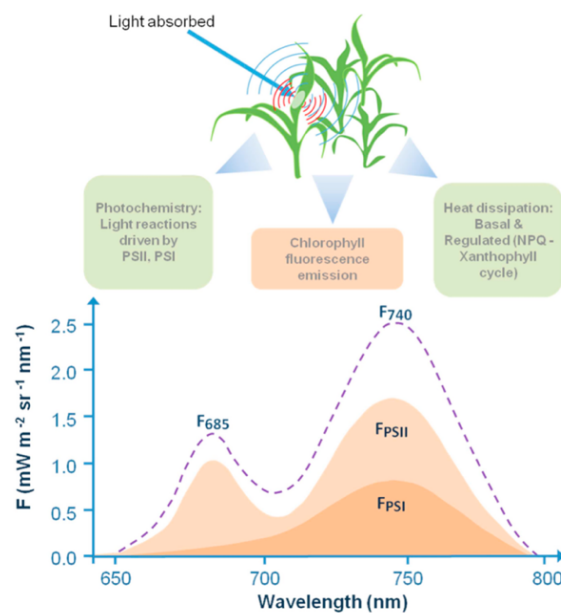


Figure 3.1: A diagram of the light absorbed by vegetation which is used for photochemistry, dissipated as heat or re-emitted as fluorescence (top). Total chlorophyll fluorescence (dashed line) is made of the PSI and PSII contribution (bottom).^[91]

Chlorophyll fluorescence is used as a proxy for photosynthetic activity, to be correlated with the health conditions of the plants. In a landmark study in 1988, Lichtenthaler and Rinderle used for the first time this indicator to describe the photosynthetic activity of plants in the laboratory.^[92] Nowadays, remote sensing allows scientists to monitor vegetation from the atmosphere or even beyond, by means of

satellite imaging projects such as the Greenhouse Gases Observing Satellite (GOSAT),^[93-94] the Global Ozone Monitoring Experiment 2 (GOME-2),^[95-96] the Scanning Imaging Absorption Spectrometer for Atmospheric CHartographY (SCIAMACHY),^[97-98] the Orbiting Carbon Observatory 2 (OCO-2),^[99] the TROPOspheric Monitoring Instrument (TROPOMI)^[100] and the Fluorescence Explorer mission (FLEX).^[101] The FLEX project is led by the European Space Agency (ESA) to study the global terrestrial vegetation state through the observation of the fluorescence of plants (Figure 3.2).

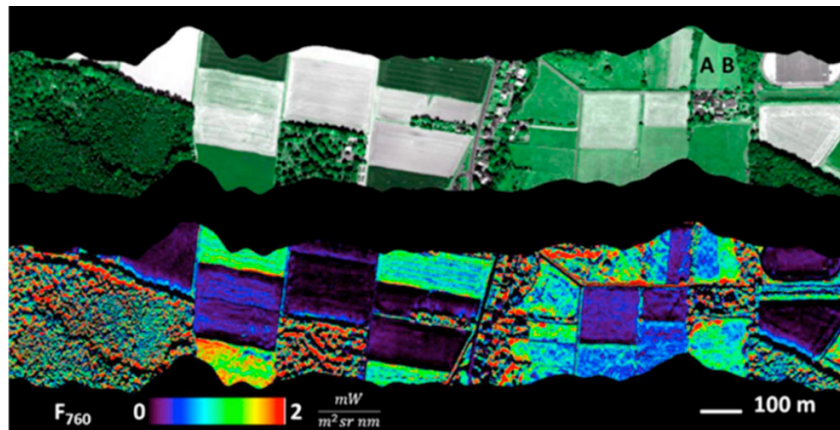


Figure 3.2: Natural reflectance (top) and fluorescence emission (bottom) images collected by the HyPlant airborne sensor from an agricultural research site close to Klein Altendorf, Germany.^[91] (Forschungszentrum Jülich)

Differently from observations on the ground, absorption of molecular oxygen occurring in the atmospheric layer surrounding the Earth affects satellite measurements. This phenomenon is specifically exploited for monitoring the fluorescence signal of chlorophyll from the space. In particular, the oxygen absorption bands O_{2A} (740-780 nm) and O_{2B} (677-697 nm) overlap with the chlorophyll fluorescence, and the FLEX “eyes” are specifically targeting these two features. The satellite is equipped with two detectors characterized by a very narrow sensitivity centered on the oxygen absorption bands in the region 500-677 nm and 697-740 nm. The variation of the chlorophyll fluorescence of forests and cultivated fields, which is affected by many factors, such as temperature, humidity, sunlight intensity and health conditions of the plants, is determined by retrieving and elaborating the reflectance signal from the space at these two specific spectral intervals. This monitoring process requires a “green calibration field” on the ground, covered with the artificial emitter, whose luminescence is constant over time, unlike the emission from the living vegetation. From time to time, the satellite will pass over the area covered by the film and, in this way, it will be constantly calibrated. The calibration area must be relatively large, i.e. at least 600 m², which corresponds to a satellite pixel.

In this work, in order to calibrate the detectors placed on the satellite of the

FLEX Mission, we prepared a luminescent film that overlaps with the fluorescence signals of green plants over a background mimicking the natural plant reflectance. Of course chlorophylls themselves would be in principle the best choice for the calibrator, but considering their poor stability outside living plants, more stable synthetic dyes are needed, which must display a key feature, i.e., an emission profile very well matched with chlorophyll fluorescence. Meso-tetraphenylporphyrin (TPP), zinc phthalocyanine (ZnPc) and styryl 9M (Figure 3.3) were selected as a suitable combination of dyes to make the films with NIR fluorescence. Their photophysical properties were investigated in poly (bisphenol A carbonate) (PBAC), poly(methylmethacrylate) (PMMA) and polystyrene (PS) with different concentrations. Ferrocene (Fc)^[102-103] was then selected as a quencher of ZnPc to control the emission intensity of the luminescent film. The quenched (reference) film is studied in parallel with the ZnPc fluorescence one. For large-area production of calibration films, the printing technology was used. This is required to carry out tests by aircrafts, which are a key preliminary step towards satellite monitoring. A green water-based paint was selected to simulate the NIR reflectance of green plants and ZnPc was incorporated in the green film. The investigation of the photophysical properties was targeted at optimizing an engineered surface for satellite calibration.

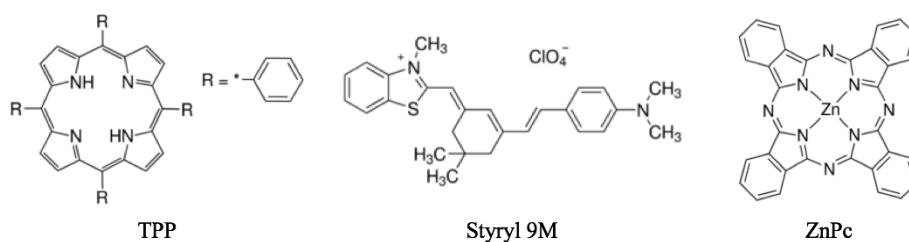


Figure 3.3: Chemical structure of the selected dyes (TPP, styryl 9M and ZnPc).

3.2 Experimental section

3.2.1 Preparation of luminescent films

PBAC, PMMA and PS were purchased from Sigma-Aldrich with average MW \approx 45000, 350000 and 280000 (by GPC), respectively. The luminescent dyes (styryl 9M, TPP and ZnPc) were obtained from Sigma-Aldrich and used as received without further purification. To dissolve the dyes and polymers, a spectrofluorimetric grade dichloromethane (DCM) was used (Merck Uvasol®). Dye-polymer films (0.5%, 0.2%, 0.1% and 0.025% w/w) were prepared by dissolving 200 mg of PBAC/PMMA/PS in 4 mL dye-DCM solutions (0.25, 0.1, 0.05 and 0.0125 mg/mL, respectively). Solvent was then evaporated overnight in a 5 cm glass Petri dish, and the resulted dye-polymer films were separated through sonication from the glass dish. Films undergoing fluorescence quenching were obtained by additionally introducing different amounts of quencher (Fc) into the ZnPc-PBAC-DCM solutions before solvent evaporation. The thickness of the

resulted films was measured as $71 \pm 4 \mu\text{m}$.

3.2.2 Photophysical measurements

Transmission and reflection spectra of the dye-polymer films were measured with a PerkinElmer Lambda 950 spectrophotometer equipped with 100 mm diffuse reflectance and transmission integrating sphere accessory, including PMT/PbS detectors. And the absorption factors (A%) of the dye-polymer films were calculate as:

$$A\% = 100 - T\% - R\% \quad (3.1)$$

where T% and R% are the transmittance and reflectance, respectively. Fluorescence spectra of the dye-polymer films were collected and corrected through an Edinburgh Instruments FLS920 spectrometer equipped with a Peltier-cooled Hamamatsu R928P photomultiplier tube (185-900 nm), and the films were placed in a solid sample holder. Light excitation was performed with a 450 W xenon arc lamp. Photoluminescence quantum yields (Φ_{PL}) were determined with the absolute method by using a barium sulfate-coated integrating sphere (diameter of 3 inches), elaborating corrected emission spectra.^[25] The excited state lifetimes (τ) were measured by the time-correlated single photon counting (TCSPC) technique with an HORIBA Jobin Yvon IBH FluoroHub equipped with a pulsed NanoLED ($\lambda_{\text{exc}} = 465 \text{ nm}$) excitation source and a TBX-05C Picosecond Photon Detection Module (300-850 nm) as the detector. The luminescence decay profiles were analyzed with the DAS6 Decay Analysis Software Software, and the quality of the fit was assessed with the χ^2 value (close to unity) and with the residuals randomly distributed along the time axis. Experimental uncertainties are estimated to be $\pm 8\%$ for τ determinations, $\pm 20\%$ for Φ_{PL} , and $\pm 2 \text{ nm}$ and $\pm 5 \text{ nm}$ for absorption and emission peaks, respectively.

3.3 Results and Discussion

3.3.1 Photophysics in PMMA films

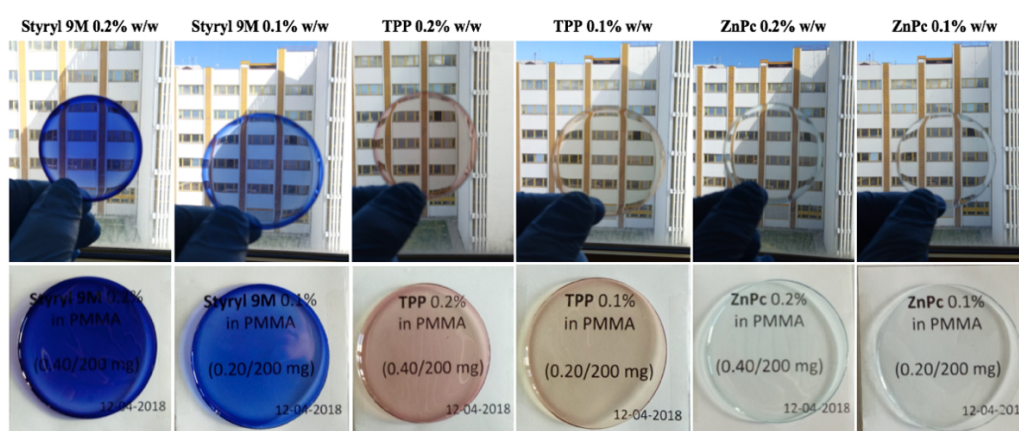


Figure 3.4: Pictures of styryl 9M, TPP and ZnPc in PMMA matrix with different concentrations (0.2% and 0.1% w/w).

In PMMA matrix, the films were prepared with two different dye concentrations (0.2% and 0.1% w/w) through evaporation of DCM solutions. Figure 3.4 shows the dye-PMMA films under daylight. Styryl 9M in PMMA matrix exhibits a deep blue color and the transparency of the film at high concentration (0.2% w/w) is very low. TPP in PMMA matrix forms a light-red film with good transparency (Figure 3.4). ZnPc in PMMA matrix just shows a very weak cyan color, the transparency being almost the same as the pure PMMA film without dyes.

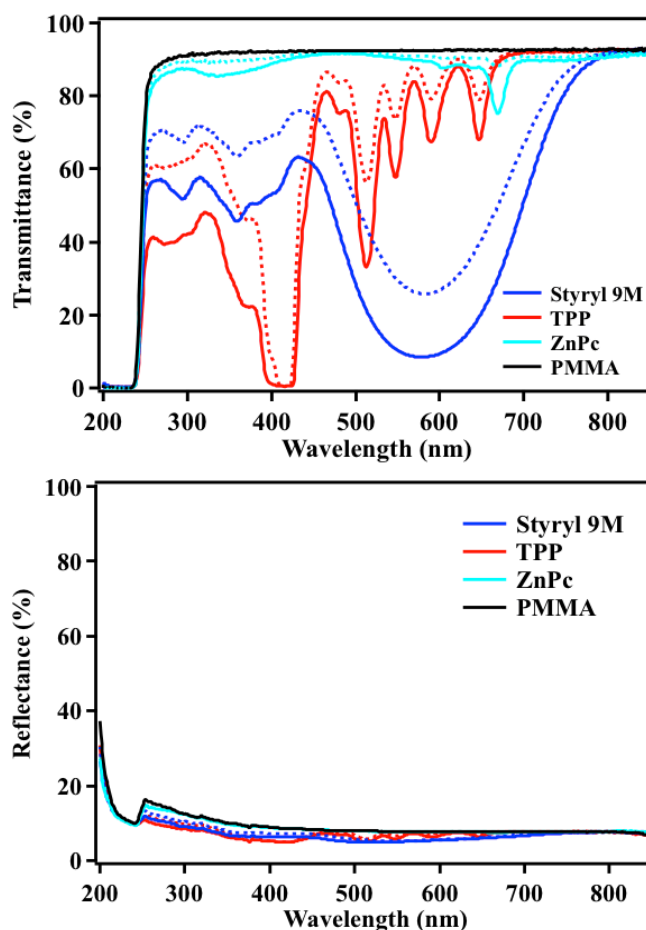


Figure 3.5: Transmittance (top) and reflectance (bottom) spectra of the dyes (styryl 9M, TPP and ZnPc) at concentrations of 0.2% (full line) and 0.1% w/w (dotted line) in PMMA matrix.

In Figure 3.5 are reported the transmittance (top) and reflectance (bottom) spectra of the dye-PMMA films with different concentrations, and the corresponding calculated absorbance (absorption factor) spectra are gathered in Figure 3.6. Styryl 9M-PMMA films absorb a large portion of light in the visible region, this is why the films show strong color and low transparency. Compared to styryl 9M, TPP-PMMA films absorb much less visible light, and strong absorption peaks occur in the purple spectral region, which result in the light red color and the good transparency of the films. ZnPc in PMMA only exhibits a weak absorption peak at ~670 nm with absorbance less below 20% (0.2% w/w).

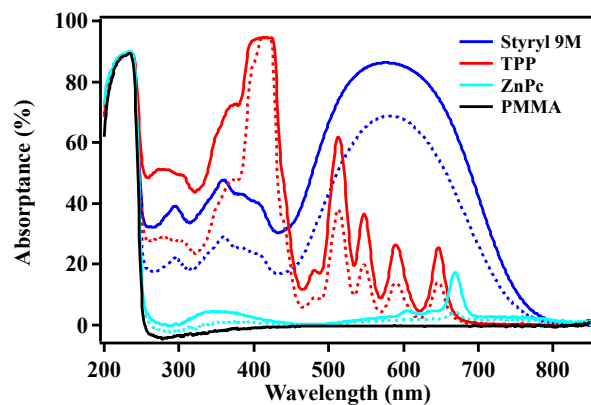


Figure 3.6: The calculated absorbance spectra of the dyes at concentrations of 0.2% (full line) and 0.1% w/w (dotted line) in PMMA matrix.

The fluorescence spectra of styryl 9M, TPP and ZnPc in PMMA films at different concentrations (0.5%, 0.2% and 0.1% w/w) are collected in Figure 3.7, and the related photophysical data are reported in Table 3.1. Styryl 9M-PMMA films emit mainly in the NIR region, and the emission peaks are red-shifted upon concentration increase, due to reabsorption effects.^[80-81] For TPP and ZnPc-PMMA films, the emission spectra are not affected by reabsorption effects, due to the weaker absorption. TPP in PMMA shows two emission peaks at ~652 nm and ~717 nm. ZnPc-PMMA films exhibit a strong emission peak at ~675 nm and a weak peak at ~747 nm, which are close to the chlorophyll emission (685 nm and 740 nm).

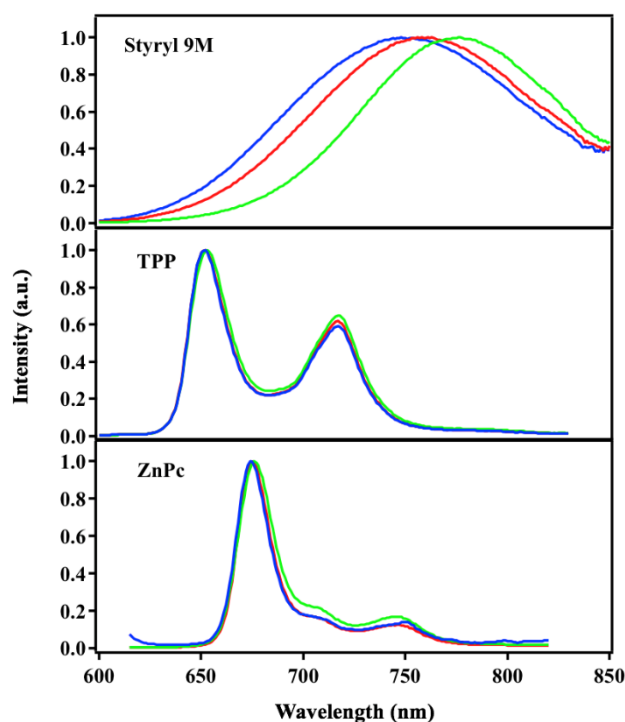


Figure 3.7: Normalized emission spectra of styryl 9M, TPP and ZnPc in PMMA matrix at the concentration of 0.5% (green line), 0.2% (red line) and 0.1% w/w (blue line). The excitation wavelengths for styryl 9M, TPP and ZnPc are 550 nm, 510 nm and 605 nm, respectively.

Absolute emission quantum yields (Φ_{PL}) and excited state lifetimes (τ) of dye-PMMA films are reported in Table 3.1. Because of reabsorption effects, the Φ_{PL} of dye-PMMA films increase by decreasing concentration, while the excited state lifetimes are not affected. The exception of 0.1 % w/w ZnPc-PMMA film ($\Phi_{PL} = 2.1\%$) is due to the extremely weak absorption factor.

Table 3.1: Photophysical parameters of dye-PMMA films at 298 K.

	conc. (% w/w)	λ_{abs} (nm)	λ_{ems} (nm)	Φ_{PL} (%)	τ (ns)
Styryl 9M	0.5	/	776	3.8	1.5
	0.2	576	761	6.9	1.8
	0.1	580	748	11.5	1.9
TPP	0.5	/	653, 718	2.8	10.6
	0.2	513, 547, 590, 646	652, 717	3.5	9.9
	0.1	513, 547, 590, 647	652, 717	4.2	10.1
ZnPc	0.5	/	676, 746	2.5	3.8
	0.2	669	675, 747	4.7	3.5
	0.1	667	674, 750	2.1	/

3.3.2 Photophysics in PS films

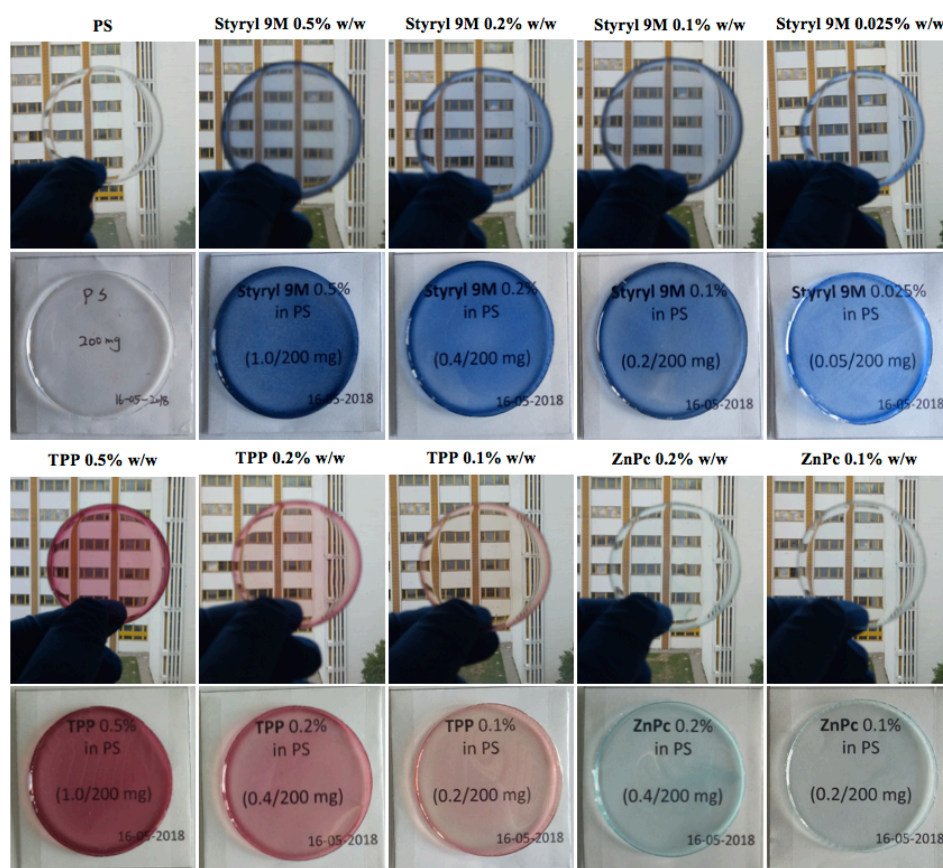


Figure 3.8: Pictures of styryl 9M, TPP and ZnPc in PS matrix with different concentrations (0.5%, 0.2%, 0.1% and 0.025% w/w).

At the same concentration (e.g. 0.2% w/w), styryl 9M in PS matrix exhibits a weaker blue color and better transparency than in PMMA (Figure 3.8). The films of TPP and ZnPc in PS are similar with the PMMA based dye-films (Figure 3.8). In Figure 3.9 are reported the transmittance (top) and reflectance (bottom) spectra of the dye-PS films with different concentrations. The calculated absorbance spectra through equation 3.1 are shown in Figure 3.10.

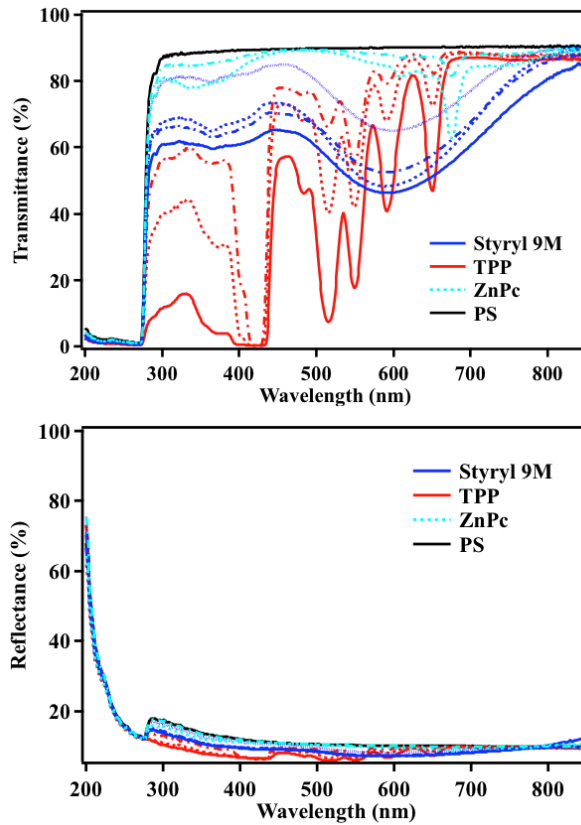


Figure 3.9: Transmittance (top) and reflectance (bottom) spectra of the dyes (styryl 9M, TPP and ZnPc) at concentrations of 0.5% (full line), 0.2% (dotted line), 0.1% (line and point) and 0.025% w/w (dashed line) in PS matrix.

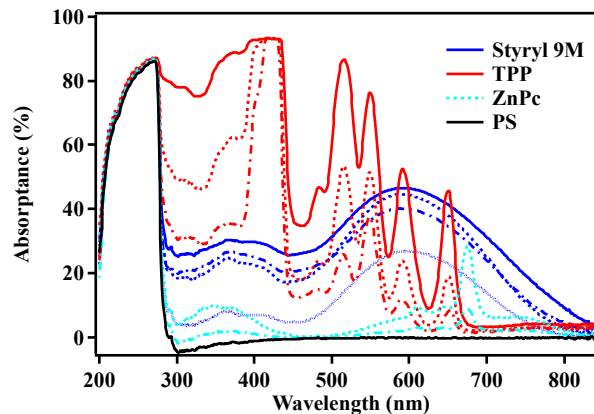


Figure 3.10: The calculated absorbance spectra of the dyes at concentrations of 0.5% (full line), 0.2% (dotted line), 0.1% (line and point) and 0.025% w/w (dashed line) in PS matrix.

In Figure 3.11 are collected the photoluminescence spectra of styryl 9M, TPP and ZnPc in PS matrix at different concentrations. In Table 3.2 are reported the related photophysical data of dye-PS films. Compared to styryl 9M in PMMA matrix (Figure 3.7), the emission peaks in PS films are not shifted with the dye concentration (Figure 3.11), due to the weaker absorptance. ZnPc-PS films show similar emission spectra in PMMA matrix. However, for TPP-PS films, an increase of the emission peak at 719 nm is observed by increasing the concentration, which is not found in PMMA (Figure 3.7) and could be related to solubility effects. In PBAC matrix, the different solubility and/or matrix interaction leads to an inversion of the fluorescence intensity of the peaks at 659 and 719 nm (Figure 3.15) for TPP.

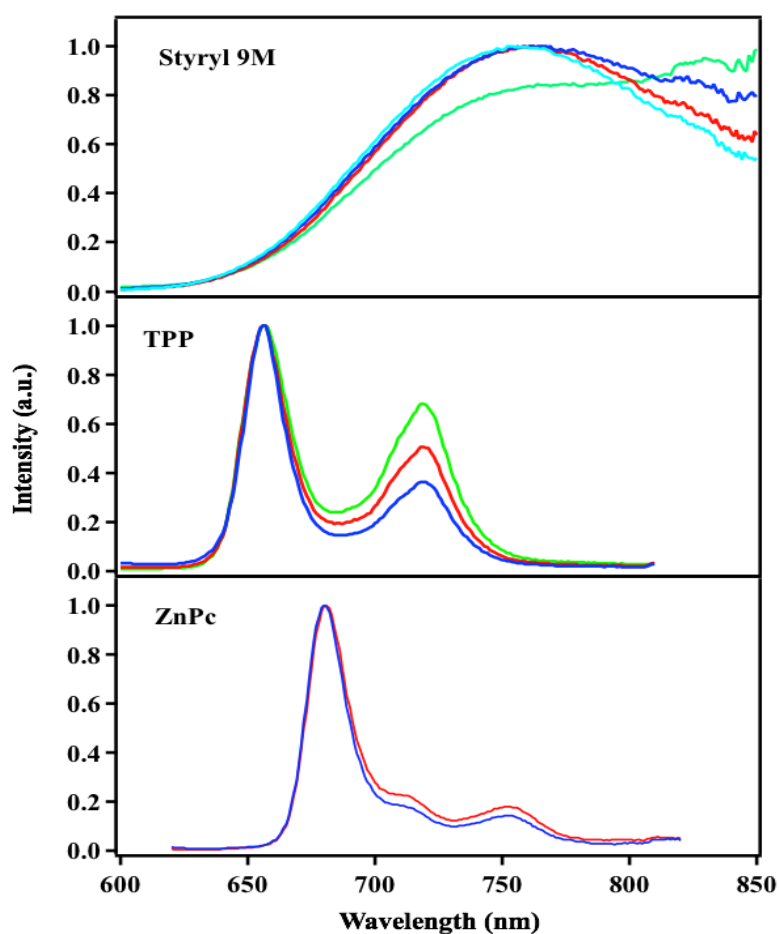


Figure 3.11: Normalized emission spectra of styryl 9M, TPP and ZnPc in PS matrix at the concentration of 0.5% (green line), 0.2% (red line), 0.1% (blue line) and 0.025% w/w (cyan line). The excitation wavelengths for styryl 9M, TPP and ZnPc are 550 nm, 510 nm and 605 nm, respectively.

Absolute emission quantum yields (Φ_{PL}) and excited state lifetimes (τ) of styryl 9M, TPP and ZnPc in PS films are collected in Table 3.2. Except for the 0.025% w/w styryl 9M-PS films, the quantum yields and excited state lifetimes of other samples are not affected by concentration.

Table 3.2: Photophysical parameters of dye-PS films at 298 K.

	conc. (% w/w)	λ_{abs} (nm)	λ_{ems} (nm)	Φ_{PL} (%)	τ (ns)
Styryl 9M	0.5	593	/	4.4	1.5
	0.2	589	759	3.4	1.5
	0.1	588	764	3.8	1.5
	0.025	604	754	7.1	1.7
TPP	0.5	515, 549, 591, 650	657, 719	2.2	12.3
	0.2	515, 549, 591, 651	657, 719	2.4	11.9
	0.1	515, 549, 590, 652	656, 719	2.2	11.8
ZnPc	0.2	675	681, 753	4.7	3.8
	0.1	675	680, 751	2.9	3.6

3.3.3 Photophysics in PBAC films

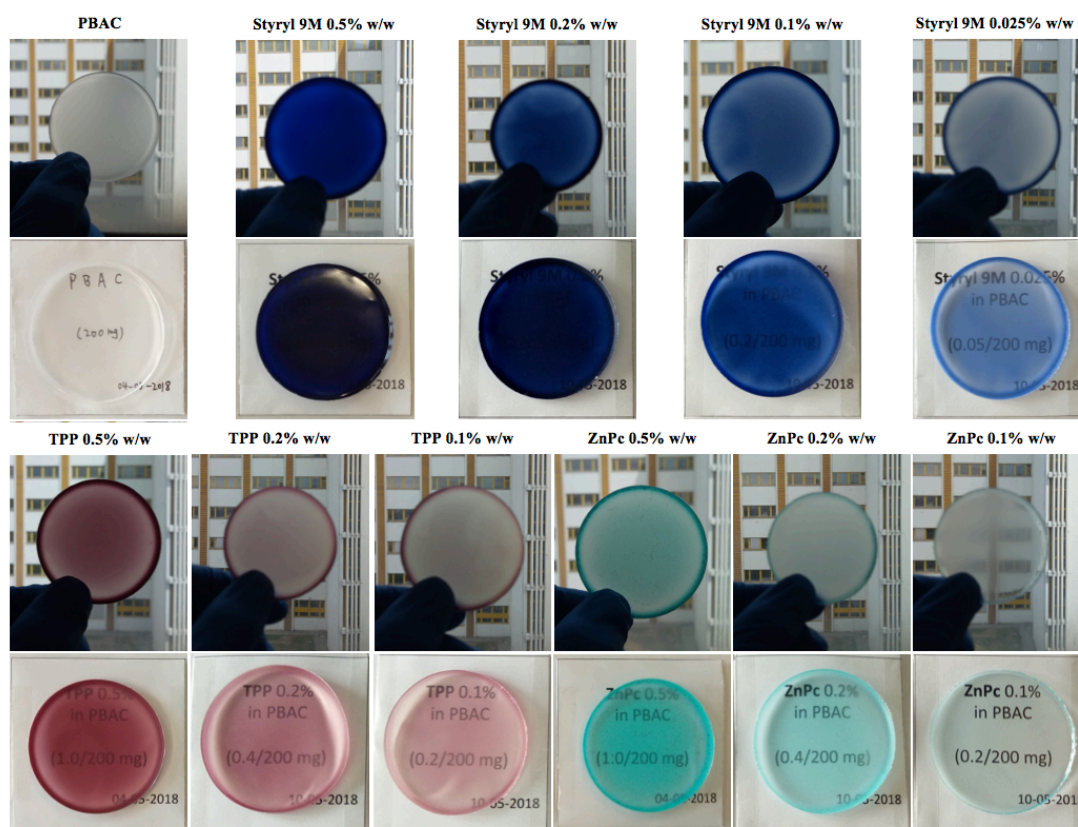


Figure 3.12: Pictures of the styryl 9M, TPP and ZnPc in PBAC matrix with different concentrations (0.5%, 0.2%, 0.1% and 0.025% w/w).

Compared with PMMA and PS, the pure PBAC film exhibits a lower transparency (Figure 3.12), and dyes in PBAC matrix show a stronger color than in PMMA and PS. Styryl 9M in PBAC matrix at high concentration (0.5% and 0.2% w/w) are almost completely opaque (Figure 3.12). ZnPc in PBAC matrix exhibits a much brighter cyan color compared to PMMA and PS. The transmittance (top) and

reflectance (bottom) spectra of the dye-PBAC films are reported in Figure 3.13; the related absorptance spectra are shown in Figure 3.14.

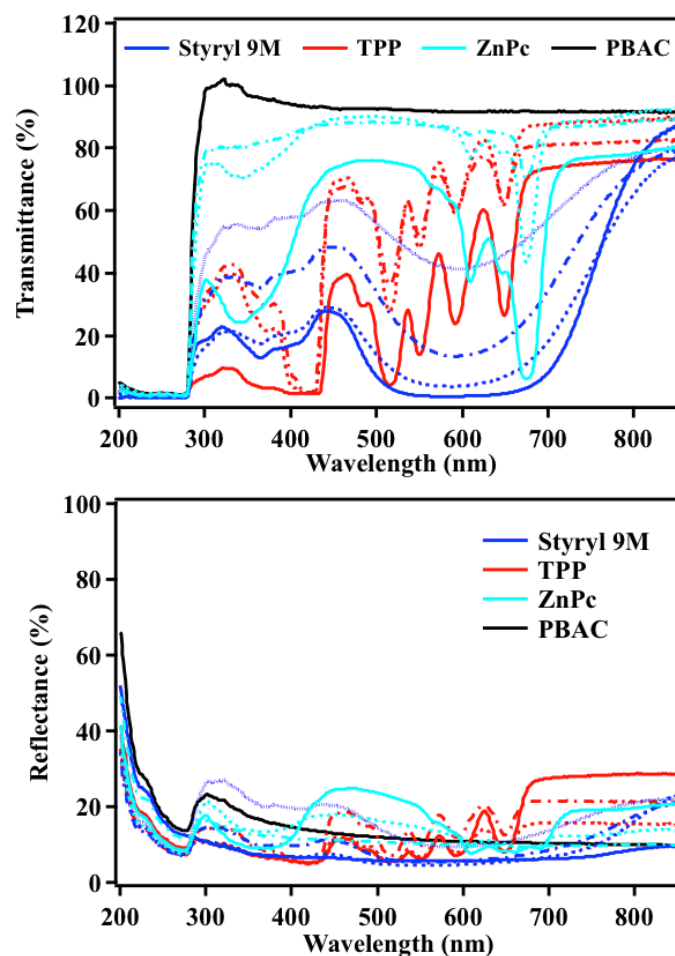


Figure 3.13: Transmittance (top) and reflectance (bottom) spectra of the dyes (styryl 9M, TPP and ZnPc) at concentrations of 0.5% (full line), 0.2% (dotted line), 0.1% (line and point) and 0.025% w/w (dashed line) in PBAC matrix.

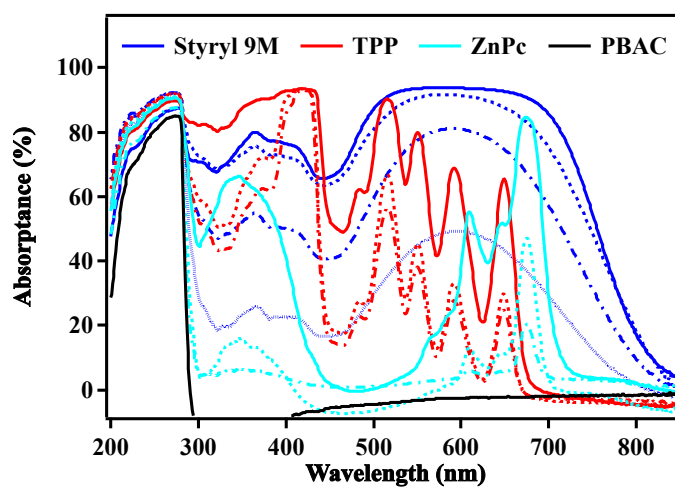


Figure 3.14: The absorptance spectra of the dyes at concentrations of 0.5% (full line), 0.2% (dotted line), 0.1% (line and point) and 0.025% w/w (dashed line) in PBAC matrix.

In PBAC matrix, the absorptance of ZnPc films is significantly stronger than in PMMA and PS at the same concentration. The emission spectra of ZnPc are also enhanced in PBAC matrix with quantum yields greater than 10% (Table 3.3) at all the concentrations that we selected. Moreover, the emission peak of ZnPc-PBAC films occurs at ~685 nm and ~750 nm, respectively. In PBAC, the fluorescence of styryl 9M occurs in the NIR region with peaks at around 800 nm. TPP in PBAC exhibits a strong emission peak at 719 nm and a weaker one at 660 nm. The peak position of TPP-PBAC films are close to TPP-PMMA, but the peak intensity is inverted compared to other matrices. In Table 3.3 are reported the photophysical parameters of absorptance and emission of the dye-PBAC films, along with the emission quantum yields and excited state lifetimes. As in PMMA matrix, the quantum yields of dyes in PBAC are affected by reabsorption effects, whereas the lifetimes are not influenced.

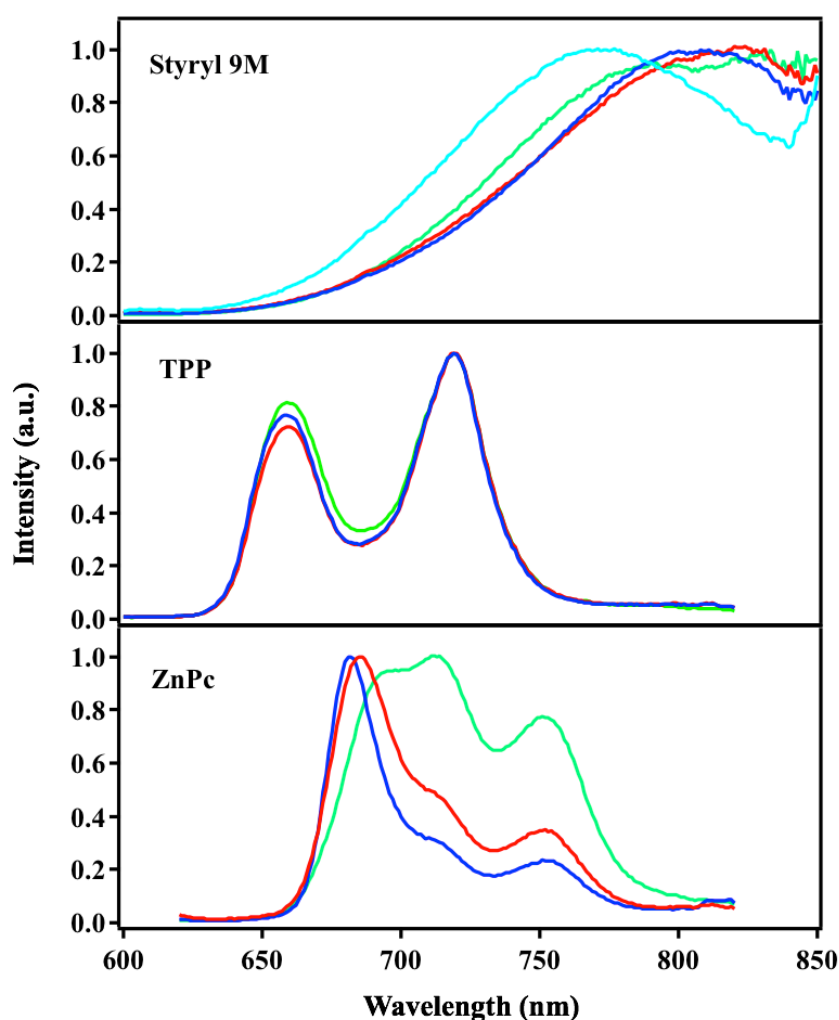


Figure 3.15: Normalized emission spectra of styryl 9M, TPP and ZnPc in PBAC matrix at the concentrations of 0.5% (green line), 0.2% (red line), 0.1% (blue line) and 0.025% w/w (cyan line). The excitation wavelengths for styryl 9M, TPP and ZnPc are 550 nm, 510 nm and 605 nm, respectively.

Table 3.3: Photophysical parameters of dye-PBAC films at 298 K

	conc. (% w/w)	λ_{abs} (nm)	λ_{ems} (nm)	Φ_{PL} (%)	τ (ns)
Styryl 9M	0.5	580	833	2.2	1.3
	0.2	580	824	5.3	1.4
	0.1	591	808	8.6	1.5
	0.025	595	767	13.9	1.5
TPP	0.5	515, 550, 592, 649	659, 719	5.6	12.3
	0.2	516, 550, 591, 648	660, 719	7.3	12.4
	0.1	516, 550, 591, 649	659, 719	8.0	12.0
ZnPc	0.5	609, 675	714, 751	12.0	3.1
	0.2	609, 674	685, 752	12.6	3.5
	0.1	675	681, 751	10.2	3.6

3.3.4 Fluorescence quenching of ZnPc in PBAC films

After investigating the photophysical properties of styryl 9M, TPP and ZnPc in PMMA, PS and PBAC matrix, the fluorescence emission spectra of ZnPc turns out to afford the best match with the chlorophyll fluorescence. Therefore, ZnPc turned out to be the best candidate for the calibration film. Mixed dyes were also studied in PBAC matrix, but the films were unstable and showed complex luminescence spectra. Therefore, the idea of using mixed dyes was abandoned. At last, pure ZnPc was selected as luminescent material to prepare the luminescent film for satellite calibration.

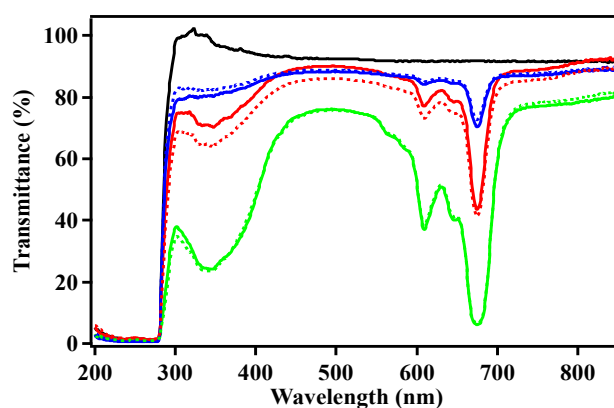


Figure 3.16: Transmittance spectra of the ZnPc-PBAC films as prepared (full lines) and after 20 days (dotted lines) at the concentration of 0.5% (green), 0.2% (red) and 0.1% w/w (blue). Black line indicates the PBAC film without ZnPc.

The satellite will deal with different conditions leading to rather different signal intensities. Therefore, we developed a method to tune the emission signal of the calibrating surface, in order to obtain fully reliable fitting curves covering a wide range of intensities. In order to control the emission intensity of the ZnPc luminescent film, ferrocene (Fc),^[102-103] methyl viologen (MV)^[104] and p-benzoquinone (BQ)^[105-106] were incorporated into the ZnPc-PBAC films as fluorescence quenchers. Due to the poor

solubility of MV in PBAC and the reaction occurring between BQ and ZnPc, the fluorescence quenching experiment was only performed with Fc. Because the emission quantum yield of ZnPc in PBAC is significantly higher than in PMMA and PS, these quenching investigations were made in PBAC matrix. First, the photothermal stability of ZnPc-PBAC films was controlled by transmittance spectra (Figure 3.16), the results show that ZnPc is stable in PBAC films for at least 20 days.

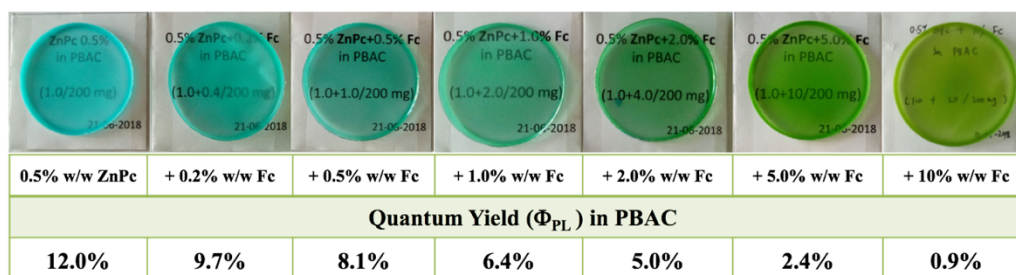


Figure 3.17: Pictures and the corresponding emission quantum yields of 0.5% w/w ZnPc with different concentration of Fc in PBAC matrix. From left to right, the concentration of Fc are 0.2%, 0.5%, 1.0%, 2.0%, 5.0% and 10% w/w, respectively.

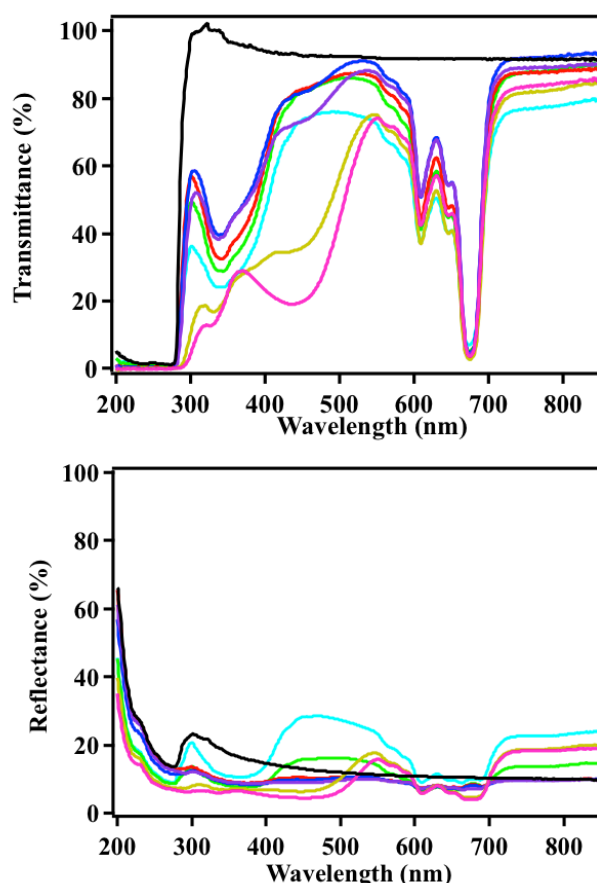


Figure 3.18: Transmittance (top) and reflectance (bottom) spectra of the 0.5% w/w ZnPc (cyan line) with different concentration of Fc in PBAC matrix. Fc concentration: 0.2% (green line), 0.5% (red line), 1.0% (blue line), 2.0% (purple line), 5.0% (yellow line) and 10% w/w (pink line). Black line indicates the PBAC without ZnPc and Fc.

The fluorescence quenching experiments were carried out with 0.5% w/w ZnPc at different concentrations of Fc in PBAC matrix (from 0.2% to 10% w/w). In Figure 3.17 are reported the pictures of 0.5% w/w ZnPc films alone and mixed with different amounts of Fc. As the Fc concentration increases, the color of the films changes from cyan to green. In parallel, the emission quantum yields of ZnPc-Fc-PBAC films decrease (from 12.0% to 0.9%) upon increasing the Fc concentration. The transmittance and reflectance spectra of these films were collected in Figure 3.18. The absorbance (top) and emission (bottom, the emission intensity is proportional to the quantum yield) spectra are gathered in Figure 3.19. The characteristic absorption peaks (609 nm and 675 nm) of ZnPc are not affected by Fc both in intensity and position. Across the region 400-500 nm, the increase of absorbance is due to Fc absorption. According to the results of fluorescence quenching experiments, Fc can be used as an effective quencher to control the emission quantum yields of ZnPc. After incorporating Fc into the ZnPc films, the generated green films are similar in color with the real plants. However, the green films lack reflection ability of NIR light. Hence, in future studies with quenching agents, green dyes with good NIR reflectivity will have to be incorporated in the luminescent calibrators.

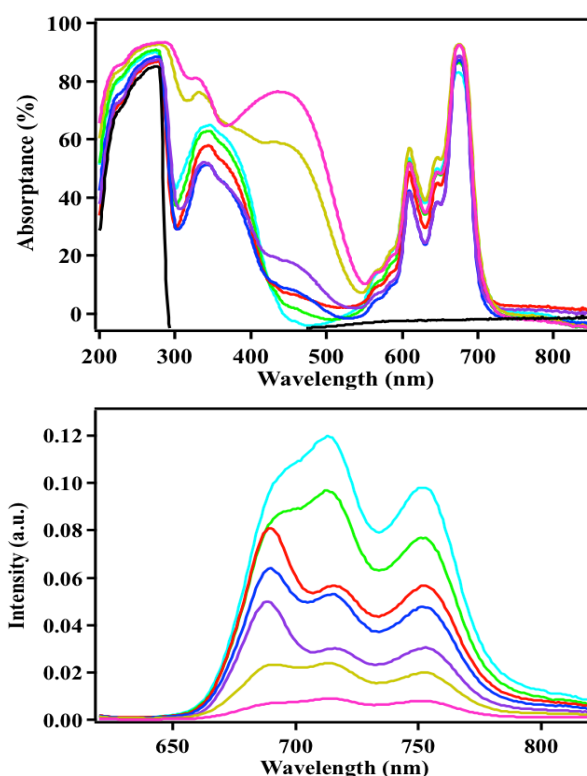


Figure 3.19: The absorbance (top) and emission (bottom, excited at 605 nm) spectra of the 0.5% w/w ZnPc (cyan line) with different concentration of Fc in PBAC matrix. Fc concentration: 0.2% (green line), 0.5% (red line), 1.0% (blue line), 2.0% (purple line), 5.0% (yellow line) and 10% w/w (pink line). Black line indicates the absorbance spectrum of PBAC without ZnPc and Fc.

3.3.5 Large area luminescent calibrator

Large-area luminescent calibration films was produced by using a proprietary printing technology. Two kinds of layers (reflective layer and fluorescent emitting layer) were coated on the plastic or wood plate (substrate). The structure of the luminescent calibrator film is shown in Figure 3.20.

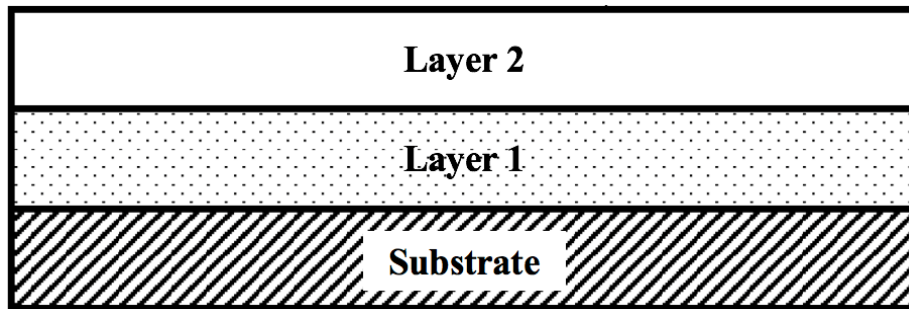


Figure 3.20: Structure of the luminescent calibrator. Two layers are coated on the substrate, layer 1 contains the reflective green dye that simulates the vegetation, layer 2 contains the fluorescent dye.

Layer 1 simulates the reflectance spectra of real plants and strongly reflects sunlight from 700 nm to 900 nm (reflectivity larger than 40%–50%). Layer 1 is prepared directly on the substrate by dispersing the dye (Ferro PS 21 4700 PK) in a transparent acrylic paint with concentration of 30 g/L. In order to not interfere with the reflection of light of layer 1, layer 2 is transparent to the visible and NIR light. Layer 2 incorporates the ZnPc (Sigma-Aldrich) matrix with concentration of 0.025% and 0.5% w/w. The thickness of the layer 1 and layer 2 are 0.5-1 mm and 0.5-2 mm, respectively.

In Figure 3.21 are reported the reflectance (top), excitation and fluorescence emission spectra (bottom) of the resulted luminescent calibrator film with ZnPc at concentration 0.025% and 0.5% w/w, respectively. The calibrator film exhibits an excellent reflectivity in the NIR region of 700–900 nm, which virtually overlaps with the reflectance spectrum of the real plants, e.g., the leaf of the *Vicia faba*. In Figure 3.22 are reported the reflectance spectra of the luminescent calibrator film and the leaf of the *Vicia faba* at the region of 400-950 nm and 730-800 nm. Fluorescence of the layer 2 occurs at 670-690 nm and 730-770 nm, which is well overlapped with the chlorophyll fluorescence. Therefore, the luminescent calibrator film is suitable to simulate the reflection and fluorescence behavior of real plants. The final large-area luminescent calibration films were coated on wood with 100×100 m² size and tested by an airplane on the field (Figure 3.23). The invention of the luminescent calibration films is under patenting (appl. 102019000020174, 31/10/2019) and is a strong candidate for use in the FLEX satellite project starting from 2023.

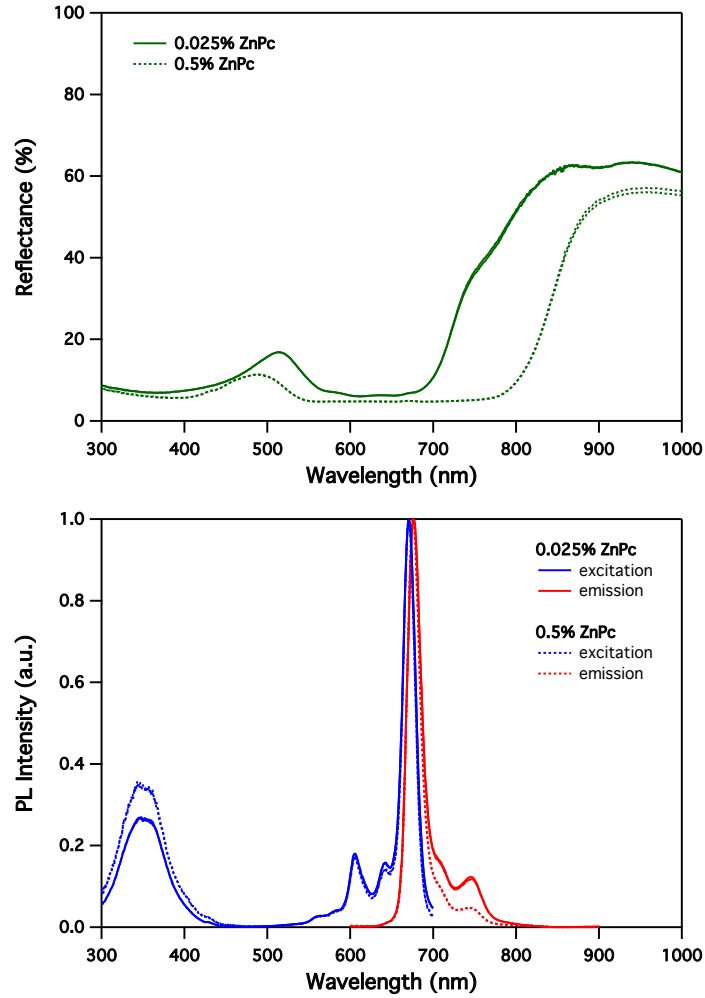


Figure 3.21: Reflectance spectra (top), excitation (collected at 710 nm) and fluorescence emission spectra (bottom, excited at 590 nm) of the luminescent calibrator film with ZnPc concentration of 0.025% and 0.5% w/w, respectively.

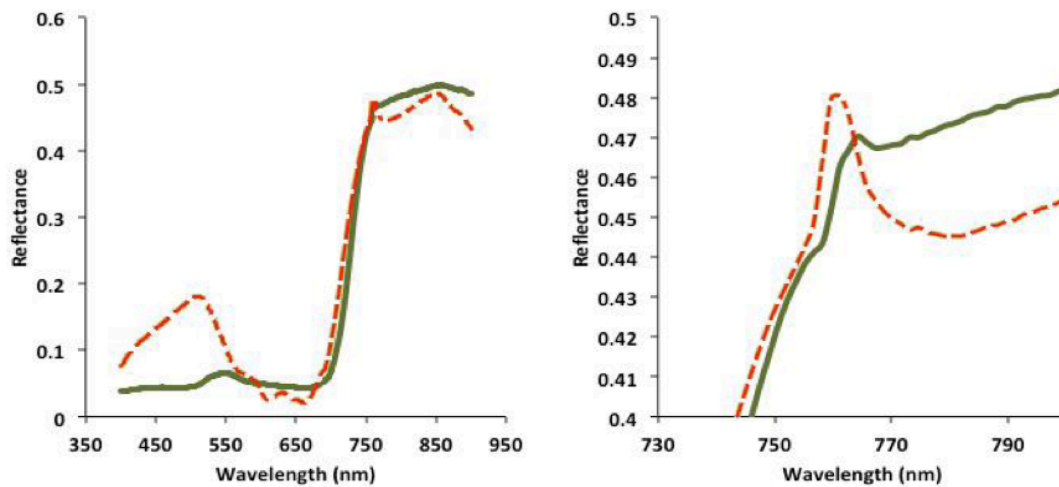


Figure 3.22: Reflectance spectra of the luminescent calibrator film (dotted lines) and the leaf of the *Vicia faba* (full lines) at the region of 400-950 nm (left) and 730-800 nm (right). The spectra were collected by a GER 3700 spectrometer under sunlight.



Figure 3.23: Picture of the large-area luminescent calibration films prepared on the field for the test by an airplane.

3.4 Conclusion

In order to determine a suitable dye to simulate the chlorophyll fluorescence for calibration of a vegetation monitoring satellite, styryl 9M, TPP and ZnPc were investigated as potential candidates. After studying the photophysical properties of the three dyes in PMMA, PS and PBAC matrix, ZnPc was selected as the best option to prepare the luminescent calibration film. Fluorescence quenching experiments of ZnPc were carried out in PBAC matrix, where Fc was screened as an effective quencher to control the emission quantum yield of ZnPc. To prepare large-area luminescent calibration films, a printing technology was used to build a double-layer structure film under a plastic plate. One layer simulates the reflectance spectra of real plants, the other one exhibits a fluorescence spectrum similar to that of chlorophyll. The resulting film is an effective luminescent calibrator that reflects NIR light similarly to real plants in the region between 700 nm to 900 nm. It emits a fluorescence signal well overlapped with that of chlorophyll and suitable for calibrating the detector of chlorophyll fluorescence that will be used in FLEX satellite mission starting from 2023.

Chapter 4

Photophysical investigations of luminescent gold(I) alkynyls complexes adorned with *N*-heterocyclic carbenes and naphthalimide chromophores

4.1 Introduction

N-heterocyclic carbene (NHC) ligands have been widely used in organometallics,^[107] metallo-supramolecular chemistry,^[108] as metallo-drugs^[109] and luminescent materials.^[110] In the past two decades, alkynyl gold complexes have received a lot of attention owing to their applications in different areas such as luminescence,^[111-112] homogeneous catalysis^[113] and more recently as therapeutic agents to fight cancer.^[114-115] In the field of luminescent materials, organo-gold(I) complexes^[116] have been extensively investigated because of their unique photoluminescence^[116-117] and self-assembling^[118] properties. In fact due to their linear structures, and the tendency of the alkynyl moiety to undergo π -coordination, they provide access to novel appealing supramolecular architectures.^[119-120] At the supramolecular level, alkynyl gold complexes tend to form metal-metal (aurophilic) interactions through the supramolecular self-assembly between Au(I) sites, which might lead to interesting luminescence properties and potential applications.^[121-122] Yam and coworkers have extensively studied the photophysical properties of alkynyl gold complexes containing a variety of phosphine ligands or within a calixcrown-cage supramolecular structure.^[118,123-124] More recent investigations have also demonstrated the importance of this type of compounds.^[125-126]

Herein, we study the photophysical properties of a novel series of alkynyl gold *N*-heterocyclic carbene complexes containing a naphthalimide (NI) chromophore. In order to explore the influence of the gold center on the photophysical properties of the naphthalimide chromophore, two types of NHC alkynyl gold compounds have been designed and synthesized (Figure 4.1). In the first family, NI is directly connected with the NHC-Au unit with the general formulae $[(L^1)\text{-Au}\equiv\text{R}]$, R = -Phenyl, (**1a**); R = -Phenyl-CF₃, (**1b**) and R = -Phenyl-*t*-Bu (**1c**). In the second group, a π -extended ligand L^2 was used where the NI and NHC-Au unit was linked through an alkyne arene bridge, and the corresponding structures of Au complexes are described as $[(L^2)\text{-Au}\equiv\text{R}]$, R = -Phenyl, (**2a**); R = -Phenyl-CF₃, (**2b**) and R = -Phenyl-*t*-Bu (**2c**). The X-ray diffraction method was used to determinate the structure of complexes **1a**, **2a** and **2b**, and the presence of Au-Au Aurophilic interactions in the crystal state. The photophysical properties of all compounds were studied in solution (CH₂Cl₂ and methanol) and in the solid state both at room temperature (298 K) and at 77 K (liquid nitrogen). Further investigations were carried out by incorporating the compounds into PMMA films. The

results of the investigations suggest that these compounds are potential candidates for future applications in optoelectronic devices.

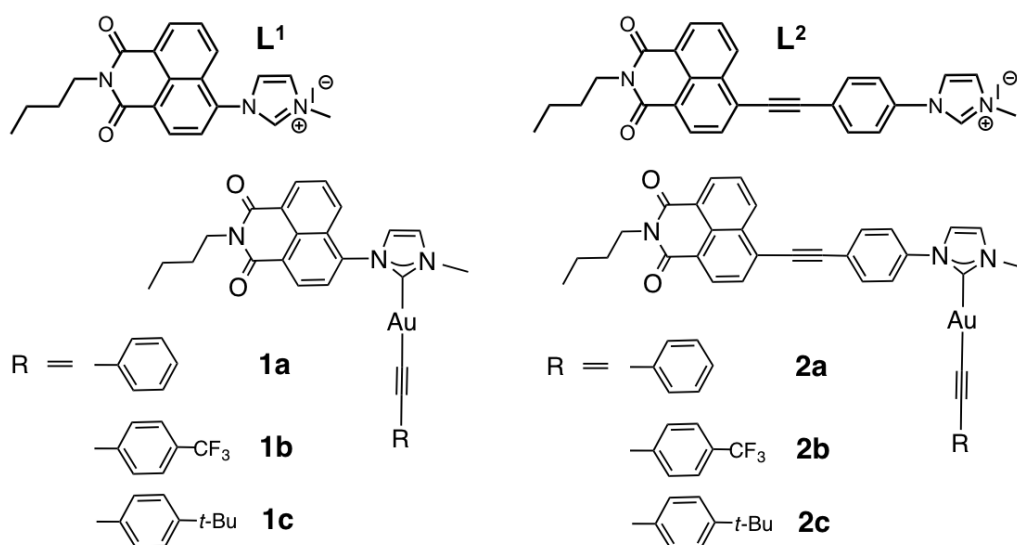


Figure 4.1: Molecular structures of the investigated ligands (L^1 and L^2) and the related alkynyl gold complexes (**1a-c** and **2a-c**).

4.2 Experimental section

4.2.1 Synthesis of NHC alkynyl gold(I) complexes

Materials and methods

All the reagents and materials for synthesis were purchased from commercial suppliers and used as received without further purification. The ligands L^1 and L^2 were synthesized with reference to the reported methods described in the articles by *Amouri* and coworkers.^[127-128] The original materials and synthetic steps for the preparation of the gold chloro-complexes follow the procedures previously reported.^[127] All the synthetic steps were carried out under the protection of argon atmosphere by using the standard Schlenk techniques. Before the experiments, solvents were dried and distilled under argon atmosphere by standard procedures. Elemental analyses were carried out on a Perkin-Elmer 2400 apparatus by ICSN microanalytical services at Gif-sur-Yvette. ^1H and ^{13}C nuclear magnetic resonance (NMR) spectra were obtained through Bruker Avance 300, 400 or Avance NEO 500 spectrometer in CD_2Cl_2 at 300MHz, 400MHz or 500 MHz for ^1H -NMR and 125 MHz for ^{13}C -NMR. Chemical shifts are reported in parts per million for NMR according to the residual solvent proton ($\delta = 5.32$ ppm) for ^1H -NMR and carbon ($\delta = 53.5$ ppm) for ^{13}C -NMR. FTIR spectra were collected for all the samples in the solid state through an Agilent Cary 630 FTIR Spectrometer.

Molecular design and synthetic route

A series of alkynyl gold(I) complexes were designed where a naphthalimide chromophore was connected to the gold center by two different *N*-heterocyclic carbene ligands in order to get different type of emissions. Due to the 5d-electrons in gold with high spin-orbit coupling constant, the target complexes are expected to exhibit a phosphorescent emission from the Au-chromophoric triplet state and a fluorescence emission occurs from the naphthalimide chromophore. In addition, the Au-Au interactions that occur in this group of complexes might also result in some special photophysical properties. As far as we know, the molecules designed in this work have not been reported before. Moreover, it is rare to find in the literature molecules exhibiting dual or triple emissions. This represents a challenging subject.^[129-130]

Complexes **1a-c** were synthesized via two steps (Figure 4.2), the first step is to prepare the chloride precursor $[(L^1)\text{-Au}\equiv\text{Cl}]$ in line with the reports found in the literature.^[127] A subsequent treatment with the appropriate alkyne in CH_3CN in the presence of NaOH resulted in the complex formation, as a white / pale yellow microcrystalline precipitate. Complexes **2a-c** were prepared by a similar procedure, however a different chloride precursor $[(L^2)\text{-Au}\equiv\text{Cl}]$ was used (Figure 4.2).

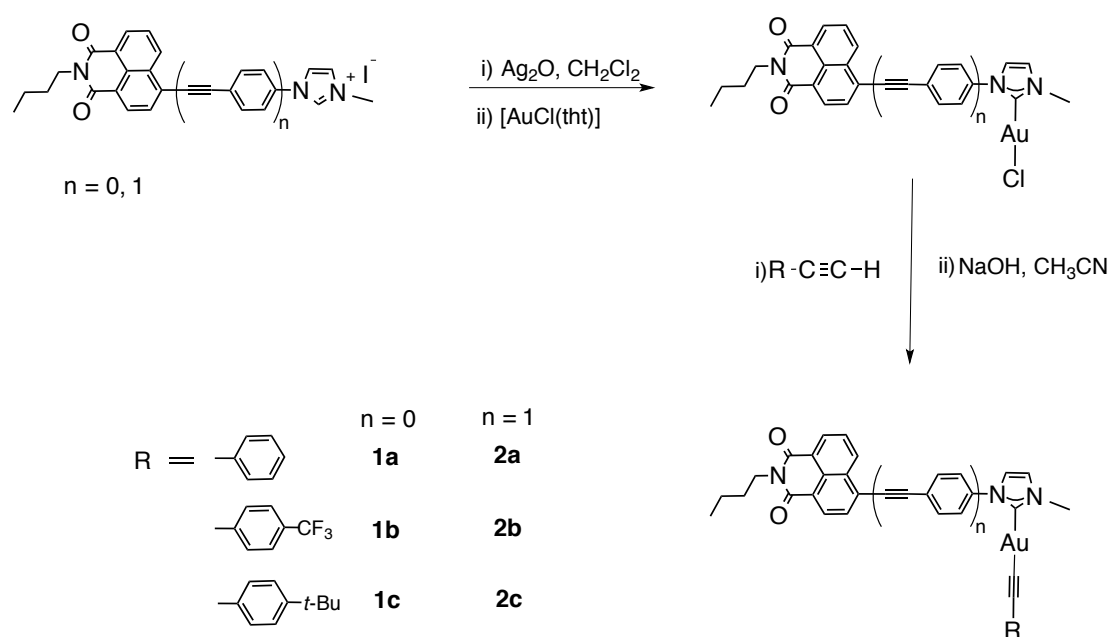


Figure 4.2: Synthesis routes of the alkynyl gold complexes **1a-c** and **2a-c**.

Synthetic details

General synthesis procedure of the NHC alkynyl gold(I) complexes 1a-c and 2a-c:

In a dried and argon protected Schlenk tube, ligand L^1 (1 eq.) or L^2 (1 eq.) and Ag_2O (0.55 eq.) were mixed with an appropriate amount of dry CH_2Cl_2 in the dark. The mixed solution was stirred for 5-6 hours at room temperature and a tiny amount of charcoal was added. The solution then was transferred via a cannula to another Schlenk

tube where the (tht)AuCl (1 eq.) was contained. The mixture was kept stirring overnight, and then transferred via a cannula to a Schlenk tube containing a solution of NaOH (2 eq.) and the appropriate alkyne (2 eq.) in dry CH₃CN. The mixture was allowed to react for 20 hours in the dark, then the solvent was removed by vacuum. The crude product was extracted by CH₂Cl₂ (2 x 10 mL) and filtered through celite into a Schlenk tube kept under argon atmosphere. The filtrate was concentrated under vacuum, then the Et₂O was added and a solid precipitate appeared. The mixture was put into freezer overnight and the solid precipitate was obtained by filtering on a Millipore membrane filter and then dried under vacuum. All the compounds obtained are soluble in most organic solvents and fully characterized by ¹H- and ¹³C-NMR spectroscopy, elemental analysis, FTIR analysis and single crystal X-ray diffraction technique (vide infra).

Complex 1a:

Complex **1a** was obtained as a white solid (66 mg) with yield of 87% by using 57 mg ligand **L**¹ (0.12 mmol), 15 mg Ag₂O (0.066 mmol), 38 mg (tht)AuCl (0.12 mmol) and 10 mL CH₂Cl₂, 10 mg NaOH (0.024 mmol), 30 μL phenylacetylene (0.24 mmol) and 6 mL CH₃CN. ¹H-NMR (500 MHz, CD₂Cl₂): 8.69 (d, J = 7.8 Hz, 1H, H₁₅), 8.67 (dd, J = 7.2, 1.2 Hz, 1H, H₂₁), 7.93 (d, J = 7.8 Hz, 1H, H₁₄), 7.92 (dd, J = 8.5, 1.2 Hz, 1H, H₁₉), 7.84 (dd, J = 8.5 Hz, 7.2 Hz, 1H, H₂₀), 7.29 (d, J = 1.9 Hz, 1H, H₂), 7.28 (d, J = 1.9 Hz, 1H, H₃), 7.20 - 7.18 (m, 2H, H₃₂), 7.16 - 7.12 (m, 2H, H₃₃), 7.11 - 7.08 (m, 1H, H₃₄), 4.20 - 4.16 (m, 2H, H₂₅), 4.06 (s, 3H, H₄), 1.74 - 1.68 (m, 2H, H₂₆), 1.44 (sext, J = 7.4 Hz, 2H, H₂₇), 0.98 (t, J = 7.4 Hz, 3H, H₂₈). ¹³C-NMR (125 MHz, CD₂Cl₂): 189.5 (C₁), 163.6 (C₂₃), 163.1 (C₂₄), 140.3 (C₁₃), 131.9 (C₂₁), 131.7 (C₃₂), 130.5 (C₁₅), 129.4 (C₂₉), 129.0 (C₁₇), 128.4 (C₁₉ and C₂₀), 128.2 (C₁₈), 127.9 (C₃₃), 126.4 (C₁₄), 126.1 (C₃₄), 126.0 (C₃₁), 124.3 (C₁₆), 123.5 (C₂₂), 123.3 (C₂), 122.7 (C₃), 103.9 (C₃₀), 40.3 (C₂₅), 38.4 (C₄), 30.2 (C₂₆), 20.4 (C₂₇), 13.7 (C₂₈). Analysis calcd for C₂₈H₂₄AuN₃O₂: C, 53.26; H, 3.83; N, 6.65; found C, 53.30; H, 3.81; N, 6.51. FTIR: 3141, 2963, 2928, 2865, 2108, 1696, 1655, 1623, 1586, 1513, 1478, 1442, 1381, 1334, 1287, 1230, 1179, 1114, 1075, 1019, 944, 911, 864, 790, 754, 726, 687, 648, 620, 586, 531, 486, 454, 407.

Complex 1b:

Complex **1b** was obtained as a white solid (67 mg) with yield of 70% by using 71 mg ligand **L**¹ (0.15 mmol), 19 mg Ag₂O (0.083 mmol), 58 mg (tht)AuCl (0.18 mmol) and 10 mL CH₂Cl₂, 12 mg NaOH (0.03 mmol) and 6 mL CH₃CN. ¹H-NMR (500 MHz, CD₂Cl₂): 8.69 (d, J = 7.7 Hz, 1H, H₁₅), 8.67 (dd, J = 7.2, 1.2 Hz, 1H, H₂₁), 7.93 (d, J = 7.7 Hz, 1H, H₁₄), 7.92 (dd, J = 8.4, 1.2 Hz, 1H, H₁₉), 7.84 (dd, J = 8.4 Hz, 7.2 Hz, 1H, H₂₀), 7.41 - 7.38 (m, 2H, H₃₃), 7.32 - 7.29 (m, 2H, H₃₂), 7.31 (d, J = 1.9 Hz, 1H, H₂), 7.29 (d, J = 1.9 Hz, 1H, H₃), 4.20 - 4.17 (m, 2H, H₂₅), 4.06 (s, 3H, H₄), 1.74 - 1.68 (m, 2H, H₂₆), 1.45 (sext, J = 7.4 Hz, 2H, H₂₇), 0.98 (t, J = 7.4 Hz, 3H, H₂₈). ¹³C-NMR (125

MHz, CD₂Cl₂): 189.0 (C₁), 163.6 (C₂₃), 163.1 (C₂₄), 140.2 (C₁₃), 133.4 (C₂₉), 132.0 (C₃₂), 131.9 (C₂₁), 130.5 (C₁₅), 130.0 (C₃₁), 129.0 (C₁₇), 128.5 (C₂₀), 128.4 (C₁₉), 128.1 (C₁₈), 127.4 (q, J_{CF} = 32.2 Hz, C₃₄), 126.4 (C₁₄), 124.8 (q, J_{CF} = 3.8 Hz, C₃₃), 124.4 (q, J_{CF} = 272.5 Hz, C₃₇), 124.3 (C₁₆), 123.5 (C₂₂), 123.4 (C₂), 122.7 (C₃), 102.7 (C₃₀), 40.3 (C₂₅), 38.4 (C₄), 30.2 (C₂₆), 20.4 (C₂₇), 13.7 (C₂₈). ¹⁹F-NMR (376 MHz, CD₂Cl₂): 62.85. Analysis calcd for C₂₉H₂₃AuF₃N₃O₂: C, 49.80; H, 3.31; N, 6.01; found C, 49.67; H, 3.24; N, 5.90. FTIR: 3174, 2960, 2872, 2108, 2050, 1748, 1705, 1664, 1593, 1560, 1513, 1474, 1446, 1401, 1369, 1343, 1312, 1269, 1232, 1170, 1123, 1060, 1012, 980, 944, 909, 879, 842, 790, 737, 687, 655, 614, 521, 484, 432.

Complex 1c:

Complex **1c** was obtained as a clear grey solid (66 mg) with yield of 70% by using 71 mg ligand **L**¹ (0.15 mmol), 19 mg Ag₂O (0.083 mmol), 58 mg (tht)AuCl (0.18 mmol) and 10 mL CH₂Cl₂, 12 mg NaOH (0.03 mmol), 60 μL 4-tert-butylphenylacetylene (0.30 mmol) and 6 mL CH₃CN. ¹H-NMR (500 MHz, CD₂Cl₂): 8.70 (d, J = 7.7 Hz, 1H, H₁₅), 8.67 (dd, J = 7.2, 1.2 Hz, 1H, H₂₁), 7.93 (d, J = 7.7 Hz, 1H, H₁₄), 7.92 (dd, J = 8.4, 1.2 Hz, 1H, H₁₉), 7.84 (dd, J = 8.4 Hz, 7.2 Hz, 1H, H₂₀), 7.29 (d, J = 1.9 Hz, 1H, H₂), 7.28 (d, J = 1.9 Hz, 1H, H₃), 7.19 - 7.16 (m, 2H, H₃₃), 7.13 - 7.10 (m, 2H, H₃₂), 4.20 - 4.17 (m, 2H, H₂₅), 4.06 (s, 3H, H₄), 1.74 - 1.68 (m, 2H, H₂₆), 1.45 (sext, J = 7.4 Hz, 2H, H₂₇), 1.24 (s, 9H, H₃₈), 0.98 (t, J = 7.4 Hz, 3H, H₂₈). ¹³C-NMR (125 MHz, CD₂Cl₂): 189.6 (C₁), 163.7 (C₂₃), 163.1 (C₂₄), 149.3 (C₃₄), 140.3 (C₁₃), 131.9 (C₂₁), 131.4 (C₃₂), 130.6 (C₁₅), 129.0 (C₁₇), 128.4 (C₁₉ and C₂₀), 128.3 (C₂₉), 128.2 (C₁₈), 126.4 (C₁₄), 124.9 (C₃₃), 124.3 (C₁₆), 123.5 (C₂₂), 123.3 (C₂), 122.9 (C₃₁), 122.6 (C₃), 103.9 (C₃₀), 40.3 (C₂₅), 38.4 (C₄), 34.4 (C₃₇), 31.0 (C₃₈), 30.2 (C₂₆), 20.4 (C₂₇), 13.7 (C₂₈). Analysis calcd for C₃₂H₃₂AuN₃O₂: C, 55.90; H, 4.69; N, 6.11; found C, 55.61; H, 4.76; N, 6.04. FTIR: 3094, 2960, 2867, 2111, 1699, 1660, 1623, 1588, 1502, 1440, 1397, 1368, 1336, 1291, 1233, 1189, 1110, 1081, 1015, 944, 879, 834, 786, 739, 683, 652, 620, 592, 564, 521, 486, 454, 411.

Complex 2a:

Complex **2a** was obtained as a yellow solid (86 mg) with yield of 65% by using 102 mg ligand **L**² (0.18 mmol), 23 mg Ag₂O (0.10 mmol) and 58 mg (tht)AuCl (0.18 mmol) and 30 mL CH₂Cl₂, 14 mg NaOH (0.36 mmol), 40 μL phenylacetylene and 10 mL CH₃CN. ¹H-NMR (500 MHz, CD₂Cl₂): 8.75 (dd, J = 8.4, 1.2 Hz, 1H, H₁₉), 8.61 (dd, J = 7.3, 1.2 Hz, 1H, H₂₁), 8.52 (d, J = 7.6 Hz, 1H, H₁₅), 7.99 (d, J = 7.6 Hz, 1H, H₁₄), 7.88 - 7.84 (m, 1H, H₂₀), 7.86 - 7.84 (m, 2H, H₉), 7.82 - 7.80 (m, 2H, H₁₀), 7.35 - 7.32 (m, 2H, H₃₂), 7.30 (d, J = 1.9 Hz, 1H, H₂), 7.22 - 7.19 (m, 2H, H₃₃), 7.17 (d, J = 1.9 Hz, 1H, H₃), 7.17 - 7.13 (m, 1H, H₃₄), 4.16 - 4.13 (m, 2H, H₂₅), 4.00 (s, 3H, H₄), 1.73 - 1.67 (m, 2H, H₂₆), 1.44 (sext, J = 7.4 Hz, 2H, H₂₇), 0.98 (t, J = 7.4 Hz, 3H, H₂₈).

^{13}C -NMR (125 MHz, CD_2Cl_2): 187.3 (C_1), 163.8 (C_{23}), 163.5 (C_{24}), 139.8 (C_5), 133.1 (C_9), 132.1 (C_{19}), 131.8 (C_{32}), 131.6 (C_{18}), 131.4 (C_{21}), 131.0 (C_{14}), 130.1 (C_{15}), 129.4 (C_{29}), 128.1 (C_{17}), 128.0 (C_{33}), 127.7 (C_{20}), 126.8 (C_{13}), 126.2 (C_{31}), 126.1 (C_{34}), 125.1 (C_{10}), 123.2 (C_{22}), 123.1 (C_8), 122.9 (C_3), 122.7 (C_{16}), 121.3 (C_2), 104.1 (C_{30}), 97.3 (C_{11}), 87.8 (C_{12}), 40.2 (C_{25}), 38.6 (C_4), 30.2 (C_{26}), 20.4 (C_{27}), 13.7 (C_{28}). Analysis calcd for $\text{C}_{36}\text{H}_{28}\text{AuN}_3\text{O}_2 \cdot 0.3\text{CH}_2\text{Cl}_2$: C, 57.59; H, 3.81; N, 5.74; found C, 57.78; H, 3.73; N, 5.68. FTIR: 3127, 2960, 2203, 2113, 1699, 1654, 1582, 1515, 1484, 1450, 1385, 1359, 1317, 1271, 1232, 1184, 1081, 1061, 1023, 956, 854, 832, 786, 744, 689, 634, 605, 581, 553, 527, 489, 470, 410.

Complex 2b:

Complex **2b** was obtained as a yellow solid (70 mg) with yield of 63% by using 102 mg ligand L^2 (0.18 mmol), 23 mg Ag_2O (0.10 mmol) and 58 mg (tht)AuCl (0.18 mmol) and 30 mL CH_2Cl_2 , 12 mg NaOH (0.30 mmol), 50 μL 4-trifluoromethylphenylacetylene (0.30 mmol) and 6 mL CH_3CN . ^1H -NMR (500 MHz, CD_2Cl_2): 8.77 (dd, $J = 8.4, 1.2$ Hz, 1H, H_{19}), 8.63 (dd, $J = 7.3, 1.2$ Hz, 1H, H_{21}), 8.55 (d, $J = 7.6$ Hz, 1H, H_{15}), 8.01 (d, $J = 7.6$ Hz, 1H, H_{14}), 7.90 - 7.87 (m, 1H, H_{20}), 7.89 - 7.86 (m, 2H, H_9), 7.82 - 7.79 (m, 2H, H_{10}), 7.48 - 7.45 (m, 2H, H_{33}), 7.46 - 7.44 (m, 2H, H_{32}), 7.31 (d, $J = 1.9$ Hz, 1H, H_2), 7.17 (d, $J = 1.9$ Hz, 1H, H_3), 4.17 - 4.14 (m, 2H, H_{25}), 4.00 (s, 3H, H_4), 1.73 - 1.67 (m, 2H, H_{26}), 1.44 (sext, $J = 7.4$ Hz, 2H, H_{27}), 0.98 (t, $J = 7.4$ Hz, 3H, H_{28}). ^{13}C -NMR (125 MHz, CD_2Cl_2): 187.0 (C_1), 163.9 (C_{23}), 163.6 (C_{24}), 139.7 (C_5), 133.1 (C_9), 132.15 (C_{19}), 132.11 (C_{32}), 131.7 (C_{18}), 131.5 (C_{21}), 131.1 (C_{14}), 130.2 (C_{31}), 130.1 (C_{15}), 128.1 (C_{17}), 127.7 (C_{20}), 126.8 (C_{13}), 125.1 (C_{10}), 124.9 (q, $J = 3.6$ Hz, C_{33}), 123.3 (C_{22}), 123.2 (C_8), 122.9 (C_3), 122.8 (C_{16}), 121.4 (C_2), 103.0 (C_{30}), 97.2 (C_{11}), 87.8 (C_{12}), 40.2 (C_{25}), 38.6 (C_4), 30.2 (C_{26}), 20.4 (C_{27}), 13.7 (C_{28}). ^{19}F -NMR (376 MHz, CD_2Cl_2): 62.80. Analysis calcd for $\text{C}_{37}\text{H}_{27}\text{AuF}_3\text{N}_3\text{O}_2 \cdot 0.1\text{CH}_2\text{Cl}_2$: C, 55.14; H, 3.39; N, 5.20; found C, 55.20; H, 3.25; N, 4.88. FTIR: 3129, 2960, 2200, 2114, 1700, 1650, 1608, 1582, 1513, 1451, 1387, 1358, 1321, 1269, 1233, 1183, 1161, 1118, 1102, 1083, 1063, 1013, 955, 851, 831, 787, 745, 707, 671, 636, 616, 598, 581, 552, 530, 506, 488, 471, 441, 415.

Complex 2c:

Complex **2c** was obtained as a green solid (32 mg) with yield of 29% by using 80 mg ligand L^2 (0.14 mmol), 19 mg Ag_2O (0.08 mmol), 48 mg (tht)AuCl (0.14 mmol) and 25 mL CH_2Cl_2 , 12 mg NaOH (0.30 mmol) and 60 μL 4-tert-butylphenylacetylene (0.30 mmol) and 6 mL CH_3CN . ^1H -NMR (500 MHz, CD_2Cl_2): 8.77 (dd, $J = 8.4, 1.2$ Hz, 1H, H_{19}), 8.62 (dd, $J = 7.2, 1.2$ Hz, 1H, H_{21}), 8.54 (d, $J = 7.6$ Hz, 1H, H_{15}), 8.01 (d, $J = 7.6$ Hz, 1H, H_{14}), 7.89 - 7.85 (m, 1H, H_{20}), 7.88 - 7.85 (m, 2H, H_9), 7.83 - 7.80 (m, 2H, H_{10}), 7.30 (d, $J = 1.9$ Hz, 1H, H_2), 7.27 - 7.25 (m, 2H, H_{32}), 7.25 - 7.23 (m, 2H,

H₃₃), 7.16 (d, J = 1.9 Hz, 1H, H₃), 4.17 - 4.13 (m, 2H, H₂₅), 4.00 (s, 3H, H₄), 1.73 - 1.67 (m, 2H, H₂₆), 1.44 (sext, J = 7.4 Hz, 2H, H₂₇), 1.27 (s, 9H, H₃₈), 0.98 (t, J = 7.4 Hz, 3H, H₂₈). ¹³C-NMR (125 MHz, CD₂Cl₂): 187.5 (C₁), 163.8 (C₂₃), 163.6 (C₂₄), 149.3 (C₃₄), 139.8 (C₅), 133.1 (C₉), 132.2 (C₁₉), 131.7 (C₁₈), 131.5 (C₃₂), 131.4 (C₂₁), 131.0 (C₁₄), 130.1 (C₁₅), 128.3 (C₂₉), 128.1 (C₁₇), 127.7 (C₂₀), 126.9 (C₁₃), 125.1 (C₁₀), 125.0 (C₃₃), 123.3 (C₂₂), 123.2 (C₃₁), 123.1 (C₈), 122.8 (C₃), 122.7 (C₁₆), 121.3 (C₂), 104.2 (C₃₀), 97.3 (C₁₁), 87.8 (C₁₂), 40.2 (C₂₅), 38.6 (C₄), 34.5 (C₃₇), 31.0 (C₃₈), 30.2 (C₂₆), 20.4 (C₂₇), 13.7 (C₂₈). Analysis calcd for C₄₀H₃₆AuN₃O₂: C, 60.99; H, 4.61; N, 5.33; found C, 60.38; H, 4.58; N, 5.26. FTIR: 3131, 2962, 2201, 2112, 1698, 1651, 1609, 1582, 1517, 1498, 1450, 1389, 1361, 1320, 1269, 1232, 1185, 1081, 1062, 955, 885, 859, 831, 789, 755, 740, 707, 671, 636, 583, 565, 552, 537, 505, 487, 472, 442, 410.

4.2.2 X-Ray crystal structure characterization

The crystals grown by vapor diffusion of diethyl ether or pentane into a CH₂Cl₂ solution of the complexes **1a**, **2a** and **2b** were suitable for single-crystal X-ray diffraction investigation. They were mounted and transferred under a cold nitrogen gas stream. Intensity data were obtained by a Bruker Kappa-APEX2 systems equipped with fine-focus sealed tube radiation. Unit-cell parameters determination, data collection strategy and integration were performed by the Bruker APEX2 suite of programs. Multi-scan absorption correction^[131] was used and the crystal structures were investigated with SHELXT-2014^[132] and refined anisotropically by full-matrix least-squares methods with SHELXL-2014^[132] by using the WinGX suite.^[133] The crystal structures of complexes were recorded at the Cambridge Crystallographic Data Centre with numbers CCDC 1477775-1477778 and can be obtained free of charge via www.ccdc.cam.ac.uk.

4.2.3 Photophysical measurements

Spectrofluorimetric grade dichloromethane (CH₂Cl₂) and methanol (MeOH) (Merck Uvasol®) were used to carry out the spectroscopic investigations of the eight compounds. A Perkin-Elmer Lambda 950 spectrophotometer was used to record the absorption spectra. In order to perform the photoluminescence experiments, solutions were put into fluorimetric Suprasil quartz gas-tight cuvettes (1 cm optical pathlength) and de-aerated for 20 minutes by bubbling argon. The emission spectra were collected with an Edinburgh Instruments FLS920 spectrometer equipped with a Peltier-cooled Hamamatsu R928P photomultiplier tube (185-900 nm) and the spectra were corrected by a calibration curve supplied with the instrument. An Edinburgh 450 W xenon arc lamp was used as the excitation light source. Photoluminescence quantum yields (Φ_{PL}) of the eight compounds in solution were determined from the corrected emission spectra, using an air-equilibrated water solution of quinine sulfate in 1 N H₂SO₄ as

reference ($\Phi_{\text{PL}} = 0.546$).^[134] Photoluminescence quantum yields were also determined with the absolute method,^[25] using a barium sulfate-coated integrating sphere (diameter of 3 in.). The excited state lifetimes (τ) were measured by the time-correlated single photon counting (TCSPC) technique with an HORIBA FluoroHub, and a TBX-05C Picosecond Photon Detection Module (300-850 nm) as the detector. The system includes two excitation sources, pulsed NanoLED ($\lambda_{\text{exc}} = 331$ nm) for the nanosecond range lifetimes and pulsed SpectraLED ($\lambda_{\text{exc}} = 370$ nm) for the microsecond and millisecond range lifetimes. The luminescence decay profiles were analyzed with the DAS6 Decay Analysis Software, and the quality of the fit was assessed with the χ^2 value (close to unity) and with the residuals randomly distributed along the time axis. Low temperature luminescence spectra at 77 K were recorded using a 2 mm inner diameter quartz tubes (sample inside) into a custom made quartz cold finger Dewar flask filled with liquid nitrogen. Singlet oxygen sensitization efficiencies of all the compounds were measured in air-equilibrated CH_2Cl_2 solutions, and an air-equilibrated CH_2Cl_2 solution of C_{60} was used as the reference ($\Phi_{\Delta} = 0.99$).^[135] Excitation wavelengths are 350 nm and 375 nm for L^1 and L^2 series compounds and the singlet oxygen sensitization efficiencies were calculated comparing the phosphorescence spectral area of the singlet oxygen. Transient absorption spectra of compounds L^2 and **2a-c** were established by collecting the transient absorbance (ΔA) values from the measured time decays at different wavelengths. During the transient measurements, the sample solutions was stirred, and a 355 nm pump laser (Oriel Instruments) was used to excite the sample. Experimental uncertainties are estimated to be $\pm 8\%$ for τ determinations, $\pm 20\%$ for Φ_{PL} , and ± 2 nm and ± 5 nm for absorption and emission peaks, respectively.

4.2.4 Preparation and characterization of the PMMA films

Poly(methyl methacrylate) (PMMA) samples (0.5% w/w) were prepared by dissolving 200 mg of PMMA powder (average MW $\sim 350,000$ by GPC, purchased from Sigma-Aldrich) in 4 mL dye- CH_2Cl_2 solutions (0.25 mg/mL), solvent were then evaporated overnight in a 5 cm glass Petri dish. The resulted PMMA films were separated through sonication from the glass dish and the thickness of the films was measured as 70 ± 8 μm . Transmission and reflection spectra of the PMMA films were obtained with a Perkin-Elmer Lambda 950 spectrophotometer equipped with 100 mm diffuse reflectance and transmission integrating sphere accessory, including PMT/PbS detectors. The absorption factors were calculated by the following equation:

$$A\% = 100 - T\% - R\% \quad (4.1)$$

in which A%, T% and R% represent the absorption factor, transmittance and reflectance, respectively. Absolute fluorescence quantum yields of the PMMA films were calculated

from the corrected emission spectra by using a barium sulfate-coated integrating sphere (diameter of 3 in.).^[25]

4.2.5 Computational details

Density functional theory (DFT) calculations^[33] were performed by using the Gaussian 16 program package^[67] (B.01 revision) with the M06 hybrid meta exchange-correlation functional.^[68-69] The 6-31+G(d) basis set was selected for C, H, N, O and F atoms,^[136] and the more suitable Stuttgart/Dresden ECP60MWB pseudopotential (SDD) basis set was chosen for Au atoms to replace the first 60 inner-core electrons.^[137] All the molecules were fully optimized (gas phase) without symmetry constraints in the electronic ground states (S_0), the lowest singlet excited states (S_1) and the lowest triplet excited states (T_1). The frequency calculation was always used to verify the stationary point found by the geometry optimization corresponding to a minimum on the potential energy surface (no imaginary frequencies). Time-dependent density functional theory calculations (TD-DFT) were used to simulate the UV-Vis spectra^[75-76,138] and to optimize the S_1 excited state. Geometry optimizations and frequency calculations of the S_0 and S_1 state were carried out at the spin-restricted M06 level of theory with a spin multiplicity of 1. The lowest triplet excited state (T_1) was optimized at the spin-unrestricted level of theory with a spin multiplicity of 3. All the pictures of molecular orbitals and spin-density surfaces were created using GaussView 6.0.16.^[77]

4.3 Results and Discussion

4.3.1 XRD structure analysis

Table 4.1: Selected bond distances and distortion angles of **1a**, **2a** and **2b**.

	Au-C1 (Å)	Au-R (Å)	C≡C (Å)	C1-N1 (Å)	C1-N2 (Å)	N2-CH ₃ (Å)	θ_{int} (°)
1a	2.016(4)	1.990(4)	1.205(6)	1.360(5)	1.342(5)	1.457(5)	76.4(2)
2a	2.017(5)	1.995(5)	1.190(7)	1.375(6)	1.348(6)	1.452(6)	32.0(2)
2b	2.027(2)	1.985(2)	1.210(3)	1.372(2)	1.349(2)	1.460(2)	36.9(2)

In Figure 4.3 the ORTEP drawings of complexes **1a**, **2a** and **2b** are shown, and the selected bond distances and angles are given in Table 4.1. The obtained crystal structures of **1a**, **2a** and **2b** certify the formation of the gold complexes, and the geometry around the Au(I) center is almost linear with a $C_{\text{carbene}}\text{-Au-acetylide}$ angle of $177.9(2)^\circ$ for **1a** and $176.3(2)^\circ$ for **2a** and $176.4(1)^\circ$ for **2b**. The bond distances of $C_{\text{carbene}}\text{-Au}$ and Au-acetylide are 2.016(4) and 1.990(4) Å for **1a**, 2.017(5) and 1.995(5) Å for **2a**, and 2.027(2) and 1.985(2) Å for **2b**, typical of those reported for previous gold complexes containing a simple carbene displaying alkynyl ligands.^[117,139-140] Interestingly, the planes of the imidazole-2-ylidene and the NI moiety show an angle of $76.4(2)^\circ$ for **1a** which is significantly larger than $32.0(2)^\circ$ and $36.9(2)^\circ$ observed for **2a**

and **2b**. This data might indicate that the gold carbene unit is more conjugated to the organic chromophore in the π -extended family **2a-c** compared to that of **1a-c**. As a result, this should affect the photophysical properties of both groups.

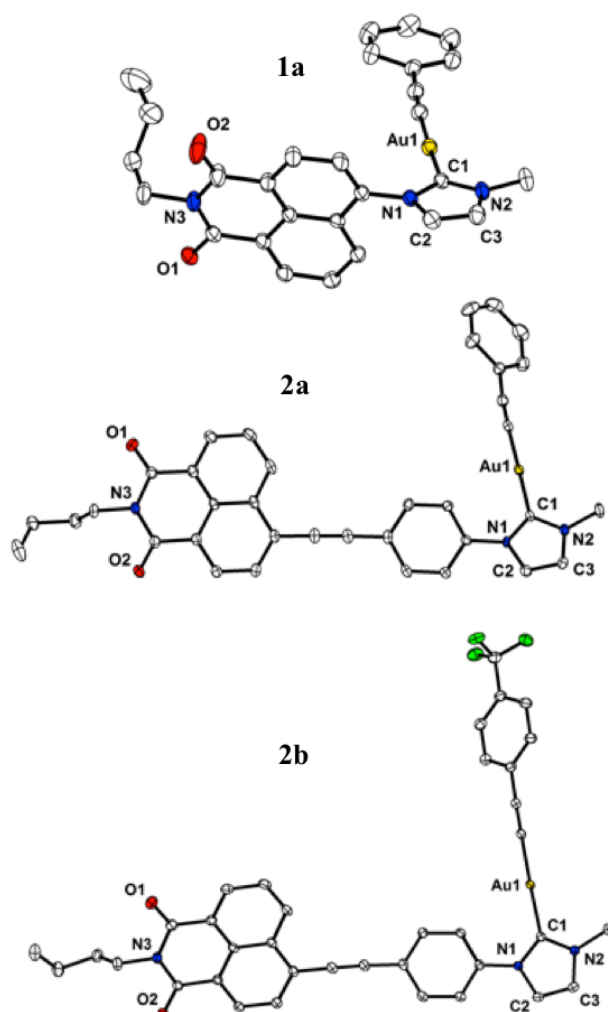


Figure 4.3: ORTEP drawings of **1a**, **2a** and **2b** with numbering system showing the different orientations of the gold-carbene unit relative to the organic NI chromophore. Thermal ellipsoids at 30% probability level, H atoms and solvent molecules are omitted for clarity.

The crystal packing analysis of the structures indicates that in complex **1a** a weak Au-Au interaction at $d = 3.531(1)$ Å occurs, and the dimer is generated through the head-to-tail style. For complexes **2a** and **2b**, shorter Au-Au interactions were found with $d = 3.319(1)$ Å for **2a** and $d = 3.263(1)$ Å for **2b**. Similarly to **1a**, complexes **2a** and **2b** display a head-to-tail orientation in the dimer structures. Additionally, each dimer assembly through π - π interactions between the NI and phenyl ring of another dimer with interplanar distance roughly is 3.4 Å ($C7-C18$ 3.370(8) Å) for **2a** and ($C9-C18$ 3.411(3) Å) for **2b** (Figure 4.4). These non-covalent interactions result in the one-dimensional (1D) supramolecular structures.

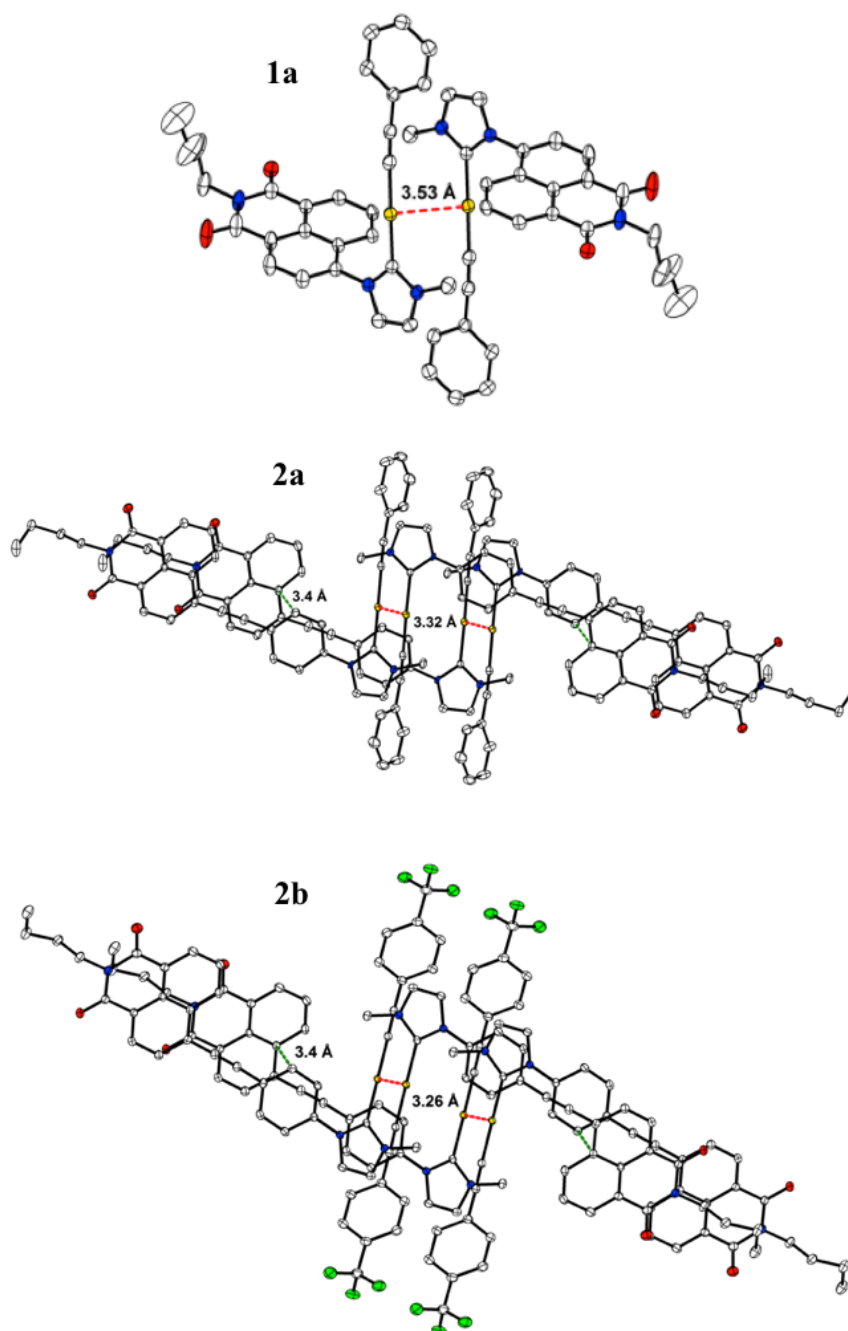


Figure 4.4: Solid-state packing shows dimer formation through Au-Au interaction in complex **1a**, and a combination of Au-Au and π - π interactions generate 1D supramolecular assemblies in complexes **2a** and **2b**.

4.3.2 Photothermal stability in solutions

Photothermal stability properties of all the compounds were checked with UV-VIS absorption spectroscopy both in dichloromethane (CH_2Cl_2) and methanol (CH_3OH). Ligand **L**¹ is stable in CH_2Cl_2 , while the ligand **L**² displays a weak attenuation of the absorption spectra in time (Figure 4.5). All the gold(I) complexes display stable absorption features in CH_2Cl_2 above 315 nm, while in the UV region

below 315 nm the absorbance values are decreasing in time. In methanol, ligand L^2 and all the gold(I) complexes are stable within six days (Figure 4.6 and 4.7).

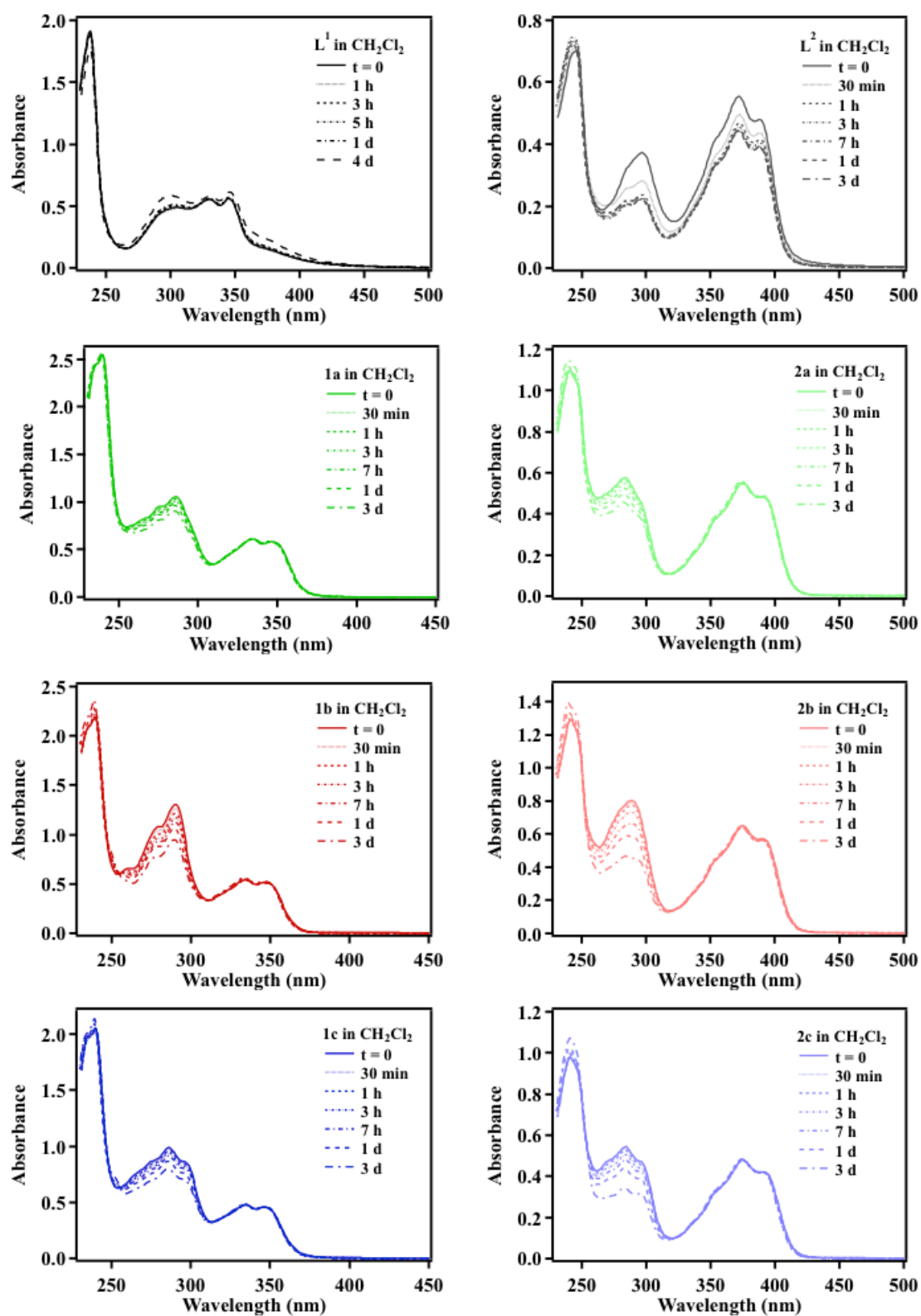


Figure 4.5: Absorption spectra of the two NHC-NI ligands L^1 , L^2 and their corresponding alkynyl gold(I) complexes **1a-c** and **2a-c** in CH_2Cl_2 at 298 K at different time after preparation under daylight.

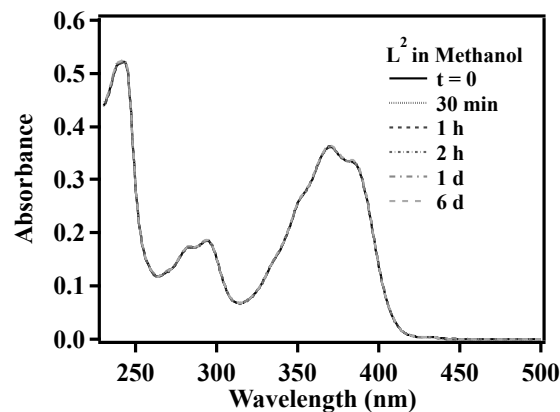


Figure 4.6: Absorption spectra of the ligand L^2 in methanol at 298 K at different time after preparation under daylight.

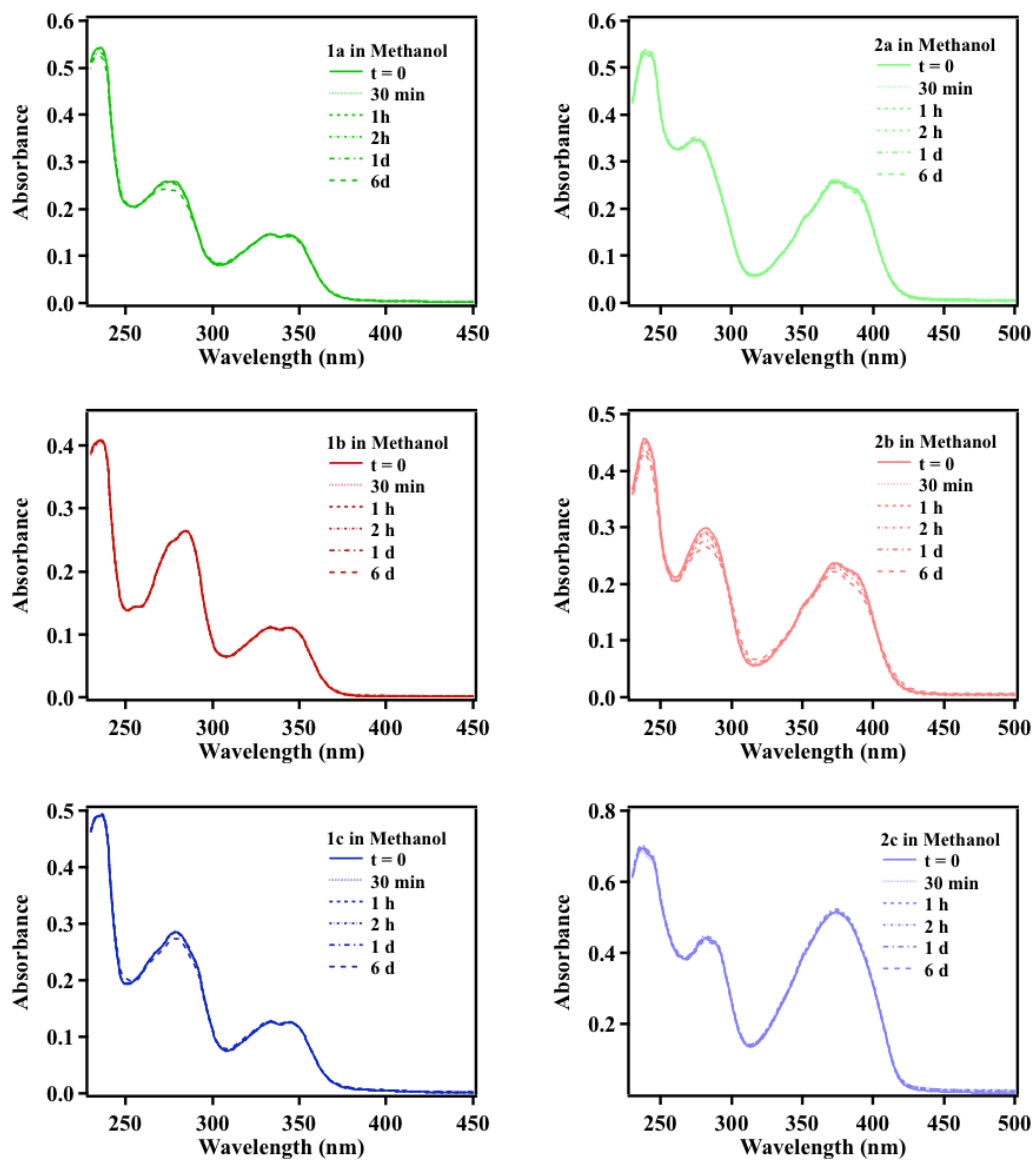


Figure 4.7: Absorption spectra of the six alkyne gold(I) complexes **1a-c** and **2a-c** in methanol at 298 K at different time after preparation under daylight.

4.3.3 Photophysics in solutions

Absorption in solution:

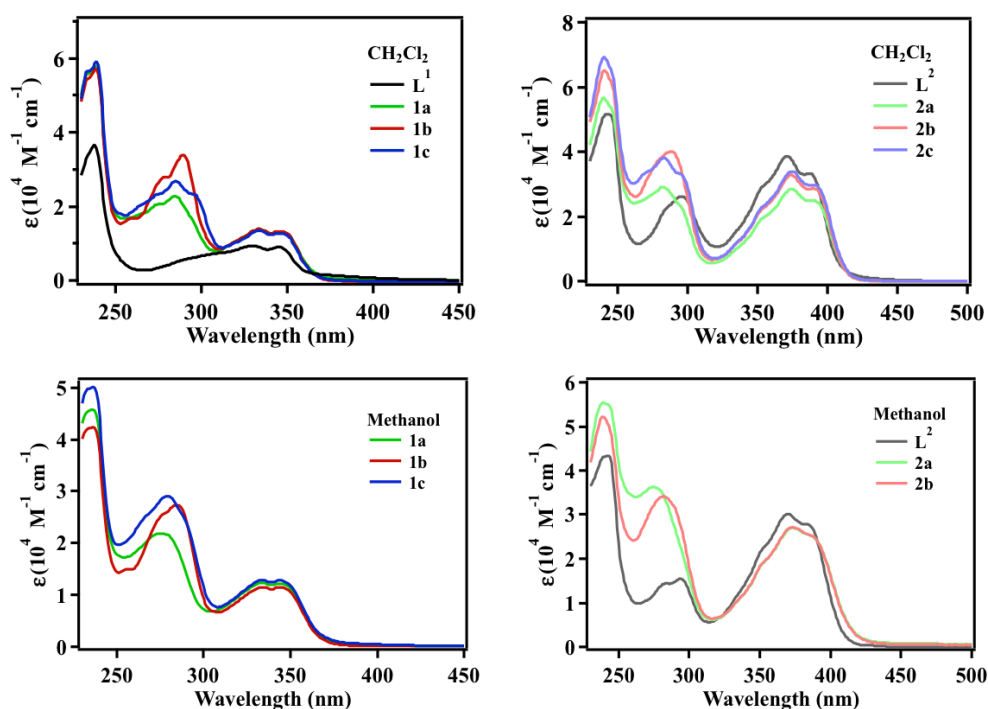


Figure 4.8: Absorption spectra of the two NHC-NI ligands L^1 , L^2 and their corresponding alkynyl gold(I) complexes **1a-c** and **2a-c** in CH_2Cl_2 and methanol solutions at 298 K.

Table 4.2: Main absorption parameters in CH_2Cl_2 and methanol solution at 298 K.

	$\lambda_{max}, nm (\epsilon_{max}, \times 10^4 M^{-1}cm^{-1})^{[a]}$	$\lambda_{max}, nm (\epsilon_{max}, \times 10^4 M^{-1}cm^{-1})^{[b]}$
L^1	330 (0.94), 345 (0.91)	/
1a	285 (2.28), 334 (1.39), 346 (1.33)	275 (2.18), 333 (1.23), 344 (1.22)
1b	289 (3.39), 334 (1.39), 345 (1.32)	284 (2.73), 334 (1.15), 344 (1.15)
1c	285 (2.68), 334 (1.35), 345 (1.28)	279 (2.90), 333 (1.28), 344 (1.28)
L^2	296 (2.62), 371 (3.86), 388 (3.33)	294 (1.54), 370 (3.01), 388 (2.64)
2a	282 (2.92), 374 (2.85), 390 (2.50)	274 (3.62), 373 (2.70), 390 (2.43)
2b	288 (4.01), 374 (3.28), 390 (2.87)	282 (3.41), 373 (2.71), 390 (2.43)
2c	283 (3.82), 375 (3.39), 390 (2.98)	/

[a] In CH_2Cl_2 solution; [b] In methanol solution.

In Figure 4.8 the absorption spectra of the eight compounds in CH_2Cl_2 and methanol are reported, and the related absorption parameters are collected in Table 4.2. The absorption features of all compounds are similar in CH_2Cl_2 and methanol. In CH_2Cl_2 solution, ligand L^1 shows two absorption peaks (at 330 and 345 nm) in the UV region. These can be attributed to $^1\pi,\pi^*$ transitions with a strong intramolecular charge

transfer (ICT) character, as commonly observed for this class of molecules.^[128] However, in the corresponding complexes **1a-c** a new absorption feature in the range of 250-315 nm appears. The attribution of these transitions is not straightforward and TD-DFT calculations are still running and the results will be discussed further in a paper under preparation. A similar analysis and attribution to the absorption bands can be applied to the second series (**L²**, **2a-c**). However, the presence of the alkynyl-phenyl fragment connecting the naphthalimide and the N-heterocyclic carbene moieties induces a bathochromic shift of the low energy absorption bands with respect to those observed in the first series (**L¹**, **1a-c**) to 374 and 390 nm, respectively. This suggests a possible π -interaction between Au(I) 5d orbitals and the alkynyl-phenyl π -orbitals.

Emission in solution:

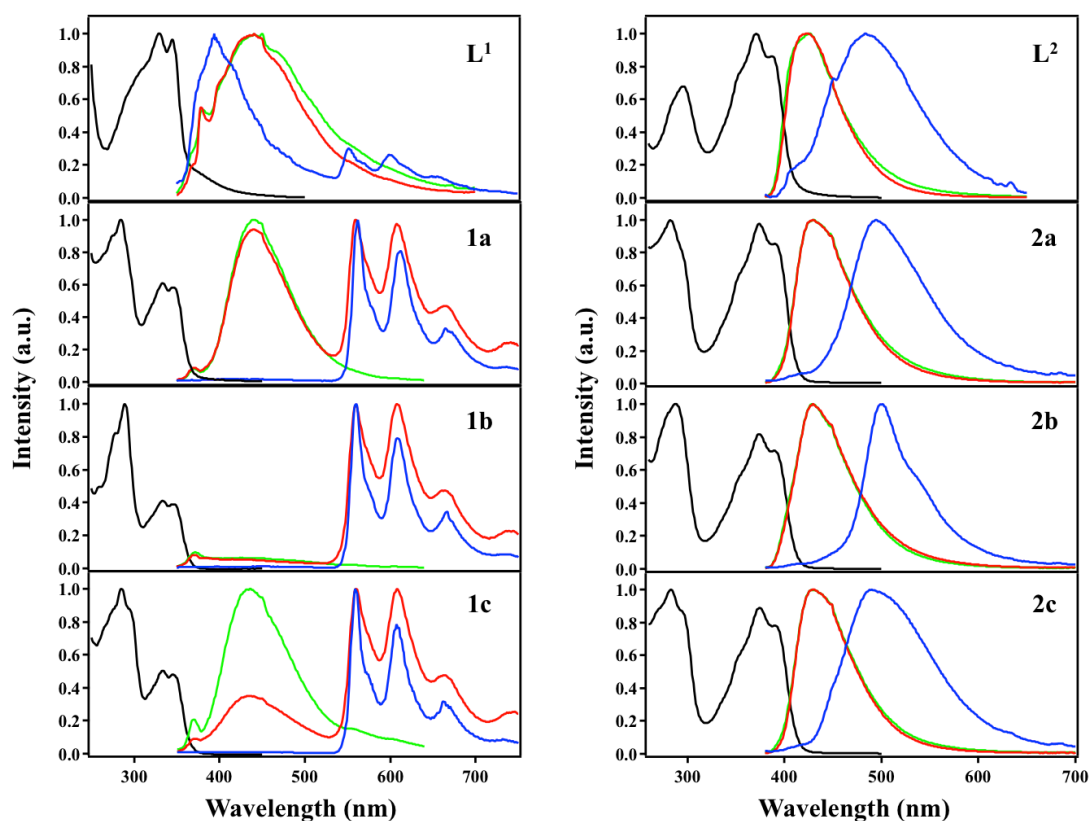


Figure 4.9: Normalized absorption spectra (black lines) and emission spectra of the two NHC-NI ligands **L¹**, **L²** and their corresponding alkynyl gold(I) complexes **1a-c** and **2a-c** in air-equilibrated (green lines) and deoxygenated (red lines) CH_2Cl_2 solution both at 298 K and 77 K (blue lines). Excitation wavelength is 330 nm for **L¹**, **1a-c**, and 360 nm for **L²**, **2a-c**.

Photoluminescence properties of the eight compounds were measured both in air-equilibrated and deoxygenated CH_2Cl_2 and methanol solutions at 298 K and 77 K. The normalized absorption spectra and emission spectra of the eight compounds in CH_2Cl_2 and methanol solutions are reported in Figure 4.9, 4.11 and 4.12. In air-equilibrated CH_2Cl_2 and methanol solutions at 298 K, ligand **L¹** and complexes **1a-c**

display a faint blue emission at about 440 nm with low quantum yield (Table 4.3 and 4.4). On the other hand, the ligand **L**² and complexes **2a-c** exhibit a strong fluorescence, especially the emission quantum yield of the ligand **L**² can reach up to 71.2% in air-equilibrated methanol solution (Table 4.4).

Table 4.3: Main emission parameters in CH₂Cl₂.

	298 K			77 K ^[b]	
	λ_{fluo} , nm (λ_{phos} , nm)	Φ_{fluo} , % (Φ_{phos} , %)	τ_{fluo} , ns (τ_{phos} , μs)	λ_{fluo} , nm (λ_{phos} , nm)	τ_{fluo} , ns (τ_{phos} , $\mu\text{s/ms}$)
L ¹	441 ^[a1] 441 ^[a2]	0.4 ^[a1] 0.4 ^[a2]	6.4 ^[a1] 5.9 ^[a2]	394 (552, 599, 650)	3.6 ns (9.2 μs)
1a	439 ^[a1] 440 (559, 608, 664) ^[a2]	0.7 ^[a1] 0.5 (0.6) ^[a2]	5.4 ^[a1] 5.5 (181.4) ^[a2]	(562, 612, 665)	($\tau_1=6.0$ ms $\tau_2=35.9$ ms)
1b	(560, 608, 663) ^[a2]	(0.6) ^[a2]	(154.5) ^[a2]	(560, 608, 666)	($\tau_1=3.7$ ms $\tau_2=10.4$ ms)
1c	435 ^[a1] 440 (560, 608, 662) ^[a2]	0.3 ^[a1] 0.2 (0.5) ^[a2]	5.3 ^[a1] 5.4 (204.6) ^[a2]	(559, 607, 662)	($\tau_1=4.0$ ms $\tau_2=11.6$ ms)
L ²	427 ^[a1] 423 ^[a2]	41.1 ^[a1] 45.2 ^[a2]	1.4 ^[a1] 1.4 ^[a2]	483	$\tau_1=4.2$ ns $\tau_2=19.0$ ns
2a	430 ^[a1] 429 ^[a2]	23.3 ^[a1] 14.7 ^[a2]	0.8 ^[a1] 0.8 ^[a2]	494	$\tau_1=4.8$ ns $\tau_2=14.9$ ns
2b	428 ^[a1] 430 ^[a2]	24.3 ^[a1] 17.5 ^[a2]	0.8 ^[a1] 0.8 ^[a2]	499	$\tau_1=6.2$ ns $\tau_2=12.6$ ns
2c	428 ^[a1] 431 ^[a2]	20.8 ^[a1] 13.9 ^[a2]	0.8 ^[a1] 0.8 ^[a2]	488	$\tau_1=4.1$ ns $\tau_2=15.5$ ns

[a1] In air-equilibrated CH₂Cl₂ solution at 298 K; [a2] In deoxygenated CH₂Cl₂ solution at 298 K; [b] In CH₂Cl₂ at 77 K.

After removing the oxygen from the CH₂Cl₂ and methanol solutions by bubbling argon, the alkynyl gold(I) complexes **1a-c** also exhibit a room temperature phosphorescence besides the fluorescence emission (Figure 4.9 and 4.12). A similar phosphorescence emission was found for other types of gold complexes in the literature.^[116,141-144] The phosphorescence nature of the low energy emission was also confirmed using a pulse excitation light source, and the spectra recorded in time gated mode are shown in Figure 4.10 and 4.13.

The complex **1b** in de-aerated CH₂Cl₂ and methanol solutions only displays the phosphorescence emission, being the fluorescence signal too weak to be detected by our apparatus (Figure 4.9 and 4.12). At odd with the ligand **L**¹ and complexes **1a-c**, the photophysical properties of ligand **L**² and complexes **2a-c** are almost unaffected by

molecular oxygen (Figure 4.9, 4.11 and 4.12). In Figure 4.9, the fluorescence emission spectra of L^2 and complexes **2a-c** collected from air-equilibrated and deoxygenated CH_2Cl_2 solutions almost overlap. All the photophysical data of the eight compounds in air-equilibrated CH_2Cl_2 and methanol solutions both at 298 K and 77 K were collected in Table 4.3 and 4.4, respectively. The emission lifetimes of the fluorescence fall in the nanoseconds range, while the phosphorescence lifetimes in deoxygenated solutions are on the order of hundreds of microseconds.

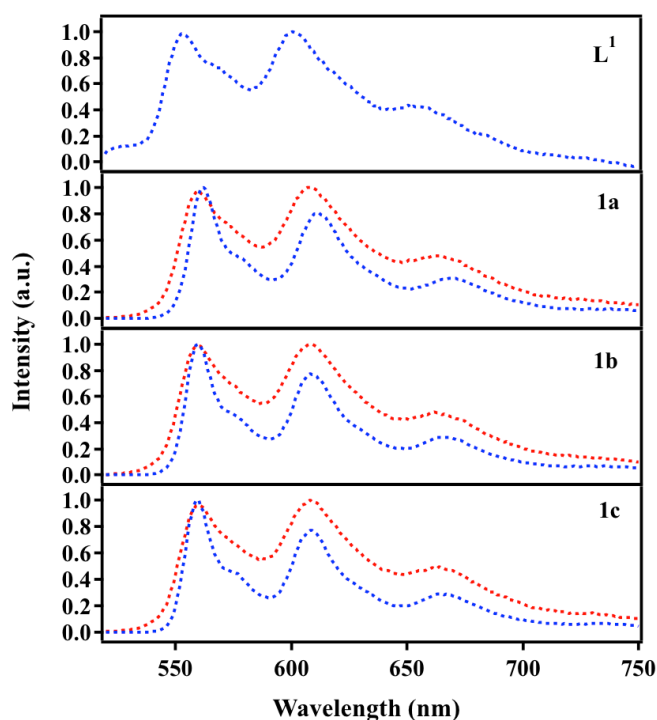


Figure 4.10: Normalized phosphorescence emission spectra (excited at 330 nm) of ligand L^1 and complexes **1a-c** in deoxygenated CH_2Cl_2 at 298 K (red lines) and in rigid matrix of CH_2Cl_2 at 77 K (blue lines). The spectra were collected by time gated detection.

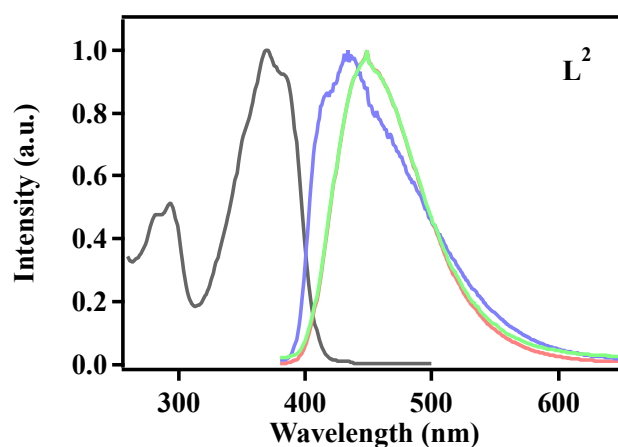


Figure 4.11: Normalized absorption spectrum (black line) and emission spectra (excited at 360 nm) of the ligand L^2 in air-equilibrated (green line) and deoxygenated (red line) methanol solution both at 298 K and 77 K (blue line).

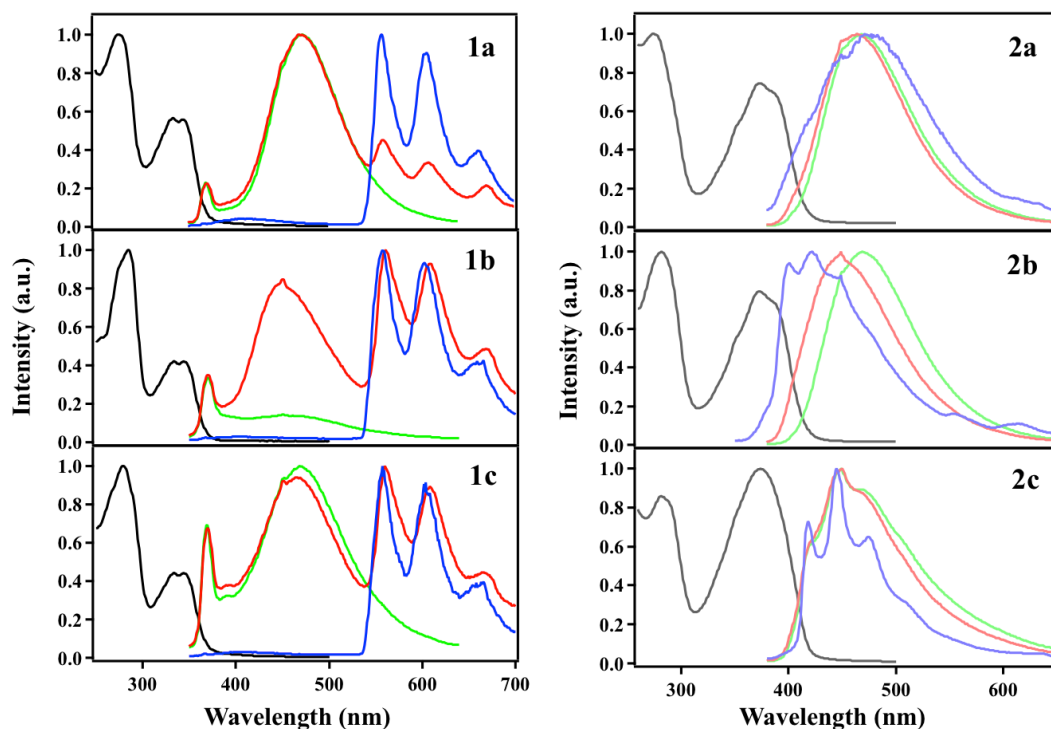


Figure 4.12: Normalized absorption spectra (black lines) and emission spectra of the complexes **1a-c** and **2a-c** in air-equilibrated (green lines) and deoxygenated (red lines) methanol solution both at 298 K and 77 K (blue lines). Excitation wavelength is 330 nm for **1a**, **1b**, **1c**, and 360 nm for **2a**, **2b**, **2c**. Complex **2b** at 77 K was excited at 340 nm.

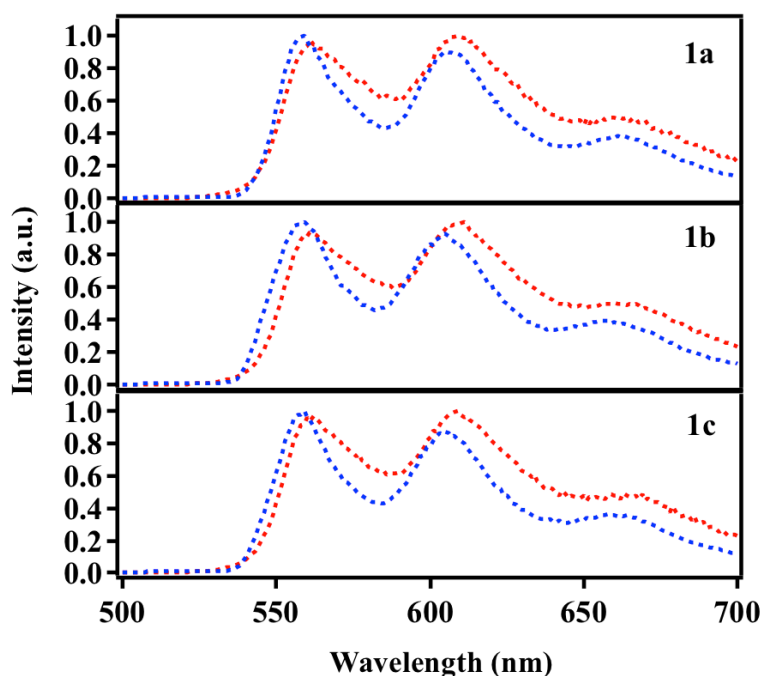


Figure 4.13: Normalized phosphorescence emission spectra (excited at 330 nm) of complexes **1a-c** in deoxygenated methanol at 298 K (red lines) and in rigid matrix of methanol at 77 K (blue lines). The spectra were collected by time gated detection.

Low temperature photoluminescence experiments were performed in frozen CH₂Cl₂ and methanol at 77 K. Figure 4.9, 4.11 and 4.12 show the emission spectra of the eight compounds in CH₂Cl₂ and methanol glassy solution at 77 K under steady state excitation conditions. The relevant phosphorescence emission spectra collected using the pulsed light source are reported in Figure 4.10 and 4.13. At 77 K, ligand **L**¹ in CH₂Cl₂ exhibits a strong fluorescence and a weak phosphorescence, but the related alkynyl gold complexes **1a-c** only show a strong phosphorescence. For ligand **L**² and complexes **2a-c**, no phosphorescence was found, but their fluorescence emissions displays an important red-shift in frozen CH₂Cl₂. The reason might be attributed to the formation of a precipitate in frozen CH₂Cl₂, giving rise to emission spectra that are similar to that of powder sample (Figure 4.17). Anyway, further DFT and TD-DFT calculations are carrying out to study the triplet excited states for these compounds. We are confident that the results will provide an explanation for the absence of phosphorescence in **L**² and **2a-c**. The emission lifetimes of all the samples in CH₂Cl₂ and methanol at 77 K were gathered in Table 4.3 and 4.4. At low temperature, alkynyl gold complexes **1a-c** gave us an extra-long phosphorescence lifetime in the millisecond range.

Table 4.4: Main emission parameters in methanol.

	298 K			77 K ^[b]	
	λ_{fluo} , nm (λ_{phos} , nm)	Φ_{fluo} , % (Φ_{phos} , %)	τ_{fluo} , ns (τ_{phos} , μs)	λ_{fluo} , nm (λ_{phos} , nm)	τ_{fluo} , ns (τ_{phos} , ms)
1a	472 ^[a1] 470 (559, 608, 670) ^[a2]	0.4 ^[a1] 0.4 (0.2) ^[a2]	6.0 ^[a1] 6.1 (52.9) ^[a2]	(557, 606, 662)	(10.1)
1b	451 (561, 608, 665) ^[a2]	0.2 (0.2) ^[a2]	$\tau_1=2.1$ $\tau_2=6.9$ (88.9) ^[a2]	(557, 602, 666)	(10.8)
1c	471 ^[a1] 464 (560, 608, 666) ^[a2]	0.2 ^[a1] 0.2 (0.1) ^[a2]	5.5 ^[a1] $\tau_1=5.6$ $\tau_2=20.3$ (55.6) ^[a2]	(557, 604, 666)	(10.6)
L ²	449 ^[a1] 449 ^[a2]	71.2 ^[a1] 74.7 ^[a2]	2.0 ^[a1] 2.1 ^[a2]	434	$\tau_1=2.1$ $\tau_2=19.8$
2a	468 ^[a1] 464 ^[a2]	4.7 ^[a1] 4.9 ^[a2]	1.9 ^[a1] 1.9 ^[a2]	471	$\tau_1=1.3$ $\tau_2=6.1$
2b	469 ^[a1] 449 ^[a2]	20.2 ^[a1] 13.0 ^[a2]	2.0 ^[a1] 2.1 ^[a2]	424	$\tau_1=2.0$ $\tau_2=7.0$
2c	449 ^[a1] 450 ^[a2]	1.8 ^[a1] 1.7 ^[a2]	2.0 ^[a1] 2.1 ^[a2]	418, 445, 474	$\tau_1=1.4$ $\tau_2=7.7$

[a1] In air-equilibrated methanol solution at 298 K; [a2] In deoxygenated methanol solution at 298 K; [b] In methanol at 77 K.

The color coordinates in the CIE 1931 color space were calculated for the ligand

L¹ and gold complexes **1a-c** in deoxygenated CH₂Cl₂ solutions from the relevant corrected emission spectra, and the results are shown in Figure 4.14. It is obvious that ligand **L¹** emits the blue-violet light (0.16, 0.07), complex **1a** and **1c** release the fuchsia (0.32, 0.24) and orange-red (0.42, 0.33) light, respectively. In deoxygenated CH₂Cl₂ solution, only the phosphorescence was observed for complex **1b**. Hence, the radiant light of **1b** move to the pure orange region (0.51, 0.43).

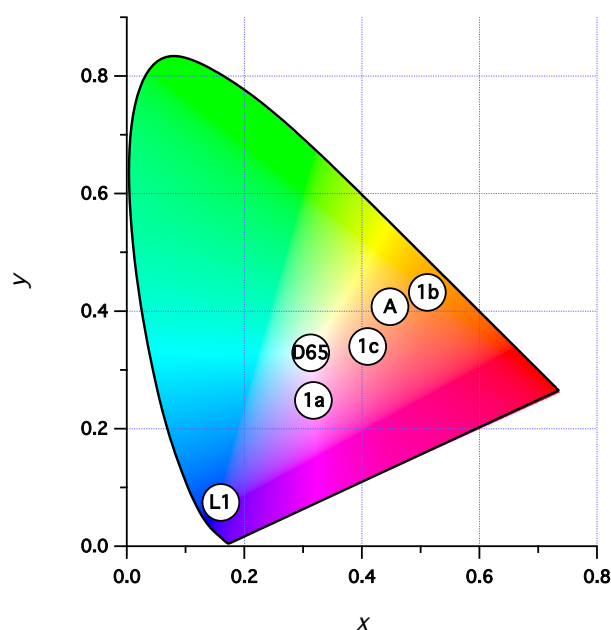


Figure 4.14: CIE 1931 spectral chromaticity coordinates of ligand **L¹** and complexes **1a-c** in deoxygenated CH₂Cl₂ solution at room temperature. The standard illuminants A (tungsten lamp) and D65 (noon daylight) are reported as sake of comparison.

Singlet oxygen sensitization:

In air-equilibrated solutions, ligand **L¹** and complexes **1a-c** do not show any phosphorescence emissions. This implies that the occurrence of a triplet-triplet energy transfer from our molecules to molecular oxygen, which results in the formation of singlet oxygen excited species ¹O₂. The process can be schematized as:



in which, P is the photosensitizer (our ligands and complexes), ¹P* and ³P* represent the lowest singlet and triplet excited states of the sensitizer and ISC is the intersystem crossing process.

Singlet oxygen can release a typical luminescence centered at 1280 nm. The sensitization quantum yields of singlet oxygen (Φ_Δ) can be calculated by comparing the emission intensity of this typical luminescence with that of a reference molecule. In Figure 4.15 the emission spectra of ¹O₂ in air-equilibrated CH₂Cl₂ solutions for ligands

L¹, **L**² and their related alkyne gold complexes **1a-c** and **2a-c** are reported, where fullerene (C₆₀) as the reference with $\Phi_{\Delta} = 0.99$. The values of the singlet oxygen sensitization efficiencies of all the compounds were gathered in Table 4.5. The sensitization quantum yields of ligand **L**¹ and **L**² are 46.2% and 30.1%. For all the alkyne gold (I) complexes, this number is around 90%, except **2b** with 77%.

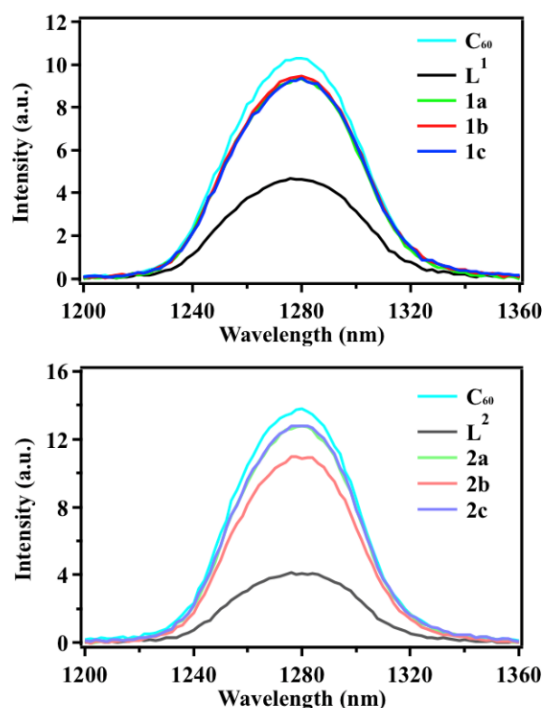


Figure 4.15: Emission spectra of ¹O₂ in air-equilibrated CH₂Cl₂ solutions for ligands **L**¹, **L**² and their related alkyne gold complexes **1a-c** and **2a-c**. Fullerene (C₆₀) as the reference, and the emission spectra area has been rescaled to the relevant quantum yield of sensitization. Excitation wavelengths are 350 nm and 375 nm for **L**¹ and **L**² series compounds, respectively.

Table 4.5: Singlet oxygen sensitization efficiencies.

	Φ_{Δ} (%)		Φ_{Δ} (%)
L ¹	46.2	L ²	30.1
1a	88.4	2a	90.3
1b	92.1	2b	77.0
1c	90.7	2c	91.8

Transient absorption properties:

In order to investigate the excited state properties for ligand **L**² and complexes **2a-c**, which do not display phosphorescence emission, the transient absorption measurements were carried out using the third harmonic of a Nd-YAG pulsed laser (355 nm) as excitation source. In Figure 4.16 the transient absorption spectra of the ligand **L**² and related gold complexes **2a-c** in deoxygenated CH₂Cl₂ solutions are reported.

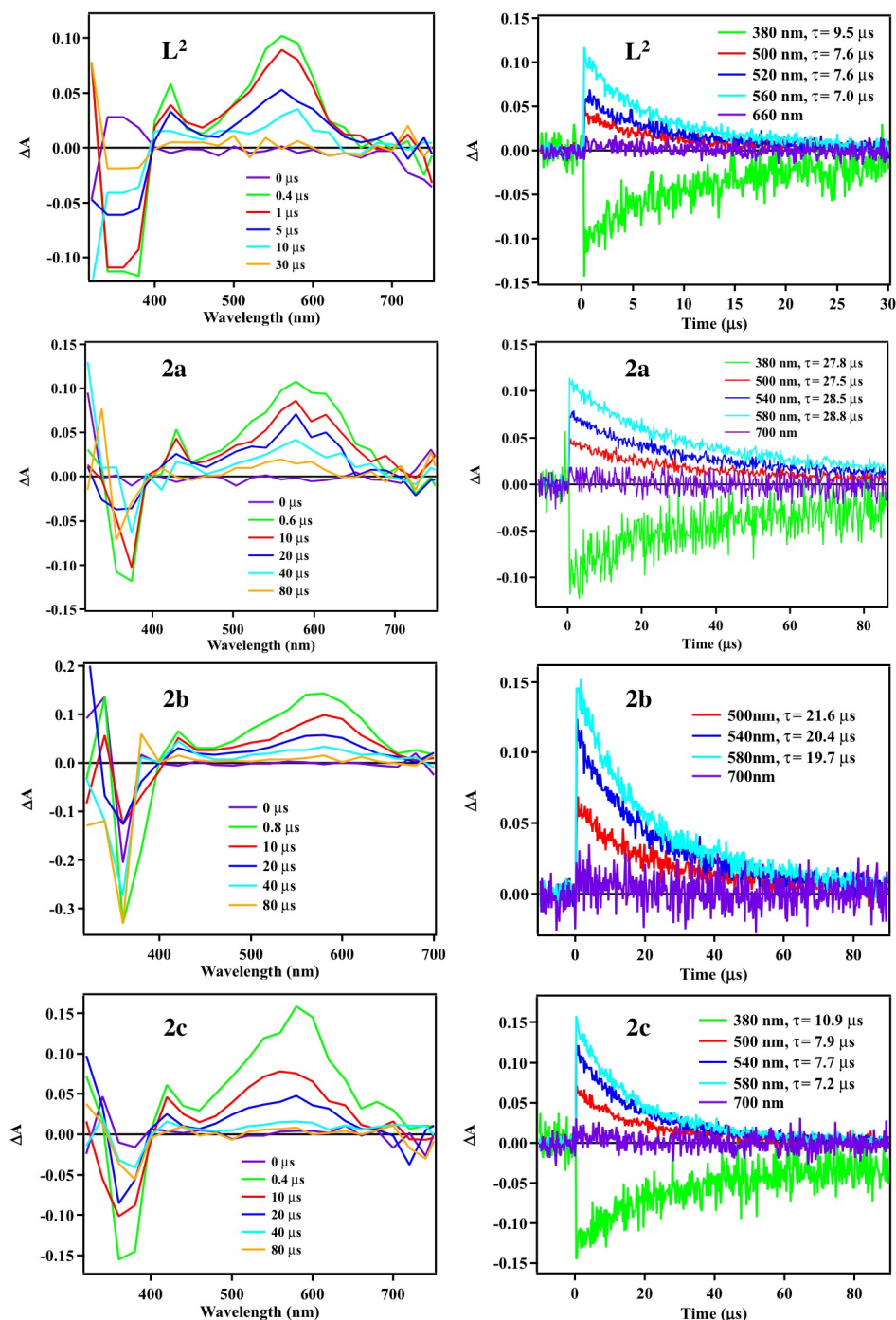


Figure 4.16: Transient absorption spectra (left) of the ligand L^2 and related alkynyl gold complexes **2a-c** in deoxygenated CH_2Cl_2 solutions collected at the different times on the time decays. In the right, some pivotal time decays and their corresponding calculated lifetimes were selected to report.

For all the compounds, the negative peak below 400 nm indicates the ground state bleaching (GSB), which corresponds to the main ground state absorption band. In fact, the depletion of the ground state by the absorption of laser excitation will result in a negative absorption difference of the sample before and after the laser excitation. A broad positive peak appears at 450-700 nm is attributed to the excited state absorption

(ESA), which means that the excited molecules can jump from the first to higher electronic excited states. The calculated lifetimes for each compound at different wavelengths are almost the same, and some typical decays and corresponding lifetimes are shown in Figure 4.16. The lifetime of ligand L^2 at ESA peak (560 nm) is 7.0 μ s, and 28.8, 19.7 and 7.2 μ s for complexes **2a**, **2b** and **2c** at 580 nm, respectively.

4.3.4 Photophysics of the solid samples

Photophysical properties of the eight compounds were also checked at 298 K in the solid state. Almost no emission was observed for the solid ligands L^1 , L^2 and complexes **1a-c**. The fluorescence of solid complexes **2a-c** are quite strong, their emission spectra were collected in Figure 4.17, and the relevant key emission parameters were reported in Table 4.6. The emission quantum yields of complexes **2a-c** in the solid state are 1.7%, 7.1% and 1.2%, respectively. The solid state lifetimes of **2a-c** are 3.6 ns, 4.2 ns and 4.0 ns, which are longer than in solutions. These are consistent with the fluorescence nature of the emission.

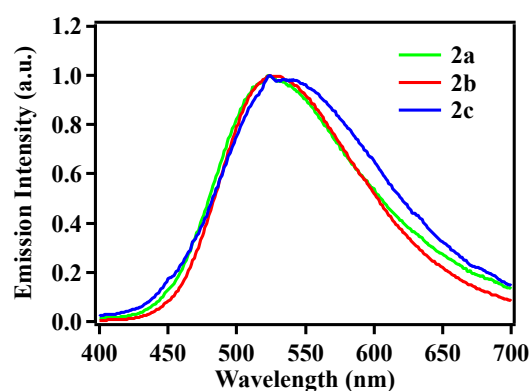


Figure 4.17: Normalized emission spectra of the complexes **2a-c** collected from the solid powder film at 298 K. Excitation wavelength is 360 nm for **2a**, **2b** and **2c**.

Table 4.6: Main emission parameters of the powder samples.

	λ_{fluo} , nm	Φ_{fluo} , %	τ_{fluo} , ns
2a	523	1.7	3.6
2b	524	7.1	4.2
2c	524	1.2	4.0

4.3.5 Photophysics in PMMA matrix

Further photophysical investigations for the two ligands and their corresponding gold (I) complexes were carried out in the PMMA matrix.^[145-147] In Figure 4.18 the pictures of the eight PMMA films with concentration of 0.5% w/w under daylight and UV light are shown. Due to the poor solubility in PMMA matrix, compound L^2 forms a turbid film with microcrystals inside. Except L^2 , other films are fully transparent

under sunlight. The transmittance, reflectance and the calculated absorptance spectra of all the films were gathered in Figure 4.19. The photothermal stability of these films was also checked by transmission spectra; the results show that all the samples are stable in PMMA matrix within 5 days (Figure 4.19).

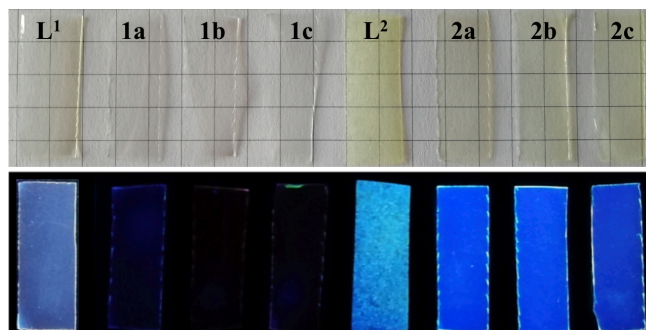


Figure 4.18: Pictures of the eight compounds in PMMA films (0.5% w/w) at room temperature under daylight (top) and UV light (bottom).

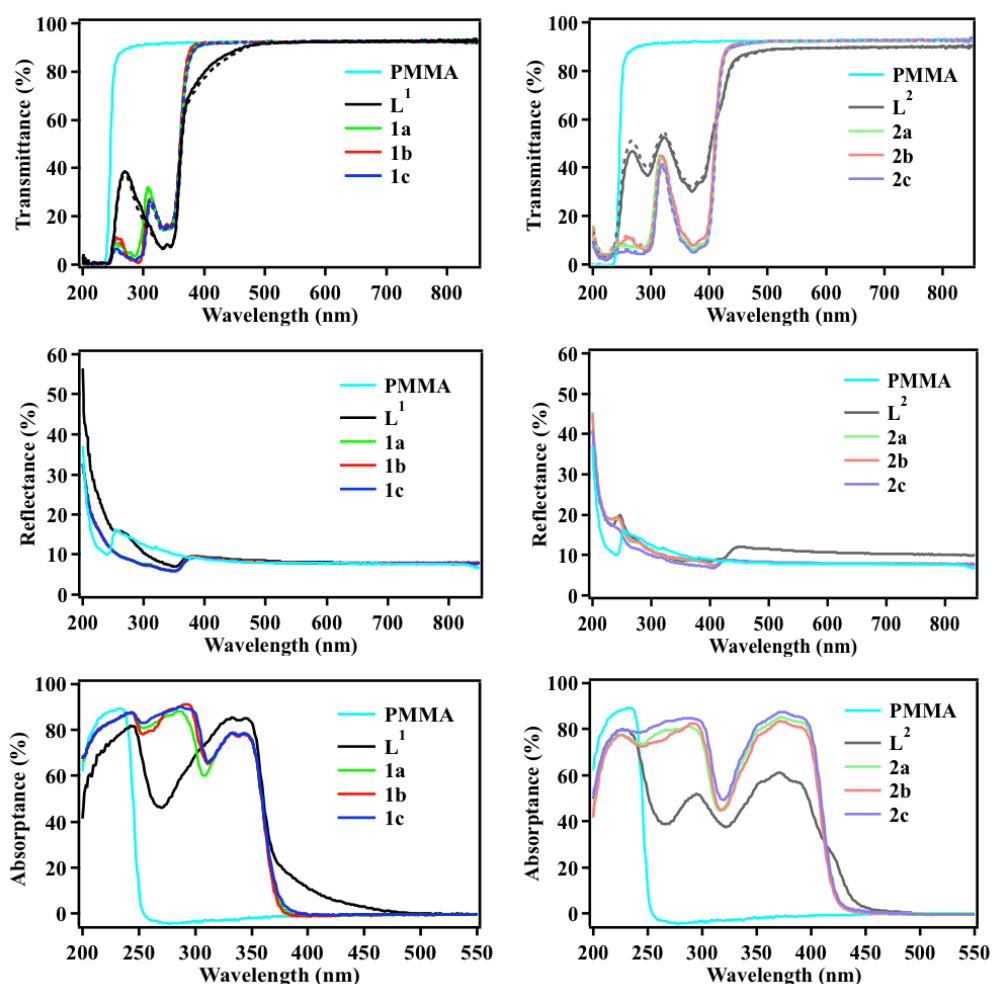


Figure 4.19: Transmittance (top), reflectance (middle) and the calculated absorptance (bottom) spectra of the eight compounds in PMMA film with concentration of 0.5% w/w. Cyan line indicates the pure PMMA film. The transmittance spectra (dotted lines) were collected in five days after in order to check the stability of the PMMA samples.

In Figure 4.20 and Table 4.7 are reported the normalized absorbance, emission spectra and the relevant photophysical parameters of the eight PMMA films. Because of the oxygen was isolated by PMMA matrix, ligand L^1 exhibits a double emission including both fluorescence and phosphorescence. Complexes **1a-c** show a weak fluorescence, but exhibits a strong phosphorescence emission, with emission lifetimes in the milliseconds range. The phosphorescence spectra of ligand L^1 and complexes **1a-c** were also collected through time gated detection, and the results are shown in Figure 4.21. For ligand L^2 and complexes **2a-c**, a strong blue fluorescence was observed in PMMA matrix (Figure 4.20).

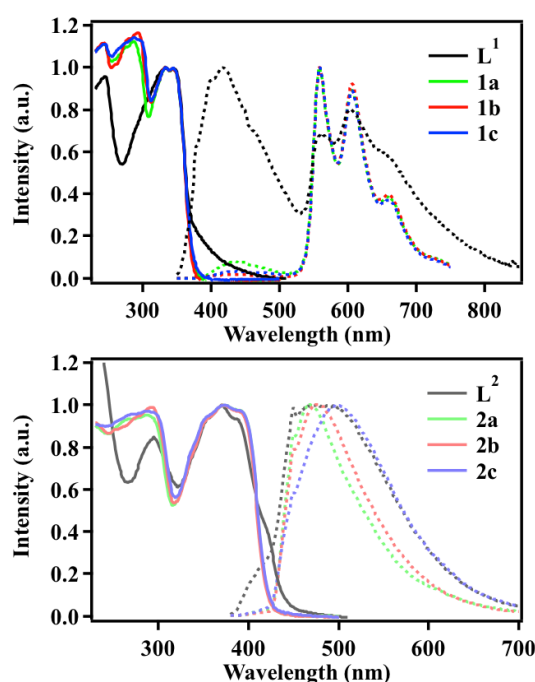


Figure 4.20: Normalized absorbance (solid lines) and emission (dotted lines) spectra of the eight compounds in PMMA matrix at room temperature. Excitation wavelength is 330 nm for L^1 , **1a**, **1b**, **1c**, and 360 nm for L^2 , **2a**, **2b**, **2c**.

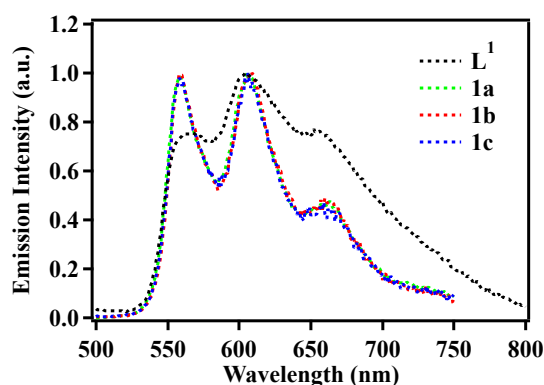


Figure 4.21: Normalized phosphorescence emission spectra (excited at 330 nm) of the ligand L^1 and complexes **1a-c** in PMMA matrix at room temperature. The spectra were collected by time gated detection.

Table 4.7: Photophysical data in PMMA matrix at 298 K.

	λ_{abs} , nm	λ_{fluor} , nm (λ_{phos} , nm)	Φ_{fluor} , % (Φ_{phos} , %)	τ_{fluor} , ns (τ_{phos} , $\mu\text{s/ms}$)
L¹	332, 344	417 (560, 604, 652)	0.1 (0.4)	4.0 ($\tau_1 = 23.3 \mu\text{s}$ $\tau_2 = 157.3 \mu\text{s}$)
1a	285, 332, 343	438 (558, 606, 660)	0.5 (0.3)	5.2 (1.4 ms)
1b	291, 332, 343	443 (558, 606, 658)	0.4 (0.3)	4.9 (1.5 ms)
1c	286, 332, 343	437 (559, 606, 657)	0.5 (0.4)	5.4 (1.4 ms)
L²	294, 370, 389	482	4.3	1.5
2a	268, 372	466	8.3	2.3
2b	290, 371	477	9.4	2.3
2c	271, 373	496	6.0	2.2

4.3.6 Theoretical calculation results

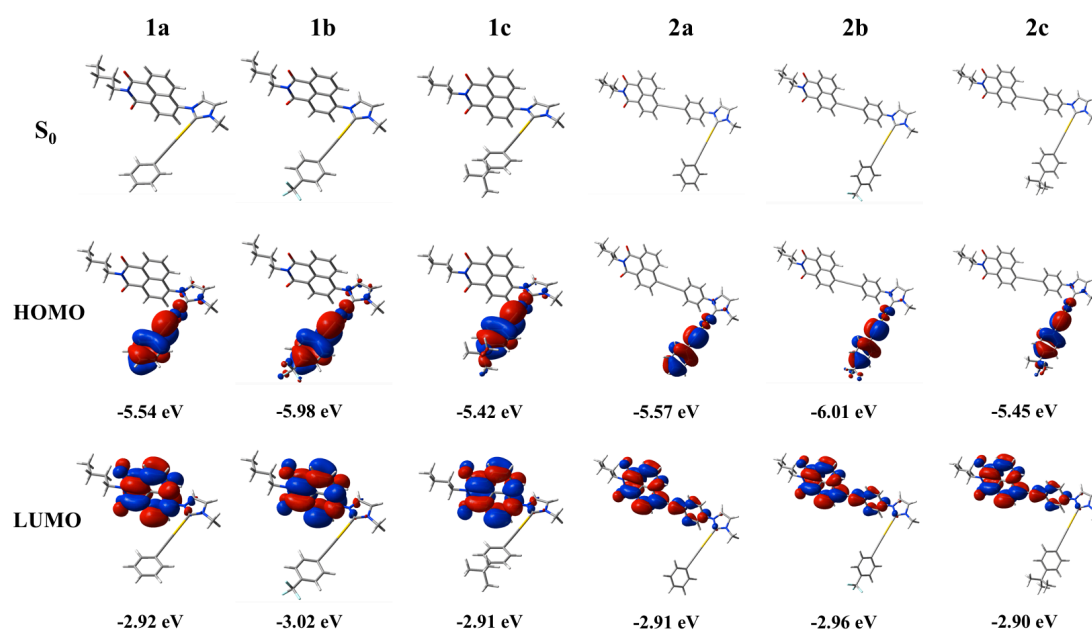


Figure 4.22: Optimized ground state (S_0) molecular geometries and the calculated HOMO and LUMO surfaces of the six alkynyl gold(I) complexes (**1a-c** and **2a-c**) at the M06/6-31+G(d) and SDD level of theory (surface isovalue = $0.02 e^{1/2} \text{ bohr}^{-3/2}$).

Theoretical calculations were performed by using the density functional theory (DFT) to investigate the molecular structure and energy of the two groups of alkynyl gold complexes. Figure 4.22 shows the optimized ground state (S_0) geometries, the isodensity plots of the highest occupied molecular orbital (HOMO) and lowest unoccupied molecular orbital (LUMO) of the six gold complexes. Complexes **1a-c** in S_0 state, the phenylacetylene fragment keeps on the same plane with the gold center and NHC

fragment, and the NI chromophore keeps a certain angle ($\sim 81^\circ$) with the NHC unit. For complexes **2a-c**, the NI fragment and the adjacent phenylacetylene unit are on the same plane, the angle between the plane and NHC unit are $\sim 45^\circ$. The calculated angle between NI plane and NHC unit are very close to the XRD analysis result (76.4° for **1a**, 32.0° for **2a** and 36.9° for **2b**). At odd with the complexes **1a-c**, the phenylacetylene fragment (connected to gold center) of the complexes **2a-c** in S_0 state are not on the same plane with the NHC unit. For all the six complexes, the HOMO only focus on the gold center and the connected phenylacetylene group, while the LUMO is mainly distributed on the NI fragment (in complexes **2a-c**, the neighboring phenylacetylene fragment also included). The calculated HOMO-LUMO energy gap for complexes **1a**, **1b**, **1c** and **2a**, **2b**, **2c** are 2.62 eV, 2.96 eV, 2.51 eV and 2.66 eV, 3.05 eV, 2.55 eV, respectively.

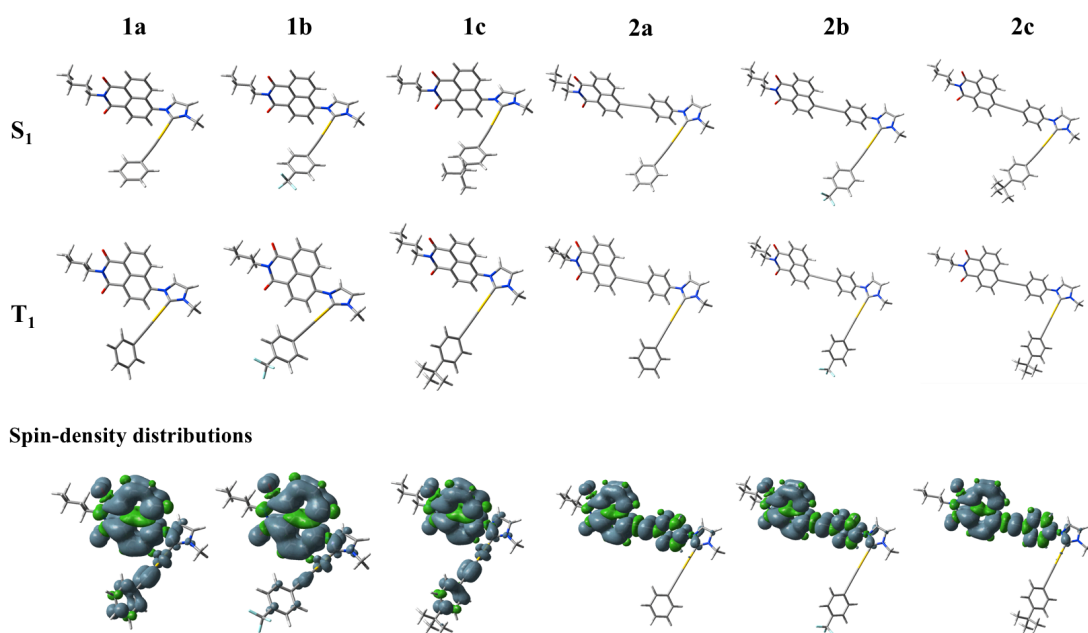


Figure 4.23: Optimized singlet excited states (S_1) and the triplet excited states (T_1) molecular geometries of the six alkyne gold(I) complexes at the M06/6-31+G(d) and SDD level of theory (UM06 for the T_1 optimization). Spin-density distributions were calculated from the fully relaxed lowest triplet state (T_1) at the same level of theory with T_1 optimization (surface isovalue = $0.0004 \text{ e bohr}^{-3}$).

In Figure 4.23, the geometries of the optimized singlet excited states (S_1) and the triplet excited states (T_1) of the six complexes were reported. The S_1 state geometries of the complexes **1a-c** are similar with the S_0 state, but the phenylacetylene fragments of the complexes **2a-c** is rotated to the same plane of the gold center and NHC fragment. In T_1 excited state, the phenylacetylene fragments of all the six complexes keep an angle with the NHC fragment. The spin-unrestricted DFT calculations were carried out by fully optimizing the lowest triplet state (T_1) of the six complexes, and the spin-density distribution are shown in Figure 4.23. It is clear that

the phenylacetylene fragments and the connected gold center of the complexes **2a-c** do not bear any spin-density distribution, but for complexes **1a-c**, the spin-density is distributed almost throughout the molecules. The phenylacetylene fragment and the connected gold center do not contribute to the triplet excited states of the complexes **2a-c**, this is the reason why we did not find the phosphorescence for them.

4.4 Conclusion

A novel series of alkynyl gold (I) *N*-heterocyclic carbene complexes containing a naphthalimide chromophore were designed, synthesized and fully characterized by ^1H and ^{13}C -NMR spectroscopy, FTIR, elemental and single crystal XRD analysis. Photophysical properties of these complexes were investigated in solution, solid state and PMMA matrix. Ligand **L²** and complexes **2a-c** exhibit the strong blue fluorescence, and the PLQY of the ligand **L²** in methanol can reach 74.7%. Ligand **L¹** and complexes **1a-c** show a noticeable double emission from the singlet (fluorescence) and triplet (phosphorescence) excited state in the deoxygenated solution and PMMA matrix at room temperature, while at 77 K only the phosphorescence feature is observed with a long phosphorescence lifetime at the millisecond level. Singlet oxygen sensitization experiments indicate that all the complexes are very sensitive to oxygen, with almost unit sensitization quantum yield. On the other hand, the presence of oxygen completely quenches the phosphorescence, as observed in the experiments. Theoretical calculations were also performed to investigate the molecular structure and energy of the two groups of complexes. The calculated molecular structures are very close to the XRD analysis results, and the calculated spin-density distributions indicates the difference on triplet excited states of the two series of complexes.

Chapter 5

Photophysical properties of molecular motors based on star-shaped ruthenium complexes containing a tripodal ligand

5.1 Introduction

A molecular machine is a system that can undergo mechanical movement on the nanometric scale, upon a suitable external stimulus.^[148-149] Artificial molecular machines^[150] are potentially relevant for applications in nanoscience,^[151] biomedicine^[152] and material science.^[153] According to the movement mechanisms in spatial dimension, they are classified as linear^[154] (e.g. muscle fibers) or rotary^[155-156] (e.g. ATP synthase). Due to the specific movement, rotary machines are sometimes also called molecular motors.^[157-158] As tiny movable entities, molecular machines can be stimulated, i.e. moved, by chemical, electrical and optical inputs. There is no doubt that electrons and photons are the best driving elements to trigger movements in molecular machines. The latter are particularly clean, effective, easy to operate and non-invasive.^[159-160] Therefore, it is essential to determine the photophysical properties to fully rationalize the behavior of molecular motors under illumination.

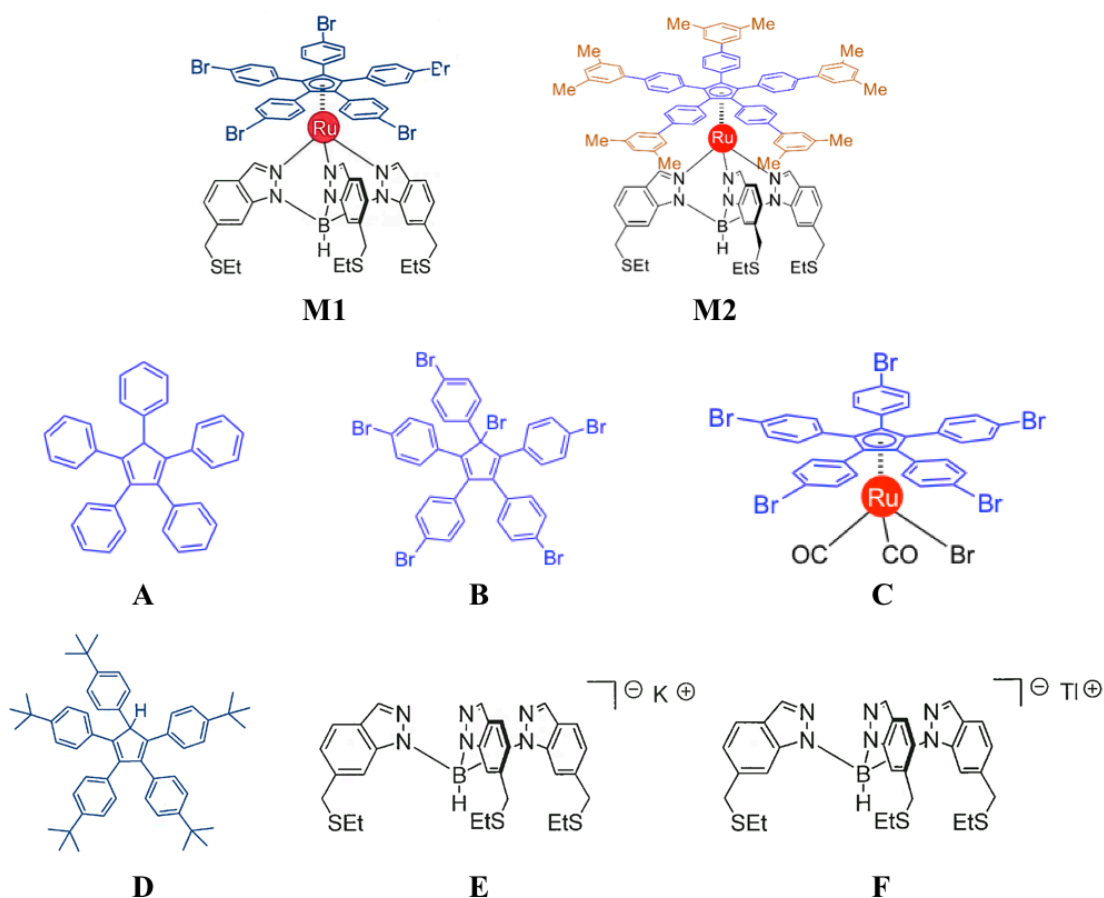


Figure 5.1: Structures of two systems that may undergo molecular rotary movements (**M1** and **M2**), along with their related ligands/moieties **A-F**.

Gear-shaped molecular motors^[161] have attracted a lot of attention from synthetic and physical chemists.^[162] In France, Prof. Gwenael Rapenne and coworkers designed, synthesized and studied a series of star-shaped molecular motors based on ruthenium complexes equipped with a scorpionate hydrotris(indazolyl)borate base and a penta(aryl)cyclopentadienyl top moiety which can rotate.^[163-164] In the frame of a collaboration with Rapenne's group, we have investigated two of such star-shaped systems^[165] and their corresponding ligands/moieties. In this work, we studied the stability and photophysical properties of these systems which can operate as prototype molecular rotary motors when attached onto a surface, along with those of their related ligands/moieties in tetrahydrofuran (THF) solution both at 298 and 77 K. In Figure 5.1 are shown the molecular structures of these compounds; even if some of the intermediate compounds or ligands are not stable, the key target systems (**M1** and **M2**) show good stability in THF solution. The photophysical properties of **M1** and **M2** can help to clarify if they may be suitable to design light-triggered molecular machines.

5.2 Experimental section

Photophysical measurements

In order to perform the spectroscopic studies on the two molecular motors and their related ligands/moieties, spectrofluorimetric grade tetrahydrofuran (THF) (Merck Uvasol®) was used without further treatments. The absorption spectra of all of the compounds were recorded by a Perkin-Elmer Lambda 950 spectrophotometer. Photoluminescence experiments in solution were performed in fluorimetric Suprasil quartz gas-tight cuvettes (1 cm), purging oxygen for 20 minutes by bubbling argon. An Edinburgh Instruments FLS920 spectrometer equipped with a Peltier-cooled Hamamatsu R928P photomultiplier tube (185-900 nm) and an Edinburgh 450 W xenon arc lamp (excitation light source) was used to record the emission spectra, which were corrected by a calibration curve supplied by the instrument manufacturer. Photoluminescence quantum yields (Φ_{PL}) in solution were obtained from the corrected emission spectra by using an air-equilibrated water solution of quinine sulfate in 1 N H₂SO₄ as reference ($\Phi_{\text{PL}} = 0.546$).^[166] The excited state lifetimes (τ) were collected by a time-correlated single photon counting (TCSPC) spectrometer equipped with an HORIBA Jobin Yvon IBH FluoroHub, and a TBX-05C Picosecond Photon Detection Module (300-850 nm) as detector. Two pulsed LED excitation light sources were used, i.e., NanoLEDs ($\lambda_{\text{exc}} = 368$ nm for **M1**, **M2** and **A-D**; $\lambda_{\text{exc}} = 283$ nm for **E** and **F**) for lifetimes in the nanosecond range and SpectraLEDs ($\lambda_{\text{exc}} = 370$ nm, FWHM = 11 nm) in the microsecond range. The profiles of the luminescence decays were analyzed by the DAS6 Decay Analysis Software, and the quality of the fit was assessed with the χ^2 value (close to unity) and with the residuals randomly distributed along the time axis.

Low temperature (77 K) luminescence spectra were measured with a 2 mm inner diameter quartz tubes (sample solutions inside) into a special quartz cold finger Dewar flask filled with liquid nitrogen. Experimental uncertainties are estimated to be $\pm 8\%$ for τ determinations, $\pm 20\%$ for Φ_{PL} , and ± 2 nm and ± 5 nm for absorption and emission peaks, respectively.

5.3 Results and Discussion

5.3.1 Photothermal stability in THF

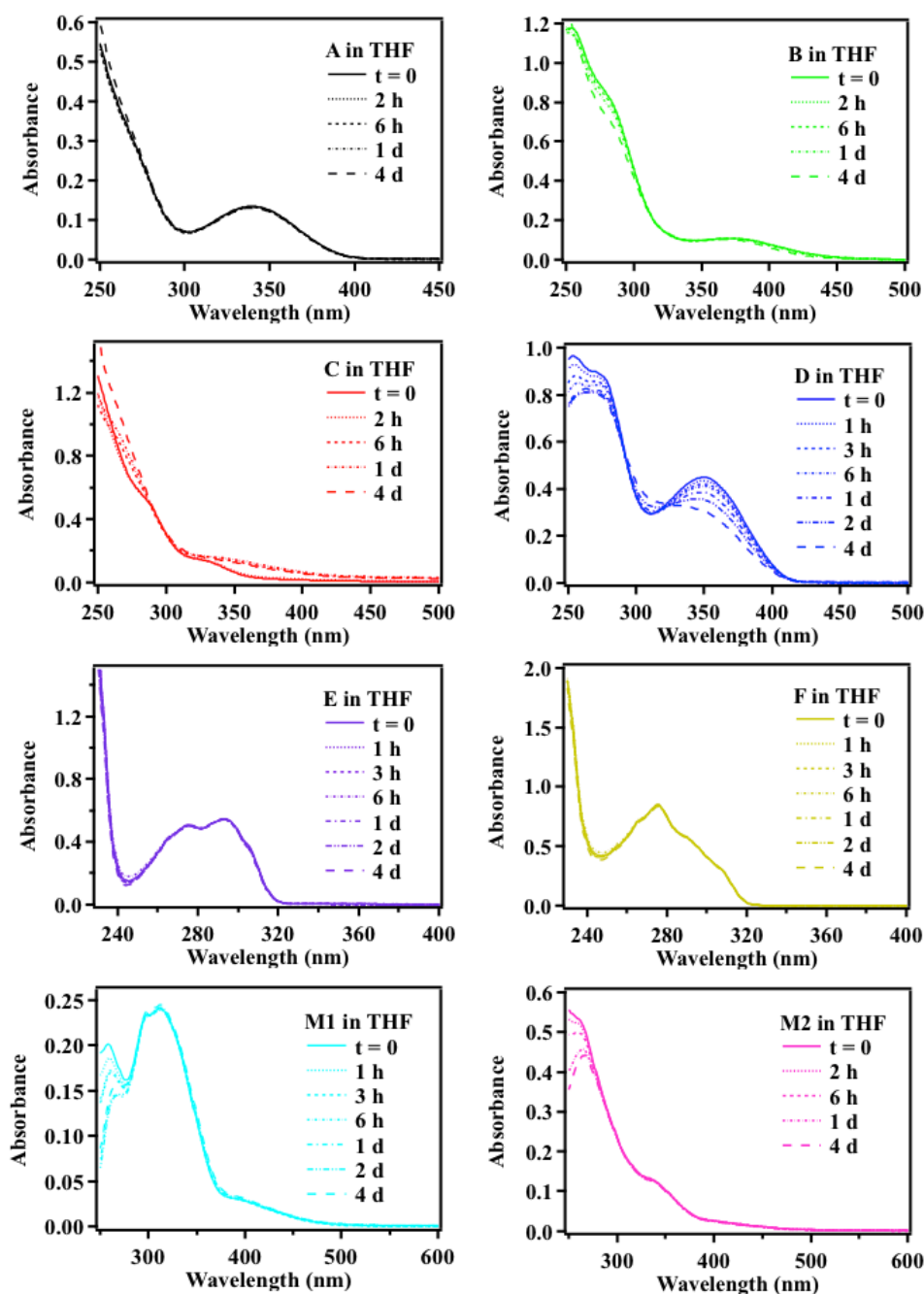


Figure 5.2: Absorption spectra under daylight of **M1** and **M2** and their related ligands/moieties **A-F** at different times after preparation; THF, 298 K.

The photothermal stability properties of all of the compounds were checked through UV-VIS absorption spectroscopy in THF solutions. The time-dependent absorption spectra (Figure 5.2) show that the potential molecular motors **M1** and **M2** and the compounds **A**, **B**, **E** and **F** are stable at room temperature for at least four days. On the contrary, **C** and **D** are not stable in THF (Figure 5.2).

5.3.2 Absorption in THF

In Figure 5.3 are reported the UV-VIS absorption spectra of **M1** and **M2** and of the related ligands/intermediates in THF solution. The key absorption peaks (λ_{\max}) and the corresponding molar absorption coefficient (ϵ_{\max}) are gathered in Table 5.1. Compared with **C** and **E/F**, complex **M1** exhibits a new absorption feature between 380 and 470 nm, possibly due to a charge transfer band involving the Ru center and the hydrotris(indazolyl)borate ligand. **M2** exhibits a strong absorption in the UV region ($\epsilon = 129900 \text{ M}^{-1}\text{cm}^{-1}$ at 267 nm), along with some new absorption features in the visible region (390–480 nm), which indicate the formation of the Ru complex. The absorption spectra of **E** and **F** are similar, but the molar absorption coefficient of **E** is slightly smaller than that of **F** probably because of the lower purity of **E** (90%). DFT calculations on these compounds are in progress and the nature of their excited states will be addressed by future studies.

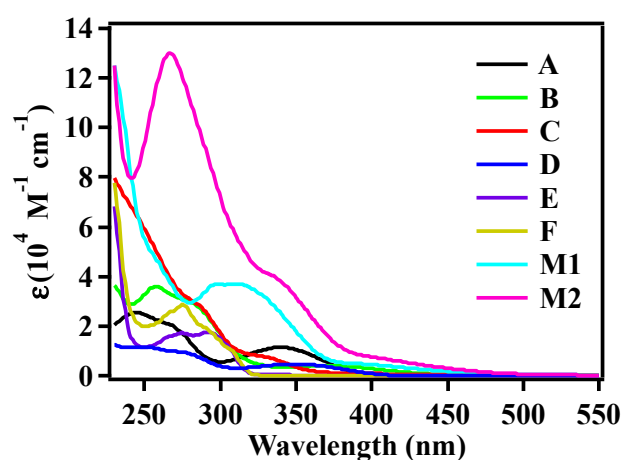


Figure 5.3: Absorption spectra of **M1** and **M2** and their related ligands/moieties **A-F** in THF solutions at 298 K.

Table 5.1: Main absorption parameters in THF solution at 298 K.			
	λ_{\max} , nm (ϵ_{\max} , $\times 10^4 \text{ M}^{-1}\text{cm}^{-1}$)		λ_{\max} , nm (ϵ_{\max} , $\times 10^4 \text{ M}^{-1}\text{cm}^{-1}$)
A	245 (2.54), 339 (1.14)	E	275 (1.72), 292 (1.75)
B	275 (3.59), 371 (0.39)	F	275 (2.87)
C	283 (2.95), 338 (0.62)	M1	311 (3.71)
D	349 (0.47)	M2	267 (12.99)

5.3.3 Emission in THF

Since the stability of **C** and **D** is limited in THF, all of the photophysical properties were measured within 3 hours using freshly prepared solutions. In Figure 5.4 are collected the normalized absorption and emission spectra of **M2** and of the related ligands/moieties **A-F** in air-equilibrated and deoxygenated THF solutions both at 298 K and 77 K. The related emission parameters are gathered in Table 5.2.

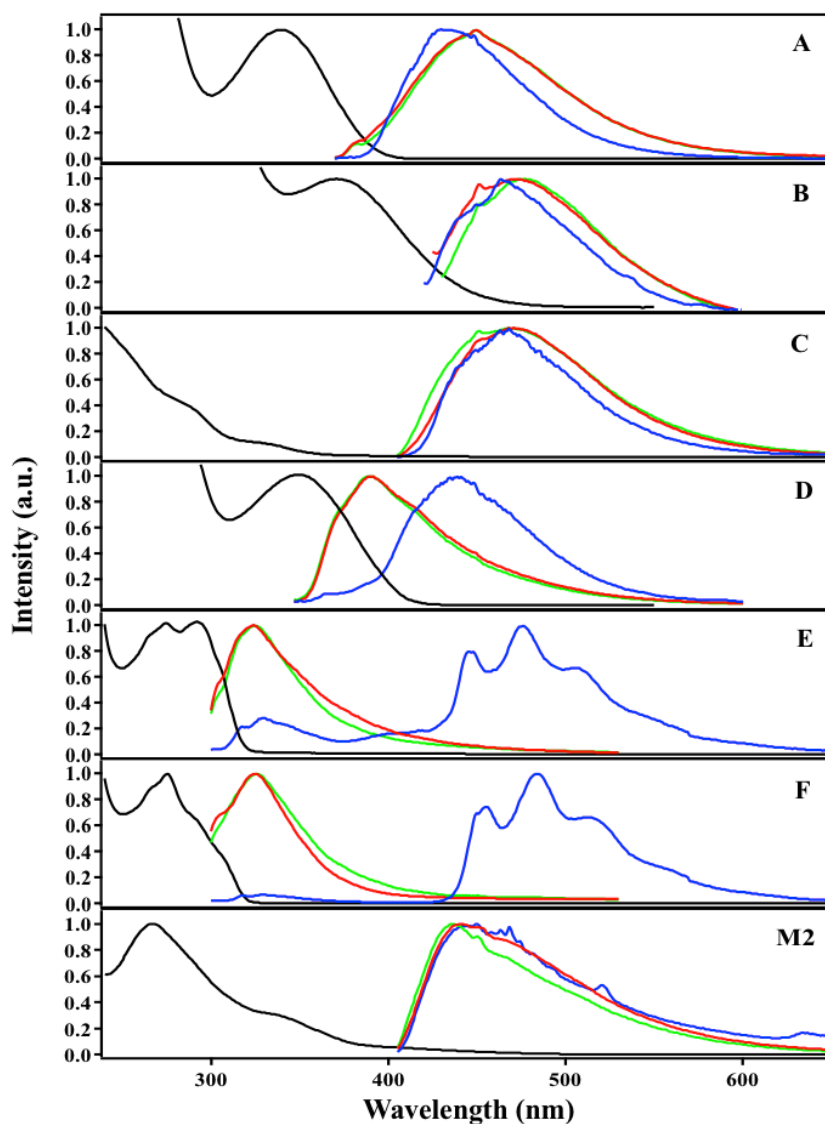


Figure 5.4: Normalized absorption spectra (black line) and emission spectra of **M2** and of the related ligands/moieties **A-F** in air-equilibrated (green) and deoxygenated (red) THF both at 298 K and 77 K (blue). The excitation wavelengths are 340 nm for **A**, 370 nm for **B**, 360 nm for **C** and **M2**, 310 nm for **D**, 275 nm for **E** and **F**.

Compound **A** exhibits a weak fluorescence ($\Phi_{\text{PL}} = 0.75\%$) peaked at 450 nm in air-equilibrated and deoxygenated THF solution at 298 K. At low temperature (77 K), the emission of **A** is slightly enhanced and the emission peak moves to 430 nm. Compared to **A**, due to the influence of Br residues,^[167-168] both the absorption and

emission spectra of **B** are red-shifted; in air-equilibrated THF at 298 K, λ_{abs} : 245 nm \rightarrow 257 nm, λ_{emi} : 450 nm \rightarrow 477 nm. Compound **C** shows emission spectra similar to **B**, with a peak at 468 nm in THF both at 298 K and 77 K. However, the emission quantum yield of **C** ($\Phi_{\text{PL}} = 2.7\%$) is significantly higher than that of **B** ($\Phi_{\text{PL}} = 0.3\%$). **D** has a structure similar to **B**, with bromine atoms replaced by tert-butyl and hydrogen residues. The fluorescence of **D** appears at shorter wavelength with respect to **B**, with a peak at about 390 nm in THF at 298 K. At 77 K, the emission peak of **D** is shifted to 441 nm. Compound **E** and **F** show a weak emission in the UV region both in air-equilibrated and deoxygenated THF at 298 K, accompanied by a relatively strong phosphorescence at 77 K. The phosphorescence spectra of **E** and **F** have been collected at 77 K by using the pulsed excitation light source (Figure 5.5).

Table 5.2: Main emission parameters in THF.

	298 K ^[a]			77 K ^[b]	
	λ_{fluo} , nm	Φ_{fluo} , %	τ_{fluo} , ns	λ_{fluo} , nm (λ_{phos} , nm)	τ_{fluo} , ns (τ_{phos} , μs)
A	450	0.75	1.9, 1.9*	430	3.1
B	477	0.30	/	464	3.2
C	468	2.67	/	468	3.5
D	389	2.82	$\tau_1=1.0$ $\tau_2=3.5$ $\tau_1=1.1$ $\tau_2=5.2^*$	441	3.0
E	325	2.44	3.0, 4.0*	329 (446, 476, 506)	3.0 (1.4)
F	325	0.69	3.4, 5.0*	330 (455, 483, 514)	3.3 (1.2)
M2	437	0.27	$\tau_1=1.1$ $\tau_2=3.2$ $\tau_1=1.1$ $\tau_2=3.6^*$	442	$\tau_1=1.8$ $\tau_2=6.2$

[a] In THF solution at 298 K; [b] In THF glass solution at 77 K; *Lifetimes collected from deoxygenated THF solutions.

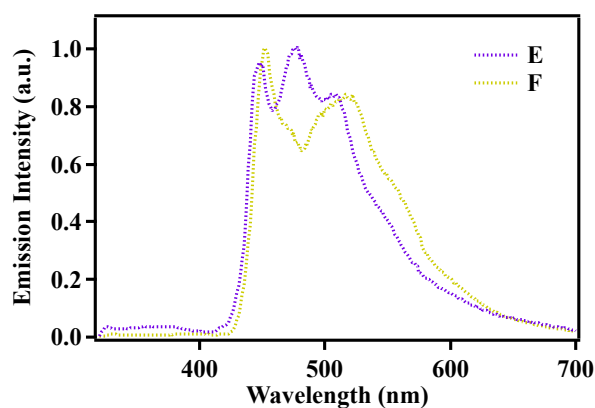


Figure 5.5: Normalized phosphorescence spectra (excited at 275 nm) of compounds **E** and **F** in rigid THF matrix at 77 K, collected *via* time gated detection.

The emission of **M1** is faint, whereas **M2** exhibits a stronger emission in the visible region peaked at about 440 nm. In order to investigate the excitation wavelength-dependent emission spectra of **M2**, emission maps were collected at different excitation wavelengths, i.e., from 300 nm to 395 nm. In Figure 5.6 are shown the emission maps of **M2** in air-equilibrated and deoxygenated THF solutions both at 298 K and 77 K. In air-equilibrated and deoxygenated THF at 298 K, excitation at shorter wavelengths results in stronger emission intensity. At 77 K, the emission spectra of **M2** excited at different wavelengths are more uniform and exhibit a peak at about 465 nm. We also recorded the emission map of **C** at different excitation wavelengths from 300 nm to 395 nm; results are shown in Figure 5.7. **C** exhibits a stronger fluorescence than **M2** with emission peak around 468 nm.

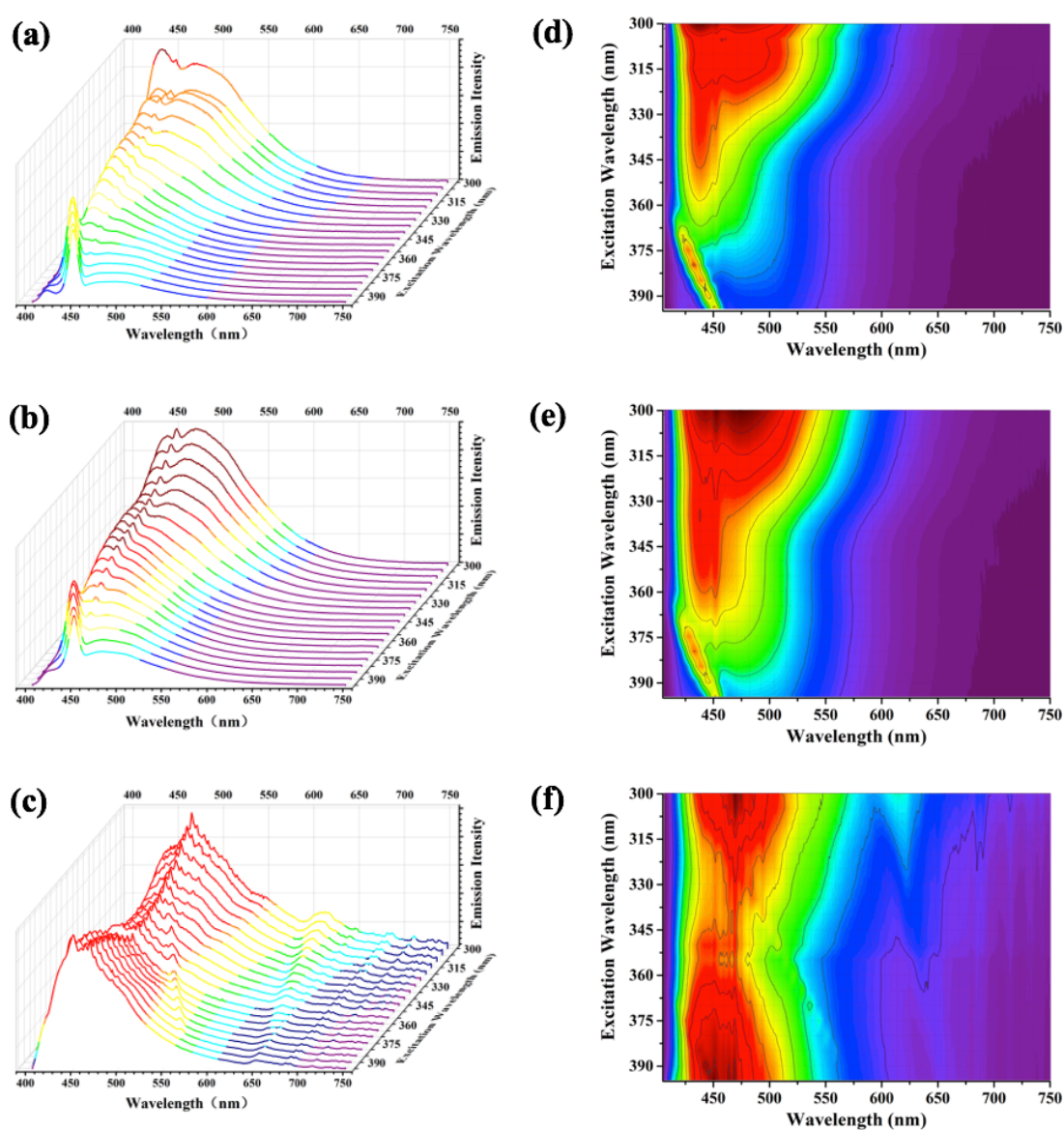


Figure 5.6: Emission maps of **M2** in air-equilibrated (a and d) and deoxygenated (b and e) THF, both at 298 K, and 77 K (c and f). Excitation from 300 nm to 395 nm, 5 nm steps.

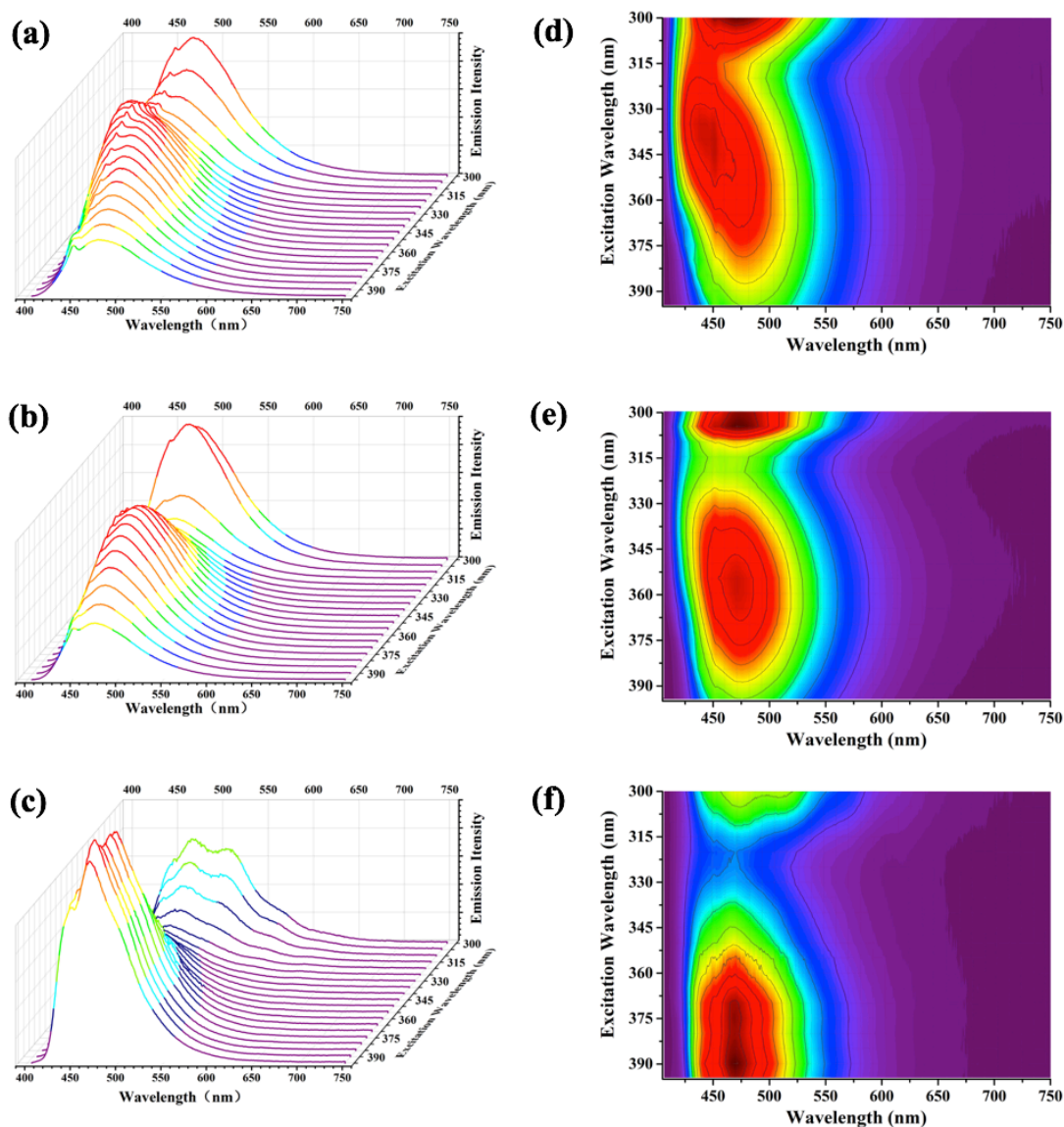


Figure 5.7: Emission maps of **C** in air-equilibrated (a and d) and deoxygenated (b and e) THF, both at 298 K, and 77 K (c and f). Excitation from 300 nm to 395 nm, 5 nm steps.

5.4 Conclusion

The photophysical properties of two star-shaped systems that may serve as molecular motors (**M1** and **M2**) and their corresponding ligands/moieties have been investigated in THF solution. The photothermal stability measurements for **M1** and **M2** indicate they are stable in THF and new absorption features at lower energy suggests the presence of charge transfer excited states. As far as luminescence is concerned, no emission was found for **M1**, whereas **M2** shows a weak fluorescence with quantum yield of 0.27% in THF. All in all, these two star-shaped systems do not exhibit strong photoluminescence. Accordingly, in order to improve the light-induced properties of these potential molecular motors equipped with a rotating moiety, fluorescent units such as bodipys and porphyrins are being introduced in the structure.

Chapter 6

Photophysical properties of *N*-heterocyclic carbenes based half-sandwich iridium/rhodium complexes containing naphthalimide chromophore

6.1 Introduction

Due to the unique structure and special properties, half-sandwich metal complexes^[169] have received a lot of attention in the fields of photochemistry,^[170] materials science,^[171] catalysis^[172-173] and medicinal chemistry.^[174-175] As a strongly coordinating ligand, *N*-heterocyclic carbene (NHC)^[176] have been widely applied in organometallics,^[107] metallo-supramolecular systems,^[108] metallo-drugs^[109] and luminescent materials.^[110] Metal centers (e.g. Ir/Rh) can be stabilized by *N*-heterocyclic carbene (NHC) ligands to form the considerably stable organometallic complexes.^[177] Iridium^[178-179] (Ir) and rhodium^[180] (Rh) are two efficient and versatile metal ions to prepare various kinds of luminescent organometallic materials with interesting photophysical and photochemical properties.^[181-182] But so far, there are only few examples on NHC based half-sandwich metal complexes.^[173,183] Therefore, in the area of photochemistry/photophysics, the investigations of NHC half-sandwich metal complexes are very important for the developments of organic light-emitting diodes (OLEDs),^[184-185] near infrared (NIR) materials^[186] and other photonic applications.^[187-188]

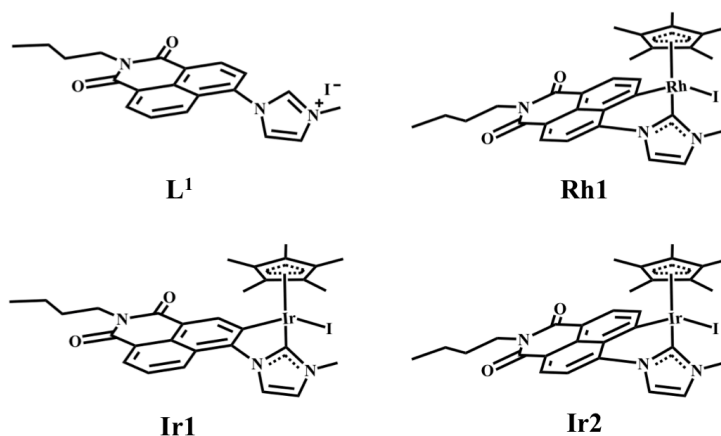


Figure 6.1: Molecular structures of the investigated NHC half-sandwich Ir/Rh complexes (**Rh1**, **Ir1** and **Ir2**) and ligand **L¹**.

In this work, we received three NHC half-sandwich Ir/Rh metal complexes (Figure 6.1) from Prof. Hani Amouri's group and investigated their photophysical properties in CH₂Cl₂ solution both at room temperature (298 K) and at 77 K (liquid nitrogen). Further investigations were carried out on these complexes by doping them into PMMA matrix to form the unique luminescent films. These compounds were

synthesized according to the procedure described in the literature.^[127-128,177] In the process of synthesis, Hani Amouri's group found that the metal center (Ir) can be connected with the naphthalimide chromophore (NI) and *N*-heterocyclic carbene (NHC) fragment in two different ways.^[177] According to the different connection styles, the three complexes can be described as two types. In complex **Ir1** only one aromatic ring of NI was coordinated with the metal center (Ir) and NHC fragment to form the five-membered structure, but for **Rh1** and **Ir2**, two fused arenes participate in the coordination, which generate the six-membered ring structure. For what the photophysical behavior is concerned, the tiny differences in structure may result in great differences in properties and applications. Herein, the photophysical investigations showed that these complexes may be potential candidates for organic optoelectronic and phosphorescent materials.

6.2 Experimental section

6.2.1 Photophysical measurements

For the spectroscopic investigations of the ligand **L¹** and the related Rh/Ir complexes **Rh1**, **Ir1** and **Ir2**, a spectrofluorimetric grade dichloromethane (CH₂Cl₂) (Merck Uvasol[®]) was used to dissolve the solid samples. The absorption spectra of the liquid sample were collected using a Perkin-Elmer Lambda 950 spectrophotometer. Photoluminescence investigations on solutions were carried using fluorimetric Suprasil quartz gas-tight cuvettes (1 cm). Before the measurements, the dissolved oxygen was removed from the solutions by freeze-pump-thaw method for three times, and low temperature was provided by liquid nitrogen (77 K). Photoluminescence spectra were collected by an Edinburgh Instruments FLS920 spectrometer equipped with a Peltier-cooled Hamamatsu R928P photomultiplier tube (185-900 nm) and the Edinburgh 450 W xenon arc lamp was used as the excitation light source. Corrected photoluminescence spectra were obtained by using a calibration curve supplied with the instrument. Photoluminescence quantum yields (Φ_{PL}) in solution were determined from the corrected emission spectra by using an air-equilibrated water solution of quinine sulfate in 1 N H₂SO₄ as reference ($\Phi_{\text{PL}}=0.546$)^[166] for ligand **L¹**, and a Coumarin 153 ($\Phi_{\text{PL}}=0.53$)^[25] ethanol solution for complexes **Rh1**, **Ir1** and **Ir2**. The nanosecond (ns) excited state lifetimes (τ) were measured by the time-correlated single photon counting (TCSPC) technique with an HORIBA Jobin Yvon FluoroHub equipped with a pulsed NanoLED ($\lambda_{\text{exc}}=368$ nm) excitation source and a TBX-05C Picosecond Photon Detection Module (300-850 nm) as the detector. The nanosecond luminescence decay profiles were analyzed with the DAS6 Decay Analysis Software, and the quality of the fit was assessed by the χ^2 value (close to unity) and by the residuals randomly distributed along the time axis. Microsecond (μs) lifetimes were collected using the Edinburgh Instruments FLS920 spectrometer equipped with an Edinburgh μF 920H

pulse excitation light source. Low temperature luminescence investigations at 77 K were performed by inserting a 2 mm inner diameter quartz tubes (sample inside) into a custom made quartz cold finger Dewar flask filled with liquid nitrogen. Experimental uncertainties are estimated to be $\pm 8\%$ for τ determinations, $\pm 20\%$ for Φ_{PL} , and ± 2 nm and ± 5 nm for absorption and emission peaks, respectively.

6.2.2 Preparation and characterization of the PMMA films

The films of the four compounds in poly(methyl methacrylate) (PMMA) matrix were fabricated by dissolving 200 mg of PMMA powder (average MW \sim 350,000 by GPC, from Sigma-Aldrich) in 4 mL dye-CH₂Cl₂ solutions (0.25 mg/mL). After the solvent was evaporated overnight in a 5 cm glass Petri dish, the generated films were separated from the glass dish by means of sonication.^[189] The resulted PMMA film thickness was measured as 70 ± 8 μm . In order to obtain the transmission and reflection spectra for the PMMA films, a Perkin-Elmer Lambda 950 spectrophotometer was used and equipped with a 100 mm diffuse reflectance and transmittance integrating sphere accessory (including PMT/PbS detectors). The corresponding absorption factors (absorbance) of the PMMA films were calculated as:

$$A\% = 100 - T\% - R\% \quad (6.1)$$

where A%, T% and R% represent the absorption factor, transmittance and reflectance, respectively. The diffuse reflection mode was used to measure the photoluminescence spectra and excited state lifetimes of the PMMA samples by using the solid sample stage. Absolute photoluminescence quantum yields of the PMMA samples were obtained from the corrected emission spectra by using a barium sulfate-coated integrating sphere (diameter of 3 in.)^[25] and a pure PMMA film was used as the reference.

6.2.3 Computational details

Density functional theory (DFT) calculations^[33] were carried out for all molecules by using the Gaussian 16 program package^[67] (B.01 revision) in combination with the M06 hybrid meta exchange-correlation functional.^[68-69] The Pople 6-31+G(d) basis set was adopted for C, H, N and O atoms,^[136] and the more suitable LANL2DZ pseudopotential basis set was selected for Ir and Rh atoms to replace the first 60 and 28 inner-core electrons, respectively.^[190] Solvent effects was considered by using the polarizable continuum model (PCM) in dichloromethane.^[51,191] Before performing further calculations, all the molecules were fully optimized in CH₂Cl₂ without symmetry constraints in the electronic ground states (S_0), the lowest singlet excited states (S_1) and the lowest triplet excited states (T_1). In order to verify that the stationary point found by the geometry optimization corresponds to a minimum on the potential energy surface, the frequency calculation was always used for all optimization process

to check for imaginary frequencies. Time-dependent density functional theory calculations (TD-DFT) were used to compute the Franck-Condon excitations (simulate the absorption spectra) and to optimize the S_1 excited state.^[75-76] Geometry optimizations and frequency calculations of the S_0 and S_1 excited state were carried out at the spin-restricted M06 level of theory with a spin multiplicity of 1. The spin-unrestricted level of theory was adopted for the optimization of the lowest triplet excited state (T_1) with a spin multiplicity of 3. All the pictures of molecular structures, orbitals and spin-density surfaces were created by GaussView 6.^[77]

6.3 Results and discussion

6.3.1 Photothermal stability in solutions

Before further photophysical investigations, the photothermal stability of all the compounds was assessed in CH_2Cl_2 solutions by UV/Vis absorption spectroscopy. In Figure 6.2 the time-dependent UV/Vis absorption spectra of the ligand **L¹** and the related Rh/Ir complexes **Rh1**, **Ir1** and **Ir2** in CH_2Cl_2 solutions are reported. The results indicate that all the compounds are stable in air-equilibrated CH_2Cl_2 solutions at 298 K under daylight within 4 days.

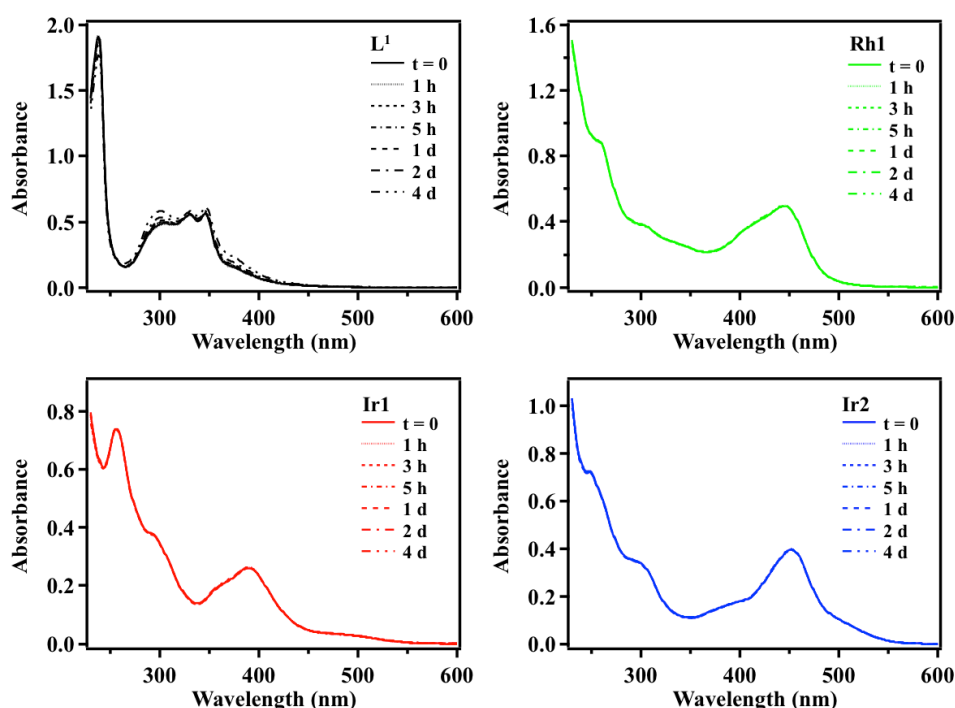


Figure 6.2: Absorption spectra of ligand **L¹** and complexes **Rh1**, **Ir1** and **Ir2** in CH_2Cl_2 at 298 K at different time after preparation under daylight.

6.3.2 Photophysics in solutions

Absorption in solution:

UV/Vis absorption spectra of the compounds **L¹**, **Rh1**, **Ir1** and **Ir2** in CH_2Cl_2

solutions are collected in Figure 6.3, and the related absorption parameters are gathered in Table 6.1. The ligand **L¹** displays a strong absorption band in the UV region (270-360 nm) with two peaks at 330 nm and 345 nm. A weak absorption band was observed in the region of 360-450 nm which is possibly due to the aggregation of **L¹** in CH₂Cl₂, as reported in the literature.^[127,192] Compared with the ligand **L¹**, Rh and Ir based complexes **Rh1** and **Ir2** are similar in structure and generate a new and analogous absorption band at longer wavelengths (350-550 nm) with absorption peak at 445 nm and 452 nm, respectively. As an isomer of **Ir2**, complex **Ir1** exhibits a different absorption spectrum located in the shorter wavelength region with a peak at 389 nm, because of the smaller conjugate structure of Ir with NI and NHC fragments. As often is the case for the cyclometalated iridium complexes the assignment of the nature of the absorption bands is not an easy task. In order to assess the nature of the excited states of these complexes, further TD-DFT calculations are carrying out and the results are still under investigation.

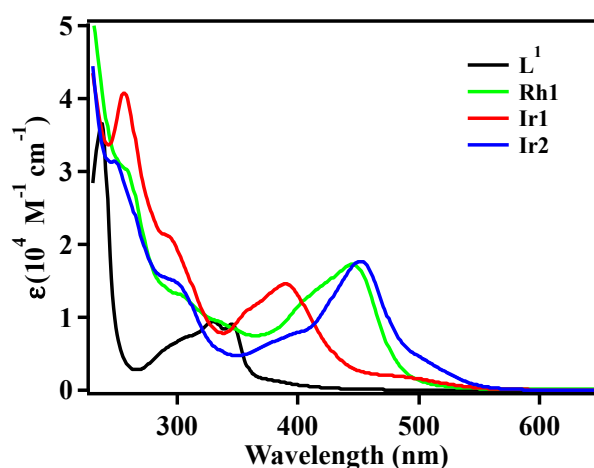


Figure 6.3: Absorption spectra of ligand **L¹** and complexes **Rh1**, **Ir1** and **Ir2** in CH₂Cl₂ solutions at 298 K.

Table 6.1: Main absorption parameters in CH₂Cl₂ solution at 298 K.

	λ_{max} , nm (ϵ_{max} , M ⁻¹ cm ⁻¹)
L¹	238 (36,602), 330 (9,447), 345 (9,119)
Rh1	257 (30,386), 300 (13,245), 445 (17,271)
Ir1	256 (40,826), 290 (21,296), 389 (14,592)
Ir2	248 (31,373), 291 (15,369), 452 (17,655)

Emission in solution:

In Figure 6.4 the normalized absorption and emission spectra of the compounds **L¹**, **Rh1**, **Ir1** and **Ir2** in air-equilibrated and deoxygenated CH₂Cl₂ solutions both at 298

K and 77 K are reported. The relevant photoluminescence parameters are collected in Table 6.2. The emission spectra of all compounds are not significantly affected by molecular oxygen, but their photoluminescence behavior displays a great change at the low temperature (77 K).

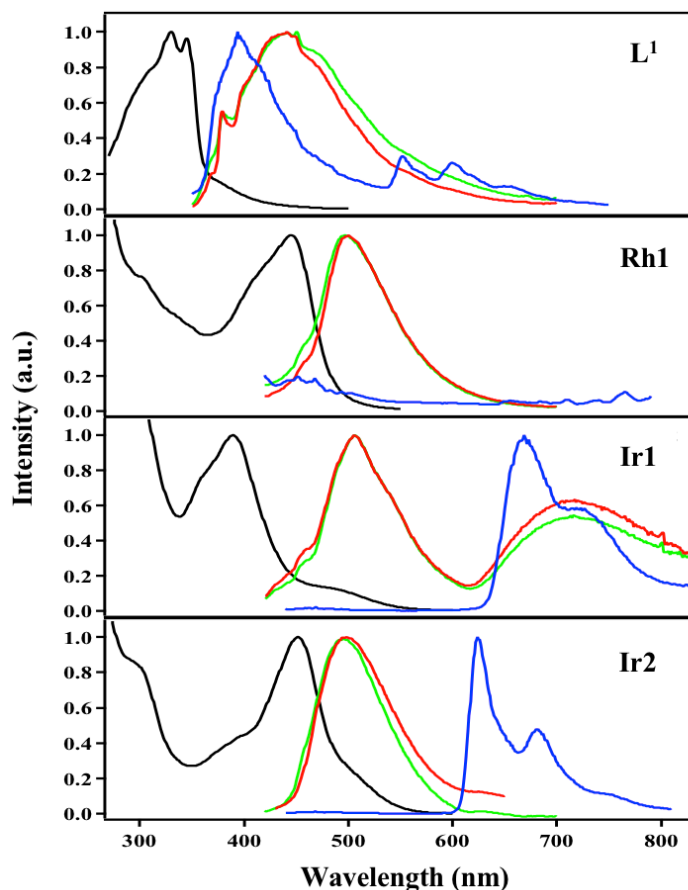


Figure 6.4: Normalized absorption spectra (black lines) and emission spectra of **L¹**, **Rh1**, **Ir1** and **Ir2** in air-equilibrated (green lines) and deoxygenated (red lines) CH_2Cl_2 solution both at 298 K and 77 K (blue lines). Excitation wavelengths is 330 nm for **L¹**, 400 nm for **Rh1**, **Ir1** and **Ir2**.

At room temperature (298 K) both in air-equilibrated and de-aerated CH_2Cl_2 solutions, ligand **L¹** shows a weak fluorescence emission with emission quantum yield $\Phi_{\text{PL}} = 0.4\%$. On the other hand, at low temperature (77 K) the ligand **L¹** not only shows the fluorescence emission, but also exhibits a weak phosphorescence with lifetime $\tau = 9.2 \mu\text{s}$. Complex **Rh1** in CH_2Cl_2 at 298 K shows the fluorescence emission with a peak around 500 nm. No photoluminescence was observed at 77 K (Figure 6.4). Ir based complex **Ir1** shows a double emission (fluorescence and phosphorescence) in CH_2Cl_2 at 298 K, whereas the isomer **Ir2** only shows a fluorescence emission at room temperature. After optimizing the test conditions, an extremely weak phosphorescence emission spectrum was extracted from the emission spectrum of **Ir2** by subtracting the high baseline (Figure 6.5).

Table 6.2: Main emission parameters in CH₂Cl₂.

	298 K			77 K ^[b]	
	λ_{fluo} , nm (λ_{phos} , nm)	Φ_{fluo} , % (Φ_{phos} , %)	τ_{fluo} , ns (τ_{phos} , μs)	λ_{fluo} , nm (λ_{phos} , nm)	τ_{fluo} , ns (τ_{phos} , μs)
L¹	441 ^[a1] 441 ^[a2]	0.4 ^[a1] 0.4 ^[a2]	6.4 ^[a1] 5.9 ^[a2]	394 (552, 599, 650)	3.6 (9.2)
Rh1	497 ^[a1] 500 ^[a2]	0.3 ^[a1] 0.3 ^[a2]	7.8 ^[a1] 8.2 ^[a2]	/	/
Ir1	506 (716) ^[a1] 505 (719) ^[a2]	0.1 (0.1) ^[a1] 0.1 (0.1) ^[a2]	7.9 (8.8) ^[a1] 8.5 (8.9) ^[a2]	(669, 723)	(14.1)
Ir2	495 (636, 691) ^[a1] 498 (635, 689) ^[a2]	0.3 ^[a1] 0.3 ^[a2]	9.0 (8.9) ^[a1] 10.1 (13.1) ^[a2]	(624, 680, 750)	(48.7)

[a1] In air-equilibrated CH₂Cl₂ solution at 298 K; [a2] In deoxygenated CH₂Cl₂ solution at 298 K; [b] In CH₂Cl₂ at 77 K.

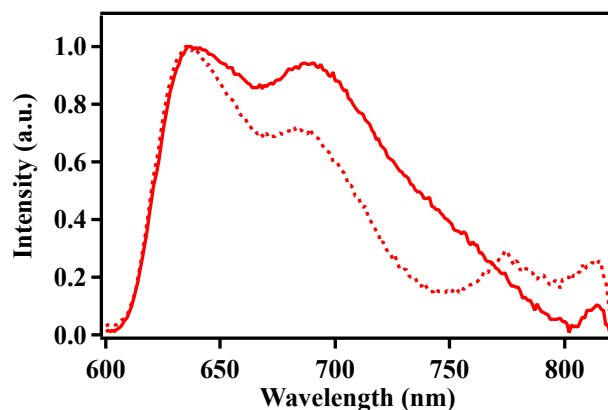


Figure 6.5: Normalized phosphorescence emission spectra (excited at 400 nm) of complex **Ir2** in air-equilibrated (solid line) and deoxygenated (dotted line) CH₂Cl₂ solution at 298 K. The spectra were treated by subtracting the high baseline.

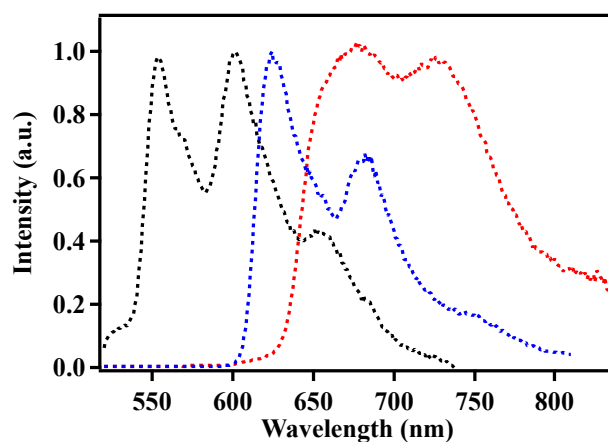


Figure 6.6: Normalized phosphorescence emission spectra of **L¹** (black line), **Ir1** (red line) and **Ir2** (blue line) in CH₂Cl₂ at 77 K. The spectra were collected by time gated detection. Excitation wavelength is 330 nm for **L¹**, 400 nm for **Ir1** and **Ir2**.

At low temperature (77 K), only the phosphorescence emission was detected for both complexes **Ir1** and **Ir2**. The phosphorescence emission of ligand **L¹**, complexes **Ir1** and **Ir2** in CH₂Cl₂ at 77 K were also recorded with time gated detection and the obtained emission spectra are collected in Figure 6.6. In Table 6.2 the phosphorescence lifetimes of the complexes **Ir1** and **Ir2** in air-equilibrated and deoxygenated CH₂Cl₂ solutions both at 298 K and 77 K are collected, and the corresponding phosphorescence lifetime decays are shown in Figure 6.7. The phosphorescence lifetime of complex **Ir1** is not significantly affected by temperature and oxygen. But for the isomer **Ir2**, the phosphorescence lifetime is obviously lengthened by low temperature. For the three Rh/Ir complexes, further DFT and TD-DFT calculations are still running to assist in the interpretation of the luminescence behaviour of **Rh1** at 77 K.

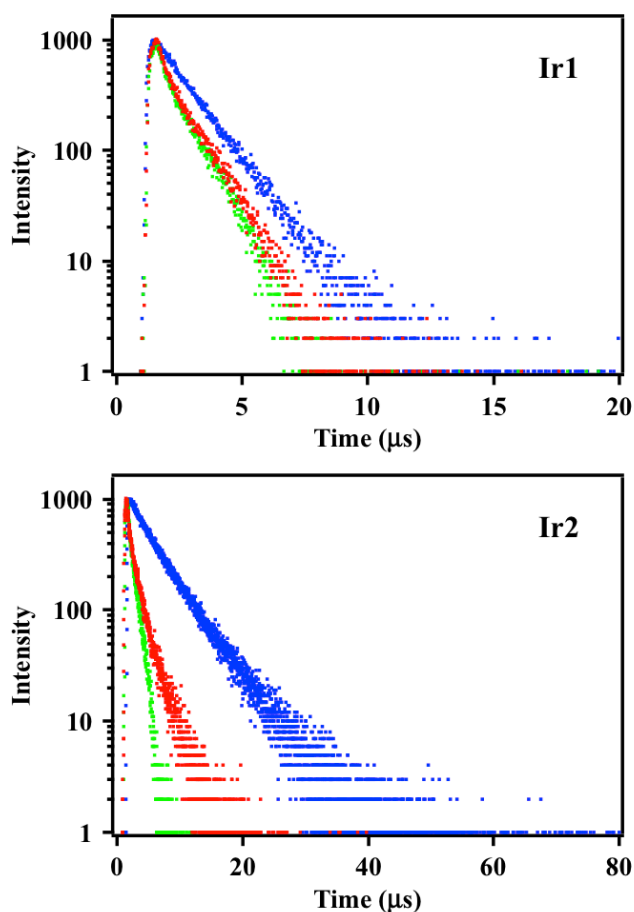


Figure 6.7: Phosphorescence lifetime decays of complexes **Ir1** and **Ir2** in air-equilibrated (green dots) and deoxygenated (red dots) CH₂Cl₂ solutions both at 298 K and 77 K (blue dots).

6.3.3 Photophysics in PMMA matrix

In PMMA matrix under daylight, the ligand **L¹** shows a colorless transparent film, complexes **Rh1**, **Ir1** and **Ir2** exhibit yellow transparent films (Figure 6.8). Compared with the complex **Ir1**, isomer **Ir2** in PMMA film gave a deeper yellow color.

Under UV light at 298 K, a blue fluorescence was observed from **L¹**-PMMA film, while Rh based complex **Rh1** shows a weak green fluorescence. Complexes **Ir1** and **Ir2** exhibit a weak red emission in PMMA films under UV light at 298 K. The emission intensity was significantly enhanced at 77 K (Figure 6.8). Before the further photophysical investigations, the photothermal stability properties of all the PMMA films was measured by transmission spectroscopy (Figure 6.9), and the result indicates that all samples are stable at room temperature.

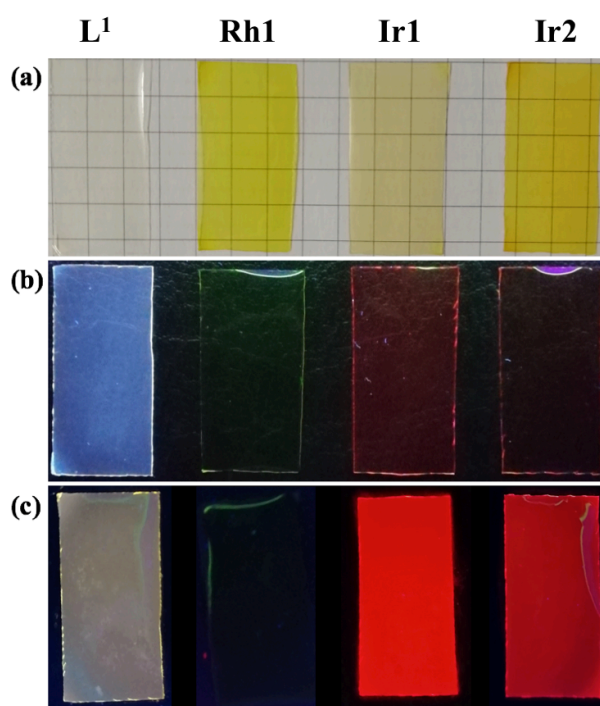


Figure 6.8: Pictures of the four compounds in PMMA films (0.5% w/w) under daylight (a, 298 K) and UV light (b, 298 K), (c, 77 K).

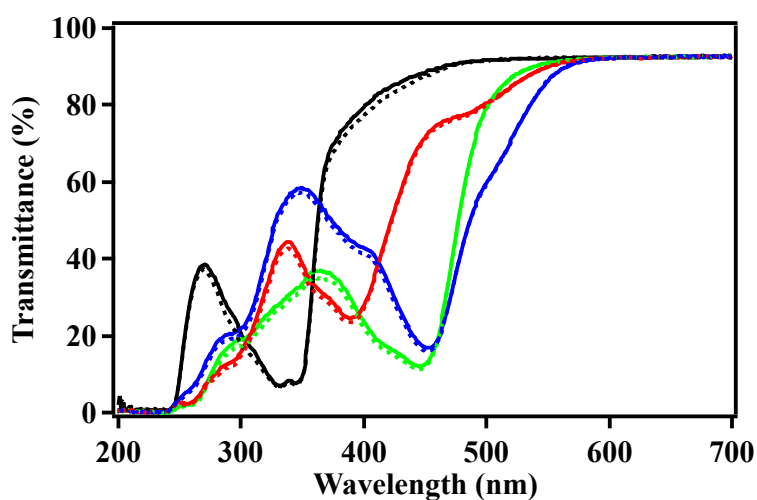


Figure 6.9: Transmittance spectra of the compounds **L¹** (black lines), **Rh1** (green lines), **Ir1** (red lines) and **Ir2** (blue lines) in PMMA film as prepared (full lines) and after 14 days (dotted lines) at the concentration of 0.5% w/w.

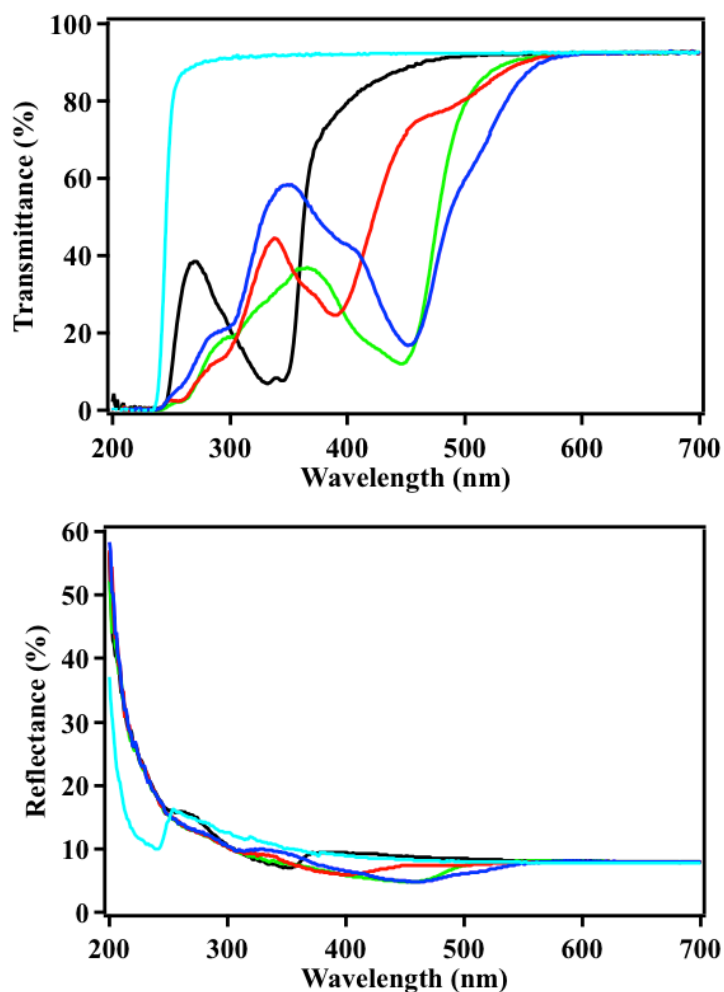


Figure 6.10: Transmittance (top) and reflectance (bottom) spectra of the compounds L^1 (black lines), $Rh1$ (green lines), $Ir1$ (red lines) and $Ir2$ (blue lines) in PMMA film with concentration of 0.5% w/w. Cyan line indicates the pure PMMA film.

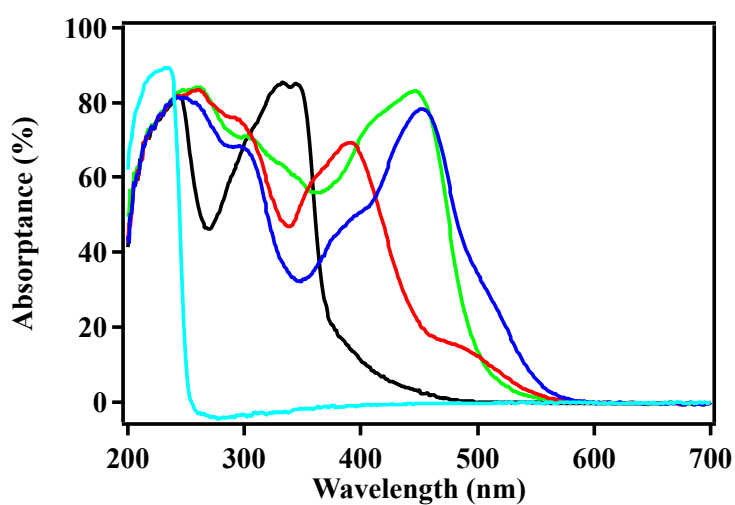


Figure 6.11: The absorbance spectra of the compounds L^1 (black line), $Rh1$ (green line), $Ir1$ (red line) and $Ir2$ (blue line) in PMMA film with concentration of 0.5% w/w. Cyan line indicates the pure PMMA film.

In Figure 6.10 the transmittance and reflectance spectra of all the PMMA samples are reported, and the corresponding calculated absorbance spectra are gathered in Figure 6.11. In PMMA films, the absorption features of all the samples are similar to those obtained in liquid solution (in CH₂Cl₂). The main absorption parameters in PMMA matrix are collected in Table 6.3.

The normalized absorbance and emission spectra of the four PMMA samples are reported in Figure 6.12. The ligand **L**¹ in PMMA matrix shows both the fluorescence and phosphorescence emission. However, the Rh based complex **Rh1** only exhibits a weak fluorescence emission peaking at 499 nm. For Ir based complexes **Ir1** and **Ir2**, both the fluorescence and phosphorescence were observed in PMMA matrix. The phosphorescence emission spectra of compounds **L**¹, **Ir1** and **Ir2** in PMMA samples were also collected through the time gated detection, and the resulted spectra are shown in Figure 6.13.

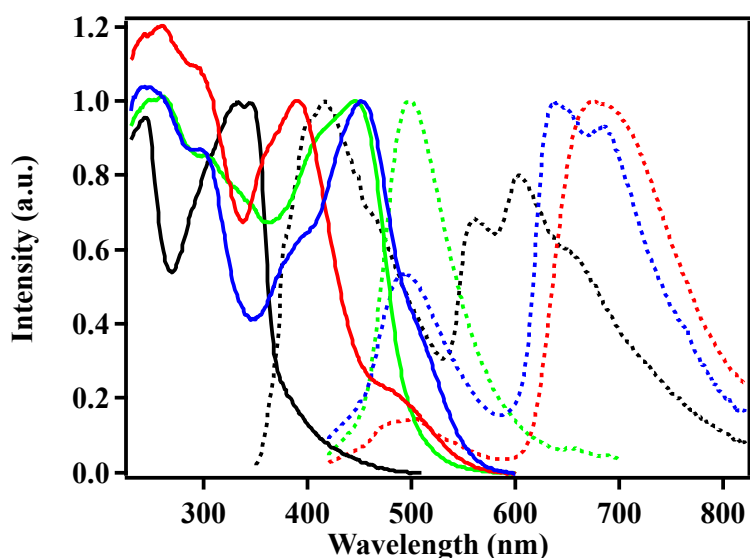


Figure 6.12: Normalized absorbance (full lines) and emission (dotted lines) spectra of compounds **L**¹ (black lines), **Rh1** (green lines), **Ir1** (red lines) and **Ir2** (blue lines) in PMMA film with concentration of 0.5% w/w at 298 K. Excitation wavelength is 330 nm for **L**¹, 400 nm for **Rh1**, **Ir1** and **Ir2**.

Table 6.3: Main photophysical parameters in PMMA matrix at 298 K.

	λ_{abs} , nm	λ_{fluo} , nm (λ_{phos} , nm)	Φ_{fluo} , % (Φ_{phos} , %)	τ_{fluo} , ns (τ_{phos} , μs)
L ¹	243, 332, 344	417 (560, 604, 652)	0.1 (0.4)	4.0 ($\tau_1 = 23.3$ $\tau_2 = 157.3$)
Rh1	244, 261, 303, 445	499	0.02	$\tau_1 = 3.2$ $\tau_2 = 38.7$
Ir1	243, 259, 296, 388	503 (675)	0.02 (1.9)	$\tau_1 = 2.6$ $\tau_2 = 16.8$ (8.1)
Ir2	244, 296, 452	494 (638, 685)	0.03 (0.2)	$\tau_1 = 2.9$ $\tau_2 = 11.9$ (9.0)

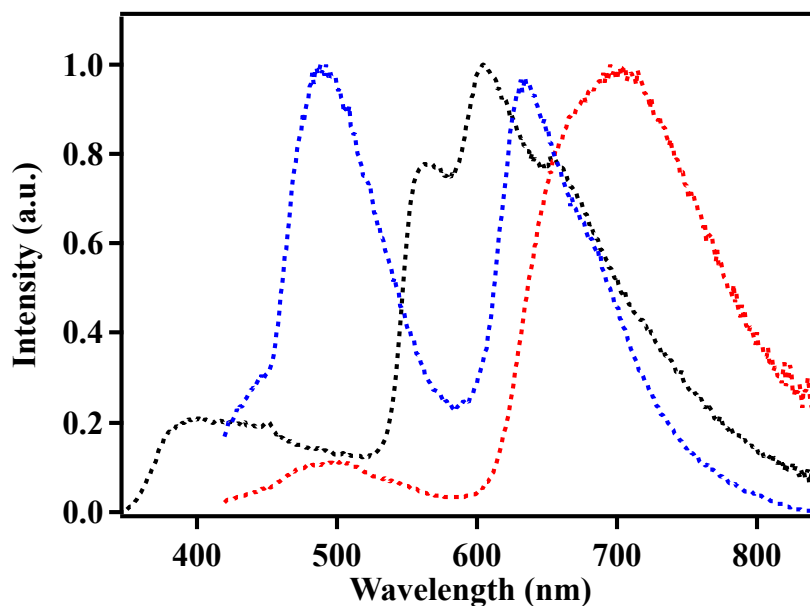


Figure 6.13: Normalized phosphorescence emission spectra of L^1 (black line), **Ir1** (red line) and **Ir2** (blue line) in PMMA matrix at 298 K. The spectra were collected by time gated detection. Excitation wavelength is 330 nm for L^1 , 400 nm for **Ir1** and **Ir2**.

In Table 6.3 the photoluminescence quantum yields and emission lifetimes of the four PMMA samples are collected, the phosphorescence lifetime decays of ligand L^1 and complexes **Ir1** and **Ir2** are shown in Figure 6.14. The phosphorescence lifetimes of **Ir1** and **Ir2** are on the order of tenth microseconds, but for the ligand L^1 a longer lifetime up to hundreds of microseconds is observed (Figure 6.14 and Table 6.3). The non-exponential decay curve of L^1 may be due to the complicated energy transitions and multiple emission behaviors.

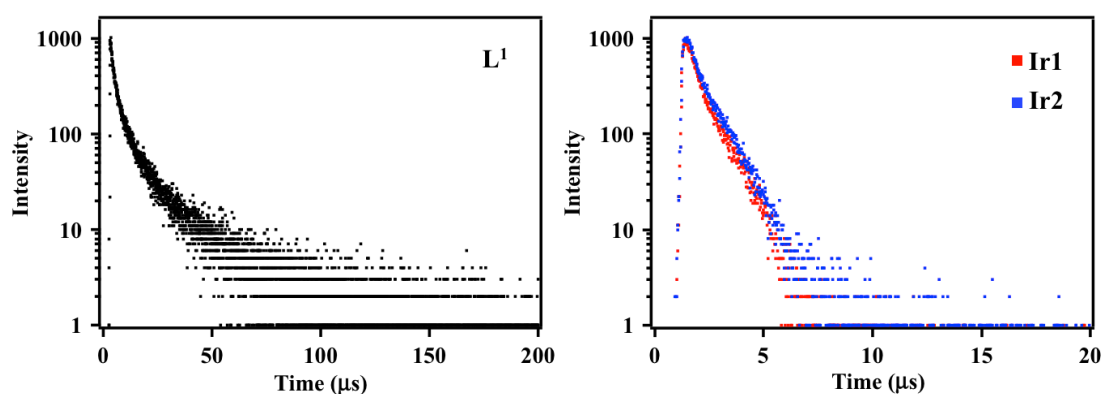


Figure 6.14: Phosphorescence lifetime decays of the compounds L^1 , **Ir1** and **Ir2** in PMMA matrix at 298 K.

6.3.4 Theoretical calculation results

Density functional theory (DFT) calculation was carried out for the complexes **Rh1**, **Ir1** and **Ir2** to investigate their molecular structure and energy distribution. In

Figure 6.15 the optimized ground state (S_0) geometries are reported, together with the isodensity plots of the highest occupied molecular orbital (HOMO) and lowest unoccupied molecular orbital (LUMO) of the three complexes. Complexes **Rh1** and **Ir2** in S_0 state show a similar structure: iodine (I), NHC and NI fragments form a tetrahedral structure with the metals (Rh/Ir) as the center, and the NI plane and NHC unit keep a small angle ($\sim 22^\circ$). At odd with the complexes **Rh1** and **Ir2**, smaller five-membered ring structure make the NI and NHC fragments of **Ir1** more close to a plane, and the dihedral angle was found as 4° for it. In the structure of **Rh1** and **Ir2**, metal center, NI and NHC fragments form a twisted six-membered ring, but for **Ir1**, the resulted five-membered ring shows a planar structure. The calculated frontier molecular orbital for the three complexes indicates that the HOMO is mainly set on the metal center, half-sandwich ring and the NHC unit, while the LUMO is mainly distributed on the NI fragment, and few orbitals are located on the metal center and NHC fragment. The calculated HOMO-LUMO energy gap for complexes **Rh1**, **Ir1** and **Ir2** are 3.32 eV, 3.17 eV and 3.37 eV, respectively. Where the HOMO-LUMO energy gap of **Ir1** is significantly lower than **Rh1** and **Ir2**.

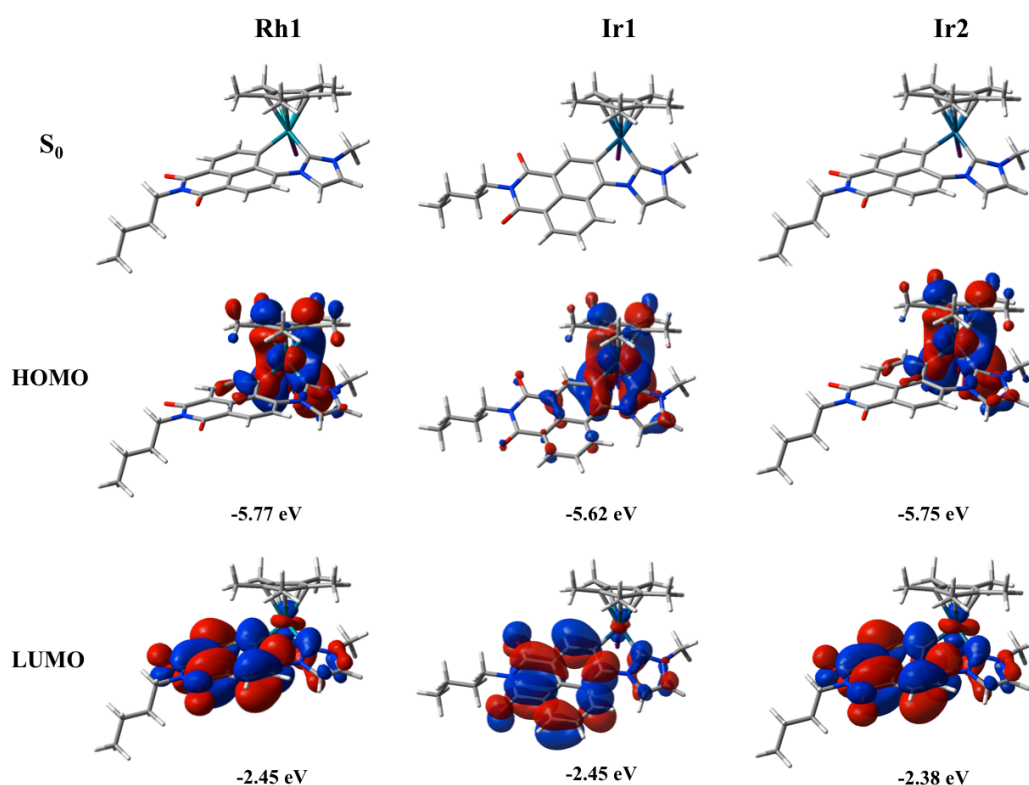


Figure 6.15: Optimized ground state (S_0) molecular geometries and the calculated HOMO and LUMO surfaces of the complexes **Rh1**, **Ir1** and **Ir2** at the M06/6-31+G(d) and LANL2DZ level of theory (surface isovalue = $0.02 e^{1/2} \text{ bohr}^{-3/2}$).

The optimized triplet excited states (T_1) geometries and the calculated spin-density distributions of the three complexes are reported in Figure 6.16. Their T_1

geometries are the same as the S_0 structure. Complexes **Rh1** and **Ir2** are similar in spin-density distributions, and mainly centered on NI chromophore and metal center, with only a minor density distribution on NHC unit. Compared with the six-membered ring complexes (**Rh1** and **Ir2**), the five-membered **Ir1** display a higher spin-density distributions on NHC fragment and Ir center (Figure 6.16).

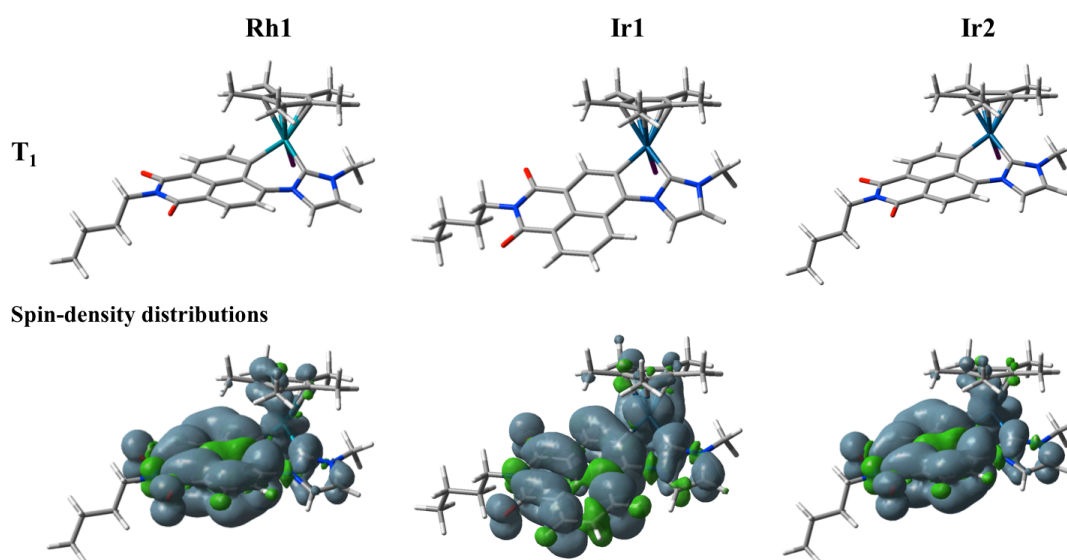


Figure 6.16: Optimized triplet excited states (T_1) molecular geometries of the complexes **Rh1**, **Ir1** and **Ir2** at the M06/6-31+G(d) and LANL2DZ level of theory (UM06 for the T_1 optimization). Spin-density distributions were calculated from the fully relaxed lowest triplet state (T_1) at the same level of theory with T_1 optimization (surface isovalue = $0.0004 \text{ e bohr}^{-3}$).

6.4 Conclusion

The photophysical properties of three *N*-heterocyclic carbenes based half-sandwich Rh/Ir complexes containing naphthalimide chromophore have been investigated in CH_2Cl_2 solution and PMMA matrix both at 298 K and 77 K. The stability test indicates that these complexes are extremely stable in CH_2Cl_2 solution and in PMMA matrix. In CH_2Cl_2 solution at 77 K, Ir based complexes exhibit a strong NIR phosphorescence with a microsecond lifetime, but the Rh based complex does not exhibit phosphorescence features. In PMMA films, Ir based complexes show the noticeable double emissions including both the fluorescence and the phosphorescence. Their phosphorescence emission is strongly enhanced at 77 K, while for Rh based complex, only the fluorescence around 500 nm was observed. At last, the density functional theory calculation results clearly indicate the difference in the structure and energy distribution for the three complexes.

Chapter 7

Conclusions and Outlook

7.1 Conclusions

In this thesis, several series of luminescent materials have been studied and investigated, along with some of their related applications. Chapter 2 presented five benzoheterodiazole dyes with donor-acceptor character embedded in PMMA and PDMS to fabricate luminescent solar concentrators. The investigated emitters exhibit large Stokes shift (up to $5,660\text{ cm}^{-1}$) and high photoluminescence quantum yield (up to 83.2%) in PMMA matrix. PMMA-based LSC allowed to achieve an optical quantum efficiency OQE as high as 47.6% at geometric gain $G = 88$, with EQE maximizing at the intermediate dye concentration of 0.5% (w/w). The OQE value can be predictably enhanced to approximately 70% by improving the quality of the PMMA film surface and, hence, the observed trapping efficiency. All in all, the performances reached by the best performing systems of the series are comparable with those reported for benchmark devices.

In chapter 3, ZnPc was selected as a suitable dye to prepare a luminescent film that simulates the chlorophyll fluorescence. Fc was screened as an effective quencher to control the emission quantum yield of ZnPc. A double-layer structure film was initially applied on plastic plates and eventually coated on large surfaces on wood, using an industrial printing technology. The proposed film formulation reflects NIR light similarly to real plants in the region 700–900 nm and emits a fluorescence signal which is well overlapped with that of chlorophyll. Accordingly, it is fully suitable to calibrate the detector of chlorophyll fluorescence that will be used in the FLEX satellite mission of the European Space Agency starting from 2023, which will monitor the health of terrestrial vegetation.

A novel series of alkynyl gold (I) *N*-heterocyclic carbene complexes containing a naphthalimide chromophore were designed, synthesized and investigated in chapter 4. Ligand **L**² and complexes **2a-c** exhibit strong blue fluorescence, with the PLQY of the ligand **L**² in methanol reaching 74.7%. Interestingly, **L**¹ and complexes **1a-c** show a noticeable double emission from the singlet (fluorescence) and triplet (phosphorescence) excited state in the deoxygenated solution and PMMA matrix at room temperature, while at 77 K only the phosphorescence feature is observed with a lifetime on the millisecond scale. According to the singlet oxygen sensitization experiments, all the complexes are sensitive to oxygen, with almost unit sensitization quantum yield. This means that the presence of oxygen completely quenches the phosphorescence. DFT calculations indicate that these molecular structures are very close to the XRD analysis results, and the calculated spin-density distributions suggest

the difference on triplet excited states of the two series of complexes.

Chapter 5 deals with the photophysical properties of two star-shaped molecular systems (**M1** and **M2**) which can behave as molecular motors when attached to surfaces and their corresponding ligands. The spectroscopic measurements indicate they are stable in THF and new absorption features at lower energy suggests the presence of charge transfer excited states. As far as luminescence is concerned, no emission was found for **M1**, whereas **M2** shows a weak fluorescence with quantum yield of 0.27% in THF. In general, these two star-shaped systems do not exhibit strong photoluminescence. Accordingly, in order to tune and improve the light-induced properties of these potential molecular motors, fluorescent moieties such as bodipys and porphyrins are being introduced in the structure.

In chapter 6, the research targets are three *N*-heterocyclic carbenes based half-sandwich Rh/Ir complexes containing naphthalimide chromophores. The stability test indicates that these complexes are extremely stable in CH₂Cl₂ solution and in PMMA matrix. In CH₂Cl₂ solution at 77 K, Ir-based complexes exhibit a strong NIR phosphorescence with a microsecond lifetime, but the Rh-based complex does not exhibit phosphorescence features. In PMMA films, Ir-based complexes show a noticeable double emission including both fluorescence and phosphorescence. Their phosphorescence is strongly enhanced at 77 K, while for the Rh based complex, only the fluorescence around 500 nm was observed. At last, DFT calculation clearly indicate the difference in the structure and energy levels for the three complexes.

7.2 Outlook

In future work, the LSC proposed here can be further implemented. For instance, in order to improve the performance, upconversion (such as triplet-triplet annihilation system) may be introduced as a strategy to exploit the near infrared region, which covers a considerable portion of the solar spectrum. Of course, other matrix materials can also be investigated for LSC, such as epoxy resins. Starting from 2023, our luminescent calibration film will possibly be implemented in the FLEX satellite mission and, eventually, some modifications and improvements may be needed. The investigated star-shaped systems do not exhibit strong photoluminescence. In the future work, fluorescent moieties such as bodipys and porphyrins will be introduced to tune and improve the light-induced properties and enhance their possibility to be used as molecular motors equipped with an easy-to-read signal output. For Au/Ir/Rh based NHC metal complexes, further DFT calculation will be carried out and some photoluminescence applications will be explored.

References

- [1] J. Théodoridès, E. Newton Harvey, a history of luminescence from the earliest times until 1900, *Rev. Hist. Sci.* **1958**, *11*, 283-284.
- [2] B. Valeur and M. N. Berberan-Santos, A brief history of fluorescence and phosphorescence before the emergence of quantum theory, *J. Chem. Educ.* **2011**, *88*, 731-738.
- [3] M. Lastusaari, T. Laamanen, M. Malkamäki, K. O. Eskola, A. Kotlov, S. Carlson, E. Welter, H. F. Brito, M. Bettinelli, H. Jungner and J. Hölsä, The Bologna Stone: history's first persistent luminescent material, *Eur. J. Mineral.* **2012**, *24*, 885-890.
- [4] H. S. Virk, History of luminescence from ancient to modern times, *Defect Diffus. Forum* **2015**, *361*, 1-13.
- [5] G. G. Stokes, On the change of refrangibility of light, *Philos. Trans. R. Soc. Lond.* **1852**, *142*, 463-562.
- [6] J. R. Lakowicz, Introduction to fluorescence, in *Principles of Fluorescence Spectroscopy*, Springer, Boston, **1999**, pp. 1-23.
- [7] E. Wiedemann, Ueber fluorescenz und phosphorescenz i. abhandlung, *Ann. Phys. Chem.* **1888**, *270*, 446-463.
- [8] J. R. Silva, W. P. Rodrigues, K. F. Ruas, J. S. Paixão, R. S. N. d. Lima, J. A. M. Filho, J. A. C. Garcia, B. Schaffer, J. C. Gonzalez and E. Campostrini, Light, photosynthetic capacity and growth of papaya (*Carica papaya* L.): a short review, *Aust. J. Crop Sci.* **2019**, *13*, 480-485.
- [9] N. R. Dhar and B. K. Mukerji, Einstein's law of photochemical equivalence, *Trans. Faraday Soc.* **1926**, *21*, 489-493.
- [10] A. Jabłoński, Über den mechanismus der photoluminescenz von farbstoffphosphoren, *Z. Phys.* **1935**, *94*, 38-46.
- [11] K. Fukui, T. Yonezawa and H. Shingu, A molecular orbital theory of reactivity in aromatic hydrocarbons, *J. Chem. Phys.* **1952**, *20*, 722-725.
- [12] C.-J. Ho, A. L. Motyka and M. R. Topp, Picosecond time-resolved S₂→S₀ fluorescence of xanthione in different fluid solvents, *Chem. Phys. Lett.* **1989**, *158*, 51-59.
- [13] A. Maciejewski and R. P. Steer, The photophysics, physical photochemistry, and related spectroscopy of thiocarbonyls, *Chem. Rev.* **1993**, *93*, 67-98.
- [14] P. Data and Y. Takeda, Recent advancements in and the future of organic emitters: TADF- and RTP-active multifunctional organic materials, *Chem.-Asian J.* **2019**, *14*, 1613-1636.
- [15] D. Dzebo, Fundamentals: light-matter interaction, in *Photon Upconversion through Triplet-Triplet Annihilation: Towards Higher Efficiency and Solid State Applications*, Chalmers University of Technology, Department of Chemistry and Chemical Engineering, **2016**, p. 13.
- [16] N. J. Turro, V. Ramamurthy, V. Ramamurthy and J. C. Scaiano, Electronic, vibrational, and spin configurations of electronically excited states, in *Principles of Molecular Photochemistry: An Introduction*, University Science Books, Sausalito, **2009**, pp. 56-57.
- [17] J. M. Charlesworth, Optical sensing of oxygen using phosphorescence quenching, *Sens. Actuators B Chem.* **1994**, *22*, 1-5.
- [18] F. Wang, D. Banerjee, Y. Liu, X. Chen and X. Liu, Upconversion nanoparticles in biological labeling, imaging, and therapy, *Analyst* **2010**, *135*, 1839-1854.
- [19] T. N. Singh-Rachford and F. N. Castellano, Photon upconversion based on sensitized triplet-triplet annihilation, *Coord. Chem. Rev.* **2010**, *254*, 2560-2573.
- [20] J. E. Moffatt, G. Tsiminis, E. Klantsataya, T. J. de Prinse, D. Ottaway and N. A. Spooner, A practical review of shorter than excitation wavelength light emission processes, *Appl. Spectrosc. Rev.* **2019**, *55*, 327-349.
- [21] H. C. Ishikawa-Ankerhold, R. Ankerhold and G. P. Drummen, Advanced fluorescence microscopy techniques - FRAP, FLIP, FLAP, FRET and FLIM, *Molecules* **2012**, *17*, 4047-4132.
- [22] J. Franck and E. G. Dymond, Elementary processes of photochemical reactions, *Trans. Faraday Soc.* **1926**, *21*, 536-542.
- [23] M. Kasha, Characterization of electronic transitions in complex molecules, *Discuss. Faraday Soc.* **1950**, *9*, 14-19.
- [24] S. Kéna-Cohen, Electronic and vibrational structure of organic crystals, in *Strong Exciton-Photon Coupling in Organic Semiconductor Microcavities*, Princeton University, Department of Electrical Engineering, **2010**, p. 23.
- [25] C. Wurth, M. Grabolle, J. Pauli, M. Spieles and U. Resch-Genger, Relative and absolute determination of fluorescence quantum yields of transparent samples, *Nat. Protoc.* **2013**, *8*, 1535-1550.

- [26] C. D. Geddes, Optical halide sensing using fluorescence quenching: theory, simulations and applications-a review, *Meas. Sci. Technol.* **2001**, *12*, R53-R88.
- [27] H. Masuhara, H. Shioyama, T. Saito, K. Hamada, S. Yasoshima and N. Mataga, Fluorescence quenching mechanism of aromatic hydrocarbons by closed-shell heavy metal ions in aqueous and organic solutions, *J. Phys. Chem.* **1984**, *88*, 5868-5873.
- [28] J. R. Lakowicz and G. Weber, Quenching of fluorescence by oxygen. A probe for structural fluctuations in macromolecules, *Biochemistry* **1973**, *12*, 4161-4170.
- [29] G. R. Seely, Quenching of pyrochlorophyll fluorescence by nitro compounds, *J. Phys. Chem.* **1969**, *73*, 125-129.
- [30] R. W. Ricci and J. M. Nesta, Inter- and intramolecular quenching of indole fluorescence by carbonyl compounds, *J. Phys. Chem.* **1976**, *80*, 974-980.
- [31] H. Sahoo, Förster resonance energy transfer - a spectroscopic nanoruler: principle and applications, *J. Photochem. Photobiol. C* **2011**, *12*, 20-30.
- [32] A. Adronov and J. M. J. Fréchet, Light-harvesting dendrimers, *Chem. Commun.* **2000**, 1701-1710.
- [33] R. G. Parr, Density functional theory of atoms and molecules, in *Horizons of Quantum Chemistry*, Springer, Dordrecht, **1980**, pp. 5-15.
- [34] E. Schrödinger, An undulatory theory of the mechanics of atoms and molecules, *Phys. Rev.* **1926**, *28*, 1049-1070.
- [35] L. H. Thomas, The calculation of atomic fields, *Mathematical Proceedings of the Cambridge Philosophical Society* **2008**, *23*, 542-548.
- [36] E. Fermi, Un metodo statistico per la determinazione di alcune priorieta dell'atome, *Rend. Accad. Naz. Lincei* **1927**, *32*, 602-607.
- [37] P. Hohenberg and W. Kohn, Inhomogeneous electron gas, *Phys. Rev.* **1964**, *136*, B864-B871.
- [38] W. Kohn and L. J. Sham, Self-consistent equations including exchange and correlation effects, *Phys. Rev.* **1965**, *140*, A1133-A1138.
- [39] A. D. Becke, A multicenter numerical integration scheme for polyatomic molecules, *J. Chem. Phys.* **1988**, *88*, 2547-2553.
- [40] A. K. Rajagopal and J. Callaway, Inhomogeneous electron gas, *Phys. Rev. B* **1973**, *7*, 1912-1919.
- [41] A. D. Becke, A new mixing of Hartree-Fock and local density - functional theories, *J. Chem. Phys.* **1993**, *98*, 1372-1377.
- [42] S. Grimme, Semiempirical hybrid density functional with perturbative second-order correlation, *J. Chem. Phys.* **2006**, *124*, 0341081-03410815.
- [43] H. Iikura, T. Tsuneda, T. Yanai and K. Hirao, A long-range correction scheme for generalized-gradient-approximation exchange functionals, *J. Chem. Phys.* **2001**, *115*, 3540-3544.
- [44] M. Elstner, P. Hobza, T. Frauenheim, S. Suhai and E. Kaxiras, Hydrogen bonding and stacking interactions of nucleic acid base pairs: a density-functional-theory based treatment, *J. Chem. Phys.* **2001**, *114*, 5149-5155.
- [45] K. Burke, J. Werschnik and E. K. Gross, Time-dependent density functional theory: past, present, and future, *J. Chem. Phys.* **2005**, *123*, 0622061-0622069.
- [46] E. Engel, Relativistic density functional theory: foundations and basic formalism, in *Relativistic Electronic Structure Theory*, Elsevier, **2002**, pp. 523-621.
- [47] T. Salagaram, R. Andrew and N. Chetty, Simplified pseudopotential problems for the classroom, *Comput. Sci. Eng.* **2015**, *17*, 46-53.
- [48] I. M. Alecu, J. Zheng, Y. Zhao and D. G. Truhlar, Computational thermochemistry: scale factor databases and scale factors for vibrational frequencies obtained from electronic model chemistries, *J. Chem. Theory Comput.* **2010**, *6*, 2872-2887.
- [49] J. C. Slater, Atomic shielding constants, *Phys. Rev.* **1930**, *36*, 57-64.
- [50] F. Jensen, Atomic orbital basis sets, *Wiley Interdiscip. Rev. Comput. Mol. Sci.* **2013**, *3*, 273-295.
- [51] J. Tomasi, B. Mennucci and R. Cammi, Quantum mechanical continuum solvation models, *Chem. Rev.* **2005**, *105*, 2999-3093.
- [52] P. Moraitis, R. E. I. Schropp and W. G. J. H. M. van Sark, Nanoparticles for luminescent solar concentrators-a review, *Opt. Mater.* **2018**, *84*, 636-645.
- [53] F. Meinardi, F. Bruni and S. Brovelli, Luminescent solar concentrators for building-integrated photovoltaics, *Nat. Rev. Mater.* **2017**, *2*, 1-9.
- [54] C. Shang, G. Wang, M. He, X. Chang, J. Fan, K. Liu, H. Peng and Y. Fang, A high performance fluorescent arylamine sensor toward lung cancer sniffing, *Sens. Actuators B Chem.* **2017**, *241*, 1316-1323.
- [55] Y. Qi, W. Xu, R. Kang, N. Ding, Y. Wang, G. He and Y. Fang, Discrimination of saturated alkanes and relevant volatile compounds via the utilization of a conceptual fluorescent sensor array based on organoboron-containing polymers, *Chem. Sci.* **2018**, *9*, 1892-1901.

- [56] M. Meroni, M. Rossini, L. Guanter, L. Alonso, U. Rascher, R. Colombo and J. Moreno, Remote sensing of solar-induced chlorophyll fluorescence: review of methods and applications, *Remote Sens. Environ.* **2009**, *113*, 2037-2051.
- [57] S. He, B. Song, D. Li, C. Zhu, W. Qi, Y. Wen, L. Wang, S. Song, H. Fang and C. Fan, A graphene nanoprobe for rapid, sensitive, and multicolor fluorescent DNA analysis, *Adv. Funct. Mater.* **2010**, *20*, 453-459.
- [58] Y. Liu, K. Ai and L. Lu, Designing lanthanide-doped nanocrystals with both up- and down-conversion luminescence for anti-counterfeiting, *Nanoscale* **2011**, *3*, 4804-4810.
- [59] Z. Gao, Y. Han and F. Wang, Cooperative supramolecular polymers with anthraceneendoperoxide photo-switching for fluorescent anti-counterfeiting, *Nat. Commun.* **2018**, *9*, 1-9.
- [60] V. Smil, Power density: a key to understanding energy sources and uses, MIT press, Cambridge, **2015**.
- [61] M. G. Debije and P. P. Verbunt, Thirty years of luminescent solar concentrator research: solar energy for the built environment, *Adv. Energy Mater.* **2012**, *2*, 12-35.
- [62] A. Reinders, P. Verlinden, W. Van Sark and A. Freundlich, The luminescent solar concentrator (LSC), in *Photovoltaic Solar Energy: From Fundamentals to Applications*, John Wiley & Sons, **2017**, pp. 420-430.
- [63] S. Flores Daorta, A. Proto, R. Fusco, L. Claudio Andreani and M. Liscidini, Cascade luminescent solar concentrators, *Appl. Phys. Lett.* **2014**, *104*, 1539011-1539014.
- [64] R. Turrisi, A. Sanguineti, M. Sassi, B. Savoie, A. Takai, G. E. Patriarca, M. M. Salamone, R. Ruffo, G. Vaccaro and F. Meinardi, Stokes shift/emission efficiency trade-off in donor-acceptor perylenemonoimides for luminescent solar concentrators, *J. Mater. Chem. A* **2015**, *3*, 8045-8054.
- [65] F. De Nisi, R. Francischello, A. Battisti, A. Panniello, E. Fanizza, M. Striccoli, X. Gu, N. Leung, B. Tang and A. Pucci, Red-emitting AIEgen for luminescent solar concentrators, *Mater. Chem. Front.* **2017**, *1*, 1406-1412.
- [66] B. McKenna and R. C. Evans, Towards efficient spectral converters through materials design for luminescent solar devices, *Adv. Mater.* **2017**, *29*, 1-23.
- [67] M. J. Frisch, G. W. Trucks, H. B. Schlegel, G. E. Scuseria, M. A. Robb, J. R. Cheeseman, G. Scalmani, V. Barone, G. A. Petersson, H. Nakatsuji, X. Li, M. Caricato, A. V. Marenich, J. Bloino, B. G. Janesko, R. Gomperts, B. Mennucci, H. P. Hratchian, J. V. Ortiz, A. F. Izmaylov, J. L. Sonnenberg, D. Williams-Young, F. Ding, F. Lipparini, F. Egidi, J. Goings, B. Peng, A. Petrone, T. Henderson, D. Ranasinghe, V. G. Zakrzewski, J. Gao, N. Rega, G. Zheng, W. Liang, M. Hada, M. Ehara, K. Toyota, R. Fukuda, J. Hasegawa, M. Ishida, T. Nakajima, Y. Honda, O. Kitao, H. Nakai, T. Vreven, K. Throssell, J. A. Montgomery, Jr., J. E. Peralta, F. Ogliaro, M. J. Bearpark, J. J. Heyd, E. N. Brothers, K. N. Kudin, V. N. Staroverov, T. A. Keith, R. Kobayashi, J. Normand, K. Raghavachari, A. P. Rendell, J. C. Burant, S. S. Iyengar, J. Tomasi, M. Cossi, J. M. Millam, M. Klene, C. Adamo, R. Cammi, J. W. Ochterski, R. L. Martin, K. Morokuma, O. Farkas, J. B. Foresman and D. J. Fox, Gaussian 16, Revision B.01, Gaussian Inc., Wallingford, CT, USA, **2016**.
- [68] Y. Zhao and D. G. Truhlar, The M06 suite of density functionals for main group thermochemistry, thermochemical kinetics, noncovalent interactions, excited states, and transition elements: two new functionals and systematic testing of four M06-class functionals and 12 other functionals, *Theor. Chem. Acc.* **2008**, *120*, 215-241.
- [69] Y. Zhao and D. G. Truhlar, Density functionals with broad applicability in chemistry, *Acc. Chem. Res.* **2008**, *41*, 157-167.
- [70] R. Li, J. Zheng and D. G. Truhlar, Density functional approximations for charge transfer excitations with intermediate spatial overlap, *Phys. Chem. Chem. Phys.* **2010**, *12*, 12697-12701.
- [71] K. A. Peterson, D. Figgen, E. Goll, H. Stoll and M. Dolg, Systematically convergent basis sets with relativistic pseudopotentials. II. Small-core pseudopotentials and correlation consistent basis sets for the post-d group 16-18 elements, *J. Chem. Phys.* **2003**, *119*, 11113-11123.
- [72] G. A. Petersson and M. A. Al - Laham, A complete basis set model chemistry. II. Open - shell systems and the total energies of the first - row atoms, *J. Chem. Phys.* **1991**, *94*, 6081-6090.
- [73] G. A. Petersson, A. Bennett, T. G. Tensfeldt, M. A. Al - Laham, W. A. Shirley and J. Mantzaris, A complete basis set model chemistry. I. The total energies of closed - shell atoms and hydrides of the first - row elements, *J. Chem. Phys.* **1988**, *89*, 2193-2218.
- [74] C. J. Cramer and D. G. Truhlar, Continuum solvation models, in *Solvent Effects and Chemical Reactivity*, Springer, Dordrecht, **2002**, pp. 1-80.
- [75] R. Bauernschmitt and R. Ahlrichs, Treatment of electronic excitations within the adiabatic approximation of time dependent density functional theory, *Chem. Phys. Lett.* **1996**, *256*, 454-464.
- [76] M. E. Casida, C. Jamorski, K. C. Casida and D. R. Salahub, Molecular excitation energies to high-lying bound states from time-dependent density-functional response theory: characterization and

- correction of the time-dependent local density approximation ionization threshold, *J. Chem. Phys.* **1998**, *108*, 4439-4449.
- [77] R. Dennington, T. A. Keith and J. M. Millam, GaussView, Version 6, Semichem Inc., Shawnee Mission, KS, USA, **2016**.
- [78] S. Benson, A. Fernandez, N. D. Barth, F. de Moliner, M. H. Horrocks, C. S. Herrington, J. L. Abad, A. Delgado, L. Kelly and Z. Chang, SCOTfluors: small, conjugatable, orthogonal, and tunable fluorophores for in vivo imaging of cell metabolism, *Angew. Chem.* **2019**, *131*, 6985-6989.
- [79] G.-G. Luo, H. Lu, Y.-H. Wang, J. Dong, Y. Zhao and R.-B. Wu, A D- π -A- π -A metal-free organic dye with improved efficiency for the application of solar energy conversion, *Dyes Pigm.* **2016**, *134*, 498-505.
- [80] F. Vollmer, W. Rettig and E. Birckner, Photochemical mechanisms producing large fluorescence Stokes shifts, *J. Fluoresc.* **1994**, *4*, 65-69.
- [81] L. R. Wilson, B. C. Rowan, N. Robertson, O. Moudam, A. C. Jones and B. S. Richards, Characterization and reduction of reabsorption losses in luminescent solar concentrators, *Appl. Opt.* **2010**, *49*, 1651-1661.
- [82] B. Zhang, H. Soleimaninejad, D. J. Jones, J. M. White, K. P. Ghiggino, T. A. Smith and W. W. Wong, Highly fluorescent molecularly insulated perylene diimides: effect of concentration on photophysical properties, *Chem. Mater.* **2017**, *29*, 8395-8403.
- [83] M. J. Currie, J. K. Mapel, T. D. Heidel, S. Goffri and M. A. Baldo, High-efficiency organic solar concentrators for photovoltaics, *Science* **2008**, *321*, 226-228.
- [84] C. H. Chou, J. K. Chuang and F. C. Chen, High-performance flexible waveguiding photovoltaics, *Sci. Rep.* **2013**, *3*, 1-8.
- [85] M. Gajic, F. Lisi, N. Kirkwood, T. A. Smith, P. Mulvaney and G. Rosengarten, Circular luminescent solar concentrators, *Sol. Energy* **2017**, *150*, 30-37.
- [86] H. Apostoleris, M. Chiesa and M. Stefancich, Improved transparency switching in paraffin-PDMS composites, *J. Mater. Chem. C* **2015**, *3*, 1371-1377.
- [87] M. G. Debije, J.-P. Teunissen, M. J. Kastelijn, P. P. Verbunt and C. W. Bastiaansen, The effect of a scattering layer on the edge output of a luminescent solar concentrator, *Sol. Energy Mater. Sol. Cells* **2009**, *93*, 1345-1350.
- [88] H. Liu, S. Li, W. Chen, D. Wang, C. Li, D. Wu, J. Hao, Z. Zhou, X. Wang and K. Wang, Scattering enhanced quantum dots based luminescent solar concentrators by silica microparticles, *Sol. Energy Mater. Sol. Cells* **2018**, *179*, 380-385.
- [89] G. D. Farquhar, J. R. Ehleringer and K. T. Hubick, Carbon isotope discrimination and photosynthesis, *Annu. Rev. Plant Biol.* **1989**, *40*, 503-537.
- [90] G. H. Krause and E. Weis, Chlorophyll fluorescence and photosynthesis: the basics, *Annu. Rev. Plant Biol.* **1991**, *42*, 313-349.
- [91] G. H. Mohammed, R. Colombo, E. M. Middleton, U. Rascher, C. van der Tol, L. Nedbal, Y. Goulas, O. Pérez-Priego, A. Damm and M. Meroni, Remote sensing of solar-induced chlorophyll fluorescence (SIF) in vegetation: 50 years of progress, *Remote Sens. Environ.* **2019**, *231*, 1-39.
- [92] U. Rinderle and H. K. Lichtenthaler, The chlorophyll fluorescence ratio F690/F735 as a possible stress indicator, in *Applications of Chlorophyll Fluorescence in Photosynthesis Research, Stress Physiology, Hydrobiology and Remote Sensing*, Springer, Dordrecht, **1988**, pp. 189-196.
- [93] J. Joiner, Y. Yoshida, A. Vasilkov and E. Middleton, First observations of global and seasonal terrestrial chlorophyll fluorescence from space, *Biogeosciences* **2011**, *8*, 637-651.
- [94] C. Frankenberg, J. B. Fisher, J. Worden, G. Badgley, S. S. Saatchi, J. E. Lee, G. C. Toon, A. Butz, M. Jung and A. Kuze, New global observations of the terrestrial carbon cycle from GOSAT: patterns of plant fluorescence with gross primary productivity, *Geophys. Res. Lett.* **2011**, *38*, 1-6.
- [95] J. Joiner, L. Guanter, R. Lindstrot, M. Voigt, A. Vasilkov, E. Middleton, K. Huemmrich, Y. Yoshida and C. Frankenberg, Global monitoring of terrestrial chlorophyll fluorescence from moderate spectral resolution near-infrared satellite measurements: methodology, simulations, and application to GOME-2, *Atmos. Meas. Tech.* **2013**, *6*, 2803-2823.
- [96] P. Köhler, L. Guanter and J. Joiner, A linear method for the retrieval of sun-induced chlorophyll fluorescence from GOME-2 and SCIAMACHY data, *Atmos. Meas. Tech.* **2015**, *8*, 2589-2608.
- [97] J. Joiner, Y. Yoshida, A. Vasilkov, E. Middleton, P. Campbell, Y. Yoshida and A. Huze, Filling-in of near-infrared solar lines by terrestrial fluorescence and other geophysical effects: simulations and space-based observations from SCIAMACHY and GOSAT, *Atmos. Meas. Tech.* **2012**, *5*, 809-829.
- [98] N. Khosravi, M. Vountas, V. V. Rozanov, A. Bracher, A. Wolanin and J. P. Burrows, Retrieval of terrestrial plant fluorescence based on the in-filling of far-red Fraunhofer lines using SCIAMACHY observations, *Front. Environ. Sci.* **2015**, *3*, 1-15.

- [99] C. Frankenberg, C. O'Dell, J. Berry, L. Guanter, J. Joiner, P. Köhler, R. Pollock and T. E. Taylor, Prospects for chlorophyll fluorescence remote sensing from the Orbiting Carbon Observatory-2, *Remote Sens. Environ.* **2014**, *147*, 1-12.
- [100] L. Guanter, I. Aben, P. Tol, J. Krijger, A. Hollstein, P. Köhler, A. Damm, J. Joiner, C. Frankenberg and J. Landgraf, Potential of the TROPOspheric Monitoring Instrument (TROPOMI) onboard the Sentinel-5 Precursor for the monitoring of terrestrial chlorophyll fluorescence, *Atmos. Meas. Tech.* **2015**, *8*, 1337-1352.
- [101] S. Kraft, U. Del Bello, M. Bouvet, M. Drusch and J. Moreno, FLEX: ESA's Earth Explorer 8 candidate mission, in *2012 IEEE International Geoscience and Remote Sensing Symposium*, IEEE, Munich, Germany, **2012**, pp. 7125-7128.
- [102] R. Giasson, E. J. Lee, X. Zhao and M. S. Wrighton, Inter- and intramolecular quenching of the singlet excited state of porphyrins by ferrocene, *J. Phys. Chem.* **1993**, *97*, 2596-2601.
- [103] S. Fery-Forgues and B. Delavaux-Nicot, Ferrocene and ferrocenyl derivatives in luminescent systems, *J. Photochem. Photobiol. A* **2000**, *132*, 137-159.
- [104] T. Yui, T. Tsuchino, T. Itoh, M. Ogawa, Y. Fukushima and K. Takagi, Photoinduced one-electron reduction of MV²⁺ in titania nanosheets using porphyrin in mesoporous silica thin films, *Langmuir* **2005**, *21*, 2644-2646.
- [105] M. A. Jhonsi and A. Kathiravan, Oxidative fluorescence quenching of Mg-phthalocyanine by quinones, *J. Mol. Liq.* **2014**, *194*, 188-192.
- [106] M. Durmuş and T. Nyokong, Photophysical and fluorescence quenching studies of benzyloxyphenoxy-substituted zinc phthalocyanines, *Spectrochim. Acta A Mol. Biomol. Spectrosc.* **2008**, *69*, 1170-1177.
- [107] H. Clavier and S. P. Nolan, Percent buried volume for phosphine and N-heterocyclic carbene ligands: steric properties in organometallic chemistry, *Chem. Commun.* **2010**, *46*, 841-861.
- [108] D. Nuevo, M. Poyatos and E. Peris, A dinuclear Au(I) complex with a pyrene-di-N-heterocyclic carbene linker: supramolecular and catalytic studies, *Organometallics* **2018**, *37*, 3407-3411.
- [109] W. Liu and R. Gust, Metal N-heterocyclic carbene complexes as potential antitumor metallodrugs, *Chem. Soc. Rev.* **2013**, *42*, 755-773.
- [110] R. Visbal and M. C. Gimeno, N-heterocyclic carbene metal complexes: photoluminescence and applications, *Chem. Soc. Rev.* **2014**, *43*, 3551-3574.
- [111] M.-C. Tang, C.-H. Lee, M. Ng, Y.-C. Wong, M.-Y. Chan and V. W.-W. Yam, Highly emissive fused heterocyclic alkynylgold(III) complexes for multiple color emission spanning from green to red for solution-processable organic light-emitting devices, *Angew. Chem. Int. Ed.* **2018**, *57*, 5463-5466.
- [112] V. W.-W. Yam, V. K.-M. Au and S. Y.-L. Leung, Light-emitting self-assembled materials based on d⁸ and d¹⁰ transition metal complexes, *Chem. Rev.* **2015**, *115*, 7589-7728.
- [113] M. Nielsen, Sonogashira-like coupling reactions with phosphine-gold(I) alkynyl complexes, *Synthesis* **2016**, *48*, 2732-2738.
- [114] S. K. Fung, T. Zou, B. Cao, P.-Y. Lee, Y. M. E. Fung, D. Hu, C.-N. Lok and C.-M. Che, Cyclometalated gold(III) complexes containing N-heterocyclic carbene ligands engage multiple anti-cancer molecular targets, *Angew. Chem.* **2017**, *129*, 3950-3954.
- [115] R. McCall, M. Miles, P. Lascuna, B. Burney, Z. Patel, K. J. Sidoran, V. Sittaramane, J. Kocerha, D. A. Grossie, J. L. Sessler, K. Arumugam and J. F. Arambula, Dual targeting of the cancer antioxidant network with 1,4-naphthoquinone fused Gold(I) N-heterocyclic carbene complexes, *Chem. Sci.* **2017**, *8*, 5918-5929.
- [116] W. Lu, W.-M. Kwok, C. Ma, C. T.-L. Chan, M.-X. Zhu and C.-M. Che, Organic triplet excited states of gold(I) complexes with oligo(o-orm-phenyleneethynylene) ligands: conjunction of steady-state and time-resolved spectroscopic studies on exciton delocalization and emission pathways, *J. Am. Chem. Soc.* **2011**, *133*, 14120-14135.
- [117] A. L.-F. Chow, M.-H. So, W. Lu, N. Zhu and C.-M. Che, Synthesis, photophysical properties, and molecular aggregation of gold(I) complexes containing carbon-donor ligands, *Chem.-Asian J.* **2011**, *6*, 544-553.
- [118] E. Y.-H. Hong, H.-L. Wong and V. W.-W. Yam, From spherical to leaf-like morphologies: tunable supramolecular assembly of alkynylgold(I) complexes through variations of the alkyl chain length, *Chem.-Eur. J.* **2015**, *21*, 5732-5735.
- [119] S. Ibáñez and E. Peris, Chemically tunable formation of different discrete, oligomeric, and polymeric self-assembled structures from digold metallotweezers, *Chem.-Eur. J.* **2018**, *24*, 8424-8431.
- [120] S. Ibáñez and E. Peris, A rigid trigonal-prismatic hexagold metallocage that behaves as a coronene trap, *Angew. Chem. Int. Ed.* **2019**, *58*, 6693-6697.

- [121] F. K.-W. Hau, K.-L. Cheung, N. Zhu and V. W.-W. Yam, Calixarene-based alkynyl-bridged gold(i) isocyanide and phosphine complexes as building motifs for the construction of chemosensors and supramolecular architectures, *Org. Chem. Front.* **2019**, *6*, 1205-1213.
- [122] V. W.-W. Yam and E. C.-C. Cheng, Highlights on the recent advances in gold chemistry-a photophysical perspective, *Chem. Soc. Rev.* **2008**, *37*, 1806-1813.
- [123] S.-K. Yip, E. C.-C. Cheng, L.-H. Yuan, N. Zhu and V. W.-W. Yam, Supramolecular assembly of luminescent gold(I) alkynylcalix[4]crown-6 complexes with planar η^2, η^2 -coordinated gold(I) centers, *Angew. Chem. Int. Ed.* **2004**, *43*, 4954-4957.
- [124] K. M.-C. Wong, X. Zhu, L.-L. Hung, N. Zhu, V. W.-W. Yam and H.-S. Kwok, A novel class of phosphorescent gold(iii) alkynyl-based organic light-emitting devices with tunable colour, *Chem. Commun.* **2005**, *23*, 2906-2908.
- [125] L. Gao, D. V. Partyka, J. B. Updegraff, N. Deligonul and T. G. Gray, Synthesis, structures, and excited-state geometries of alkynylgold(I) complexes, *Eur. J. Inorg. Chem.* **2009**, *2009*, 2711-2719.
- [126] A. A. Penney, V. V. Sizov, E. V. Grachova, D. V. Krupenya, V. V. Gurzhiy, G. L. Starova and S. P. Tunik, Auophilicity in action: fine-tuning the gold(I)-gold(I) distance in the excited state to modulate the emission in a series of dinuclear homoleptic gold(I)-NHC complexes, *Inorg. Chem.* **2016**, *55*, 4720-4732.
- [127] P.-H. Lanoë, B. Najjari, F. Hallez, G. Gontard and H. Amouri, N-heterocyclic carbene coinage metal complexes containing naphthalimide chromophore: design, structure, and photophysical properties, *Inorganics* **2017**, *5*, 1-11.
- [128] P.-H. Lanoë, J. Chan, A. Groué, G. Gontard, A. Jutand, M.-N. Rager, N. Armaroli, F. Monti, A. Barbieri and H. Amouri, Cyclometalated N-heterocyclic carbene iridium(iii) complexes with naphthalimide chromophores: a novel class of phosphorescent heteroleptic compounds, *Dalton Trans.* **2018**, *47*, 3440-3451.
- [129] P. Ai, M. Mauro, A. A. Danopoulos, A. Muñoz-Castro and P. Braunstein, Dual emission of a cyclic hexanuclear gold(I) complex. Interplay between Au₃ and Au₂ ligand-supported luminophores, *J. Phys. Chem. C* **2018**, *123*, 915-921.
- [130] C.-W. Hsu, C.-C. Lin, M.-W. Chung, Y. Chi, G.-H. Lee, P.-T. Chou, C.-H. Chang and P.-Y. Chen, Systematic investigation of the metal-structure-photophysics relationship of emissive d10-complexes of group 11 elements: the prospect of application in organic light emitting devices, *J. Am. Chem. Soc.* **2011**, *133*, 12085-12099.
- [131] R. H. Blessing, An empirical correction for absorption anisotropy, *Acta Crystallogr. A: Found. Crystallogr.* **1995**, *51*, 33-38.
- [132] G. M. Sheldrick, A short history of SHELX, *Acta Crystallogr. A: Found. Crystallogr.* **2007**, *64*, 112-122.
- [133] L. J. Farrugia, WinGXsuite for small-molecule single-crystal crystallography, *J. Appl. Crystallogr.* **1999**, *32*, 837-838.
- [134] M. Montalti, A. Credi, L. Prodi and M. T. Gandolfi, in *Handbook of photochemistry*, CRC Press, Boca Raton, FL, **2006**, p. 572-575.
- [135] F. Prat, R. Stackow, R. Bernstein, W. Qian, Y. Rubin and C. S. Foote, Triplet-state properties and singlet oxygen generation in a homologous series of functionalized fullerene derivatives, *J. Phys. Chem. A* **1999**, *103*, 7230-7235.
- [136] M. M. Francl, W. J. Pietro, W. J. Hehre, J. S. Binkley, M. S. Gordon, D. J. DeFrees and J. A. Pople, Self-consistent molecular orbital methods. XXIII. A polarization-type basis set for second-row elements, *J. Chem. Phys.* **1982**, *77*, 3654-3665.
- [137] D. Andrae, U. Huermann, M. Dolg, H. Stoll and H. Preu, Energy-adjusted ab initio pseudopotentials for the second and third row transition elements, *Theor. Chim. Acta* **1990**, *77*, 123-141.
- [138] R. E. Stratmann, G. E. Scuseria and M. J. Frisch, An efficient implementation of time-dependent density-functional theory for the calculation of excitation energies of large molecules, *J. Chem. Phys.* **1998**, *109*, 8218-8224.
- [139] A. Gutiérrez-Blanco, V. Fernández-Moreira, M. C. Gimeno, E. Peris and M. Poyatos, Tetra-Au(I) complexes bearing a pyrene tetraalkynyl connector behave as fluorescence torches, *Organometallics* **2018**, *37*, 1795-1800.
- [140] T. J. Robilotto, N. Deligonul, J. B. Updegraff and T. G. Gray, Azido, triazolyl, and alkynyl complexes of gold(I): syntheses, structures, and ligand effects, *Inorg. Chem.* **2013**, *52*, 9659-9668.
- [141] K. T. Chan, G. S. M. Tong, W.-P. To, C. Yang, L. Du, D. L. Phillips and C.-M. Che, The interplay between fluorescence and phosphorescence with luminescent gold(i) and gold(iii) complexes bearing heterocyclic arylacetylides ligands, *Chem. Sci.* **2017**, *8*, 2352-2364.

- [142] Y. Kuroda, S.-y. Nakamura, K. Srinivas, A. Sathyanarayana, G. Prabusankar, K. Hisano and O. Tsutsumi, Thermochemically stable liquid-crystalline gold(I) complexes showing enhanced room temperature phosphorescence, *Crystals* **2019**, *9*, 1-13.
- [143] S. Wan and W. Lu, Reversible photoactivated phosphorescence of gold(I) arylethynyl complexes in aerated DMSO solutions and gels, *Angew. Chem. Int. Ed.* **2017**, *56*, 1784-1788.
- [144] M. Kriechbaum, G. Winterleitner, A. Gerisch, M. List and U. Monkowius, Synthesis, characterization and luminescence of gold complexes bearing an NHC ligand based on the imidazo[1,5-a]quinolinol scaffold, *Eur. J. Inorg. Chem.* **2013**, *2013*, 5567-5575.
- [145] J. L. Banal, K. P. Ghigginio and W. W. Wong, Efficient light harvesting of a luminescent solar concentrator using excitation energy transfer from an aggregation-induced emitter, *Phys. Chem. Chem. Phys.* **2014**, *16*, 25358-25363.
- [146] F. Meinardi, A. Colombo, K. A. Velizhanin, R. Simonutti, M. Lorenzon, L. Beverina, R. Viswanatha, V. I. Klimov and S. Brovelli, Large-area luminescent solar concentrators based on 'Stokes-shift-engineered' nanocrystals in a mass-polymerized PMMA matrix, *Nat. Photonics* **2014**, *8*, 392-399.
- [147] A. Gavriluta, T. Fix, A. Nonat, A. Slaoui, J.-F. Guillemoles and L. J. Charbonnière, Tuning the chemical properties of europium complexes as downshifting agents for copper indium gallium selenide solar cells, *J. Mater. Chem. A* **2017**, *5*, 14031-14040.
- [148] R. P. Feynman, There's plenty of room at the bottom, *Eng. Sci.* **1960**, *23*, 22-36.
- [149] R. P. Feynman, The wonders that await a micro-microscope, *Sat. Rev.* **1960**, *43*, 45-47.
- [150] V. Balzani, A. Credi, F. M. Raymo and J. F. Stoddart, Artificial molecular machines, *Angew. Chem. Int. Ed.* **2000**, *39*, 3348-3391.
- [151] V. Balzani, Nanoscience and nanotechnology: The bottom-up construction of molecular devices and machines, *Pure Appl. Chem.* **2008**, *80*, 1631-1650.
- [152] Y. B. Zheng, B. Kiraly and T. J. Huang, Molecular machines drive smart drug delivery, *Nanomedicine* **2010**, *5*, 1309-1312.
- [153] S. Ø. Scottwell and J. D. Crowley, Ferrocene-containing non-interlocked molecular machines, *Chem. Commun.* **2016**, *52*, 2451-2464.
- [154] J.-P. Collin, C. Dietrich-Buchecker, P. Gaviña, M. C. Jimenez-Molero and J.-P. Sauvage, Shuttles and muscles: linear molecular machines based on transition metals, *Acc. Chem. Res.* **2001**, *34*, 477-487.
- [155] K. Kinbara, T. Muraoka and T. Aida, Chiral ferrocenes as novel rotary modules for molecular machines, *Org. Biomol. Chem.* **2008**, *6*, 1871-1876.
- [156] A. G. Stewart, E. M. Laming, M. Sobti and D. Stock, Rotary ATPases-dynamic molecular machines, *Curr. Opin. Struct. Biol.* **2014**, *25*, 40-48.
- [157] M. Schliwa and G. Woehlke, Molecular motors, *Nature* **2003**, *422*, 759-765.
- [158] S. Kassem, T. van Leeuwen, A. S. Lubbe, M. R. Wilson, B. L. Feringa and D. A. Leigh, Artificial molecular motors, *Chem. Soc. Rev.* **2017**, *46*, 2592-2621.
- [159] V. Balzani, A. Credi and M. Venturi, Light powered molecular machines, *Chem. Soc. Rev.* **2009**, *38*, 1542-1550.
- [160] S. Silvi, M. Venturi and A. Credi, Light operated molecular machines, *Chem. Commun.* **2011**, *47*, 2483-2489.
- [161] D. K. Frantz, A. Linden, K. K. Baldrige and J. S. Siegel, Molecular spur gears comprising triptycene rotators and bibenzimidazole-based stators, *J. Am. Chem. Soc.* **2012**, *134*, 1528-1535.
- [162] H. Ube, Y. Yasuda, H. Sato and M. Shionoya, Metal-centred azaphosphatriptycene gear with a photo- and thermally driven mechanical switching function based on coordination isomerism, *Nat. Commun.* **2017**, *8*, 1-6.
- [163] U. G. E. Perera, F. Ample, H. Kersell, Y. Zhang, G. Vives, J. Echeverria, M. Grisolia, G. Rapenne, C. Joachim and S. W. Hla, Controlled clockwise and anticlockwise rotational switching of a molecular motor, *Nat. Nanotechnol.* **2012**, *8*, 46-51.
- [164] C. Kammerer and G. Rapenne, Scorpionate hydrotris(indazolyl)borate ligands as tripodal platforms for surface-mounted molecular gears and motors, *Eur. J. Inorg. Chem.* **2016**, *2016*, 2214-2226.
- [165] G. Erbland, S. Abid, Y. Gisbert, N. Saffon-Merceron, Y. Hashimoto, L. Andreoni, T. Guérin, C. Kammerer and G. Rapenne, Star-shaped ruthenium complexes as prototypes of molecular gears, *Chem.-Eur. J.* **2019**, *25*, 16328-16339.
- [166] S. R. Meech and D. Phillips, Photophysics of some common fluorescence standards, *J. Photochem.* **1983**, *23*, 193-217.
- [167] C. A. DeRosa, C. Kerr, Z. Fan, M. Kolpaczynska, A. S. Mathew, R. E. Evans, G. Zhang and C. L. Fraser, Tailoring oxygen sensitivity with halide substitution in difluoroboron dibenzoylmethane polylactide materials, *ACS Appl. Mater. Inter.* **2015**, *7*, 23633-23643.

- [168] W. Chen, S. Zhang, G. Dai, Y. Chen, M. Li, X. Zhao, Y. Chen and L. Chen, Tuning the photophysical properties of symmetric squarylium dyes: investigation on the halogen modulation effects, *Chem.-Eur. J.* **2019**, *25*, 469-473.
- [169] Z.-J. Yao and W. Deng, Half-sandwich late transition metal complexes based on functionalized carborane ligands, *Coord. Chem. Rev.* **2016**, *309*, 21-35.
- [170] M. Schulze, A. Steffen and F. Würthner, Near-IR phosphorescent ruthenium(II) and iridium(III) perylene bisimide metal complexes, *Angew. Chem. Int. Ed.* **2015**, *54*, 1570-1573.
- [171] D. B. Grotjahn, D. B. Brown, J. K. Martin, D. C. Marelius, M.-C. Abadjian, H. N. Tran, G. Kalyuzhny, K. S. Vecchio, Z. G. Specht, S. A. Cortes-Llamas, V. Miranda-Soto, C. van Niekerk, C. E. Moore and A. L. Rheingold, Evolution of iridium-based molecular catalysts during water oxidation with ceric ammonium nitrate, *J. Am. Chem. Soc.* **2011**, *133*, 19024-19027.
- [172] E. Peris, Smart N-heterocyclic carbene ligands in catalysis, *Chem. Rev.* **2017**, *118*, 9988-10031.
- [173] J. L. Gomez-Lopez, D. Chávez, M. Parra-Hake, A. T. Royappa, A. L. Rheingold, D. B. Grotjahn and V. Miranda-Soto, Synthesis and reactivity of bis(protic N-heterocyclic carbene)iridium(III) complexes, *Organometallics* **2016**, *35*, 3148-3153.
- [174] W. Ma, L. Guo, Z. Tian, S. Zhang, X. He, J. Li, Y. Yang and Z. Liu, Rhodamine-modified fluorescent half-sandwich iridium and ruthenium complexes: potential application as bioimaging and anticancer agents, *Dalton Trans.* **2019**, *48*, 4788-4793.
- [175] Y. Yang, L. Guo, Z. Tian, Y. Gong, H. Zheng, S. Zhang, Z. Xu, X. Ge and Z. Liu, Novel and versatile imine-N-heterocyclic carbene half-sandwich iridium(III) complexes as lysosome-targeted anticancer agents, *Inorg. Chem.* **2018**, *57*, 11087-11098.
- [176] S. Kuwata and F. E. Hahn, Complexes bearing protic N-heterocyclic carbene ligands, *Chem. Rev.* **2018**, *118*, 9642-9677.
- [177] A. Groué, J.-P. Tranchier, M.-N. Rager, G. Gontard, M. Jean, N. Vanthuyne, H. R. Pearce, A. L. Cooksy and H. Amouri, Unique class of enantiopure N-heterocyclic carbene half-sandwich iridium(III) complexes with stable configurations: probing five-membered versus six-membered iridacycles, *Inorg. Chem.* **2019**, *58*, 2930-2933.
- [178] E. Matteucci, F. Monti, R. Mazzoni, A. Baschieri, C. Bizzarri and L. Sambri, Click-derived triazolylidenes as chelating ligands: achievement of a neutral and luminescent iridium(III)-triazolide complex, *Inorg. Chem.* **2018**, *57*, 11673-11686.
- [179] M. Mydlak, C. Bizzarri, D. Hartmann, W. Sarfert, G. Schmid and L. De Cola, Positively charged iridium(III) triazole derivatives as blue emitters for light-emitting electrochemical cells, *Adv. Funct. Mater.* **2010**, *20*, 1812-1820.
- [180] Y.-F. Han, W.-G. Jia, W.-B. Yu and G.-X. Jin, Stepwise formation of organometallic macrocycles, prisms and boxes from Ir, Rh and Ru-based half-sandwich units, *Chem. Soc. Rev.* **2009**, *38*, 3419-3434.
- [181] C.-H. Yang, J. Beltran, V. Lemaur, J. Cornil, D. Hartmann, W. Sarfert, R. Fröhlich, C. Bizzarri and L. De Cola, Iridium metal complexes containing N-heterocyclic carbene ligands for blue-light-emitting electrochemical cells, *Inorg. Chem.* **2010**, *49*, 9891-9901.
- [182] K. K.-W. Lo, Luminescent rhenium(I) and iridium(III) polypyridine complexes as biological probes, imaging reagents, and photocytotoxic agents, *Acc. Chem. Res.* **2015**, *48*, 2985-2995.
- [183] C. Johnson and M. Albrecht, Piano-stool N-heterocyclic carbene iron complexes: Synthesis, reactivity and catalytic applications, *Coord. Chem. Rev.* **2017**, *352*, 1-14.
- [184] W. C. H. Choy, W. K. Chan and Y. Yuan, Recent advances in transition metal complexes and light-management engineering in organic optoelectronic devices, *Adv. Mater.* **2014**, *26*, 5368-5399.
- [185] N. Thejo Kalyani and S. J. Dhoble, Organic light emitting diodes: energy saving lighting technology-a review, *Renew. Sust. Energ. Rev.* **2012**, *16*, 2696-2723.
- [186] H. Xiang, J. Cheng, X. Ma, X. Zhou and J. J. Chruma, Near-infrared phosphorescence: materials and applications, *Chem. Soc. Rev.* **2013**, *42*, 6128-6185.
- [187] D. A. Valyaev, O. A. Filippov, N. Lugan, G. Lavigne and N. A. Ustynyuk, Umpolung of methylenephosphonium ions in their manganese half-sandwich complexes and application to the synthesis of chiral phosphorus-containing ligand scaffolds, *Angew. Chem.* **2015**, *127*, 6413-6417.
- [188] Y.-F. Han and G.-X. Jin, Half-sandwich iridium- and rhodium-based organometallic architectures: rational design, synthesis, characterization, and applications, *Acc. Chem. Res.* **2014**, *47*, 3571-3579.
- [189] S. Gao, B. Balan, K. Yoosaf, F. Monti, E. Bandini, A. Barbieri and N. Armaroli, Highly efficient luminescent solar concentrators based on benzoheterodiazole dyes with large Stokes shifts, *Chem.-Eur. J.* **2020**, *26*, 11013-11023.
- [190] P. J. Hay and W. R. Wadt, Ab initio effective core potentials for molecular calculations. Potentials for the transition metal atoms Sc to Hg, *J. Chem. Phys.* **1985**, *82*, 270-283.
- [191] J. Tomasi and M. Persico, Molecular interactions in solution: an overview of methods based on continuous distributions of the solvent, *Chem. Rev.* **1994**, *94*, 2027-2094.

[192] A. K. Srivastava, A. Singh and L. Mishra, Tuning of aggregation enhanced emission and solid state emission from 1,8-naphthalimide derivatives: nanoaggregates, spectra, and DFT calculations, *J. Phys. Chem. A* **2016**, *120*, 4490-4504.

Acknowledgements

There are many people I am indebted with for their kind support and patient guidance during my PhD studies. First, special thanks are due to my supervisors Nicola Armaroli and Letizia Sambri, who gave me the chance to carry out my PhD project in Bologna and kindly guided my study and work. Great thanks to Andrea Barbieri and Filippo Monti for the help and assistance in my experimental work and daily life. I would also like to thank Barbara Ventura, Alessandro Venturini, Elisa Bandini and Enrico Leoni for their help in the different aspects of my PhD program. Of course, I also thank my colleagues, friends and family for their support and company. My deep gratitude goes to the China Scholarship Council (CSC) for my PhD fellowship (file n. 201706870014).

In the cooperation with CSIR-NIIST, CNR-IBIMET, Renner Italia S.p.A., IPCM-CNRS and CEMES-CNRS, I would like thank to Bamisha Balan and Karuvath Yoosaf for their provision of the benzoheterodiazole dyes in chapter 2; Luigi Benni, Lorenzo Genesio and Francesco Miglietta for the preparation and on field studies of the large-area calibration film in chapter 3; Hani Amouri's group for their design and synthesis of the NHC based Au, Ir and Rh metal complexes in chapter 4 and 6; Gwenael Rapenne's group for the preparation and delivery of the star-shaped molecular motors and the related ligands/moieties in chapter 5.